



Provided by the author(s) and University of Galway in accordance with publisher policies. Please cite the published version when available.

Title	An investigation into computational modelling strategies to predict the in vitro performance of aortic valve replacements
Author(s)	Whiting, Robert
Publication Date	2023-06-19
Publisher	NUI Galway
Item record	http://hdl.handle.net/10379/17819

Downloaded 2024-05-08T02:18:11Z

Some rights reserved. For more information, please see the item record link above.



**AN INVESTIGATION INTO COMPUTATIONAL
MODELLING STRATEGIES TO PREDICT THE IN
VITRO PERFORMANCE OF AORTIC VALVE
REPLACEMENTS**

Robert Whiting B.E.



OLLSCOIL NA GAILLIMHÉ

UNIVERSITY OF GALWAY

A thesis submitted to the University of Galway as fulfilment of the requirements for the
Degree of Doctor of Philosophy

2022

Discipline of Biomedical Engineering,
School of Engineering, College of Science and Engineering,
University of Galway

Supervisors of Research:

Dr. Ted J. Vaughan

Dr. Claire Conway

ABSTRACT

The development and design of effective aortic valve replacements (AVRs) presents significant challenges given the structural and hemodynamic performance requirements that must be achieved. Conventional design approaches require substantial amounts of experimental testing, involving complex pulsatile flow rigs that mimic the conditions of the cardiac cycle while allowing for accurate measurements of valve performance. While these experiments are extremely valuable, they are time-consuming and require multiple iterations of physical prototypes during the testing phase. Computational simulations could overcome these challenges, streamlining the design process and optimising the structural and hydrodynamic performance of AVRs under development. The objective of this thesis is to investigate the potential of computational modelling to predict hemodynamic and structural performance of aortic valves through a combined experimental-computational approach. In particular, the thesis investigates both finite element and fluid-structure interaction based approaches, implemented through Abaqus commercial software, and assesses their potential to robustly predict both the structural and hydrodynamic performance of AVRs.

In this thesis, a tri-leaflet polymeric AVR, which was developed at the University of Galway, formed the basis for both experimental and computational work. All devices were manufactured in-house through compression moulding and a series of experimental bench top studies were carried out using an in vitro pulsatile flow rig to investigate the hydrodynamic performance of different valve designs according to ISO 5840. In parallel, a finite element based computational framework was developed to predict the systolic and diastolic configurations from in vitro testing and a range of surrogate parameters were proposed to provide direct insight into the in vitro hydrodynamic performance. This approach was then used to examine the effects of asymmetric and regional calcification patterns on the stenosed hydrodynamics of the aortic valve. Finally, a fluid-structure interaction model was developed using the Abaqus Coupled Eulerian Lagrangian (CEL) approach to predict the structural and hydrodynamic performance of the AVRs and to investigate the potential to conduct in silico bench testing of valve devices. To enable this, a bench top rig was designed and manufactured to enable detailed measurements of leaflet deformation and serve as validation for the Fluid Structure Interaction (FSI) simulations conducted.

Through in vitro testing and in silico modelling, it was found that three-dimensional finite element modelling could be used as a predictor of the in vitro hydrodynamic performance of tri-leaflet aortic valve implants. Specifically, several surrogate measures were identified through regression analysis, whereby leaflet coaptation area, geometric orifice area and opening pressure were found to be suitable indicators of experimental in vitro hydrodynamic parameters of regurgitant fraction, effective orifice area and transvalvular pressure drop performance, respectively. This finite element framework was used to show that asymmetric and non-uniform calcification of aortic valves had a distinct effect on the predicted hydrodynamic performance, measured parameters and the indicated in vitro hydrodynamic performance. In particular, it was found that asymmetric calcification coverage was highly detrimental to the systolic Geometric Orifice Area (GOA), while symmetric calcification was actually more detrimental to diastolic parameters of diastolic GOA and Leaflet Coaptation Area (LCA). Finally, it was found that the Abaqus/CEL fluid-structure interaction approach could accurately predict experimentally observed leaflet deformations under two-dimensional flow conditions. In predicting the three-dimensional performance of a tri-leaflet valve, it was found that the computational model could capture certain features of the experimental performance across both a bicuspid and tricuspid valve, including peak systolic GOA, but failed to accurately capture bulk measures of performance that were present over the loading cycle (e.g. Effective Orifice Area (EOA)). This thesis highlights the distinct challenges in validating FSI-based models of structural and hydrodynamic performance of AVRs, while provided much-needed experimental data to this community.

LIST OF PUBLICATIONS

Journal Articles

The following publications have arisen from the work presented in this thesis:

- **Whiting, R.**, Sander, E., Conway, C., Vaughan, TJ., 2022. In-silico modelling of aortic valve implants—predicting in vitro performance using finite element analysis. *J. Med. Eng. Technol.* 46, 220–230. <https://doi.org/10.1080/03091902.2022.2026506>
Published
- **Whiting, R.**, Conway, C., Vaughan, TJ. In-silico modelling the effects of asymmetrical and regional calcification on aortic valve hemodynamics (2023). *In Preparation*
- Y. M., Fan, **Whiting, R.**, Conway, C., Vaughan, TJ., Roche, E., Benchmarking of FSI methods for Aortic Valve Modelling (2023). *In Preparation*

International Conference Proceedings

- Mcloone, M., Fan, Y., **Whiting, R.**, Conway, C., Roche, E., Quinlan, N. ‘Fluid-Structure Interaction of a Thin Elastic Leaflet – a Comparison of Computational Methods’, European Society of Biomechanics, 2021.
- **Whiting, R.**, Sander, E., Conway, C., Vaughan, TJ. ‘In-silico Modelling Of Aortic Valves – Can Finite Element Analysis Predict In Vitro Hydrodynamic Performance?’, 26th European Society of Biomechanics, accepted for presentation at the 26th European Society of Biomechanics conference, July 2020.
- **Whiting, R.**, Conway, C., Vaughan, TJ. ‘Design of a Polymeric Valve using a Combined Experimental and Computational Approach’, European Society of Biomechanics, July 2019, Vienna, Austria.

ACKNOWLEDGEMENTS

First, I would like to give my sincerest thanks to my supervisor Dr. Ted J. Vaughan for his vast contribution of knowledge, time and effort. His drive, passion for research, and reliability made sure I had direction and an example to follow. I am thankful for the many opportunities he encouraged me to take and his sound advice.

I would like to thank my co-supervisor Dr. Claire Conway for her support, expertise and for providing valuable opportunities through the MIT MISTI exchange and the RCSI. Thanks to Elle Sander and William Hickey for their collaboration and expertise in polymeric valves and experimental testing. Thanks to Yiling Fan and Dr. Ellen Roche for their collaboration and work together developing the benchtop flow rig.

Thanks to the University of Galway, the Royal College of Surgeons Ireland (RCSI) and Massachusetts Institute of Technology (MIT) for use of their facilities. To recognise my funding sources, the Hardiman Research Scholarship at the University of Galway, and the Irish Centre for High-End Computing (ICHEC) for the provision of essential computational facilities.

Thanks to all the members of the Vaughan and Ronan research groups and those on the third floor research office for your friendship and advice.

I would like to thank my parents, siblings and good friends for their motivation and support.

To my loving wife Amy, who brings out the best in me and has been by my side throughout the whole PhD. Thanks for your patience, support and love.

Finally, thanks to God.

DECLARATION OF ORIGINALITY

I declare that the work presented in this thesis is my own.

Robert Whiting

LIST OF COMMONLY USED ACRONYMS

ALE	Arbitrary Lagrangian Eulerian
AVA	Aortic Valve Area
AVR	Aortic Valve Replacement
BHV	Bioprosthetic Heart Valve
BPM	Beats Per Minute
CAVD	Calcific Aortic Valve Disease
CEL	Coupled Eulerian Lagrangian
CFD	Computational Fluid Dynamics
CO	Cardiac Output
EOA	Effective Orifice Area
FDA	Food and Drug Administration
FEA	Finite Element Analysis
FSI	Fluid Structure Interaction
GOA	Geometric Orifice Area
IB	Immersed Boundary
ISO	International Organisation for Standardisation
LCA	Leaflet Coaptation Area
MAP	Mean Aortic Pressure
MHV	Mechanical Heart Valve
RF	Regurgitant Fraction
SAVR	Surgical Aortic Valve Replacement
SV	Stroke Volume
TAVR	Transcatheter Aortic Valve Replacement
ΔP	Pressure Drop

TABLE OF CONTENTS

1. Introduction	10
1.1 Aortic Valve Disease.....	10
1.2 Aortic Valve Replacements.....	12
1.3 In Vitro Testing	14
1.4 Computational Modelling of Aortic Valve Biomechanics.....	16
1.4.1 Computational Fluid Dynamics and Finite Element Analysis	16
1.4.2 Fluid-Structure Interaction Modelling.....	17
1.5 Objectives.....	18
1.6 Thesis Structure.....	19
1.7 References	21
2. Literature Review	26
2.1 The Cardiac Cycle.....	26
2.2 Heart Valves.....	28
2.2.1 Aortic Valve Anatomy	29
2.2.2 Aortic Valve Tissue.....	30
2.2.3 Mechanical Properties of the Aortic Valve	31
2.2.4 Hemorheology	32
2.2.5 Aortic Valve Stenosis and Calcific Aortic Valve Disease	32
2.3 Aortic Valve Mechanics.....	36
2.3.1 Hemodynamics of Healthy and Stenosed Aortic Valve	36
2.4 Aortic Valve Replacements.....	39
2.4.1 Surgical Aortic Valve Replacements (SAVRs).....	40
2.4.2 Transcatheter Aortic Valve Replacements (TAVRs).....	43
2.4.3 Polymer Valve Technologies	45
2.5 Design and Testing of Aortic Valve Replacements	47
2.5.1 ISO 5840 Standard for Heart Valves.....	47
2.6 Computational Approaches for Aortic Valve Biomechanics.....	50
2.6.1 Structural Finite Element Modelling of Aortic Valves	50

2.6.2 Fluid-Structure Interaction Modelling of Aortic Valves	55
2.7 Conclusions	61
2.8 References	68
3. Theoretical Background	81
3.1 Continuum Mechanics	81
3.1.1 Notation	81
3.1.2 Deformation and Motion	82
3.1.3 Strain Measures	84
3.1.4 Stress Measures	85
3.2 Material Constitutive Behaviours	87
3.2.1 Elasticity	87
3.2.2 Isotropic Hyperelasticity	88
3.3 Finite Element Method.....	89
3.3.1 Implicit Finite Element Method	90
3.3.2 Explicit Finite Element Method	92
3.4 Navier Stokes	94
3.5 Immersed Boundary Method.....	94
3.6 References	96
4. In Silico Modelling of Aortic Valve Implants – Predicting in Vitro Performance using Finite Element Analysis	97
4.1 Introduction	97
4.2 Materials and Methods	101
4.2.1 Valve Design and Manufacture	101
4.2.2 In Vitro Testing	103
4.2.3 In Silico Modelling Framework	105
4.2.4 Surrogate hydrodynamic measures.....	108
4.3 Results	109
4.3.1 Evaluation of Valve Deformation	109
4.3.2 In Vitro Testing	110
4.3.3 Finite Element Analysis	112
4.3.4 Surrogate Measures	113
4.4 Discussion	114
4.5 Conclusions	118

4.6 References	119
5. An In Vitro and In Silico Investigation on the Effects of Calcification on Hydrodynamic Performance of Aortic Valves	123
5.1 Introduction	123
5.2 Materials and Methods	128
5.2.1 Valve Design and Manufacture	128
5.2.2 In Silico Model of Calcification Progression	129
5.2.3 In Vitro Testing of Stiffened Valve Hydrodynamics	131
5.2.4 In Silico Performance of Stiffened Valve	133
5.3 Results	135
5.3.1 In Vitro Testing	135
5.3.2 In Silico Analysis	137
5.4 Discussion	143
5.5 Conclusion.....	147
5.6 References	148
6. 2D Fluid-Structure Interaction Modelling of Aortic Leaflet Dynamics using the Abaqus Coupled Eulerian Lagrangian (CEL) Approach	152
6.1 Introduction	152
6.2 Materials and Methods	155
6.2.1 In Vitro Flow Rig Design, Build and Testing	155
6.2.2 Coupled Eulerian Lagrangian Fluid-Structure Interaction	158
6.2.3 Abaqus/CEL Modelling of In Silico 2D Valve Flow	166
6.3 Results	168
6.3.1 In Vitro and In Silico Fluid-Structure Interaction of Leaflet Deformation	168
6.3.2 Fluid-structure Interaction of a 2D Aortic Valve	172
6.3.3 Measurement of Hydrodynamic Parameters	174
6.4 Discussion	175
6.5 Conclusions	178
6.6 References	179
7. 3D Fluid-Structure Interaction Modelling of Bicuspid and Tricuspid Aortic Valve Hydrodynamic Performance	182
7.1 Introduction	182
7.2 Materials and Methods	185

7.2.1 Aortic Valve Design	185
7.2.2 In Vitro Hydrodynamic Testing	186
7.2.3 FSI Model Formulation	187
7.2.4 Hydrodynamic Parameters	190
7.3 Results	191
7.3.1 In Vitro and In Silico Comparison	191
7.3.2 In Silico Hydrodynamic Testing	193
7.3.3 Fluid and Structural In Silico Results.....	194
7.4 Discussion	197
7.5 Conclusions	200
7.6 References	202
8. Concluding Remarks and Future Perspectives	205
8.1 Summary of Key Contributions	205
8.2 Future Recommendations.....	208
8.3 References	211

CHAPTER 1

Introduction

1.1 Aortic Valve Disease

Aortic stenosis is a valvular heart disease, whereby calcification build-up on the native valve leaflets leads to decreased blood flow during the cardiac cycle (Adams et al., 2019). In Europe, it is estimated that ~10% of people over the age of 80 suffer from aortic stenosis, with this number expected to double by the year 2040 (Hartley et al., 2021). Aortic stenosis can result from rheumatic heart disease, or due to a congenital bicuspid aortic valve (Mordi and Tzemos, 2012), although the most common cause is due to calcific aortic valve disease (CAVD) (Otto et al., 1997). In CAVD, leaflet calcification is caused by native valvular interstitial cells acquiring a pro-calcific profile, due to calcium phosphate levels or low-density lipoprotein accumulation (Sun et al., 2013). This progressive calcification leads to stiffening of the aortic valve, which impedes the opening of the valve leaflets and restricts blood flow. CAVD can also result in blood flow regurgitation, whereby valve leaflets are unable to achieve full closure in the diastolic phase. This places increased pressure on the heart to maintain the required cardiac output, with patients experiencing left ventricular hypertrophy and potentially heart failure (Adams et al., 2019). Figure 1.1 shows examples of a minimally diseased and calcified valves.

It has been found that the progression of calcification of the native aortic valve follows regions of high strain (Arzani and Mofrad, 2017; Fisher et al., 2013; Weinberg et al., 2009) and is more likely to occur on the aortic side of the leaflets (Otto et al., 1997). Due to the complex mechanical environment of the native aorta, patterns are generally non-uniform and, in some instances, asymmetric (Larroche et al., 2020; Thubrikar et al., 1986). Figures 1.1C and D show clinical images of asymmetric calcification being observed (Larroche et al., 2020), whereby calcification has almost exclusively occurred on a single aortic leaflet. While it is well-known that valvular calcification leads to progressive stiffening and narrowing of the aortic valve orifice, there remain distinct challenges in clinical assessment of calcification and there is limited understanding of how non-uniform and/or asymmetric calcification of valve leaflets impacts hemodynamic performance.

In a clinical setting, the effect of CAVD can be determined using computed tomography (CT) imaging to quantify the presence and severity of calcification, however this approach provides limited insight into the actual performance of the native valve. Alternatively, Doppler echocardiography may be used to estimate the hemodynamic parameters of the valve (Baumgartner et al., 2009). This approach directly estimates the jet velocity and overall hemodynamic performance. It enables the aortic valve area (AVA) to be determined, which provides a quantitative metric for aortic stenosis, which is classified as mild for $AVA \geq 1.5 \text{ cm}^2$, moderate for $1.5 \text{ cm}^2 \geq AVA \geq 1.0 \text{ cm}^2$ or severe for $AVA < 1.0 \text{ cm}^2$. While additional parameters, such as transvalvular pressure drop (ΔP) and jet velocity, provide further guidance to clinicians on whether surgical intervention may be required, it remains critical that aortic stenosis and CAVD are treated early and efficiently due to the increased risk of fatality as the disease progresses (Padala et al., 2010). **While the current clinical approaches to assess valve performance provide bulk measures of calcification and hemodynamics, there remains a lack of understanding of the relationship between specific features of aortic**

stenosis, the progression of calcification, and overall hemodynamic performance of the native valve.

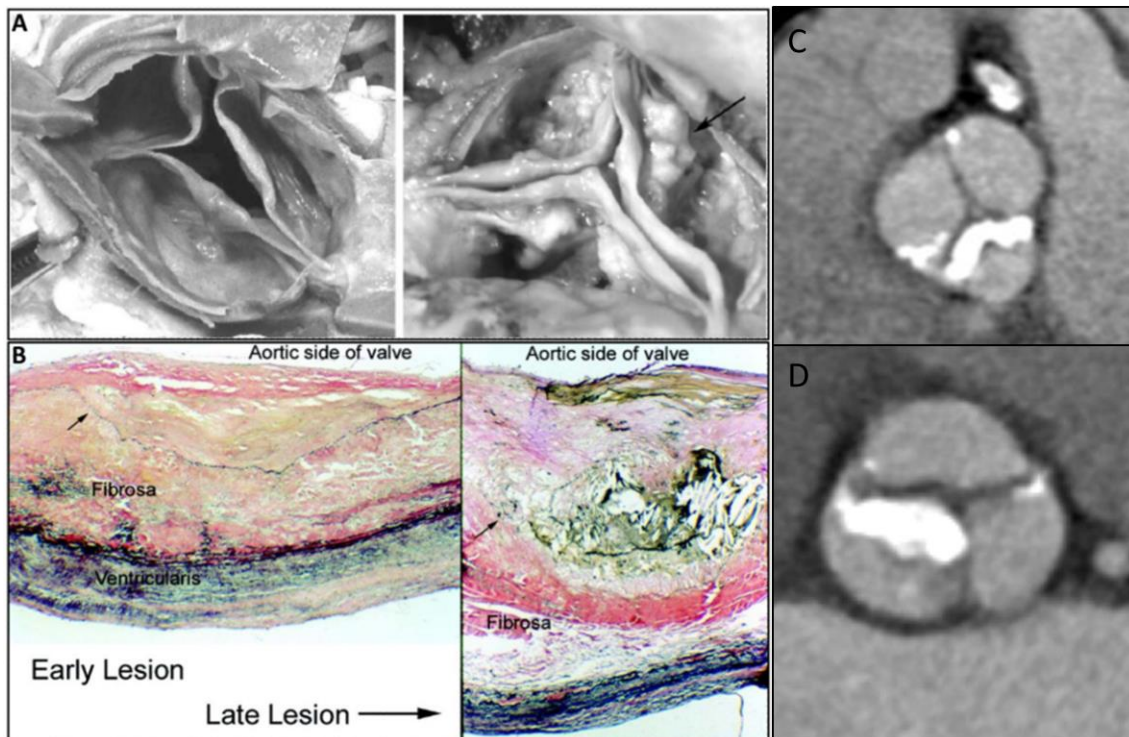


Figure 1.1 Images of aortic valve calcification, adapted from Zhiduleva et al. (2018). A) Minimally diseased valve (left) compared with severely diseased and calcified valve (right). B) Early stages of valve calcification (left) compared with late stage lesions (right). C, D) planar images of aortic calcification, with several in vivo examples of asymmetric calcification from Larroche et al. (2020)

1.2 Aortic Valve Replacements

Severe aortic stenosis is treated with either surgical or transcatheter aortic valve replacement (SAVR or TAVR). Over 300,000 valve replacements are performed globally each year (Manji et al., 2012). The complicated design of the native valve presents significant design challenges when developing an aortic valve replacement (AVR). Originally, the first valve replacements that were used clinically were mechanical valves, which included the Edwards-Starr ball-and-cage valve (Starr and Edwards, 1961). This was followed by the development of several hinge leaflet valves, with examples including the Medtronic Open Pivot Bileaflet and St Jude Medical Bileaflet (as shown in Figure 1.2a). In parallel, bioprosthetic heart valves (BHV) were being

developed, which are now widely used and consist of either bovine or porcine tissue leaflets treated with glutaraldehyde and mounted on a stent frame. These devices can be implanted surgically, although the recent trend has been towards minimally invasive delivery in the form of TAVR. While bioprosthetic devices have demonstrated positive clinical outcomes (Daubert et al., 2017), there is significant room for further design improvements to enhance structural durability and long-term hemodynamic performance. Durability is a problem, particularly in younger patients when the onset of structural valve degeneration can occur 10 to 15 years post-implantation, then requiring re-intervention (Bradley, 2013; Friedewald et al., 2007; Kostyunin et al., 2020; Nishimura et al., 2014). Recently, there has been increasing interest in developing synthetic polymer leaflets as an alternative to bioprosthetic tissue leaflets in both SAVR and TAVR devices. Several groups have developed polymer-based AVRs that have demonstrated promising results from in vitro (De Gaetano et al., 2015; Rahmani et al., 2017), pre-clinical (Rahmani et al., 2016; Stasiak et al., 2020) and clinical testing (Kereiakes et al., 2021). While these polymeric valve devices are at an earlier stage of development, they have the potential to provide superior patient outcomes, as well as vastly improved efficiency in the manufacturability and reproducibility of TAVR devices (Claiborne et al., 2013a; Rotman et al., 2019). However, several key issues arise in the development of polymer AVRs, such as the degradation of the polymer by hydrolysis affecting its mechanical properties (Ciolacu et al., 2022), thrombosis and the onset of calcification (Ghanbari et al., 2009; Kidane et al., 2009).

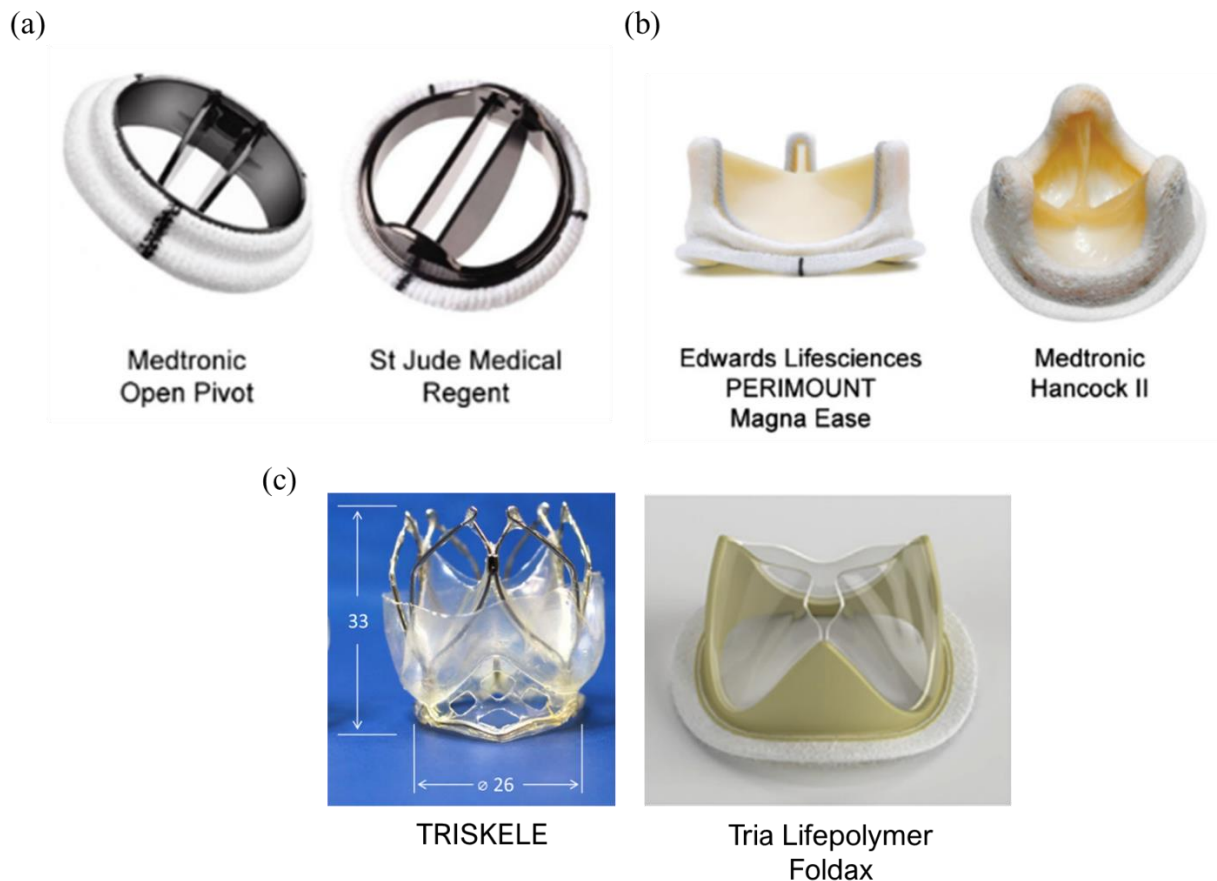


Figure 1.2 Examples of mechanical (a) and bioprosthetic (b) heart valves from major manufacturers, adapted from Kheradvar *et al.* (2015). (c) Polymeric heart valves in development (left) TRISKELE from Rahmani *et al.* (2017), (right) TRIA Lifepolymer, Foldax (Kereiakes *et al.*, 2021)

1.3 In Vitro Testing

The high performance required by AVRs means that each device must meet strict requirements that are set in the ISO 5840 standard series for “Cardiovascular implants — Cardiac valve prostheses” (International Organisation for Standardisation, 2021a, 2021b, 2021c). Part 1 (ISO 5840-1:2021) refers to the general requirements of cardiac valve design and outlines the selection of appropriate qualification tests and methods for heart valve substitutes. Part 2 (ISO 5840-2:2021) refers specifically to the implantation of surgical cardiac valves, while Part 3 (ISO 5840-3:2021) deals with transcatheter cardiac valve requirements. The ISO 5840 standard series outlines the preclinical testing conditions and physical parameters which are required for

approval by the FDA and EU governing bodies. Hydrodynamic and long-term durability testing are two of the key requirements for in vitro bench testing. These involve testing of AVR designs using pulsatile flow rigs that simulate left heart conditions, such as the Vivitro Pulse Duplicator shown in Figure 1.3. For hydrodynamic testing, the key parameters required by the ISO 5840 are the measurement of effective orifice area (EOA), regurgitant fraction (RF) and transvalvular ΔP . Many comprehensive studies comparing these parameters across valve designs have been carried out on commercial flow rigs (Rahmani et al., 2017, 2012; Rotman et al., 2019; Stasiak et al. 2020), which are also capable of investigating additional parameters such as the left ventricular energy loss and leakage volumes. These are further indicators of valve performance and are useful in the design process. While durability and hydrodynamic testing according to ISO 5840 provides a comprehensive assessment of the structural and hemodynamic performance of valves, the development pathway typically involves a trial-and-error process of design, prototyping and testing. Relying solely on this method contributes to high development costs and increased time to market for aortic valve devices.



Figure 1.3 Vivitro Pulse Duplicator, adapted from Sathananthan et al. (2019)

1.4 Computational Modelling of Aortic Valve Biomechanics

Computational modelling approaches are often used to aid the development of AVRs and optimise functional performance. These *in silico* approaches have the potential to reduce the scale of bench testing required, providing insight and optimisation into both structural and hemodynamic performance, thereby lowering development costs and reducing the overall time-to-market for devices. However, predicting the structural and hemodynamic behaviour of aortic valve implants *in silico* is a complex problem requiring the coupling of structural and fluid modelling techniques. Fluid-structure interaction (FSI) simulations have been developed and used to analyse valve kinematics (Luraghi et al. 2017), the flow profiles of valves and resulting wall shear stress (Kandail et al., 2018; Sodhani et al., 2018), as well as estimating the hemodynamic parameters of EOA, RF and transvalvular ΔP (Mao et al., 2016; Tango et al., 2018). The FSI approach is not without its drawbacks, as its complexity means it is difficult to implement and requires a large amount of computational power. As a result, uncoupled approaches have commonly been used to investigate the aortic valve (Claiborne et al., 2013b).

1.4.1 Computational Fluid Dynamics and Finite Element Analysis

Computational fluid dynamics (CFD) enables the analysis of hemodynamic flow through the valve and surrounding vessels, with the results of these simulations providing pressure contours, flow velocities, or local fluid parameters such as wall shear stress. For CFD simulations, it assumes that all boundaries are rigid, which means that valve opening, closing and/or deformation cannot be captured unless a moving wall condition is prescribed. As a result, CFD provides surprisingly limited information on the performance of AVRs in the context of the parameters specified in ISO 5840. These key parameters of EOA, transvalvular ΔP and RF are fundamental measures that are derived from valve opening and closing and require the structural deformation of the valve to be accounted for. As such, finite element analysis (FEA) provides a framework for structural simulations of the aortic valve, as shown

in Figure 1.4, allowing predictions of deformation and stress quantities under systolic and diastolic pressure conditions (Arcidiacono et al., 2005; Burriesci et al., 2010; Claiborne et al., 2013a; De Gaetano et al., 2015; Haj-Ali et al., 2008; Kim et al., 2008; Li and Sun, 2017, 2010; Serrani et al., 2016; Smuts et al., 2011). Several studies have already demonstrated how FEA can be used for structural optimisation of valve design, with a view to reducing fatigue and increasing durability (Claiborne et al., 2013a; Serrani et al., 2016; Smuts et al., 2011). However, very few studies have examined the potential of structural FEA valve modelling to examine the hemodynamic performance of the aortic valve. **Since the bulk hemodynamic parameters required by ISO 5840 are directly related to compliance of the valve, there is an opportunity to investigate the potential of FEA to provide insight into the hydrodynamic performance of AVRs.**

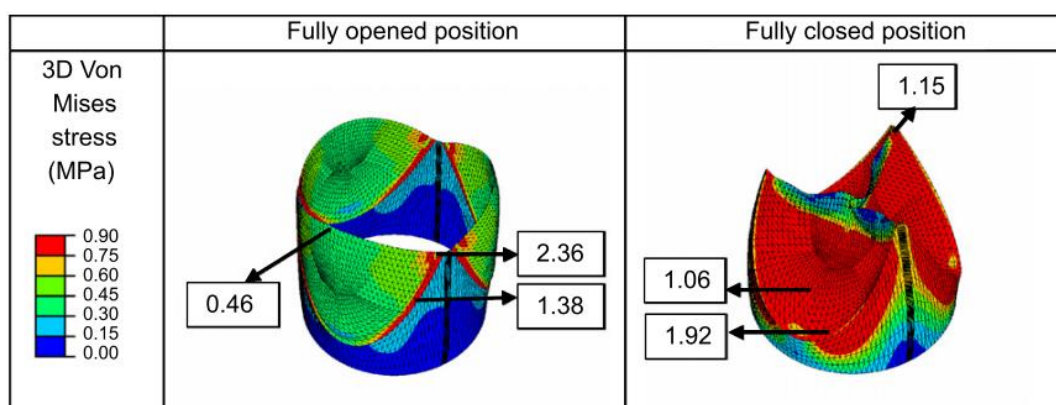


Figure 1.4 Structural von Mises stress analysis of an aortic valve at fully open and closed positions, adapted from Haj-Ali et al., (2008)

1.4.2 Fluid-Structure Interaction Modelling

To fully represent the hemodynamic flow and its effect on leaflet biomechanics, a coupled FSI simulation is required. Many FSI models have been developed to investigate heart valve biomechanics, with studies investigating the effects of calcification on TAVR performance (Halevi et al., 2016; Luraghi et al., 2020), comparing the hydrodynamic performance between SAVR and TAVR valves (Ghosh et al., 2018) and also providing insight into the performance

of the native valve (Chen and Luo, 2018). FSI has the added benefit of enabling detailed predictions of parameters not measurable *in vivo*, such as wall shear stress (Laadhari and Székely, 2017; Sodhani et al., 2018). A limited number of studies have sought to use FSI models to conduct *in silico* bench testing, with various authors estimating hydrodynamic performance of AVRs (Ghosh et al., 2018; Luraghi et al., 2019; Piatti et al., 2016, Tango et al., 2018). FSI has the potential to speed up the design and development process by replicating the *in vitro* hydrodynamic testing required for ISO 5840. While several studies have measured these parameters (Mao et al., 2016; Piatti et al., 2016), very few have conducted any experimental validation of the predicted parameters from *in silico* bench testing. In fact, only a limited number of FSI studies have experimentally validated their FSI models by comparing them to *in vitro* testing through pulsatile flow rigs (Gharaie et al., 2018; Luraghi et al., 2017; Piatti et al., 2016; Tango et al., 2018). Many studies have only presented computational results from FSI simulations, and not included any experimental validation (Borowski et al., 2018; Chen and Luo, 2018; Hedayat et al., 2017; Kandail et al., 2018). **There remains a significant need for approaches that provide experimental validation to FSI techniques before they can be more widely used for *in silico* bench testing.**

1.5 Objectives

The objective of this thesis is to investigate the potential of computational modelling to predict hemodynamic and structural performance of AVRs through a combined experimental-computational approach. In particular, the thesis investigates both finite element and fluid-structure interaction based approaches, implemented through Abaqus commercial software, and assesses their potential to robustly predict the *in vitro* performance of AVRs. The specific aims of this research are as follows:

- (i) To investigate the potential of FEA to predict the hydrodynamic performance of aortic valve implants during the development phase.
- (ii) To investigate the role of non-uniform and asymmetric aortic stiffening on valvular performance using both in vitro testing and in silico modelling
- (iii) To investigate the potential of FSI to perform a hydrodynamic analysis of aortic valves according to the ISO 5840 standard using in vitro benchmarking and 2D modelling
- (iv) To perform full-scale 3D FSI simulations of AVRs and investigate the potential of the FSI framework to conduct in silico bench testing to streamline the hydrodynamic assessment of AVRs according to the ISO 5840.

1.6 Thesis Structure

The outline of this thesis is as follows:

Chapter 2 outlines the existing literature relevant to this thesis. It provides a background to the aortic valve, its pathologies and treatment, with particular focus on AVRs. An overview of the design and testing process for AVRs through ISO5840 is provided and computational approaches for simulating aortic valve biomechanics are reviewed, with particular focus on FEA and FSI based approaches.

Chapter 3 presents a review of the fundamental theory of continuum mechanics, in the context of the finite element method. The equations described provide the basis for developing models that simulate structural and fluid dynamics problems. The core concepts of continuum mechanics are introduced, then the modelling of materials using constitutive laws are examined. In the following sections, the finite element method is described and the Navier Stokes equations for fluid dynamics and the immersed boundary method for fluid-structure interactions are examined.

Chapter 4 presents an experimental investigation into the in silico modelling of aortic valves. The chapter investigates the potential of FEA to predict the hydrodynamic performance of aortic valve implants obtained during development through in vitro testing. In vitro experiments were developed in parallel with in silico models, and suitable surrogate measures were investigated as predictors of the hydrodynamic parameters.

In **Chapter 5**, a computational framework is developed to examine aortic valve calcification. Through in vitro testing and in silico modelling, this chapter examines the effects of progressive aortic valve calcification on in vitro hydrodynamic performance. The findings of this chapter are focused on the effects of regional and asymmetric aortic valve calcification distribution on hydrodynamic performance, demonstrated by the use of an in silico testing framework.

Chapter 6 establishes a methodology for in silico bench testing prior to 3D implementation (Chapter 7). It describes a 2D immersed boundary fluid-structure interaction (FSI) model to simulate aortic leaflet deformation using the Abaqus Coupled Eulerian-Lagrangian (CEL) approach, alongside an experimental flow rig that enables leaflet deformation to be visualised under 2D flow conditions.

Chapter 7 details the development of a 3D aortic valve FSI simulation. The study considers two unique valve configurations, a bicuspid and tricuspid valve while comparing the in silico simulations with an in vitro pulsatile flow rig and polymer prosthetic valves. The FSI method was evaluated for its capability to measure hydrodynamic performance parameters.

Chapter 8 summarises the conclusions of this thesis and discusses recommendations for future work.

1.7 References

- Adams, H.S.L., Ashokkumar, S., Newcomb, A., MacIsaac, A.I., Whitbourn, R.J., Palmer, S., 2019. Contemporary review of severe aortic stenosis. *Intern. Med. J.* 49, 297–305. <https://doi.org/10.1111/imj.14071>
- Arcidiacono, G., Corvi, A., Severi, T., 2005. Functional analysis of bioprosthetic heart valves. *J. Biomech.* 38, 1483–1490. <https://doi.org/10.1016/j.jbiomech.2004.07.007>
- Arzani, A., Mofrad, M.R.K., 2017. A strain-based finite element model for calcification progression in aortic valves. *J. Biomech.* 65, 216–220. <https://doi.org/10.1016/j.jbiomech.2017.10.014>
- Baumgartner, H., Hung, J., Bermejo, J., Chambers, J.B., Evangelista, A., Griffin, B.P., Iung, B., Otto, C.M., Pellikka, P.A., Quiñones, M., 2009. Echocardiographic Assessment of Valve Stenosis: EAE/ASE Recommendations for Clinical Practice. *J. Am. Soc. Echocardiogr.* 22, 1–23. <https://doi.org/10.1016/j.echo.2008.11.029>
- Borowski, F., Sämman, M., Pfensig, S., Wüstenhagen, C., Ott, R., Kaule, S., Siewert, S., Grabow, N., Schmitz, K.P., Stiehm, M., 2018. Fluid-structure interaction of heart valve dynamics in comparison to finite-element analysis. *Curr. Dir. Biomed. Eng.* 4, 259–262. <https://doi.org/10.1515/cdbme-2018-0063>
- Bradley, S.M., 2013. Aortic Valve Insufficiency in the Teenager and Young Adult: The Role of Prosthetic Valve Replacement. *World J. Pediatr. Congenit. Hear. Surg.* 4, 397–402. <https://doi.org/10.1177/2150135113488781>
- Burriesci, G., Marincola, F.C., Zervides, C., 2010. Design of a novel polymeric heart valve. *J. Med. Eng. Technol.* 34, 7–22. <https://doi.org/10.3109/03091900903261241>
- Chen, Y., Luo, H., 2018. A computational study of the three-dimensional fluid–structure interaction of aortic valve. *J. Fluids Struct.* 80, 332–349. <https://doi.org/10.1016/j.jfluidstructs.2018.04.009>
- Ciolacu, D.E., Nicu, R., Ciolacu, F., 2022. Natural Polymers in Heart Valve Tissue Engineering: Strategies, Advances and Challenges. *Biomedicines* 10, 1095. <https://doi.org/10.3390/biomedicines10051095>
- Claiborne, T.E., Sheriff, J., Kuetting, M., Steinseifer, U., Slepian, M.J., Bluestein, D., 2013a. In vitro evaluation of a novel hemodynamically optimized trileaflet polymeric prosthetic heart valve. *J. Biomech. Eng.* 135, 021021. <https://doi.org/10.1115/1.4023235>
- Claiborne, T.E., Xenos, M., Sheriff, J., Chiu, W.C., Soares, J., Alemu, Y., Gupta, S., Judex, S., Slepian, M.J., Bluestein, D., 2013b. Toward optimization of a novel trileaflet polymeric prosthetic heart valve via device thrombogenicity emulation. *ASAIO J.* 59, 275–283. <https://doi.org/10.1097/MAT.0b013e31828e4d80>
- Daubert, M.A., Weissman, N.J., Hahn, R.T., Pibarot, P., Parvataneni, R., Mack, M.J., Svensson, L.G., Gopal, D., Kapadia, S., Siegel, R.J., Kodali, S.K., Szeto, W.Y., Makkar, R., Leon, M.B., Douglas, P.S., 2017. Long-Term Valve Performance of TAVR and SAVR: A Report From the PARTNER I Trial. *JACC Cardiovasc. Imaging* 10, 15–25. <https://doi.org/10.1016/j.jcmg.2016.11.004>
- De Gaetano, F., Bagnoli, P., Zaffora, A., Pandolfi, A., Serrani, M., Brubert, J., Stasiak, J., Moggridge, G.D., Costantino, M.L., 2015. A newly developed tri-leaflet polymeric heart valve

- prosthesis. *J. Mech. Med. Biol.* 15, 1–8. <https://doi.org/10.1142/S0219519415400096>
- De Gaetano, F., Serrani, M., Bagnoli, P., Brubert, J., Stasiak, J., Moggridge, G.D., Costantino, M.L., 2015. Fluid dynamic characterization of a polymeric heart valve prototype (Poli-Valve) tested under continuous and pulsatile flow conditions. *Int. J. Artif. Organs* 38, 600–6. <https://doi.org/10.5301/ijao.5000452>
- Fisher, C.I., Chen, J., Merryman, W.D., 2013. Calcific nodule morphogenesis by heart valve interstitial cells is strain dependent. *Biomech. Model. Mechanobiol.* 12, 5–17. <https://doi.org/10.1007/s10237-012-0377-8>
- Friedewald, V.E., Bonow, R.O., Borer, J.S., Carabello, B.A., Kleine, P.P., Akins, C.W., Roberts, W.C., 2007. The Editor's Roundtable: Cardiac Valve Surgery. *Am. J. Cardiol.* 99, 1269–1278. <https://doi.org/10.1016/j.amjcard.2007.02.040>
- Ghanbari, H., Viatge, H., Kidane, A.G., Burriesci, G., Tavakoli, M., Seifalian, A.M., 2009. Polymeric heart valves: new materials, emerging hopes. *Trends Biotechnol.* 27, 359–367. <https://doi.org/10.1016/j.tibtech.2009.03.002>
- Gharaie, S.H., Morsi, Y., 2015. A novel design of a polymeric aortic valve. *Int. J. Artif. Organs* 38, 259–270. <https://doi.org/10.5301/ijao.5000413>
- Gharaie, S.H., Mosadegh, B., Morsi, Y., 2018. In Vitro Validation of a Numerical Simulation of Leaflet Kinematics in a Polymeric Aortic Valve Under Physiological Conditions. *Cardiovasc. Eng. Technol.* 9, 42–52. <https://doi.org/10.1007/s13239-018-0340-7>
- Ghosh, R.P., Marom, G., Rotman, O.M., Slepian, M.J., Prabhakar, S., Horner, M., Bluestein, D., 2018. Comparative fluid-structure interaction analysis of polymeric transcatheter and surgical aortic valves' hemodynamics and structural mechanics, *Journal of Biomechanical Engineering*. <https://doi.org/10.1115/1.4040600>
- Haj-Ali, R., Dasi, L.P., Kim, H.S., Choi, J., Leo, H.W., Yoganathan, A.P., 2008. Structural simulations of prosthetic tri-leaflet aortic heart valves. *J. Biomech.* 41, 1510–1519. <https://doi.org/10.1016/j.jbiomech.2008.02.026>
- Halevi, R., Hamdan, A., Marom, G., Lavon, K., Ben-Zekry, S., Raanani, E., Bluestein, D., Haj-Ali, R., 2016. Fluid–structure interaction modeling of calcific aortic valve disease using patient-specific three-dimensional calcification scans. *Med. Biol. Eng. Comput.* 54, 1683–1694. <https://doi.org/10.1007/s11517-016-1458-0>
- Hartley, A., Hammond-Haley, M., Marshall, D.C., Saliccioli, J.D., Malik, I.S., Khamis, R.Y., Shalhoub, J., 2021. Trends in Mortality From Aortic Stenosis in Europe: 2000–2017. *Front. Cardiovasc. Med.* 8, 1–9. <https://doi.org/10.3389/fcvm.2021.748137>
- Hedayat, M., Asgharzadeh, H., Borazjani, I., 2017. Platelet activation of mechanical versus bioprosthetic heart valves during systole. *J. Biomech.* 56, 111–116. <https://doi.org/10.1016/j.jbiomech.2017.03.002>
- International Organisation for Standardisation, 2021a. ISO 5840:2021 Part 1: General requirements.
- International Organisation for Standardisation, 2021b. ISO 5840:2021 Part 2: Surgically implanted heart valve substitutes.
- International Organisation for Standardisation, 2021c. ISO 5840:2021 Part 3: Heart valve substitutes implanted by transcatheter techniques.

- Kandail, H.S., Trivedi, S.D., Shaikh, A.C., Bajwa, T.K., O’Hair, D.P., Jahangir, A., LaDisa, J.F., 2018. Impact of annular and supra-annular CoreValve deployment locations on aortic and coronary artery hemodynamics. *J. Mech. Behav. Biomed. Mater.* 86, 131–142. <https://doi.org/10.1016/j.jmbbm.2018.06.032>
- Kheradvar, A., Groves, E.M., Goergen, C.J., Alavi, S.H., Tranquillo, R., Simmons, C.A., Dasi, L.P., Grande-Allen, K.J., Mofrad, M.R.K., Falahatpisheh, A., Griffith, B., Baaijens, F., Little, S.H., Canic, S., 2015. Emerging Trends in Heart Valve Engineering: Part II. Novel and Standard Technologies for Aortic Valve Replacement. *Ann. Biomed. Eng.* 43, 844–857. <https://doi.org/10.1007/s10439-014-1191-5>
- Kidane, A.G., Burriesci, G., Cornejo, P., Dooley, A., Sarkar, S., Bonhoeffer, P., Edirisinghe, M., Seifalian, A.M., 2009. Current developments and future prospects for heart valve replacement therapy. *J. Biomed. Mater. Res. - Part B Appl. Biomater.* 88, 290–303. <https://doi.org/10.1002/jbm.b.31151>
- Kim, H., Lu, J., Sacks, M.S., Chandran, K.B., 2008. Dynamic simulation of bioprosthetic heart valves using a stress resultant shell model. *Ann. Biomed. Eng.* 36, 262–275. <https://doi.org/10.1007/s10439-007-9409-4>
- Kostyunin, A.E., Yuzhalin, A.E., Rezvova, M.A., Ovcharenko, E.A., Glushkova, T. V., Kutikhin, A.G., 2020. Degeneration of bioprosthetic heart valves: Update 2020. *J. Am. Heart Assoc.* 9, 1–19. <https://doi.org/10.1161/JAHA.120.018506>
- Laadhari, A., Székely, G., 2017. Eulerian finite element method for the numerical modeling of fluid dynamics of natural and pathological aortic valves. *J. Comput. Appl. Math.* 319, 236–261. <https://doi.org/10.1016/j.cam.2016.11.042>
- Larroche, J., Panh, L., Lhermusier, T., Bataille, V., Marachet, M.A., Chollet, T., Petermann, A., Bouisset, F., Boudou, N., Marcheix, B., Rousseau, H., Galinier, M., Carrié, D., Lairez, O., Lavie-Badie, Y., 2020. Impact of aortic valve calcification severity on device success after transcatheter aortic valve replacement. *Int. J. Cardiovasc. Imaging* 36, 731–740. <https://doi.org/10.1007/s10554-019-01759-7>
- Li, K., Sun, W., 2017. Simulated transcatheter aortic valve deformation: A parametric study on the impact of leaflet geometry on valve peak stress. *Int. j. numer. method. biomed. eng.* 33, 1–14. <https://doi.org/10.1002/cnm.2814>
- Li, K., Sun, W., 2010. Simulated thin pericardial bioprosthetic valve leaflet deformation under static pressure-only loading conditions: Implications for percutaneous valves. *Ann. Biomed. Eng.* 38, 2690–2701. <https://doi.org/10.1007/s10439-010-0009-3>
- Luraghi, G., Matas, J.F.R., Beretta, M., Chiozzi, N., Iannetti, L., Migliavacca, F., 2020. The impact of calcification patterns in transcatheter aortic valve performance: a fluid-structure interaction analysis. *Comput. Methods Biomech. Biomed. Engin.* 24, 375–383. <https://doi.org/10.1080/10255842.2020.1817409>
- Luraghi, G., Migliavacca, F., García-González, A., Chiastra, C., Rossi, A., Cao, D., Stefanini, G., Rodriguez Matas, J.F., 2019. On the Modeling of Patient-Specific Transcatheter Aortic Valve Replacement: A Fluid–Structure Interaction Approach. *Cardiovasc. Eng. Technol.* 10, 437–455. <https://doi.org/10.1007/s13239-019-00427-0>
- Luraghi, G., Wu, W., De Gaetano, F., Rodriguez Matas, J.F., Moggridge, G.D., Serrani, M., Stasiak, J., Costantino, M.L., Migliavacca, F., 2017. Evaluation of an aortic valve prosthesis: Fluid-structure interaction or structural simulation? *J. Biomech.* 58, 45–51. <https://doi.org/10.1016/j.jbiomech.2017.04.004>

- Manji, R.A., Menkis, A.H., Ekser, B., Cooper, D.K.C., 2012. The future of bioprosthetic heart valves. *Indian J. Med. Res.* 135, 150–151.
- Mao, W., Li, K., Sun, W., 2016. Fluid–Structure Interaction Study of Transcatheter Aortic Valve Dynamics Using Smoothed Particle Hydrodynamics. *Cardiovasc. Eng. Technol.* 7, 374–388. <https://doi.org/10.1007/s13239-016-0285-7>
- Monteleone, A., Borino, G., Napoli, E., Burriesci, G., 2022. Fluid–structure interaction approach with smoothed particle hydrodynamics and particle–spring systems. *Comput. Methods Appl. Mech. Eng.* 392, 114728. <https://doi.org/10.1016/j.cma.2022.114728>
- Mordi, I., Tzemos, N., 2012. Bicuspid aortic valve disease: A comprehensive review. *Cardiol. Res. Pract.* 1. <https://doi.org/10.1155/2012/196037>
- Nishimura, R.A., Otto, C.M., Bonow, R.O., Carabello, B.A., Erwin, J.P., Guyton, R.A., O’Gara, P.T., Ruiz, C.E., Skubas, N.J., Sorajja, P., Sundt, T.M., Thomas, J.D., 2014. 2014 AHA/ACC guideline for the management of patients with valvular heart disease: A report of the American college of cardiology/American heart association task force on practice guidelines. *J. Am. Coll. Cardiol.* 63. <https://doi.org/10.1016/j.jacc.2014.02.536>
- Osnabrugge, R.L.J., Mylotte, D., Head, S.J., Van Mieghem, N.M., Nkomo, V.T., Lereun, C.M., Bogers, A.J.J.C., Piazza, N., Kappetein, A.P., 2013. Aortic stenosis in the elderly: Disease prevalence and number of candidates for transcatheter aortic valve replacement: A meta-analysis and modeling study. *J. Am. Coll. Cardiol.* 62, 1002–1012. <https://doi.org/10.1016/j.jacc.2013.05.015>
- Otto, C.M., Burwash, I.G., Legget, M.E., Munt, B.I., Fujioka, M., Healy, N.L., Kraft, C.D., Miyake-Hull, C.Y., Schwaegler, R.G., 1997. Prospective study of asymptomatic valvular aortic stenosis: Clinical, echocardiographic, and exercise predictors of outcome. *Circulation* 95, 2262–2270. <https://doi.org/10.1161/01.CIR.95.9.2262>
- Padala, M., Sarin, E.L., Willis, P., Babaliaros, V., Block, P., Guyton, R.A., Thourani, V.H., 2010. An Engineering Review of Transcatheter Aortic Valve Technologies. *Cardiovasc. Eng. Technol.* 1, 77–87. <https://doi.org/10.1007/s13239-010-0008-4>
- Piatti, F., Sturla, F., Marom, G., Sheriff, J., Claiborne, T.E., Slepian, M.J., Redaelli, A., Bluestein, D., 2016. Polymeric Valve Using a Fluid-Structure Interaction Approach 48, 3650–3658. <https://doi.org/10.1016/j.jbiomech.2015.08.009>. Hemodynamic
- Rahmani, B., Tzamtzis, S., Ghanbari, H., Burriesci, G., Seifalian, A.M., 2012. Manufacturing and hydrodynamic assessment of a novel aortic valve made of a new nanocomposite polymer. *J. Biomech.* 45, 1205–1211. <https://doi.org/10.1016/j.jbiomech.2012.01.046>
- Rahmani, B., Tzamtzis, S., Sheridan, R., Mullen, M.J., Yap, J., Seifalian, A.M., Burriesci, G., 2016. A new transcatheter heart valve concept (the TRISKELE): Feasibility in an acute preclinical model. *EuroIntervention* 12, 901–908. <https://doi.org/10.4244/EIJV12I7A148>
- Rahmani, B., Tzamtzis, S., Sheridan, R., Mullen, M.J., Yap, J., Seifalian, A.M., Burriesci, G., 2017. In Vitro Hydrodynamic Assessment of a New Transcatheter Heart Valve Concept (the TRISKELE). *J. Cardiovasc. Transl. Res.* 10, 104–115. <https://doi.org/10.1007/s12265-016-9722-0>
- Rotman, O.M., Kovarovic, B., Chiu, W.C., Bianchi, M., Marom, G., Slepian, M.J., Bluestein, D., 2019. Novel Polymeric Valve for Transcatheter Aortic Valve Replacement Applications: In Vitro Hemodynamic Study. *Ann. Biomed. Eng.* 47, 113–125.

<https://doi.org/10.1007/s10439-018-02119-7>

Sathananthan, J., Sellers, S., Barlow, A.M., Stanová, V., Fraser, R., Toggweiler, S., Allen, K.B., Chhatriwalla, A., Murdoch, D.J., Hensey, M., Lau, K., Alkhodair, A., Dvir, D., Asgar, A.W., Cheung, A., Blanke, P., Ye, J., Rieu, R., Pibarot, P., Wood, D., Leipsic, J., Webb, J.G., 2019. Valve-in-Valve Transcatheter Aortic Valve Replacement and Bioprosthetic Valve Fracture Comparing Different Transcatheter Heart Valve Designs: An Ex Vivo Bench Study. *JACC Cardiovasc. Interv.* 12, 65–75. <https://doi.org/10.1016/j.jcin.2018.10.043>

Serrani, M., Brubert, J., Stasiak, J., De Gaetano, F., Zaffora, A., Costantino, M.L., Moggridge, G.D., 2016. A Computational Tool for the Microstructure Optimization of a Polymeric Heart Valve Prosthesis. *J. Biomech. Eng.* 138. <https://doi.org/10.1115/1.4033178>

Smuts, A.N., Blaine, D.C., Scheffer, C., Weich, H., Doubell, A.F., Dellimore, K.H., 2011. Application of finite element analysis to the design of tissue leaflets for a percutaneous aortic valve. *J. Mech. Behav. Biomed. Mater.* 4, 85–98. <https://doi.org/10.1016/j.jmbbm.2010.09.009>

Sodhani, D., Reese, S., Aksenov, A., Soğancı, S., Jockenhövel, S., Mela, P., Stapleton, S.E., 2018. Fluid-structure interaction simulation of artificial textile reinforced aortic heart valve: Validation with an in-vitro test. *J. Biomech.* 78, 52–69. <https://doi.org/10.1016/j.jbiomech.2018.07.018>

Starr, A., Edwards, M.L., 1961. Mitral replacement: clinical experience with a ball-valve prosthesis. *Ann. Surg.* 154, 726–740. <https://doi.org/10.1097/00000658-196110000-00017>

Stasiak, J.R., Serrani, M., Biral, E., Taylor, J. V, Zaman, A.G., Jones, S., Ness, T., Gaetano, F. De, Costantino, M.L., Bruno, V.D., Suleiman, S., Ascione, R., Moggridge, D., 2020. Design, development, testing at ISO standards and in vivo feasibility study of a novel polymeric heart valve prosthesis. <https://doi.org/10.1039/d0bm00412j>

Sun, L., Rajamannan, N.M., Sucusky, P., 2013. Defining the Role of Fluid Shear Stress in the Expression of Early Signaling Markers for Calcific Aortic Valve Disease 8. <https://doi.org/10.1371/journal.pone.0084433>

Tango, A.M., Salmonsmith, J., Ducci, A., Burriesci, G., 2018. Validation and Extension of a Fluid–Structure Interaction Model of the Healthy Aortic Valve. *Cardiovasc. Eng. Technol.* 9, 739–751. <https://doi.org/10.1007/s13239-018-00391-1>

Thubrikar, M.J., Aouad, J., Nolan, S.P., 1986. Patterns of calcific deposits in operatively excised stenotic or purely regurgitant aortic valves and their relation to mechanical stress. *Am. J. Cardiol.* 58, 304–308. [https://doi.org/10.1016/0002-9149\(86\)90067-6](https://doi.org/10.1016/0002-9149(86)90067-6)

Weinberg, E.J., Schoen, F.J., Mofrad, M.R.K., 2009. A computational model of aging and calcification in the aortic heart valve. *PLoS One* 4, 1–10. <https://doi.org/10.1371/journal.pone.0005960>

Zhiduleva, E. V., Irtyuga, O.B., Shishkova, A.A., Ignat’eva, E. V., Kostina, A.S., Levchuk, K.A., Golovkin, A.S., Rylov, A.Y., Kostareva, A.A., Moiseeva, O.M., Malashicheva, A.B., Gordeev, M.L., 2018. Cellular Mechanisms of Aortic Valve Calcification. *Bull. Exp. Biol. Med.* 164, 371–375. <https://doi.org/10.1007/s10517-018-3992-2>

CHAPTER 2

Literature Review

This chapter provides an overview of the literature relevant to this thesis. It provides a background to the aortic valve, its pathologies and treatment, with particular focus on aortic valve replacements (AVRs). An overview of the design and testing process for AVRs through ISO5840 is provided. Finally, computational approaches for simulating aortic valve biomechanics are reviewed, with particular focus on finite element and fluid-structure interaction based approaches.

2.1 The Cardiac Cycle

At the core of the cardiovascular system is the heart, a muscular organ that circulates deoxygenated blood from the body to the lungs and distributes re-oxygenated blood from the lungs to all the muscles and organs in the body. The heart, shown in Figure 2.1, consists of four chambers, two atria and two ventricles, which are separated by individual valves that control the unidirectional flow of blood. The right atrium receives deoxygenated blood via the vena cava, which is pumped from the right ventricle out through the pulmonary artery. The left atrium receives oxygenated blood from the pulmonary vein, which is pumped from the left ventricle out of the heart via the aortic valve and aorta. The heart is enclosed in a pericardial

sac that contains blood vessels and electrical synapses, which control contraction of the heart during each heartbeat.

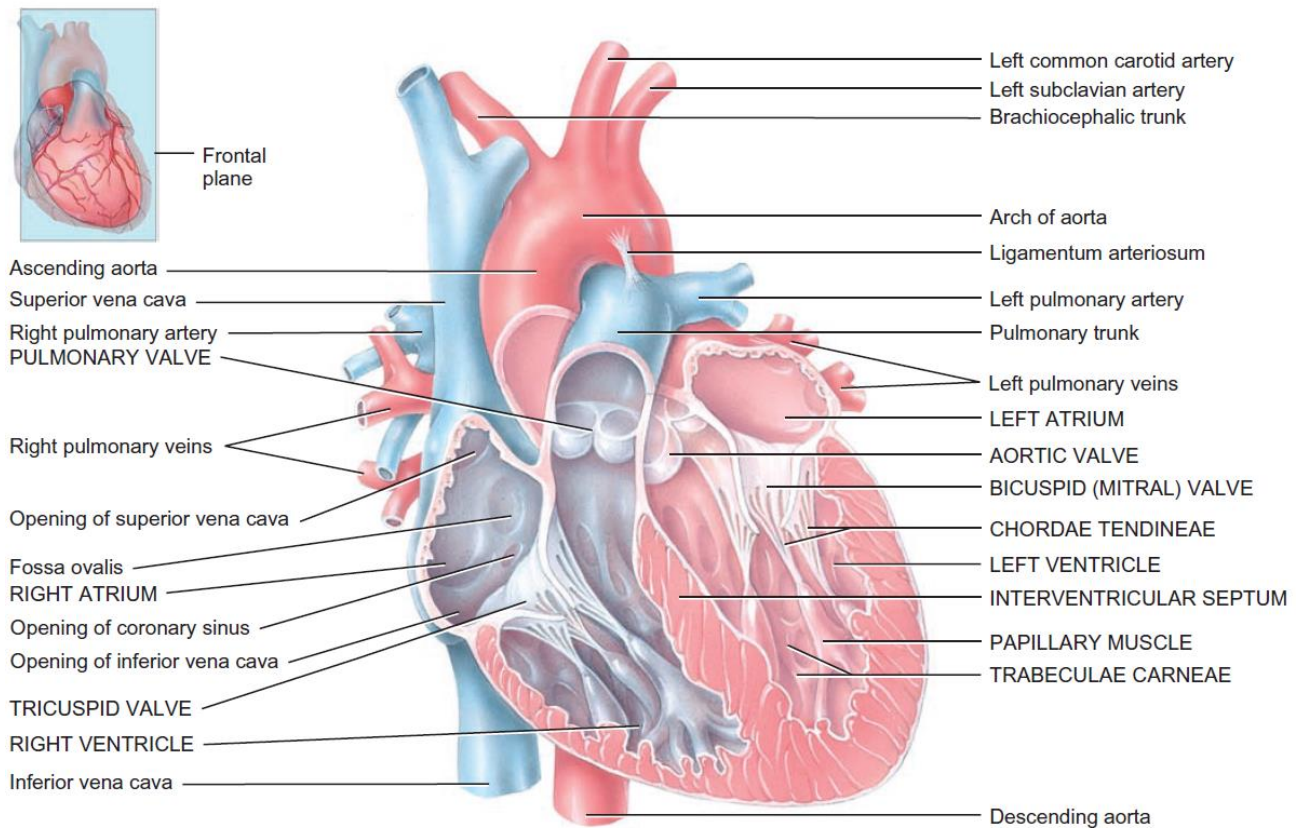


Figure 2.1 Anatomy of the heart, section view through the frontal plane (Tortora and Nielsen, 2012).

The cardiac cycle can be divided into several phases, which are represented schematically in Figure 2.2. At the beginning of the cycle, atrial contraction occurs, closing the mitral valve, while pushing blood into the left ventricle. The next stage is iso-volumetric contraction, whereby the ventricular pressure increases until it overcomes the aortic pressure, resulting in the opening of the aortic valve. In the systolic stage that follows, blood is ejected from the ventricles at high velocity through the aortic valves, until the volume in the ventricles has decreased. Iso-volumetric relaxation of the left ventricle then occurs, which results in a slight reverse in blood flow during aortic valve closure. Following this, the diastolic phase begins and the mitral valve opens, allowing blood to flow into the left ventricle, restarting the cardiac

cycle. The entire cycle lasts approximately 800-900 milliseconds. For the disease of aortic stenosis, Figure 2.2 would be characterised by an increased ventricular pressure during systole, creating a large transvalvular pressure drop.

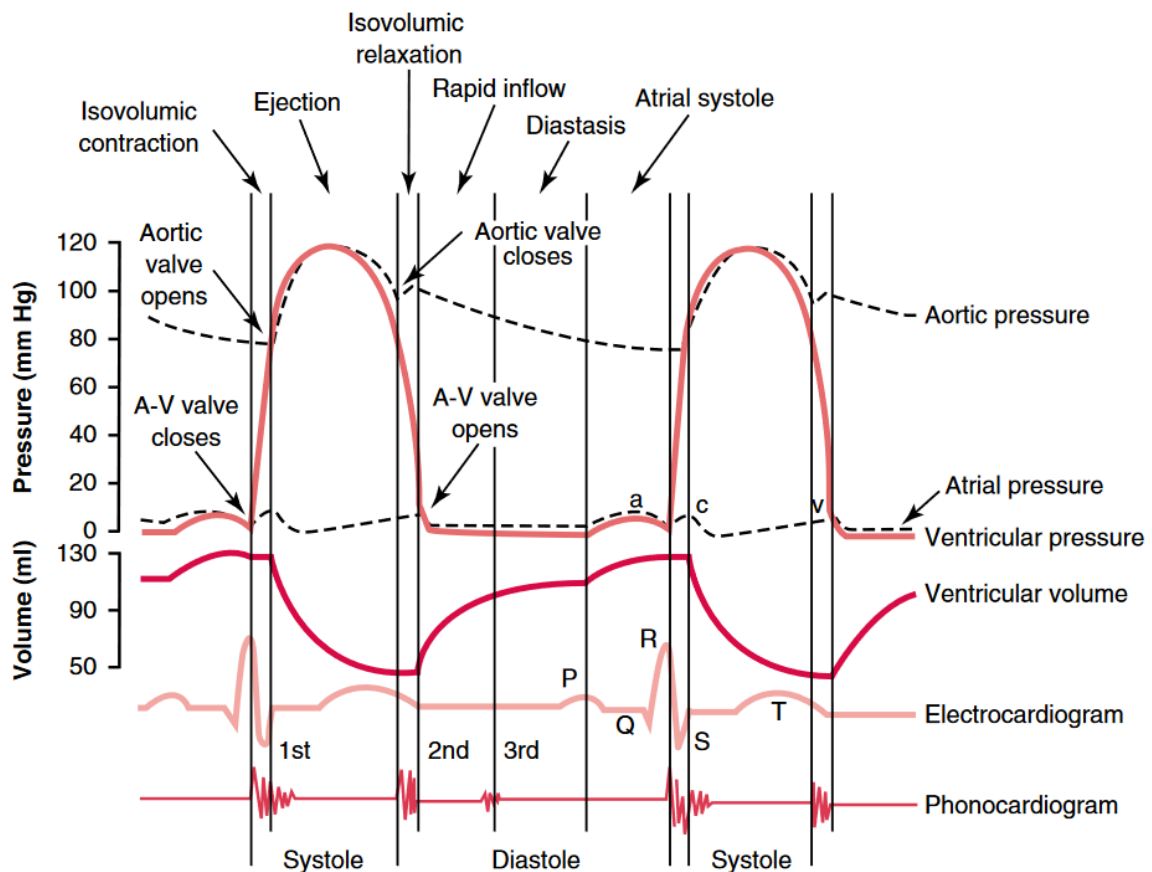


Figure 2.2 The phases of the cardiac cycle (Hall, 2015).

2.2 Heart Valves

There are four valves in the heart whose primary function is to ensure unidirectional blood flow. The tricuspid valve separates the right atrium and right ventricle, while the pulmonary valve separates the right ventricle and pulmonary artery. The mitral valve separates the left atrium and the left ventricle, while the aortic valve separates the left ventricle and the aorta. Blood from the left ventricle is pushed through the aortic valve and into the aorta at large pressures and velocities to distribute blood to the rest of the body.

2.2.1 Aortic Valve Anatomy

The aortic valve is located inside the aortic root, which is a direct continuation of the left ventricular outflow tract. The aortic root begins at the basal attachment of the aortic valve leaflets and finishes at the sinotubular junction where the leaflets attach peripherally, as shown in Figure 2.3. The aortic root is composed of the sinus of valsalva and the aortic valve leaflets. It can be described as a truncated cone because the diameter at the basal region is in general smaller than the diameter at the sinotubular junction.

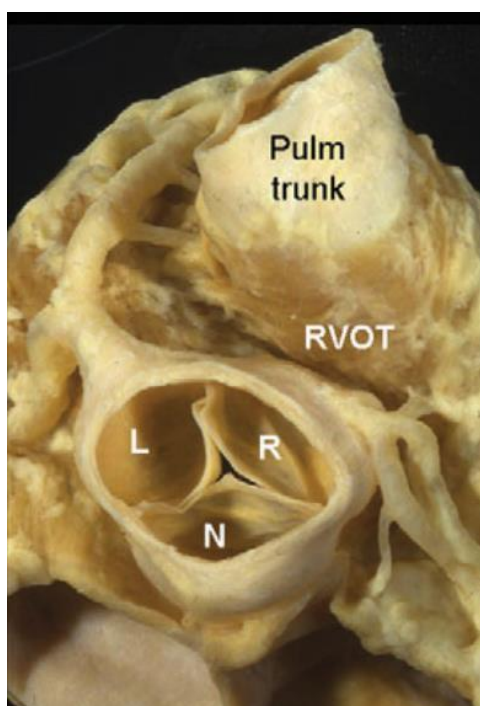


Figure 2.3 The right ventricular outlet tract (RVOT) has been pulled forward to show the left (L), right (R) and non-coronary (N) aortic sinus (Ho, 2009).

The aortic valve leaflets are cusps that are semi-lunar in shape and composed of the leaflet free edge, central leaflet belly and basal attachment regions. The leaflets tend to be unique to one other, with slight variations in volume, height, width and surface area generally observed (Vollebergh and Becker, 1977). Behind each leaflet cusp are the sinus of valsalva, which are pits that allow vortices to form in the blood to aid leaflet closure during diastole, an effect that was first suggested by Leonardo da Vinci around 1513 (Boon, 2010). The ostias of the coronary

arteries are generally located in the two anterior sinuses of valsalva, below the sinotubular junction.

2.2.2 Aortic Valve Tissue

The aortic valve is a passive tissue that maintains the unidirectional flow of blood through optimised structural organisation of its tissue components. The tissue in the valve leaflets is mainly composed of collagen, fibrin, elastin, glycosaminoglycans (GAGs), valve endothelial cells and valve interstitial cells (Zhiduleva et al., 2018). Through intricate arrangement of these tissue components, these tissue constituents enable outstanding functional capacity by the aortic valve, accommodating substantial hemodynamic loads throughout each repeated cardiac cycle.

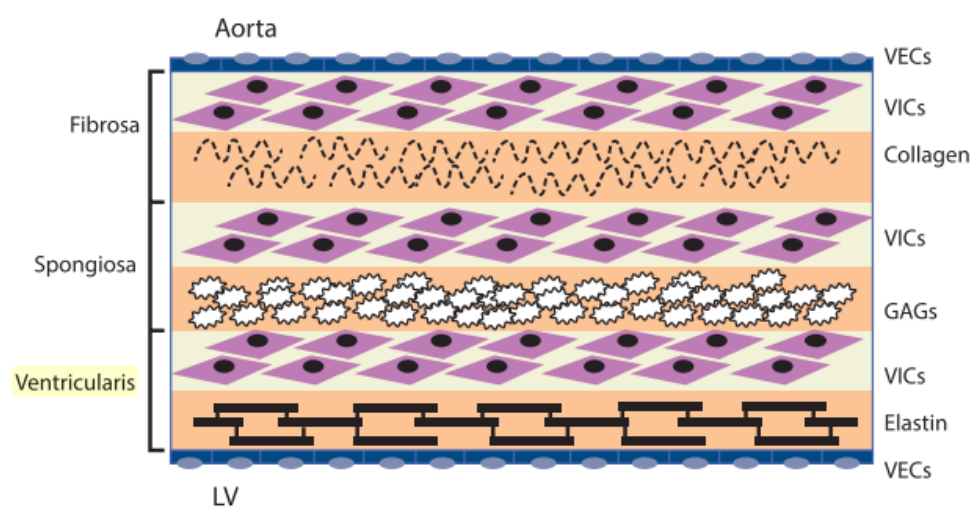


Figure 2.4 Cellular composition of the Aortic Valve Leaflets (Lerman et al., 2015).

The aortic valve leaflets are heterogeneous and composed of 3 distinct layers, the fibrosa, spongiosa and ventricularis, as shown in Figure 2.4. The fibrosa is the thickest layer and is located on the aortic side of the valve. It is the primary load bearing side and is required to withstand the backpressure of the aorta and prevent regurgitation of blood into the ventricle. It is composed primarily of Type 1 Collagen bundles, whose alignment depends on their loading. When the fibres are unloaded, they resemble a crimped wavy configuration. When the fibres

are loaded during diastole, the fibres extend and align themselves in the circumferential direction. The spongiosa is located in between the fibrosa and ventricularis and is composed primarily of gelatinous GAGs and acts as a lubricant between the two load bearing layers (Zhiduleva et al., 2018). The ventricularis is located on the ventricular side of the leaflets. Unlike the fibrosa, the surface is smooth, which promotes laminar flow. It is composed of collagen and fibrin, while the fibres are aligned in the circumferential direction, shown in Figure 2.5.

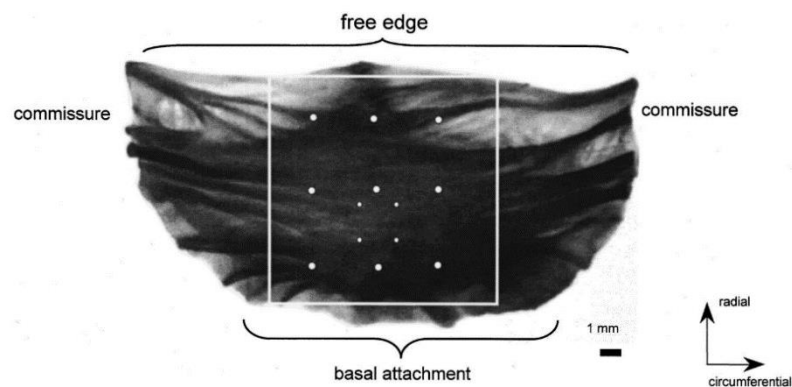


Figure 2.5 Image of an aortic cusp, highlighting the heterogeneous fibrous structure (Billiar and Sacks, 2000).

2.2.3 Mechanical Properties of the Aortic Valve

Due to the composition of the aortic valve leaflets, it exhibits anisotropic and hyperelastic mechanical responses under mechanical loading. Figure 2.6 shows a typical stress-strain response of an aortic valve leaflet, which can be divided into three main regions (Billiar and Sacks, 2000). The initial response shows a distinct toe region, where elongation of the crimped fibres in the fibrosa takes place. The second phase shows load take-up as the fibres re-orientate in the direction of loading. In Phase 3, substantial stiffening is observed as the fibres are fully elongated and orientated, providing maximum resistance. Due to the fibrous nature of the tissue, the response of the aorta in the circumferential direction is substantially stiffer than the radial direction.

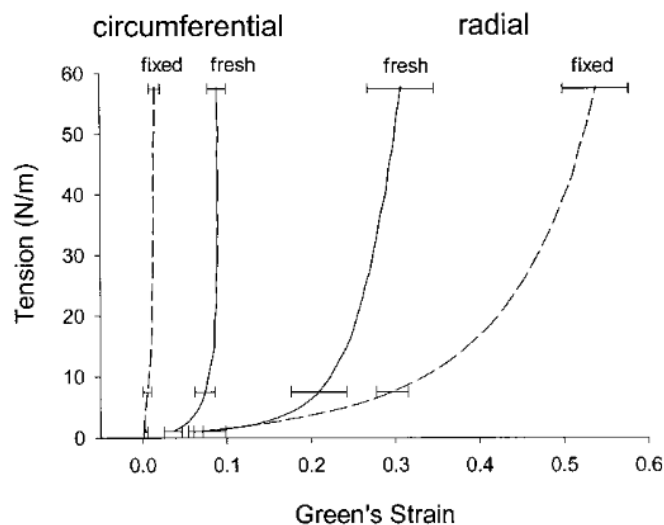


Figure 2.6. Mechanical response in the circumferential and radial direction for fixed and fresh aortic valve leaflets in a preconditioned and preloaded state (Billiar and Sacks, 2000).

2.2.4 Hemorheology

Blood is composed mainly of red blood cells, white blood cells and platelets suspended in plasma. Because of these components, blood is described as a non-Newtonian fluid, whereby its viscosity is different depending on the shear-rate (Bodnár et al., 2011; Dintenfass, 1962). At low levels of shear, blood has an increased viscous effect and has a viscosity that is roughly four times that of water (Nader et al., 2019; Pop et al., 2002). As the shear-rate increases, the viscosity reduces through the shear thinning effect. This is important to consider in the design of AVRs as devices that result in high shear forces can have negative effects on the blood, such as damage to cells and thrombus formation (Hedayat et al., 2017).

2.2.5 Aortic Valve Stenosis and Calcific Aortic Valve Disease

Reports from the American National Heart Lung and Blood Institute Framingham Heart Study estimated the prevalence of valvular heart disease at 1-2% among 26 to 84 year olds (Rosamond et al., 2007). Aortic stenosis is the most common form of valvular heart disease, whereby a narrowing of the native valve orifice leads to obstruction of the left ventricular outflow (Nkomo et al., 2006) and increased left ventricular hypertrophy (Adams et al., 2019). It occurs in 2.8%

of adults older than 75 years of age (Eveborn et al., 2013; Stewart et al., 1997). Common causes of aortic stenosis are rheumatic valve disease, bicuspid valves with superimposed calcification and calcific stenosis. The effects of these diseases on the aortic valve are represented schematically in Figure 2.7.

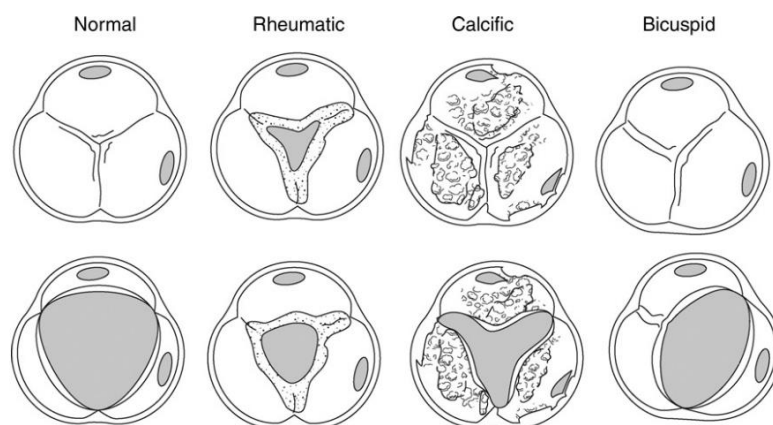


Figure 2.7 Morphology of several types of aortic stenosis, rheumatic, calcific and bicuspid (Otto, 2007).

The narrowing of the aortic orifice is often caused by aortic sclerosis, where the leaflet cusps thicken as fibroblasts differentiate to myofibroblasts. This results in an accumulation of fibrotic tissue which in turn encourages calcium deposition on the leaflets causing calcific aortic valve disease (CAVD). CAVD is a valvular heart disease that begins with changes in the leaflet cells that eventually develop to calcification in the form of calcific lesions. These lesions are generally targeted on the aortic side of the valve leaflets (Warren and Yong, 1997), and greatly restrict their mobility. Studies have shown that the development of early lesions involve inflammatory cells in a similar mechanism to that of atherosclerotic arterial calcification (Otto et al., 1994). Leaflet calcification is driven by native valve interstitial cells that acquire a pro-calcific profile in response to several pathological stimuli, such as increased calcium phosphate levels or low-density lipoprotein accumulation (Sun et al., 2013). The development of CAVD is shown in Figure 2.8.

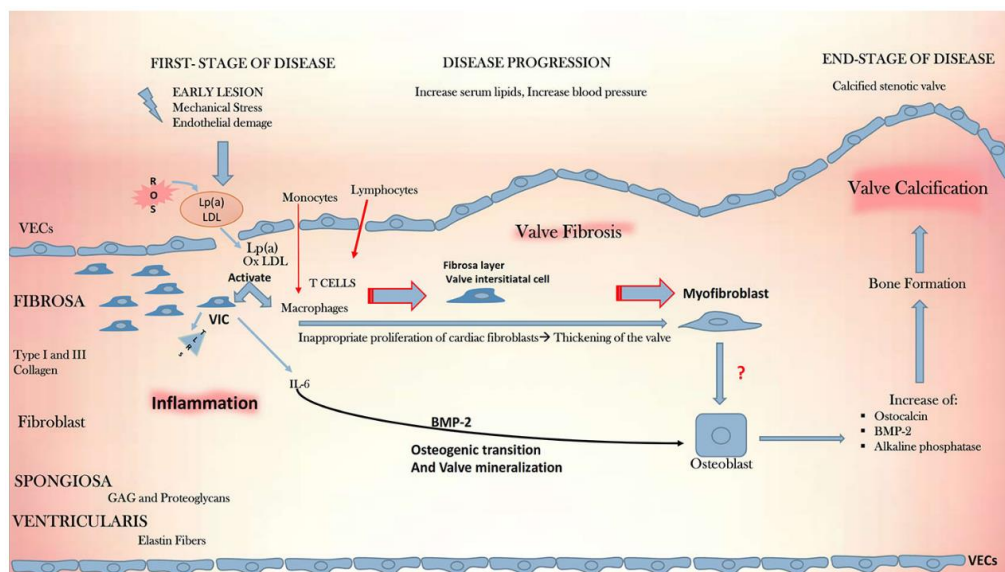


Figure 2.8 Development of calcific aortic valve disease, showing the progression from initial lesion to a calcified stenotic valve (Alushi et al., 2020).

It has been found that the development of calcification patterns on aortic valves has a mechanobiological basis, (Arzani and Mofrad, 2017; Fisher et al., 2013; Weinberg et al., 2009) with the patterns that generally arise being non-uniform and, in some cases, asymmetric. Thubrikar (1986) investigated over 300 explanted valves with calcifications and found that the majority of leaflets had calcification patterns that (i) occurred along the line of cusp coaptation (see Figure 2.9) or (ii) occurred as spokes spreading inwardly from the cusp attachment point towards cusp centre (see Figure 2.9), with a minority of cases having an indiscernible calcification pattern. There are many other studies that have observed asymmetric and non-uniform calcification in aortic valves, although these studies have, in many cases, been focused on understanding the pre-operative state of the native aortic valve prior to aortic valve implantation. For example, in assessing the impact of calcification on transcatheter aortic valve replacement (TAVR) surgery, both Larroche et al. (2020) and Milhorini Pio et al. (2020) observed highly asymmetric calcifications on native valves, as shown in Figure 2.9b (i-ii). Here, calcification is almost completely confined to a single leaflet. Other similar studies, such as those by Sakrana et al. (2016) and Vargas et al. (2009), have observed more symmetric

calcification patterns, whereby calcification is distributed across the three leaflets, as shown in Figure 2.9b (v-vi), although there can be variation in the regions where this occurs. While it is well-known that valvular calcification such as this leads to progressive stiffening/narrowing of the aortic valve orifice, there remain distinct challenges in the clinical assessment of calcification and there is limited understanding of how non-uniform and/or asymmetric calcification of valve leaflets impacts hemodynamic performance.

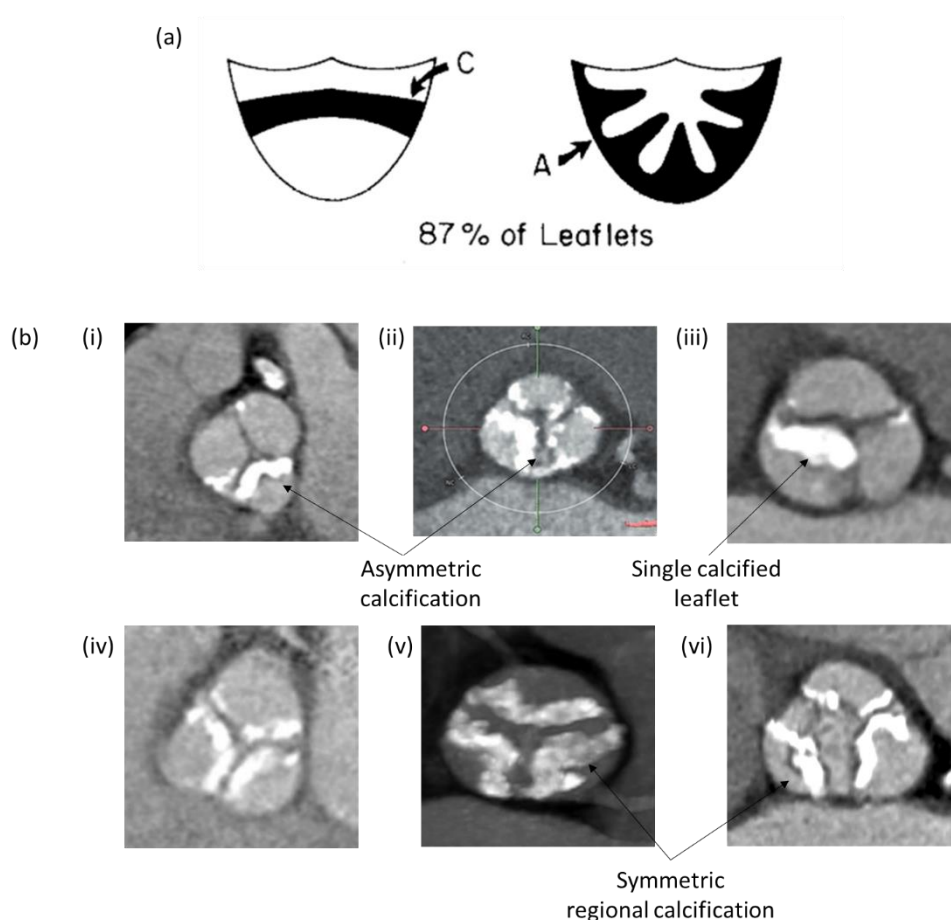


Figure 2.9 (a) diagram from Thubrikar et al.(1986) describing the calcification patterns present in 87% of explanted leaflets, where C is the line of cusp coaptation and A is the cusp attachment points and (b) planar images of aortic calcification, with several in vivo examples of asymmetric calcification (i-iii) and symmetric and regional calcification (iv-vi). Adapted from (i) Larroche et al. (2020), (ii) Milhorini et al.(2020) (iii) Tan et al. (2018) (iv) Larroche et al. (2020)(v) Sakrana et al.(2016) and (vi) Vargas et al. (2009)

In cases of severe aortic stenosis and CAVD, blood flow is restricted through the aortic orifice, which requires increased loading from the heart to maintain an adequate cardiac output. The

obstruction of the left ventricular outflow tract results in increased left ventricular systolic pressure, increased left ventricular ejection time, decreased aortic pressures and increased left ventricular end-diastolic pressure. This contributes to left ventricular hypertrophy, which can subsequently result in heart failure. The quantity and location of calcification can be determined using computed tomography (CT) imaging. An Agatston score (Agatston et al., 1990) is generally used to establish the severity of the calcification. The Agatston score is a measure of the calcified lesion area multiplied by a density score, which is established based on a Hounsfield unit density range. The Agatston score, shown in Table 2.1, is useful in determining the overall severity of calcification, but it lacks the ability to convey the location, or patterns of calcification established, as well as the actual performance of the valve. Until now, studies that have examined the severity and distribution of calcification have focused on its implications on the implantation performance of AVRs (Milhorini Pio et al., 2020). Still, there remains distinct challenges in clinical assessment of calcification and there is actually limited understanding on how the hemodynamic performance of the native valve is affected by calcification.

Table 2.1 Calcium Score by Computed Tomography in Grading of Aortic Stenosis, adapted from Baumgartner et al. (2017b) (Values are given in arbitrary units using Agatston method for quantification of valve calcification)

	Men	Women
Severe aortic stenosis very likely	$\geq 3,000$	$\geq 1,600$
Severe aortic stenosis likely	$\geq 2,000$	$\geq 1,200$
Severe aortic stenosis unlikely	$< 1,600$	< 800

2.3 Aortic Valve Mechanics

2.3.1 Hemodynamics of Healthy and Stenosed Aortic Valve

At the start of systole, the left ventricle contracts, overcoming the pressure in the aorta, forcing the aortic valve leaflets to open, and allowing blood to flow into the aortic tract. Systole lasts approximately one third of the aortic cycle, starting when the valve opens and ending when the

valve closes, lasting roughly 20-30 ms (Bellhouse, 1969). Peak flow occurs during the first third of systole, when the leaflets have fully opened. Following this, the flow decelerates, creating an adverse pressure gradient. Reverse flow and vortices occur between the leaflets and aortic sinus, which facilitate faster valve closure. (Pisani et al., 2013). As a result of faster closure, the closing volume or backflow is reduced. The amount of backflow that occurs during closure is estimated to be around 5% of the forward flow (Yoganathan et al., 2004). The valves are closed during isovolumetric contraction and isovolumetric relaxation. Healthy blood flow through the native valve can accelerate to peak values of around 1.35 ± 0.35 m/s (Rossvoll et al., 1991). Flow is helical as it transcends the aortic arch, as shown from 3D magnetic resonance velocity mapping (Kilner et al., 1993).

The standard clinical approach for diagnosing the impact of aortic stenosis on valve hemodynamics is using Doppler echocardiography, where direct imaging of the valve anatomy, calcification and flow are possible. This clinical evaluation approach is shown in Figure 2.10 and can be used to provide quantitative measurements of the hemodynamic parameters of the valve and assess the severity of stenosis (Franke et al., 2020; Garcia and Kadem, 2006).

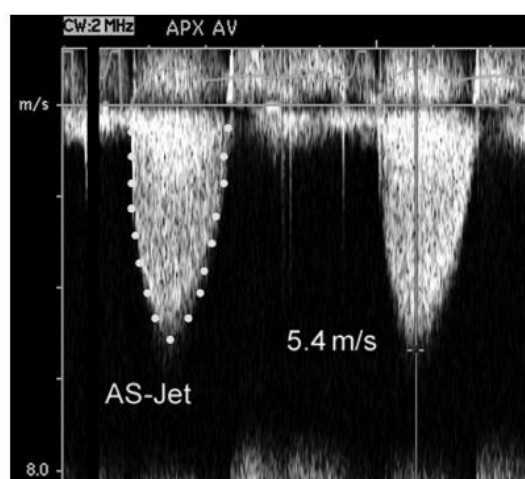


Figure 2.10 Continuous wave Doppler of severe aortic stenosis jet showing maximum jet velocity and tracing of velocity curve for mean pressure gradient calculation (Baumgartner et al., 2009).

This approach directly measures aortic jet velocity, mean trans-aortic pressure gradient and the aortic valve area (AVA), which is determined by the continuity equation. Evaluation of the AVA by this method allows for aortic stenosis quantification as mild, moderate or severe based on thresholds summarised in Table 2.2 (Baumgartner et al., 2009).

Table 2.2 Mild, Moderate and Severe Conditions for Aortic Stenosis. ^aESC Guidelines, ^bAHA/ACC Guidelines (Baumgartner et al., 2017a).

	Mild	Moderate	Severe
Aortic Jet Velocity (m/s)	2.6-2.9	3.0-4.0	>4.0
Mean Gradient (mmHg)	<20 (<30 ^a)	20-40 ^b (30-50 ^a)	>40 ^b (>50 ^a)
AVA (cm²)	>1.5	1.0-1.5	<1.0

There are further core hemodynamic parameters that are used to assess the performance of the native aortic valves by clinicians. The transvalvular ΔP and effective orifice area (EOA) are frequently used to assess the extent of valvular heart disease, but also to evaluate the performance of replacement heart valves in vivo and in vitro. The transvalvular ΔP refers to the pressure gradient across the valve during systole where the ventricles contract, ejecting blood into the aorta and pulmonary artery. It is used to assess aortic stenosis, with pressure drops of greater than 40 mmHg being considered severe (Baumgartner et al., 2009). Clinically, the transvalvular ΔP is measured indirectly from echocardiography, whereby Doppler velocity measurements (v) are used with the simplified Bernoulli equation (Eq. 2.1) to calculate the pressure (Franke et al., 2020).

$$\Delta P = 4v^2 \quad (2.1)$$

The EOA is defined as the minimal cross-sectional area of the jet formed downstream of the aortic valve, as shown in Figure 2.11. It is often used during cardiac catheterisation to assess the severity of aortic stenosis in patients (Baumgartner et al., 2017a; Nishimura et al., 2014).

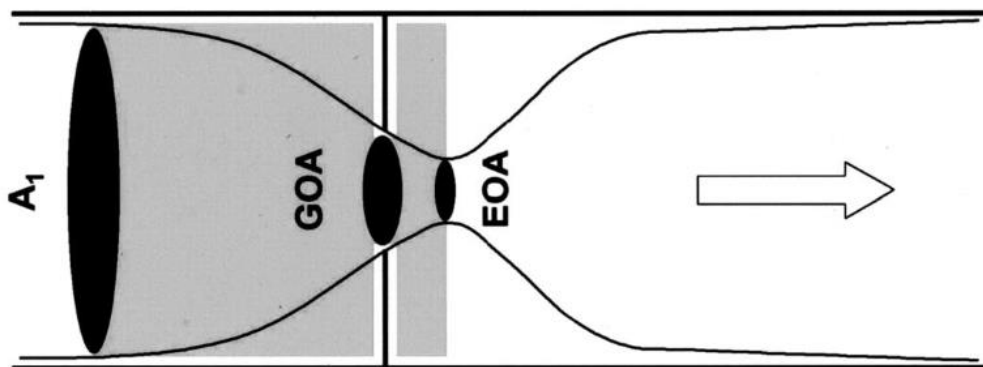


Figure 2.11 Representation of geometric orifice area (GOA) and effective orifice area (EOA) (Garcia et al., 2004).

The EOA is calculated using the Gorlin Formula (Gorlin and Gorlin, 1951) given by

$$EOA = \frac{Q_{RMS}}{51.6 \sqrt{\frac{\Delta P}{\rho}}} \quad (2.2)$$

where Q_{RMS} is the root mean squared forward flow (ml/sec), ΔP is the mean transvalvular ΔP (mmHg) and ρ is the density of the test fluid (g/cm^3). Finally, the regurgitant fraction (RF) is a measure of aortic valve leakage and is calculated by the regurgitant volume (RG) as a fraction of the stroke volume (SV), as in Eq. (2.2)

$$RF = \frac{RG}{SV} \quad (2.3)$$

where RG is the sum of the closing volume and leakage volume. Several of these metrics that describe valve performance are not only relevant clinically, but also used extensively in assessing the performance of AVRs through standardised bench testing. These aspects are discussed in much more detail in Sections 2.4 and 2.5.

2.4 Aortic Valve Replacements

While clinicians can prescribe drugs to treat aortic stenosis, with statins and angiotensin-converting enzyme (ACE) inhibitors showing beneficial effects in patients, in many cases these

are not sufficient and surgical intervention may ultimately be required with the implantation of AVRs.

2.4.1 Surgical Aortic Valve Replacements (SAVRs)

Surgical aortic valve replacements (SAVRs) are typically reserved for patients with severe aortic stenosis, as the implantation of such a device requires highly invasive and traumatic open-heart surgery. There are two main categories of SAVR, namely the Mechanical Heart Valve (MHV) and the Bioprosthetic Heart Valve (BHV).

2.4.1.1 Mechanical Heart Valves (MHVs)

The first MHV implantation was performed by Dr. Charles Hufnagel in 1952 whereby a ball-and-cage valve consisting of a Plexiglas cage surrounding a silicone coated nylon poppet was implanted in the descending aorta. In the 1960s, the Starr-Edwards ball-and-cage valve was approved by the U.S. Food and Drug Administration (FDA) (Kheradvar et al., 2015; Matthews, 1998), revolutionising treatment of valvular heart disease (Starr and Edwards, 1961). While the design was functional, it was not optimal as it featured a low EOA, high levels of shear promoting thrombus formation and therefore required extensive anticoagulant therapy. Figure 2.12 shows several examples of caged-ball valves used as SAVRs.

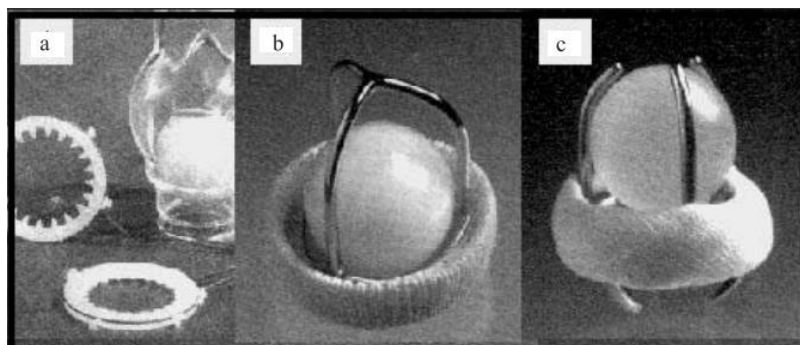


Figure 2.12 Caged ball valves (a) Hufnagel-Lucite valve, (b) Starr-Edwards, (c) Smeloff-Cutter (Nair et al., 2003).

MHV's progressed to mono-leaflet designs in 1969 and 1970, with the introduction of the Bjork Shirley and Lillehei-Kaster tilting disc valves, shown in Figure 2.13.

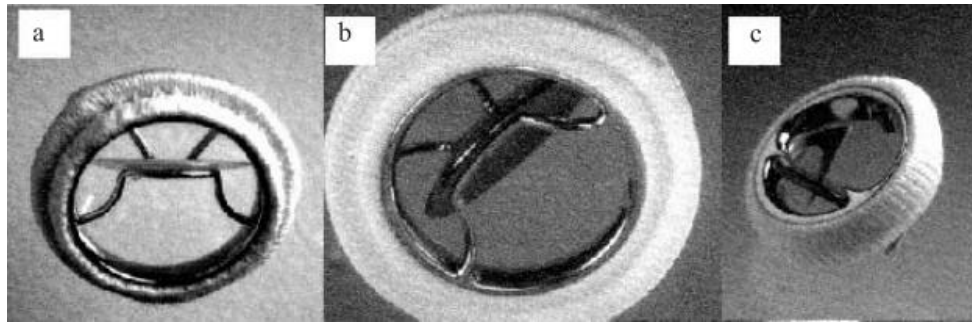


Figure 2.13 Tilting Disc Valves: (a) Bjork-Shiley Delrin valve, (b) Bjork-Shiley Standard, (c) Lillehei-Kaster (Nair et al., 2003).

Designs have since progressed to bi-leaflet mechanical valves, such as the St-Jude, Carbomedics or the Edwards Duromedics (King et al., 1996). These designs are now widely used as they offer excellent durability, being implanted in 34% of patients 30 years and younger undergoing aortic valve surgery (Bradley, 2013). In vitro pulsatile testing has shown they are more than capable of meeting the minimum requirements for EOA (Wu et al., 2019). However, the main drawbacks remain the requirement for lifelong anticoagulant therapy (Kaneko and Aranki, 2013). Peak velocities can reach velocities higher than 2 m/s and frequently high shear stresses result in thrombus formation. Figure 2.14 shows the development of AVRs from the 1950s to early 2000s.

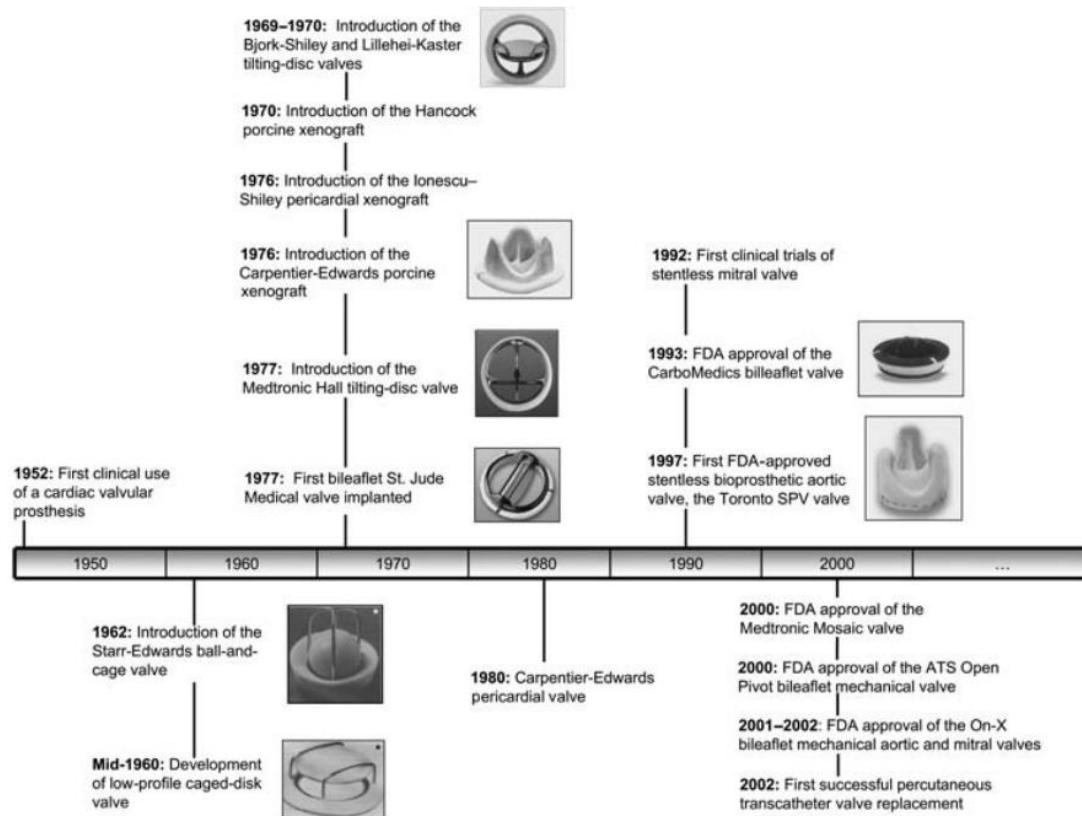


Figure 2.14 Timeline of the development of prosthetic heart valves (Dasi et al., 2009).

2.4.1.2 Bioprosthetic Heart Valves

MHV, though still popular, are beginning to be replaced by bioprosthetic heart valves (BHV). The development of such valves was helped by the development of a tissue fixation method by Carpentier in 1969 (Carpentier et al., 1969), which enabled tissue-based valves using porcine leaflets or bovine pericardium cross-linked with glutaraldehyde. This protein cross-linking technique improved the *in vivo* stability and overall durability of tissue-based leaflets (Dasi et al., 2009). BHVs mimic the design of the native valve, with three leaflets creating a central orifice that offers improved hemodynamic function compared to their mechanical counterparts. The first commercially available BHV was the Hancock Porcine Xenograft developed by Medtronic (Medtronic, Irvine, CA, USA). BHVs can be either stented or stentless. Stent frames are manufactured from materials such as Nitinol, Stainless steel or Cobalt Chromium and examples of stented BHVs include Carpentier Edwards Perimount Magna

(Figure 2.15) or Sorin Mitroflow. On the other hand, stentless BHVs do not feature a stent and, instead, the valve is sutured in position along the edge of the native leaflets. Compared to their mechanical counterparts, the durability of BHVs are lower, with clinical follow-ups finding that within 10 years 50% of patients with BHV implants develop complications (Mohammadi and Mequanint, 2011).



Figure 2.15 Carpentier-Edwards Perimount Magna Ease Aortic Valve. Adapted from Baura, (2021)

2.4.2 Transcatheter Aortic Valve Replacements (TAVRs)

While the valves discussed so far are SAVR, which require open-heart surgery for implantation, the development of minimally invasive trans-catheter aortic valve replacements (TAVR) have enabled devices to be implanted without the need for open-heart surgery. These devices are recommended for use in elderly patients, or those who would be deemed higher risk and unsuitable for open-heart surgery (Grube et al., 2014). Generally, the devices are implanted via a transfemoral approach, whereby an incision is made to the femoral artery and the valve is delivered to the aortic root via catheter. Currently, there are several FDA approved TAVRs on the US market, including Medtronic's CoreValve (Medtronic Inc., Minneapolis, Minnesota) and Edwards Sapien Valve (Edwards Lifesciences, Irvine, California), shown in Figure 2.16. The Sapien valve consists of three bovine pericardial leaflets on a Cobalt-Chromium stent of

short profile to minimise stent protrusion into the left ventricular outflow tract, while minimizing conduction interference and obstruction of the coronary arteries. The Corevalve uses porcine tissue leaflets, mounted on a self-expanding Nitinol stent of elongated and contoured profile. This enables the stent to conform to the aortic root while distributing stress to designated areas and minimising para-valvular leakage.

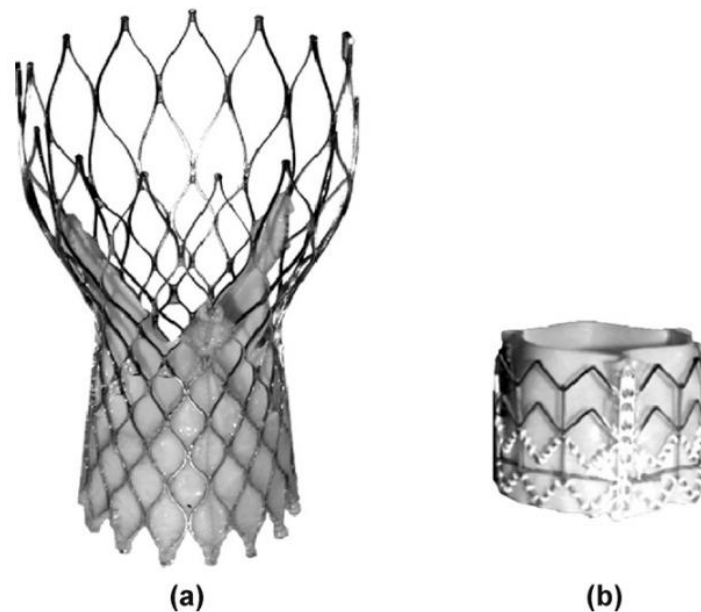


Figure 2.16 (a) Medtronic Corevalve (b) Edwards Sapien (Tzamtzis et al., 2013).

Recently, TAVR has been cleared for use in low-risk patients based on the recent global prospective multi-centre clinical trial (Bajwa et al., 2019; Mack et al., 2019). As such, there is a widely expanding and younger patient population of 270,000 new patients per year in the EU and US now eligible for TAVR based on the results of these trials (Durko et al., 2018). While the market demand for TAVR valves is increasing, the existing valves cannot fulfil this demand due to several deficiencies. Presently, all FDA approved and CE marked TAVR use animal-derived pericardium tissue as the leaflet material, generally from bovine or porcine origin (Tam et al., 2017). This must be sourced from animals residing in disease-free areas not affected by bovine spongiform encephalopathy (BSE) (Kumagai et al., 2019). The pericardium material, its chemical processing, and its hand suturing to frames alone accounts for approximately 25%

of the unit manufacturing cost of the whole TAVR system, which is a substantial cost for valve manufacturers. Additionally, there are existing challenges with pericardium leaflets including tissue deterioration, calcification, leaflet thrombosis and limited durability that affect performance of the valve in the patient (Blackman et al., 2019; Kostyunin et al., 2020; Rodriguez-Gabella et al., 2017). This has led researchers to explore robust synthetic alternatives to animal pericardium to perform the same function of a heart valve leaflets.

2.4.3 Polymer Valve Technologies

With a substantial unmet need for a durable, cost-effective, easily manufactured heart valve replacement from a traditional engineered material, there are still distinct challenges to be met in this area (Ghanbari et al., 2009). Polymer valves have been trialled since the 1960s but have been limited by structural failure, calcification and thrombosis (Resor and Bhatt, 2019). The first polymeric valve with flexible silicone leaflets resulted in high mortality due to limited durability and thrombogenicity (Roe, 1969). Polytetrafluoroethylene (PTFE) was recently used in paediatric pulmonary replacements (Ando and Takahashi, 2009), but due to historical studies showing poor performance in relation to stiffening and calcification, it has not been adopted (Nistal et al., 1990). The development of a polymer material that could replicate the geometry of the native leaflets, resist calcification, and be structurally durable is of great interest.

Several groups have developed prototypes that have performed well in in vitro testing (Coulter et al., 2019; De Gaetano et al., 2015; Rahmani et al. 2016, Rahmani et al. 2017). Burriesci and co-workers have developed a self-expanding polymeric TAVR called the TRISKELE with an adaptive sealing cuff and nitinol wire frame (Rahmani et al. 2016, Rahmani et al. 2017). Comprehensive in vitro testing of the TRISKELE valve against commercial counterparts (Edwards SAPIEN XT and Medtronic CoreValve) showed comparable, and in some cases, superior performance with significant reduction in paravalvular leakage (Rahmani et al., 2017). The TRISKELE valve also demonstrated feasibility in an acute ovine model by Rahmani et al.,

(2016), where it was shown to have successful anchoring and good leaflet motion and had the potential to mitigate complications related to imprecise valve positioning. Costantino and co-workers have also developed tri-leaflet polymeric AVR prototypes, with De Gaetano et al. (2015a, 2015b) demonstrating that computationally-optimised valve prototypes tested in vitro under continuous and pulsatile flow conditions met the ISO 5840 regurgitation fraction and EOA requirements. Durability testing showed that this polymer AVR had durability of greater than 1.2 billion cycles (30 years equivalent), with in vivo short-term (1–24 hours) feasibility demonstrating good suturability, no mechanical failure or regurgitation and good biocompatibility (Stasiak et al., 2020) Another promising polymer valve by Foldax (TRIA LifePolymer [LP], Foldax USA), shown in Figure 2.17, has recently shown promising clinical results following implantation in humans (Kereiakes et al., 2021). The valve features a newly developed siloxane-based polyurethane-urea, with 3 flexible leaflets cast onto a polyether-ether stent with a PTFE sewing ring. Based on a clinical study of 15 subjects, it was found that after one year the implanted TRIA valve resulted in normalised pressure gradients with cardiac output and improved EOA post operatively, compared to pre-implantation levels (see Figure 2.17). This valve is now being considered for a larger-scale clinical trial.

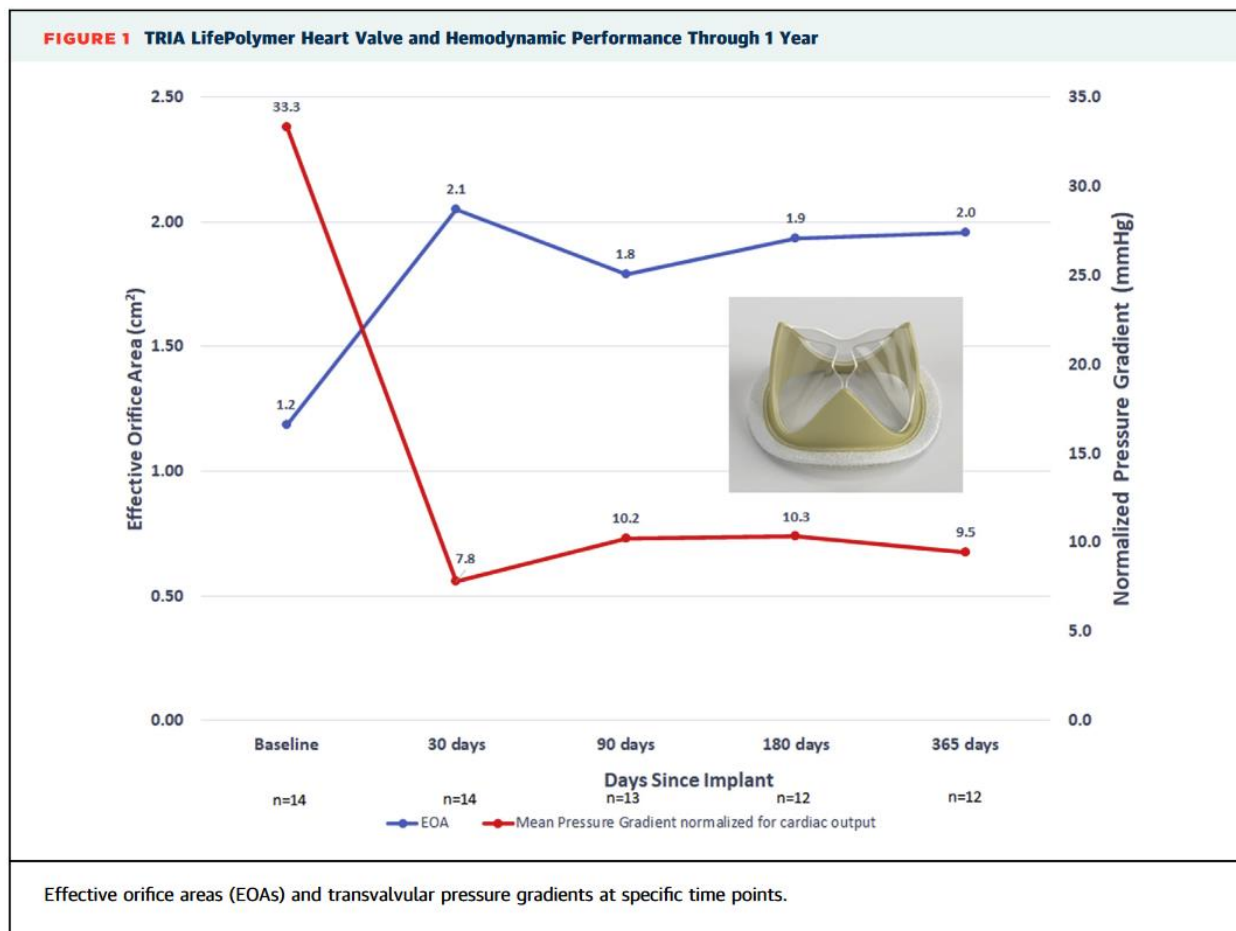


Figure 2.17 TRIA LifePolymer Heart Valve hemodynamic performance after one year, adapted from Kereiakes et al. (2021)

2.5 Design and Testing of Aortic Valve Replacements

2.5.1 ISO 5840 Standard for Heart Valves

AVRs are now widely used and have shown good clinical outcomes (Daubert et al., 2017). However, there is potential for further design improvements to enhance their structural durability and long-term hemodynamic performance. There are challenges in the development of the next-generation of AVRs that must be overcome to achieve suitable designs capable of withstanding the demanding functional requirements at the native aortic root. These mechanical requirements relate to both structural and hemodynamic performance, with the implant required to withstand high cycles of pulsatile pressures over its lifetime. Over a cardiac cycle, AVRs should provide minimal resistance to forward blood flow to maximise orifice area in the open

configuration, have a low pressure differential to revert to the closed configuration, and facilitate rapid closure to reduce volume regurgitation or forward flow energy loss. Development takes place through both in silico modelling and in vitro bench testing, with the latter being a more widely used, readily available, and standardised approach. ISO 5840:2021 (International Organisation for Standardisation, 2021a, 2021b, 2021c) describes the in vitro bench testing to be performed and is the international standard that provides guidelines, specifications, and minimum design criteria that cardiac valve prostheses must fulfil to be deemed safe and effective for patients by the FDA and relevant EU notified bodies. For durability testing, AVRs with gradual degradation failure modes must be able to withstand 200 million consecutive cardiac cycles. AVRs with the potential for immediate failure must withstand 400 million cycles to comply with the standard (International Organisation for Standardisation, 2021a). Hydrodynamic assessments are performed using pulsatile flow bench test systems, such as the Vivitro pulse duplicator system in Figure 2.18, which simulate physiological conditions and are used to assess valve hydrodynamic performance.

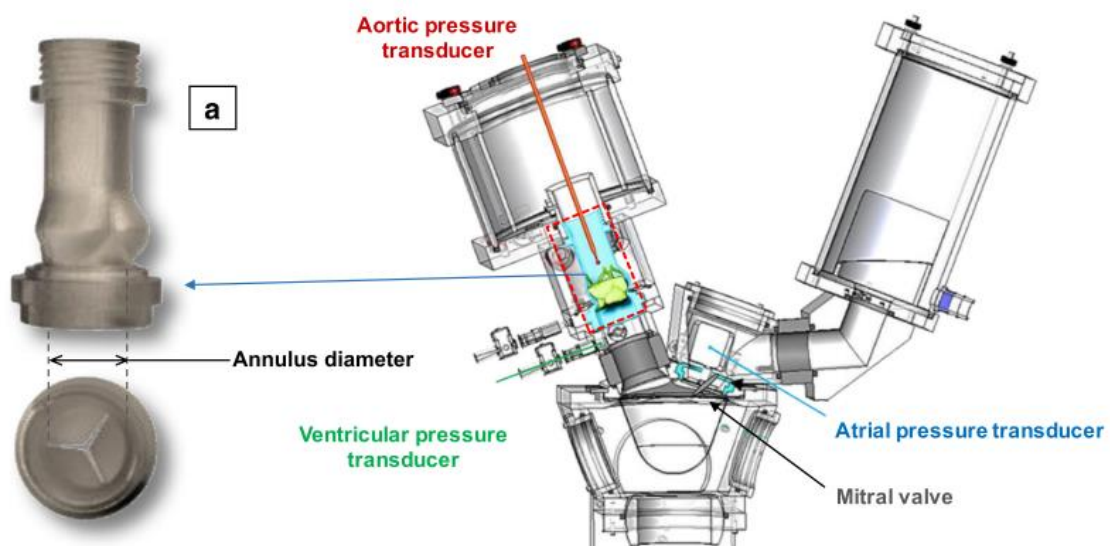


Figure 2.18 Vivitro pulse duplicator system. Adapted from Rahmani et al. (2017)

ISO 5840 defines acceptable values for key performance parameters of EOA and RF for surgical and transcatheter AVRs operating at normotensive conditions at a range of orifice sizes

(International Organisation for Standardisation, 2021c, 2021b). The required values for EOA and RF for the aortic valve are listed in Table 2.3.

Table 2.3. Minimum device performance requirements, aortic (International Organisation for Standardisation, 2021c).

Parameter	Valve size mm							
	17	19	21	23	25	27	29	31
EOA (cm ²) greater than or equal to	0.7	0.85	1.05	1.25	1.45	1.7	1.95	2.25
Total regurgitant fraction (% of forward flow volume) less than or equal to	10	10	10	10	15	15	20	20

Many comprehensive studies comparing these parameters across valve designs have been carried out on commercial flow rigs, such as that described by Rahmani et al. (2012). Studies that report hydrodynamic testing have been carried out on bioprosthetic valves to understand the correlation of long-term calcification with abnormal flow patterns (Barannyk et al., 2017), and to compare novel TAVR designs against current market offerings (Rotman et al., 2019). Such commercial flow rigs are also capable of investigating additional parameters such as the left ventricular energy loss, leakage volumes and transvalvular ΔP , which are further indicators of valve performance and useful in the design process. Rahmani et al. (2017) provides one of the most detailed studies in this area, whereby they conducted extensive hydrodynamic testing on a newly developed tri-leaflet polymer-based TRISKELE valve with an Edwards Sapien XT and Medtronic Corevalve across a range of orifice sizes using a Vivitro pulse duplicator (see Figure 2.19). Each orifice size was investigated and tested across cardiac outputs from 2-7 L/min in increments of 1 L/min. The resulting transvalvular ΔP , EOA, RF and left ventricular energy loss were recorded, with the TRISKELE offering comparable or superior performance to the control valves. The valve offered a significant reduction in paravalvular leakage with improved anchoring and sealing. De Gaetano et al. (2015a) also conducted a similar investigation on a polymeric valve, which was tested in vitro using a specially designed pulse

duplicator according to the ISO 5840 standard, which showed that prototypes met requirements in terms of both regurgitation and EOA. De Gaetano et al. (2015b) again tested a polymeric valve in vitro according to ISO 5840, meeting the requirements, and performed a comparison with other mechanical heart valves and tissue-based heart valves.

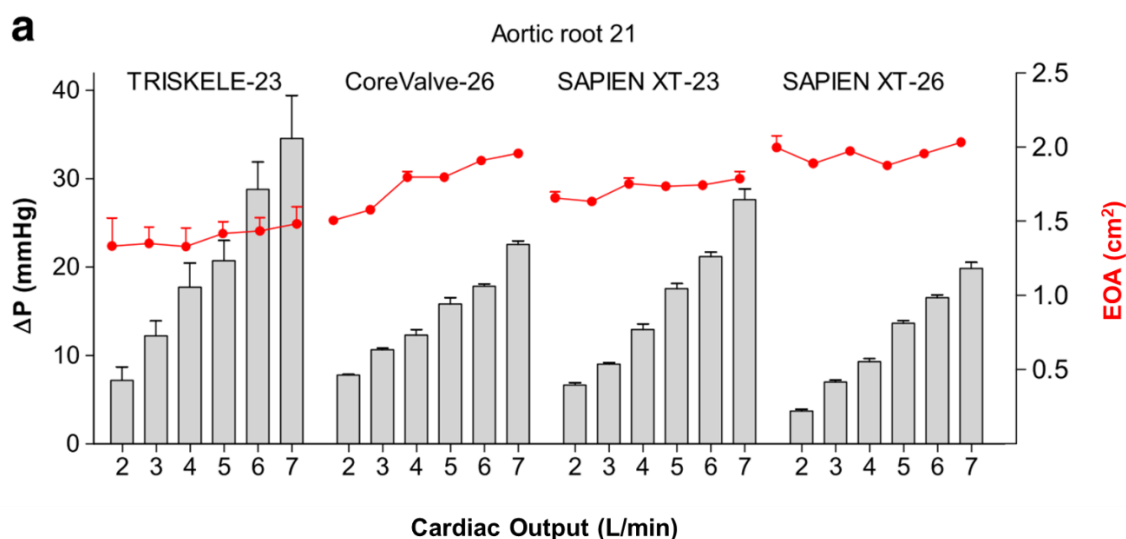


Figure 2.19 Transvalvular ΔP and EOA for each valve across cardiac outputs from 2-7 L/min, adapted from Rahmani et al. (2017).

While durability and hydrodynamic testing according to ISO 5840 provides a comprehensive assessment of structural and hemodynamic performance of valves, the development pathway typically involves a trial-and-error process of design, prototyping and testing. Each design iteration requires an extensive suite of bench tests (International Organisation for Standardisation, 2021a, 2021c, 2021b) and relying solely on this method contributes to high development costs and increased time to market for aortic valve devices.

2.6 Computational Approaches for Aortic Valve Biomechanics

2.6.1 Structural Finite Element Modelling of Aortic Valves

FEA has been widely used for structural analysis of the aortic valve, predicting leaflet deformation in open and closed configurations (Arcidiacono et al., 2005; Burriesci et al., 2010,

1999; Claiborne et al., 2013; Haj-Ali et al., 2008; Kim et al., 2008; Li and Sun, 2017, 2010; Serrani et al., 2016; Smuts et al., 2011). Many FEA studies perform a structural loading analysis (Figure 2.20), with a view to optimising leaflet or frame design to enhance fatigue behaviour and overall durability (Claiborne et al., 2013; Serrani et al., 2016; Smuts et al., 2011).

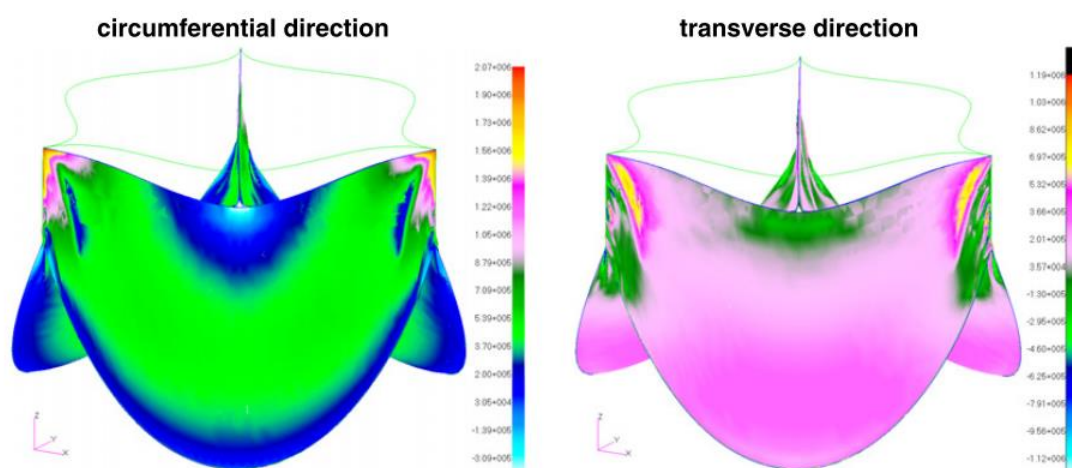


Figure 2.20 Structural FEA simulations showing stress distributions in circumferential and transverse directions across the valve leaflets (Smuts et al., 2011).

A structural FEA analysis of the aortic valve typically applies a pressure load, uniformly distributed across the valve leaflets. For systole, the load is applied at the ventricular side, while in diastole the load is applied to the aortic side of the leaflets. Different methodologies have been used to model the geometry of the valve leaflets. Several studies simplify the surrounding stent frame or aorta and isolate the simulation to the leaflet cusps, which have been modelled using both 3D elements or shell-based elements (Gnyaneshwar and Kumar, 2002; Haj-Ali et al., 2008). Smuts et al. (2011) used this approach to explore to investigate TAVR concepts, which were developed by incorporating valve design and performance parameters, along with stent constraints. Through this approach, the role of leaflet material, material orientation and abnormal valve dilation on the valve function was investigated by examining the resulting stress distribution across the valve leaflet. Smuts et al. (2011) also used FEA to simulated attachment forces and compared them to suture tearing tests performed on the pericardium

tissue. There are many benefits to structural analysis of the aortic valve. Several parameter and optimisation studies have been used to optimise the design of prosthetic valves for structural loading (Abbasi and Azadani, 2020; Hamid et al., 1984; Travaglino et al., 2020). Travaglino et al. (2020) used a Bayesian optimization (BO) based computational framework to investigate the design of transcatheter aortic valve leaflets and to optimize leaflet geometry such that its peak stress under the blood pressure of 120 mmHg was reduced. Through this approach, it was observed that peak stresses tend to concentrate near the stent-leaflet attachment edge and that increasing leaflet contact area redistributed peak stresses to the belly region, contributing to peak stress reduction. Morganti et al. (2015) proposed a new methodology to enable patient specific predictions of aortic valve closure using iso-geometric analysis for the model construction. This enabled a highly efficient method, which had two orders of magnitude fewer nodes than the finite element model, but maintained the same accuracy as the finite element-based approach

FEA has also been used extensively to investigate the effect of deployment geometry on leaflet deformation for TAVR systems (Auricchio et al., 2014; Barati et al., 2022, 2021; Dimasi et al., 2015; Gunning et al., 2014; Kusneri et al., 2021; Sturla et al., 2016). Gunning et al. (2014) simulated TAVR deployment in a patient-specific aortic root and used this to investigate the role of asymmetric stent morphology on leaflet coaptation geometries and resulting stress distributions within the leaflet (see Figure 2.21). Comparing to those of the idealized circular deployed TAVR, it was found that realistic valves had an eccentricity up to ~ 0.65 and this resulted in a more heterogeneous stress distribution than circularly deployed valves, with a higher proportion of the tissue leaflet volume experiencing stresses less than 0.2 MPa. It was concluded that preoperative planning of stent orientation could increase leaflet durability through decreased stress caused by stent distortion. FEA has also been used to examine the effect of calcification patterns on the native leaflet on TAVR stent expansion (Dimasi et al.,

2015; Sturla et al., 2016). Nappi et al. (2018) used FEA to better understand the diagnosis of thrombosis with regards to TAVR, finding a link between uncrushed calcifications, delayed dislodgement of TAVR and late thrombosis. Morganti et al. (2014) also demonstrated the ability of FEA to simulate patient-specific implantation of TAVR and used such approaches to provide predictions of patient-specific post-operative outcomes of TAVR procedure, in particular investigating the role of positioning on valve performance (Morganti et al., 2016). Tzamtzis et al. (2013) used FEA to investigate the radial force exerted by the Medtronic Corevalve and Edwards Sapien valve, finding that for both valves, the forces were substantially higher at smallest annular sizes, while for the self-expanding Corevalve, the force depended on the diameter of the left ventricular outflow tract. Several other studies have focused on the design of the TAVR itself. Rodriguez Matas and co-workers (Barati et al., 2022, 2021) have recently developed optimisation frameworks to enable patient-specific multiscale design optimization of transcatheter aortic valve stents. This multi-objective patient-specific optimization framework alters the geometrical design by targeting objectives of maximum crimping strain, radial strength, anchorage area, and the eccentricity of the stent, with optimised models providing significantly enhanced performance compared to the base design, particularly when radial strength and anchorage area were considered.

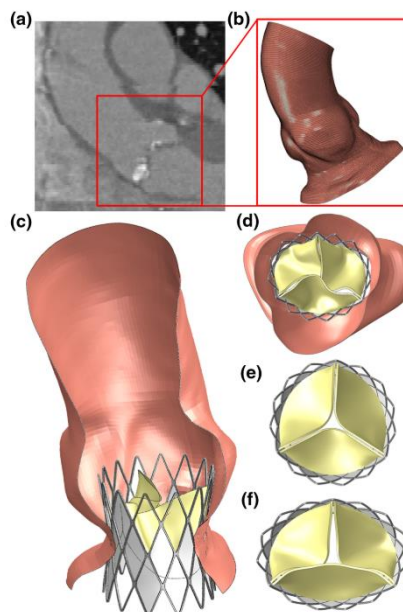


Figure 2.21 Effect of deployment geometry on TAVR leaflet deformation adapted from Gunning et al. (2014), showing (a) CT scan of aorta, (b) 3D mesh reconstruction and (c-f) TAVR deployment in several aortic root geometries.

While these studies showcase the benefits of a structural FEA simulation for aortic valves, these simulations focus primarily on stress distributions, overall deformation, or design optimizations. Very few studies have sought to directly compare the predictions from structural FEA models with experimental flow rigs or provide insight into the hydrodynamic performance of the valve. Haj-Ali et al. (2008) have presented a combined computational and experimental approach for the nonlinear structural simulations of polymeric tri-leaflet aortic valves, whereby the structural model was subject to averaged transvalvular pressure waveform measured from repeated in vitro tests conducted with a left heart simulator (see Figure 2.22). Qualitative and quantitative deformation measures were defined, and it was found that the structural model predicted kinematic deformation metrics with maximum errors around 10%, especially in systole. This approach provided a pathway to explore structural behaviour, but the simulations also provided insight into opening areas, thereby providing certain insight into hydrodynamic performance. However, only a limited number of other studies have explored this concept of interpreting hydrodynamic parameters from structural FEA (Pfensig et al., 2017).

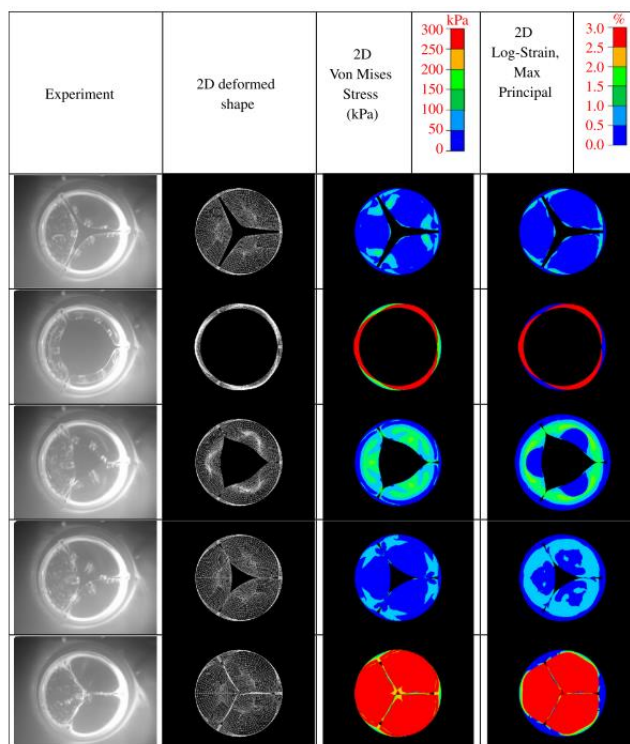


Figure 2.22 A comparison of *in vitro* deformation with *in silico* FEA models, alongside 2D von Mises Stress and 2D Log-Strain distributions, adapted from Haj-Ali et al. (2008)

2.6.2 Fluid-Structure Interaction Modelling of Aortic Valves

FSI models combine traditional computational fluid dynamics (CFD) and FEA simulations to examine the interaction between structure and fluid. For uncoupled CFD simulations, the fluid domain is limited to a static solid boundary and thus cannot replicate the dynamic motion of the leaflets, but rather investigate valve performance at different stages of the cardiac cycle. Thus, CFD has been a popular method for investigating the hemodynamics of the aortic tract (Zhu et al., 2018) and has been employed to investigate aspects such as the effect of sclerosis and stenosis on the wall shear stress and ejection force for TAVR (Dwyer et al., 2009). In the case of mechanical heart valves, it has been used to examine how vortex shedding provides the conditions for free emboli formation, where platelets exposed to high flow stresses can activate and aggregate (Bluestein et al., 2000). While CFD provides insight into flow characteristics of the aortic valve, it provides surprisingly limited information on the hydrodynamic performance parameters required by ISO 5840 (e.g. EOA, RF, transvalvular ΔP). To fully capture these

characteristics, the progressive opening and development of flow needs to be modelled, which requires coupling of fluid and structural simulations in an FSI model.

The benefits of using FSI over FE structural models for heart valve simulations have been shown to offer increased accuracy in the prediction of leaflet deformation (Luraghi et al., 2017). In addition, it provides the ability to directly measure dynamic hydrodynamic parameters of EOA, regurgitant volumes and transvalvular ΔP (Ghosh et al., 2018; Luraghi et al., 2019). FSI simulations require advanced discretisation methods. There are two primary approaches, one being monolithic and the other partitioned. In a monolithic approach, the fluid and structural domains are solved simultaneously, such as the immersed boundary (IB) method (Peskin, 2002). In this approach, the fluid mesh and structural mesh do not conform to the other, but instead the boundary conditions between structure and fluid are included in the model equations. Generally, when it comes to modelling the highly flexible thin leaflet of the aortic valve, the IB method is preferable over partitioned (Sodhani et al., 2018). In a partitioned approach, the structural and fluid domains are meshed independently of the other. Thus, as the geometry changes shape throughout a simulation, remeshing is required. The advantage of this method is that it allows independently developed CFD and FEA methods to be used together. For them to work together, an interface that passes information between each simulation is required. The Arbitrary Lagrangian-Eulerian (ALE) method is an example of a partitioned conforming mesh. Figure 2.23 shows an example of an IB and ALE formulation. Another FSI approach that can be used is the solid particle hydrodynamics (SPH) method. As a mesh-free particle-based method, it is efficient at simulating fluid flows with high levels of deformation and complex geometries, such as heart valves (Mao et al., 2017, 2016; Monteleone et al., 2022). Mao et al., (2016) compared FEA-only and SPH based FSI simulations of TAVR to simulate leaflet dynamics throughout the cardiac cycle, finding the SPH-based model could capture realistic deformation and higher peak stresses than observed in the FEA-only model.

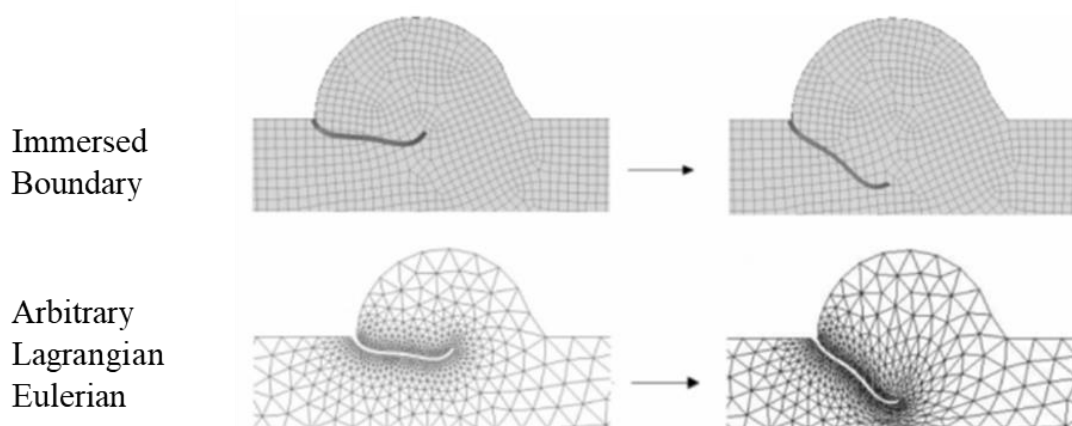


Figure 2.23 Example of an IB and ALE discretisation scheme in consequent time-steps (left to right) for a 2D flexible aortic valve leaflet, adapted from Bavo et al. (2016).

Table 2.4 summarises a range of FSI based studies in the literature. Many studies have used either ALE or IB methods to analyse aortic valve fluid and structural dynamics under a range of different conditions. Early FSI studies generally required simplifications due to the computational resources available at the time, using either two-dimensional representations or idealised aortic roots to predict valve flow and structural performance (De Hart et al., 2000). De Hart et al. (2003) presented one of the first studies on a three-dimensional valve with structural opening due to the fluid flow interaction. However, it is very noticeable from Table 2.4 that these early studies generally provided limited comparisons to experiments.

As computational power became more advanced, patient-specific cases and image-based models of the aortic root and valves could be simulated. Kandail et al. (2018) examined the annular and supra-annular locations for CoreValve deployment in patient-specific scans, with the CoreValve first deployed using a finite element approach (see Figure 2.24). FSI simulations used an ALE approach and realistic boundary conditions derived from in vivo conditions were applied. This study provided detailed predictions on how CoreValve deployment location affected hemodynamics in the ascending aorta and flow patterns in the coronary arteries, with

detailed predictions of wall shear stress, jet velocities and leaflet deformations provided. Luraghi et al. (2020) used a similar approach to investigate the effects of calcification on TAVR performance by analysing how para-valvular leakage was affected by the presence of calcium particles (Luraghi et al., 2020). Several other studies have used similar patient-specific approaches (Luraghi et al., 2019a; Luraghi et al., 2019b, Nannini et al., 2021; Qin et al., 2021), whereby FSI was used to provide detailed predictions of the in vivo performance of AVRs. However, it should be noted that there are distinct challenges, and somewhat limited efforts, to validate such models due to the difficulty in obtaining relevant measures in vivo.

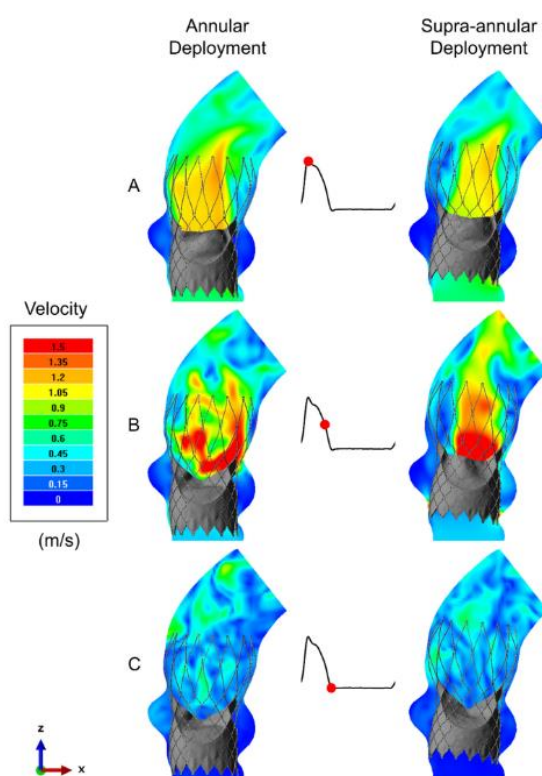


Figure 2.24 Velocity contours for CoreValve in annular and supra-annular location at time-points (A-C) during the cardiac cycle, adapted from Kandail et al. (2018)

Several studies have included an experimental component to offer a side-by-side comparison or validation for FSI models. Gharaie et al. (2018) presented an ALE-based FSI model to predict structural deformation of a custom-made polymeric aortic valve under physiological

conditions. This study predicted leaflet kinematics and geometric orifice area and compared these to experimental measurements from an in vitro pulsatile flow rig, finding good agreement with the experimental results with a maximum error of only 15% in a single cardiac cycle. Similarly, Piatti et al. (2016) examined a polymeric aortic valve prototype with an ALE-based FSI model and in vitro hydrodynamic testing to assess the validity of the model, finding a max error of <5% between experimental and simulated EOA. Ghosh et al. (2018) compared the leaflet kinematics and EOA of a TAVR between a Vivitro pulsatile flow rig and in silico ALE FSI models, finding good agreement in measured cardiac output and leaflet kinematics, while EOA of 2.03cm^2 was measured in vitro and 2.34cm^2 measured in silico. Sodhani et al. (2018) created an IB FSI simulation for a prosthetic aortic valve to replicate an in vitro experiment, measuring the geometric orifice area and flow rate across one cycle, with good agreement between the model and experimental results during systole.

Luraghi and colleagues directly compared the leaflet deformation across a structural FEA, FSI and in vitro experiment, finding that the FSI results better replicated the experimental valve kinematics than the FEA (Luraghi et al., 2017) (see Figure 2.25). There was a maximum difference of 5% between the experimental and FSI GOA at max opening time, compared to a difference of 46.5% between the experimental and FE GOA. Bavo et al. (2016) presents a comparison of the ALE method with the IB method for modelling the highly dynamic motion of the aortic valve under pulsatile flow. The method described by Bavo was the Coupled Eulerian Lagrangian (CEL) method, present in the commercially available Abaqus software. Currently, this is the only instance of the Abaqus/CEL method being used to model the aortic valve in the literature. The study also lacks an experimental component for validation and does not attempt to extract the hydrodynamic parameters required in in vitro testing. Here, the author of this thesis acknowledged room for further investigation to the Abaqus/CEL method for modelling the aortic valve, which is addressed in Chapters 6 and 7.

In addition to research, there has been a recent push in industry for verification and validation of simulations to aid the development of medical devices. This allows industry to accelerate testing of new devices in circumstances where experimental tests can be achieved computationally. To help define where using simulations are appropriate, the American Society of Mechanical Engineers (ASME) Verification and Validation (V&V) 40 standard has been developed (ASME, 2018). This is an FDA-recognised standard that provides a risk-based protocol to help evaluate the credibility requirements of a computational model. Morrison et al., (2019) have demonstrated how the framework can be applied to the evaluation of a centrifugal blood pump, and there are several examples of its use in vascular stent design (Antonini et al., 2021; Berti et al., 2021). However, a rigorous and systematic presentation of valve performance has not yet been addressed in a V&V context.

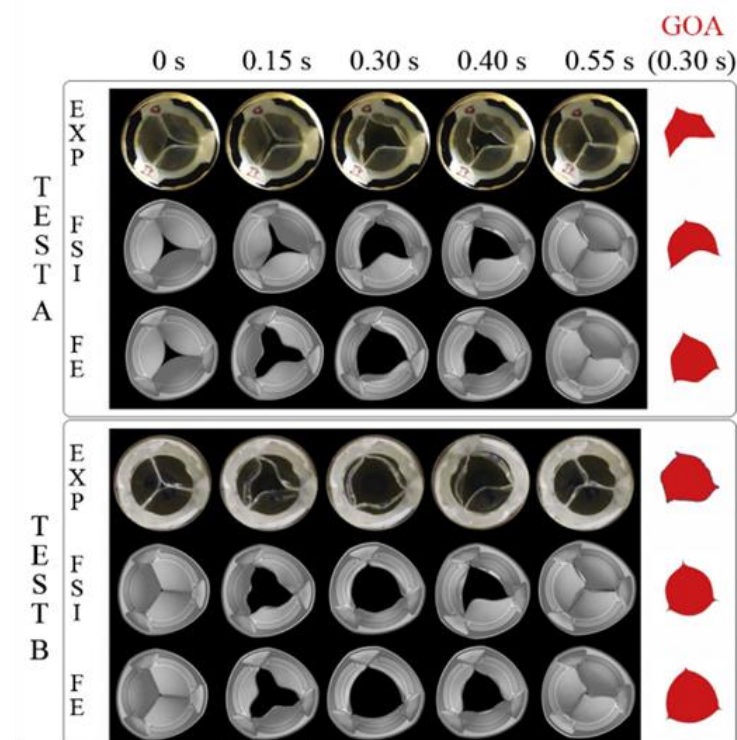


Figure 2.25 Comparison of geometric orifice area across experimental, structural finite element and FSI analysis of an aortic valve replacement (Luraghi et al., 2017).

2.7 Conclusions

This review of the literature has established the background of this thesis in relation to the development of AVRs, with particular focus on the bench testing requirements that are needed during development. Furthermore, a review of computational approaches for simulating aortic valve biomechanics were presented, with particular focus on finite element and fluid-structure interaction based models used to predict AVR performance.

The review observed the usefulness of structural finite element modelling for valve design, but that there was a lack of literature investigating its ability to predict hemodynamic performance. In particular, it was found that finite element analysis (FEA) had been widely used to predict the structural performance of the aortic valve by simulating opening and closing configurations (Arcidiacono et al., 2005; Burriesci et al., 2010; Claiborne et al., 2013; Haj-Ali et al., 2008; Kim et al., 2008; Li and Sun, 2017, 2010; Serrani et al., 2016; Smuts et al., 2011). However, to date, these studies have been mainly used during the design process to reduce stress in the leaflet and/or frame with a view to enhancing durability of the valve. To date, few studies have sought to use FEA to examine hydrodynamic performance of the valve.

In relation to FSI models of AVR performance, it is clear that FSI has been widely applied to AVRs to provide insight into structural and hemodynamic performance of the valve. However, the majority of FSI studies have not included an experimental validation component, which brings into question their wider applicability. Even for studies that do include experimental validation, this typically takes place using bulk in vitro testing on AVRS using pulsatile flow rigs (Gharaie et al., 2018; Luraghi et al., 2017), which can present challenges in fully understanding leaflet deformation. While FSI models have the potential to speed up the design and development process by replicating the in vitro hydrodynamic testing required for ISO

5840, there remains a significant need for approaches that provide robust experimental validation to FSI techniques to maximise their application during the design process.

Table 2.4. Overview of Valve Fluid-Structure Interaction Studies, experimental components and hydrodynamic parameters.

Author & Year	Study Description	FSI Method	Aortic Valve	Experimental Validation	Hydrodynamic Parameters evaluated
(Qin et al., 2021)	3D patient-specific fluid-structure interaction (FSI) simulations of bicuspid aortic valve (BAV) with fully coupled flow dynamics and valve motions throughout the cardiac cycle to investigate BAV hemodynamics	Fully coupled Abaqus solid particle hydrodynamics (SPH) and FE	Native bicuspid	Clinical data, pressure gradients and CT scans	Peak velocity, normalized flow displacement, and jet angle
(Nannini et al., 2021)	A fluid-structure interaction (FSI) protocol, based on patient-specific geometry and boundary conditions, to assess impact of proximal aortic grafts on downstream aortic hemodynamics and distensibility.	2-way FSI coupling FE and CFD	Native	Cardiac magnetic resonance (CMR), including MRA, cine-CMR and 4D flow sequences	Velocity, aortic distensibility, stress and strain and wall shear stress
(Terahara et al., 2020)	An isogeometric sequentially-coupled FSI (SCFSI) method that can address the challenges of unsteady flow through a complex geometry, solid surfaces with large motion, and contact between the valve leaflet with an outcome of high-fidelity flow solutions	Sequentially coupled FSI (SCFSI)	BHV	No	Velocity, wall shear stress
(Luraghi et al., 2019)	Assessing the affect of clinical data quality on fluid-structure interaction simulations of patient-specific stenotic aortic valve models	ALE	Stenosed Native Aortic Valve	Doppler Echocardiography	Jet Velocity, GOA

Author & Year	Study Description	FSI Method	Aortic Valve	Experimental Validation	Hydrodynamic Parameters evaluated
(Luraghi et al., 2019)	Modeling of a patient-specific transcatheter aortic valve replacement with a fluid structure interaction approach	Coupled CFD and FE	TAVR	Yes - Doppler echocardiography	Flow rate, GOA, regurgitant volume, EOA
(Abu Bakar et al., 2018)	Particle image velocimetry and finite volume method study of bi-leaflet artificial heart valve	2-way FSI coupling CFD and FEA	MHV	Yes - Particle image velocimetry (PIV)	WSS, pressure, stress analysis, Doppler velocity index
(Borowski et al., 2018)	Fluid-structure interaction of heart valve dynamics in comparison to finite-element analysis	ALE, FEA and CFD	BHV	No	Leaflet opening area, displacement
(Chen and Luo, 2018)	A computational study of the three-dimensional fluid structure interaction of aortic valve	IB	BHV	No	GOA, Flow Rate, Pressure Distribution
(Gharaie et al., 2018)	In vitro validation of a numerical simulation of leaflet kinematics in a polymeric aortic valve under physiological conditions	ALE	SAVR	Yes - Custom flow rig	GOA, Vortices
(Ghosh et al., 2018)	Comparative fluid-structure interaction analysis of polymeric transcatheter and surgical aortic valves' hemodynamics and structural mechanics	ALE	TAVR and SAVR	Yes - Vivitro	GOA, EOA, WSS, Stress
(Kandail et al., 2018)	Impact of annular and supra-annular CoreValve deployment locations on aortic and coronary artery hemodynamics	Finite-volume based boundary conforming sub-grid geometry resolution (SGGR)	TAVR	No	WSS, Velocity

Author & Year	Study Description	FSI Method	Aortic Valve	Experimental Validation	Hydrodynamic Parameters evaluated
(Sodhani et al., 2018)	Fluid-structure interaction simulation of artificial textile reinforced aortic heart valve: Validation with an in-vitro test	IB – SGGR	SAVR	Yes – Custom flow rig	GOA, Flow Rate, WSS
(Tango et al., 2018)	Validation and extension of a fluid–structure interaction model of the healthy aortic valve	ALE	Native Aortic Valve	Yes - PIV	Velocities, EOA
(Amindari et al., 2017)	Assessment of calcified aortic valve leaflet deformations and blood flow dynamics using fluid-structure interaction modelling	FSI, CFD and FEA	2D Native Valve	Echocardiography velocity measurements for BC's	Opening Ratio, Transvalvular ΔP , WSS
(Hedayat et al., 2017)	Platelet activation of mechanical versus bioprosthetic heart valves during systole	IB	MHV and bioprosthetic	No	Platelet Activation
(Laadhari and Székely, 2017)	Eulerian finite element method for the numerical modelling of fluid dynamics of natural and pathological aortic valves	Resistive Immersed Surface Model	TAVR	No	Pressure, Flow rates, WSS
(Luraghi et al., 2017)	Evaluation of an aortic valve prosthesis: Fluid-structure interaction or structural simulation?	Immersed finite element	AVR	Yes – In house pulse duplicator	Geometric Orifice Area, Velocity
(Vahidkhah and Azadani, 2017)	Assessing if supra-annular valve-in-valve implantation reduces blood stasis on the transcatheter aortic valve leaflets	1-way coupled FE and CFD	TAVR	No	WSS
(Bavo et al., 2016)	Fluid-structure interaction simulation of prosthetic aortic valves: comparison between immersed boundary and arbitrary lagrangian-eulerian techniques for the mesh representation	IB and ALE	AVR	No	Rapid Valve Opening Time (RVOT), Pressure, Velocity

Author & Year	Study Description	FSI Method	Aortic Valve	Experimental Validation	Hydrodynamic Parameters evaluated
(Flamini et al., 2016)	Immersed boundary-finite element model of fluid structure interaction in the aortic root	IB	Native	No	Flow rate, velocities, stress
(Mao et al., 2016)	Fluid structure interaction study of transcatheter aortic valve dynamics using smoothed particle hydrodynamics	SPH	TAVR	No	Mean systolic ΔP , peak ΔP , EOA, GOA, RF, Flow Rate
(Piatti et al., 2016)	Polymeric valve using a fluid-structure interaction approach	Lagrangian-Eulerian	SAVR	Yes - Vivitro	EOA, ΔP , RVOT, Rapid Valve Closing Time (RVCT), Flow Rate
(Wu et al., 2016)	Fluid structure interaction model of a percutaneous aortic valve: comparison with an in vitro test and feasibility study in a patient-specific case	ALE	AVR	Yes – Accelerated durability tester	LOA, RVOT, RVCT, Pressure velocity contours
(Hsu et al., 2015)	Dynamic and fluid structure interaction simulations of bioprosthetic heart valves using parametric design with T-splines and Fung-type material models	ALE	BHV	No	Flow Rate, GOA, Regurgitant Volume, Effective Regurgitant Orifice Area
(Kalyana Sundaram et al., 2015)	Aortic valve dynamics using a fluid structure interaction model – The physiology of opening and closing	N/A	Native	No	EOA, pressure gradients, RF
(Gharaie and Morsi, 2015)	FSI simulation of a novel design of a polymeric aortic valve	ALE 2-way coupled	AVR	No	EOA, ΔP , closing volume, GOA
(Borazjani, 2013)	Fluid-structure interaction, immersed boundary-finite element method simulations of bio-prosthetic heart valves	IB	AVR	No	Vorticity, Shear, Stress,

Author & Year	Study Description	FSI Method	Aortic Valve	Experimental Validation	Hydrodynamic Parameters evaluated
(Griffith, 2012)	Immersed boundary model of aortic heart valve dynamics with physiological driving and loading conditions	IB	AVR	No	Transvalvular ΔP
(Sirois et al., 2011)	Fluid simulation of a transcatheter aortic valve deployment into a patient-specific aortic root	Uncoupled FE and CFD	TAVR	With Clinical Data, patient specific geometry	EOA, ΔP
(Shadden et al., 2010)	Computational analysis of an aortic valve jet with Lagrangian coherent structures	Fictitious Domain (FD)	Native	No	EOA, GOA
(Griffith, 2009)	Prosthetic heart valves using the immersed boundary method	IB	AVR	No	Velocity, pressures
(Nobili et al., 2008)	Numerical simulation of the dynamics of a bileaflet prosthetic heart valve using a fluid-structure interaction approach	ALE	MHV	Yes – pulsatile open loop mock circulatory system (MCS)	Transvalvular ΔP , Velocity
(Morsi et al., 2007)	Transient fluid-structure coupling for simulation of a trileaflet heart valve using weak coupling	ALE	AVR	No	Velocity, WSS
(Carmody et al., 2006)	An approach to the simulation of fluid-structure interaction in the aortic valve	ALE	Native	No	Pressures, Velocities
(De Hart et al., 2003)	A three-dimensional computational analysis of fluid-structure interaction in the aortic valve	FD	Native	No	Velocities, stresses

2.8 References

- Abbasi, M., Azadani, A.N., 2020. A geometry optimization framework for transcatheter heart valve leaflet design. *J. Mech. Behav. Biomed. Mater.* 102, 103491. <https://doi.org/10.1016/j.jmbbm.2019.103491>
- Abu Bakar, H., Abas, A., Mokhtar, N.H., Razak, N., Hamid, M.N.B.A., 2018. Particle image velocimetry and finite volume method study of bi-leaflet artificial heart valve. *J. Appl. Fluid Mech.* 11, 1365–1375. <https://doi.org/10.29252/jafm.11.05.28808>
- Adams, H.S.L., Ashokkumar, S., Newcomb, A., MacIsaac, A.I., Whitbourn, R.J., Palmer, S., 2019. Contemporary review of severe aortic stenosis. *Intern. Med. J.* 49, 297–305. <https://doi.org/10.1111/imj.14071>
- Agatston, A.S., Janowitz, W.R., Hildner, F.J., Zusmer, N.R., Viamonte, M., Detrano, R., 1990. Quantification of coronary artery calcium using ultrafast computed tomography. *J. Am. Coll. Cardiol.* 15, 827–832. [https://doi.org/10.1016/0735-1097\(90\)90282-T](https://doi.org/10.1016/0735-1097(90)90282-T)
- Alushi, B., Curini, L., Christopher, M.R., Grubitzch, H., Landmesser, U., Amedei, A., Lauten, A., 2020. Calcific Aortic Valve Disease-Natural History and Future Therapeutic Strategies. *Front. Pharmacol.* 11, 1–12. <https://doi.org/10.3389/fphar.2020.00685>
- Amindari, A., Saltik, L., Kirkkopru, K., Yacoub, M., Yalcin, H.C., 2017. Assessment of calcified aortic valve leaflet deformations and blood flow dynamics using fluid-structure interaction modeling. *Informatics Med. Unlocked* 9, 191–199. <https://doi.org/10.1016/j.imu.2017.09.001>
- Ando, M., Takahashi, Y., 2009. Ten-year experience with handmade trileaflet polytetrafluoroethylene valved conduit used for pulmonary reconstruction. *J. Thorac. Cardiovasc. Surg.* 137, 124–131. <https://doi.org/10.1016/j.jtcvs.2008.08.060>
- Antonini, L., Mandelli, L., Berti, F., Pennati, G., Petrini, L., 2021. Validation of the computational model of a coronary stent: a fundamental step towards in silico trials. *J. Mech. Behav. Biomed. Mater.* 122, 104644. <https://doi.org/10.1016/j.jmbbm.2021.104644>
- Arcidiacono, G., Corvi, A., Severi, T., 2005. Functional analysis of bioprosthetic heart valves. *J. Biomech.* 38, 1483–1490. <https://doi.org/10.1016/j.jbiomech.2004.07.007>
- Arzani, A., Mofrad, M.R.K., 2017. A strain-based finite element model for calcification progression in aortic valves. *J. Biomech.* 65, 216–220. <https://doi.org/10.1016/j.jbiomech.2017.10.014>
- ASME V&V 40-2018, 2018. Assessing credibility of computational modeling through verification and validation: application to medical devices.
- Auricchio, F., Conti, M., Morganti, S., Reali, A., 2014. Simulation of transcatheter aortic valve implantation: a patient-specific finite element approach. *Comput. Methods Biomech. Biomed. Engin.* 17, 1347–1357. <https://doi.org/10.1080/10255842.2012.746676>
- Bajwa, T., Heiser, J.C., Merhi, W., Kleiman, N.S., Askew, J., Sorajja, P., Rovin, J., Chetcuti, S.J., Adams, D.H., Teirstein, P.S., Iii, G.L.Z., Forrest, J.K., Tchétché, D., Resar, J., Walton, A., Boulware, M.J., Ph, D., Qiao, H., Ph, D., Mugglin, A.S., Ph, D., 2019. Transcatheter Aortic-Valve Replacement with a Self-Expanding Valve in Low-Risk Patients. <https://doi.org/10.1056/NEJMoa1816885>

Barannyk, O., Fraser, R., Oshkai, P., 2017. A correlation between long-term in vitro dynamic calcification and abnormal flow patterns past bioprosthetic heart valves. *J. Biol. Phys.* 43, 279–296. <https://doi.org/10.1007/s10867-017-9452-9>

Barati, S., Fatouraee, N., Nabaei, M., Berti, F., Petrini, L., Migliavacca, F., Rodriguez Matas, J.F., 2021. A computational optimization study of a self-expandable transcatheter aortic valve. *Comput. Biol. Med.* 139, 104942. <https://doi.org/10.1016/j.compbimed.2021.104942>

Barati, S., Fatouraee, N., Nabaei, M., Petrini, L., Migliavacca, F., Luraghi, G., Matas, J.F.R., 2022. Patient-specific multi-scale design optimization of transcatheter aortic valve stents. *Comput. Methods Programs Biomed.* 221, 106912. <https://doi.org/https://doi.org/10.1016/j.cmpb.2022.106912>

Baumgartner, H., Falk, V., Bax, J.J., De Bonis, M., Hamm, C., Holm, P.J., Iung, B., Lancellotti, P., Lansac, E., Muñoz, D.R., Rosenhek, R., Sjögren, J., Tornos Mas, P., Vahanian, A., Walther, T., Wendler, O., Windecker, S., Zamorano, J.L., Roffi, M., Alfieri, O., Agewall, S., Ahlsson, A., Barbato, E., Bueno, H., Collet, J.P., Coman, I.M., Czerny, M., Delgado, V., Fitzsimons, D., Folliguet, T., Gaemperli, O., Habib, G., Harringer, W., Haude, M., Hindricks, G., Katus, H.A., Knuuti, J., Kolh, P., Leclercq, C., McDonagh, T.A., Piepoli, M.F., Pierard, L.A., Ponikowski, P., Rosano, G.M.C., Ruschitzka, F., Shlyakhto, E., Simpson, I.A., Sousa-Uva, M., Stepinska, J., Tarantini, G., Tche, D., Aboyans, V., Kzhdryan, H.K., Mascherbauer, J., Samadov, F., Shumavets, V., Van Camp, G., Loncar, D., Lovric, D., Georgiou, G.M., Linhartova, K., Ihlemann, N., Abdelhamid, M., Pern, T., Turpeinen, A., Srbínovska-Kostovska, E., Cohen, A., Bakhutashvili, Z., Ince, H., Vavuranakis, M., Temesvari, A., Gudnason, T., Mylotte, D., Kuperstein, R., Indolfi, C., Pya, Y., Bajraktari, G., Kerimkulova, A., Rudzitis, A., Mizariene, V., Lebrun, F., Demarco, D.C., oukerraj, L., Bouma, B.J., Steigen, T.K., Komar, M., De Moura Branco, L.M., Popescu, B.A., Uspenskiy, V., Foscoli, M., Jovovic, L., Simkova, I., Bunc, M., de Prada, J.A.V., Stagmo, M., Kaufmann, B.A., Mahdhaoui, A., Bozkurt, E., Nesukay, E., Brecker, S.J.D., 2017a. 2017 ESC/EACTS Guidelines for the management of valvular heart disease, *European Heart Journal*. <https://doi.org/10.1093/eurheartj/ehx391>

Baumgartner, H., Hung, J., Bermejo, J., Chambers, J.B., Edvardsen, T., Goldstein, S., Lancellotti, P., LeFevre, M., Miller, F., Otto, C.M., 2017b. Recommendations on the Echocardiographic Assessment of Aortic Valve Stenosis: A Focused Update from the European Association of Cardiovascular Imaging and the American Society of Echocardiography. *J. Am. Soc. Echocardiogr.* 30, 372–392. <https://doi.org/10.1016/j.echo.2017.02.009>

Baumgartner, H., Hung, J., Bermejo, J., Chambers, J.B., Evangelista, A., Griffin, B.P., Iung, B., Otto, C.M., Pellikka, P.A., Quiñones, M., 2009. Echocardiographic Assessment of Valve Stenosis: EAE/ASE Recommendations for Clinical Practice. *J. Am. Soc. Echocardiogr.* 22, 1–23. <https://doi.org/10.1016/j.echo.2008.11.029>

Baura, G., 2021. Chapter 6 – Heart valves, in: Baura, G. (Ed.), *Medical Device Technologies (Second Edition)*. Academic Press, pp. 149–178. <https://doi.org/https://doi.org/10.1016/B978-0-12-811984-6.00006-4>

Bavo, A.M., Rocatello, G., Iannaccone, F., Degroote, J., Vierendeels, J., Segers, P., 2016. Fluid-Structure Interaction Simulation of Prosthetic Aortic Valves: Comparison between Immersed Boundary and Arbitrary Lagrangian-Eulerian Techniques for the Mesh Representation. *PloS One* 11. <https://doi.org/10.1371/journal.pone.0154517>

Bellhouse, B.B.J., 1969. Velocity and pressure distributions in the aortic valve 37, 587–600.

- Berti, F., Antonini, L., Poletti, G., Fiuza, C., Vaughan, T.J., Migliavacca, F., Petrini, L., Pennati, G., 2021. How to Validate in silico Deployment of Coronary Stents: Strategies and Limitations in the Choice of Comparator. *Front. Med. Technol.* 3. <https://doi.org/10.3389/fmedt.2021.702656>
- Billiar, K.L., Sacks, M.S., 2000. Biaxial mechanical properties of the natural and glutaraldehyde treated aortic valve cusp – Part I: Experimental results. *J. Biomech. Eng.* 122, 23–30. <https://doi.org/10.1115/1.429624>
- Blackman, D.J., Saraf, S., MacCarthy, P.A., Myat, A., Anderson, S.G., Malkin, C.J., Cunnington, M.S., Somers, K., Brennan, P., Manoharan, G., Parker, J., Aldalati, O., Brecker, S.J., Dowling, C., Hoole, S.P., Dorman, S., Mullen, M., Kennon, S., Jerrum, M., Chandrala, P., Roberts, D.H., Tay, J., Doshi, S.N., Ludman, P.F., Fairbairn, T.A., Crowe, J., Levy, R.D., Banning, A.P., Ruparelia, N., Spence, M.S., Hildick-Smith, D., 2019. Long-Term Durability of Transcatheter Aortic Valve Prostheses. *J. Am. Coll. Cardiol.* 73, 537–545. <https://doi.org/10.1016/j.jacc.2018.10.078>
- Bluestein, D., Rambod, E., Gharib, M., 2000. Vortex shedding as a mechanism for free emboli formation in mechanical heart valves. *J. Biomech. Eng.* 122, 125–134. <https://doi.org/10.1115/1.429634>
- Bodnár, T., Sequeira, A., Prosi, M., 2011. On the shear-thinning and viscoelastic effects of blood flow under various flow rates. *Appl. Math. Comput.* 217, 5055–5067. <https://doi.org/10.1016/j.amc.2010.07.054>
- Boon, B., 2010. Leonardo da Vinci on atherosclerosis and the function of the sinuses of Valsalva. *Netherlands Hear. J.* 17, 496–499. <https://doi.org/10.1007/s12471-010-0010-3>
- Borazjani, I., 2013. Fluid-structure interaction, immersed boundary-finite element method simulations of bio-prosthetic heart valves. *Comput. Methods Appl. Mech. Eng.* 257, 103–116. <https://doi.org/10.1016/j.cma.2013.01.010>
- Borowski, F., Sämman, M., Pfensig, S., Wüstenhagen, C., Ott, R., Kaule, S., Siewert, S., Grabow, N., Schmitz, K.P., Stiehm, M., 2018. Fluid-structure interaction of heart valve dynamics in comparison to finite-element analysis. *Curr. Dir. Biomed. Eng.* 4, 259–262. <https://doi.org/10.1515/cdbme-2018-0063>
- Bradley, S.M., 2013. Aortic Valve Insufficiency in the Teenager and Young Adult: The Role of Prosthetic Valve Replacement. *World J. Pediatr. Congenit. Hear. Surg.* 4, 397–402. <https://doi.org/10.1177/2150135113488781>
- Burriesci, G., Howard, I.C., Patterson, E.A., 1999. Influence of anisotropy on the mechanical behaviour of bioprosthetic heart valves. *J. Med. Eng. Technol.* 23, 203–215. <https://doi.org/10.1080/030919099294050>
- Burriesci, G., Marincola, F.C., Zervides, C., 2010. Design of a novel polymeric heart valve. *J. Med. Eng. Technol.* 34, 7–22. <https://doi.org/10.3109/03091900903261241>
- Campbell, J.M., 1950. An artificial aortic valve; preliminary report. *J. Thorac. Surg.* 19, 312–318.
- Carmody, C.J., Burriesci, G., Howard, I.C., Patterson, E.A., 2006. An approach to the simulation of fluid-structure interaction in the aortic valve. *J. Biomech.* 39, 158–169. <https://doi.org/10.1016/j.jbiomech.2004.10.038>

- Carpentier, A., Lemaigre, G., Robert, L., Carpentier, S., Dubost, C., 1969. Biological factors affecting long-term results of valvular heterografts. *J. Thorac. Cardiovasc. Surg.* 58, 467–483.
- Chen, Y., Luo, H., 2018. A computational study of the three-dimensional fluid–structure interaction of aortic valve. *J. Fluids Struct.* 80, 332–349. <https://doi.org/10.1016/j.jfluidstructs.2018.04.009>
- Claiborne, T.E., Sheriff, J., Kuetting, M., Steinseifer, U., Slepian, M.J., Bluestein, D., 2013. In vitro evaluation of a novel hemodynamically optimized trileaflet polymeric prosthetic heart valve. *J. Biomech. Eng.* 135, 021021. <https://doi.org/10.1115/1.4023235>
- Coulter, F.B., Schaffner, M., Faber, J.A., Rafsanjani, A., Smith, R., Appa, H., Zilla, P., Bezuidenhout, D., Studart, A.R., 2019. Bioinspired Heart Valve Prosthesis Made by Silicone Additive Manufacturing. *Matter* 1, 266–279. <https://doi.org/10.1016/j.matt.2019.05.013>
- Dasi, L.P., Simon, H.A., Sucusky, P., Yoganathan, A.P., 2009. Fluid mechanics of artificial heart valves. *Clin. Exp. Pharmacol. Physiol.* 36, 225–237. <https://doi.org/10.1111/j.1440-1681.2008.05099.x>
- Daubert, M.A., Weissman, N.J., Hahn, R.T., Pibarot, P., Parvataneni, R., Mack, M.J., Svensson, L.G., Gopal, D., Kapadia, S., Siegel, R.J., Kodali, S.K., Szeto, W.Y., Makkar, R., Leon, M.B., Douglas, P.S., 2017. Long-Term Valve Performance of TAVR and SAVR: A Report From the PARTNER I Trial. *JACC Cardiovasc. Imaging* 10, 15–25. <https://doi.org/10.1016/j.jcmg.2016.11.004>
- De Gaetano, F., Bagnoli, P., Zaffora, A., Pandolfi, A., Serrani, M., Brubert, J., Stasiak, J., Moggridge, G.D., Costantino, M.L., 2015a. A newly developed tri-leaflet polymeric heart valve prosthesis. *J. Mech. Med. Biol.* 15, 1–8. <https://doi.org/10.1142/S0219519415400096>
- De Gaetano, F., Serrani, M., Bagnoli, P., Brubert, J., Stasiak, J., Moggridge, G.D., Costantino, M.L., 2015b. Fluid dynamic characterization of a polymeric heart valve prototype (Poli-Valve) tested under continuous and pulsatile flow conditions. *Int. J. Artif. Organs* 38, 600–6. <https://doi.org/10.5301/ijao.5000452>
- De Hart, J., Peters, G.W.M., Schreurs, P.J.G., Baaijens, F.P.T., 2003. A three-dimensional computational analysis of fluid-structure interaction in the aortic valve. *J. Biomech.* 36, 103–112. [https://doi.org/10.1016/S0021-9290\(02\)00244-0](https://doi.org/10.1016/S0021-9290(02)00244-0)
- De Hart, J., Peters, G.W.M., Schreurs, P.J.G., Baaijens, F.P.T., 2000. A two-dimensional fluid-structure interaction model of the aortic valve. *J. Biomech.* 33, 1079–1088. [https://doi.org/10.1016/S0021-9290\(00\)00068-3](https://doi.org/10.1016/S0021-9290(00)00068-3)
- Dimasi, A., Stevanella, M., Votta, E., Sturla, F., Burriesci, G., Redaelli, A., 2015. Finite element analysis of transcatheter aortic valve implantation in the presence of aortic leaflet calcifications. *Lect. Notes Appl. Comput. Mech.* 74, 101–115. https://doi.org/10.1007/978-3-319-10981-7_7
- Dintenfass, L., 1962. Thixotropy of Blood and Proneness to Thrombus Formation. *Circ. Res.* 233–239.
- Durko, A.P., Osnabrugge, R.L., Mieghem, N.M. Van, Milojevic, M., Mylotte, D., Nkomo, V.T., Kappetein, A.P., 2018. Annual number of candidates for transcatheter aortic valve implantation per country: current estimates and future projections 2635–2642. <https://doi.org/10.1093/eurheartj/ehy107>

- Dwyer, H.A., Matthews, P.B., Azadani, A., Jaussaud, N., Ge, L., Guy, T.S., Tseng, E.E., 2009. Computational fluid dynamics simulation of transcatheter aortic valve degeneration☆☆☆. *Interact. Cardiovasc. Thorac. Surg.* 9, 301–308. <https://doi.org/10.1510/icvts.2008.200006>
- Eveborn, G.W., Schirmer, H., Heggelund, G., Lunde, P., 2013. The evolving epidemiology of valvular aortic stenosis . *The Tromsø Study* 396–400. <https://doi.org/10.1136/heartjnl-2012-302265>
- Fisher, C.I., Chen, J., Merryman, W.D., 2013. Calcific nodule morphogenesis by heart valve interstitial cells is strain dependent. *Biomech. Model. Mechanobiol.* 12, 5–17. <https://doi.org/10.1007/s10237-012-0377-8>
- Flamini, V., DeAnda, A., Griffith, B.E., 2016. Immersed boundary-finite element model of fluid–structure interaction in the aortic root. *Theor. Comput. Fluid Dyn.* 30, 139–164. <https://doi.org/10.1007/s00162-015-0374-5>
- Franke, B., Weese, J., Waechter-Stehle, I., Brüning, J., Kuehne, T., Goubergrits, L., 2020. Towards improving the accuracy of aortic transvalvular pressure gradients: rethinking Bernoulli. *Med. Biol. Eng. Comput.* 58, 1667–1679. <https://doi.org/10.1007/s11517-020-02186-w>
- Friedman, M., Van den Bovenkamp, G.J., 1966. The pathogenesis of a coronary thrombus. *Am. J. Pathol.* 48, 19–44.
- Garcia, D., Kadem, L., 2006. What do you mean by aortic valve area: Geometric orifice area, effective orifice area, or Gorlin area? *J. Heart Valve Dis.* 15, 601–608.
- Garcia, D., Pibarot, P., Landry, C., Chayer, B., Dumesnil, J.G., Durand, L., 2004. Estimation of Aortic Valve Effective Orifice Area by Doppler Echocardiography : Effects of Valve Inflow Shape and Flow Rate 756–765. <https://doi.org/10.1016/j.echo.2004.03.030>
- Gharaie, S.H., Morsi, Y., 2015. A novel design of a polymeric aortic valve. *Int. J. Artif. Organs* 38, 259–270. <https://doi.org/10.5301/ijao.5000413>
- Gharaie, S.H., Mosadegh, B., Morsi, Y., 2018. In Vitro Validation of a Numerical Simulation of Leaflet Kinematics in a Polymeric Aortic Valve Under Physiological Conditions. *Cardiovasc. Eng. Technol.* 9, 42–52. <https://doi.org/10.1007/s13239-018-0340-7>
- Ghosh, R.P., Marom, G., Rotman, O.M., Slepian, M.J., Prabhakar, S., Horner, M., Bluestein, D., 2018. Comparative fluid-structure interaction analysis of polymeric transcatheter and surgical aortic valves’ hemodynamics and structural mechanics, *Journal of Biomechanical Engineering*. <https://doi.org/10.1115/1.4040600>
- Gnyaneshwar, R., Kumar, R.K., 2002. Original article : cardiovascular Dynamic analysis of the aortic valve using a finite 73, 3–6.
- Gorlin, R., Gorlin, S.G., 1951. Hydraulic formula for calculation of the area of the stenotic mitral valve, other cardiac valves, and central circulatory shunts. I. *Am. Heart J.* 41, 1–29. [https://doi.org/10.1016/0002-8703\(51\)90002-6](https://doi.org/10.1016/0002-8703(51)90002-6)
- Griffith, B.E., 2012. Immersed boundary model of aortic heart valve dynamics with physiological driving and loading conditions. *Int. j. numer. method. biomed. eng.* 28, 317–345. <https://doi.org/10.1002/cnm.1445>
- Griffith, B.E., 2009. Prosthetic Heart Valves Using the Immersed Boundary Method. *J. Appl.*

Mech. 1, 137–177.

Grube, E., Sinning, J.M., Vahanian, A., 2014. The year in cardiology 2013: Valvular heart disease (focus on catheter-based interventions). *Eur. Heart J.* 35, 490–494. <https://doi.org/10.1093/eurheartj/ehs558>

Gunning, P.S., Vaughan, T.J., McNamara, L.M., 2014. Simulation of self expanding transcatheter aortic valve in a realistic aortic root: Implications of deployment geometry on leaflet deformation. *Ann. Biomed. Eng.* 42, 1989–2001. <https://doi.org/10.1007/s10439-014-1051-3>

Haj-Ali, R., Dasi, L.P., Kim, H.S., Choi, J., Leo, H.W., Yoganathan, A.P., 2008. Structural simulations of prosthetic tri-leaflet aortic heart valves. *J. Biomech.* 41, 1510–1519. <https://doi.org/10.1016/j.jbiomech.2008.02.026>

Hall, J.E., 2015. Guyton and Hall Textbook of Medical Physiology, 13th Edition (online access included). ProtoView. 2.

Hamid, M.S., Sabbah, H.N., Stein, P.D., 1984. Computer-assisted methods for design optimization of cardiac bioprosthetic valves. *Henry Ford Hosp. Med. J.* 32, 178–181.

Hedayat, M., Asgharzadeh, H., Borazjani, I., 2017. Platelet activation of mechanical versus bioprosthetic heart valves during systole. *J. Biomech.* 56, 111–116. <https://doi.org/10.1016/j.jbiomech.2017.03.002>

Ho, S.Y., 2009. Structure and anatomy of the aortic root. *Eur. J. Echocardiogr.* 10, 3–10. <https://doi.org/10.1093/ejechocard/jen243>

Hsu, M.C., Kamensky, D., Xu, F., Kiendl, J., Wang, C., Wu, M.C.H., Mineroff, J., Reali, A., Bazilevs, Y., Sacks, M.S., 2015. Dynamic and fluid–structure interaction simulations of bioprosthetic heart valves using parametric design with T-splines and Fung-type material models. *Comput. Mech.* 55, 1211–1225. <https://doi.org/10.1007/s00466-015-1166-x>

Hufnagel, C.A., 1989. In the beginning. *Ann. Thorac. Surg.* 47, 475–476. [https://doi.org/10.1016/0003-4975\(89\)90403-7](https://doi.org/10.1016/0003-4975(89)90403-7)

International Organisation for Standardisation, 2021a. ISO 5840:2021 Part 1: General requirements.

International Organisation for Standardisation, 2021b. ISO 5840:2021 Part 3: Heart valve substitutes implanted by transcatheter techniques.

International Organisation for Standardisation, 2021c. ISO 5840:2021 Part 2: Surgically implanted heart valve substitutes.

Jun, B.H., Saikrishnan, N., Arjunon, S., Yun, B.M., Yoganathan, A.P., 2014. Effect of hinge gap width of a St. Jude medical bileaflet mechanical heart valve on blood damage potential-an in vitro micro particle image velocimetry study. *J. Biomech. Eng.* 136, 1–11. <https://doi.org/10.1115/1.4027935>

Kalyana Sundaram, G.B., Balakrishnan, K.R., Kumar, R.K., 2015. Aortic valve dynamics using a fluid structure interaction model - The physiology of opening and closing. *J. Biomech.* 48, 1737–1744. <https://doi.org/10.1016/j.jbiomech.2015.05.012>

Kandail, H.S., Trivedi, S.D., Shaikh, A.C., Bajwa, T.K., O’Hair, D.P., Jahangir, A., LaDisa, J.F., 2018. Impact of annular and supra-annular CoreValve deployment locations on aortic and

- coronary artery hemodynamics. *J. Mech. Behav. Biomed. Mater.* 86, 131–142. <https://doi.org/10.1016/j.jmbbm.2018.06.032>
- Kaneko, T., Aranki, S.F., 2013. Anticoagulation for Prosthetic Valves. *Thrombosis* 2013, 1–4. <https://doi.org/10.1155/2013/346752>
- Kereiakes, D.J., Answini, G.A., Yakubov, S.J., Rai, B., Smith, J.M., Duff, S., Shannon, F.L., Sakwa, M., Beith, J., Heimansohn, D., 2021. Preliminary Evaluation of a Novel Polymeric Valve Following Surgical Implantation for Symptomatic Aortic Valve Disease. *JACC Cardiovasc. Interv.* 14, 2754–2756. <https://doi.org/10.1016/j.jcin.2021.08.071>
- Kheradvar, A., Groves, E.M., Goergen, C.J., Alavi, S.H., Tranquillo, R., Simmons, C.A., Dasi, L.P., Grande-Allen, K.J., Mofrad, M.R.K., Falahatpisheh, A., Griffith, B., Baaijens, F., Little, S.H., Canic, S., 2015. Emerging Trends in Heart Valve Engineering: Part II. Novel and Standard Technologies for Aortic Valve Replacement. *Ann. Biomed. Eng.* 43, 844–857. <https://doi.org/10.1007/s10439-014-1191-5>
- Kilner, P.J., Yang, G.Z., Mohiaddin, R.H., Firmin, D.N., Longmore, D.B., 1993. Helical and retrograde secondary flow patterns in the aortic arch studied by three-directional magnetic resonance velocity mapping. *Circulation* 88, 2235–2247. <https://doi.org/10.1161/01.CIR.88.5.2235>
- Kim, H., Lu, J., Sacks, M.S., Chandran, K.B., 2008. Dynamic simulation of bioprosthetic heart valves using a stress resultant shell model. *Ann. Biomed. Eng.* 36, 262–275. <https://doi.org/10.1007/s10439-007-9409-4>
- King, M.J., Corden, J., David, T., Fisher, J., 1996. A three-dimensional, time-dependent analysis of flow through a bileaflet mechanical heart valve: Comparison of experimental and numerical results. *J. Biomech.* 29, 609–618. [https://doi.org/10.1016/0021-9290\(95\)00107-7](https://doi.org/10.1016/0021-9290(95)00107-7)
- Kini, V., Bachmann, C., Fontaine, A., Deutsch, S., Tarbell, J.M., 2000. Flow visualization in mechanical heart valves: occluder rebound and cavitation potential. *Ann. Biomed. Eng.* 28, 431–441. <https://doi.org/10.1114/1.281>
- Kostyunin, A.E., Yuzhalin, A.E., Rezvova, M.A., Ovcharenko, E.A., Glushkova, T. V., Kutikhin, A.G., 2020. Degeneration of Bioprosthetic Heart Valves : Update 2020 1–19. <https://doi.org/10.1161/JAHA.120.018506>
- Kumagai, S., Daikai, T., Onodera, T., 2019. Bovine Spongiform Encephalopathy – A Review from the Perspective of Food Safety 7, 21–47. <https://doi.org/10.14252/foodsafetyfscj.2018009>
- Kusneri, J., Luraghi, G., Khodaei, F., Matas, J.F.L.R., Migliavacca, F., Edelman, E.R., Nezami, F.R., 2021. Understanding TAVR device expansion as it relates to morphology of the bicuspid aortic valve: A simulation study. *PLoS One* 16, 1–9. <https://doi.org/10.1371/journal.pone.0251579>
- Laadhari, A., Székely, G., 2017. Eulerian finite element method for the numerical modeling of fluid dynamics of natural and pathological aortic valves. *J. Comput. Appl. Math.* 319, 236–261. <https://doi.org/10.1016/j.cam.2016.11.042>
- Lerman, D.A., Prasad, S., Alotti, N., 2015. Structural Cardiac and Vascular Disease: Molecular Mechanisms and Therapeutic Approaches. *Eur. Cardiol.* 10, 108–112.
- Li, K., Sun, W., 2017. Simulated transcatheter aortic valve deformation: A parametric study on the impact of leaflet geometry on valve peak stress. *Int. j. numer. method. biomed. eng.* 33, 1–

14. <https://doi.org/10.1002/cnm.2814>

Li, K., Sun, W., 2010. Simulated thin pericardial bioprosthetic valve leaflet deformation under static pressure-only loading conditions: Implications for percutaneous valves. *Ann. Biomed. Eng.* 38, 2690–2701. <https://doi.org/10.1007/s10439-010-0009-3>

Luraghi, G., Matas, J.F.R., Beretta, M., Chiozzi, N., Iannetti, L., Migliavacca, F., 2020. The impact of calcification patterns in transcatheter aortic valve performance: a fluid-structure interaction analysis. *Comput. Methods Biomech. Biomed. Engin.* 24, 375–383. <https://doi.org/10.1080/10255842.2020.1817409>

Luraghi, G., Migliavacca, F., García-González, A., Chiastra, C., Rossi, A., Cao, D., Stefanini, G., Rodriguez Matas, J.F., 2019. On the Modeling of Patient-Specific Transcatheter Aortic Valve Replacement: A Fluid–Structure Interaction Approach. *Cardiovasc. Eng. Technol.* 10, 437–455. <https://doi.org/10.1007/s13239-019-00427-0>

Luraghi, G., Wu, W., De Gaetano, F., Rodriguez Matas, J.F., Moggridge, G.D., Serrani, M., Stasiak, J., Costantino, M.L., Migliavacca, F., 2017. Evaluation of an aortic valve prosthesis: Fluid-structure interaction or structural simulation? *J. Biomech.* 58, 45–51. <https://doi.org/10.1016/j.jbiomech.2017.04.004>

Mack, M.J., Leon, M.B., Thourani, V.H., Makkar, R., Kodali, S.K., Russo, M., Kapadia, S.R., Malaisrie, S.C., Cohen, D.J., Pibarot, P., Leipsic, J., Hahn, R.T., Blanke, P., Williams, M.R., McCabe, J.M., Brown, D.L., Babaliaros, V., Goldman, S., Szeto, W.Y., Genereux, P., Pershad, A., Pocock, S.J., Alu, M.C., Webb, J.G., Smith, C.R., 2019. Transcatheter Aortic-Valve Replacement with a Balloon-Expandable Valve in Low-Risk Patients. *N. Engl. J. Med.* 380, 1695–1705. <https://doi.org/10.1056/nejmoa1814052>

Mao, W., Caballero, A., McKay, R., Primiano, C., Sun, W., 2017. Fully-coupled fluid-structure interaction simulation of the aortic and mitral valves in a realistic 3D left ventricle model. *PLoS One* 12, 1–21. <https://doi.org/10.1371/journal.pone.0184729>

Mao, W., Li, K., Sun, W., 2016. Fluid–Structure Interaction Study of Transcatheter Aortic Valve Dynamics Using Smoothed Particle Hydrodynamics. *Cardiovasc. Eng. Technol.* 7, 374–388. <https://doi.org/10.1007/s13239-016-0285-7>

Matthews, A.M., 1998. The development of the Starr-Edwards heart valve. *Texas Hear. Inst. J.* 25, 282–293.

Mohammadi, H., Mequanint, K., 2011. Prosthetic aortic heart valves: Modeling and design. *Med. Eng. Phys.* 33, 131–147. <https://doi.org/10.1016/j.medengphy.2010.09.017>

Monteleone, A., Borino, G., Napoli, E., Burriesci, G., 2022. Fluid–structure interaction approach with smoothed particle hydrodynamics and particle–spring systems. *Comput. Methods Appl. Mech. Eng.* 392, 114728. <https://doi.org/10.1016/j.cma.2022.114728>

Morganti, S., Conti, M., Aiello, M., Valentini, A., Mazzola, A., Reali, A., Auricchio, F., 2014. Simulation of transcatheter aortic valve implantation through patient-specific finite element analysis: Two clinical cases. *J. Biomech.* 47, 2547–2555. <https://doi.org/10.1016/j.jbiomech.2014.06.007>

Morganti, S., Auricchio, F., Benson, D.J., Gambarin, F.I., Hartmann, S., Hughes, T.J.R., Reali, A., 2015. Patient-specific isogeometric structural analysis of aortic valve closure. *Comput. Methods Appl. Mech. Eng.* 284, 508–520. <https://doi.org/10.1016/j.cma.2014.10.010>

- Morganti, S., Brambilla, N., Petronio, A.S., Reali, A., Bedogni, F., Auricchio, F., 2016. Prediction of patient-specific post-operative outcomes of TAVI procedure: The impact of the positioning strategy on valve performance. *J. Biomech.* 49, 2513–2519. <https://doi.org/10.1016/j.jbiomech.2015.10.048>
- Morrison, T.M., Hariharan, P., Funkhouser, C.M., Afshari, P., Goodin, M., Horner, M., 2019. Assessing computational model credibility using a risk-based framework: Application to hemolysis in centrifugal blood pumps. *ASAIO J.* 65, 349–360. <https://doi.org/10.1097/MAT.0000000000000996>
- Morsi, Y.S., Yang, W.W., Wong, C.S., Das, S., 2007. Transient fluid-structure coupling for simulation of a trileaflet heart valve using weak coupling. *J. Artif. Organs* 10, 96–103. <https://doi.org/10.1007/s10047-006-0365-9>
- Nader, E., Skinner, S., Romana, M., Fort, R., Lemonne, N., Guillot, N., Gauthier, A., Antoine-Jonville, S., Renoux, C., Hardy-Dessources, M.D., Stauffer, E., Joly, P., Bertrand, Y., Connes, P., 2019. Blood rheology: Key parameters, impact on blood flow, role in sickle cell disease and effects of exercise. *Front. Physiol.* 10, 1–14. <https://doi.org/10.3389/fphys.2019.01329>
- Nair, K., Muraleedharan, C. V., Bhuvaneshwar, G.S., 2003. Developments in mechanical heart valve prosthesis. *Sadhana - Acad. Proc. Eng. Sci.* 28, 575–587. <https://doi.org/10.1007/BF02706448>
- Nannini, G., Caimi, A., Palumbo, M.C., Saitta, S., Girardi, L.N., Gaudino, M., Roman, M.J., Weinsaft, J.W., Redaelli, A., 2021. Aortic hemodynamics assessment prior and after valve sparing reconstruction: A patient-specific 4D flow-based FSI model. *Comput. Biol. Med.* 135, 104581. <https://doi.org/10.1016/j.combiomed.2021.104581>
- Nappi, F., Mazzocchi, L., Avtaar Singh, S.S., Morganti, S., Sablayrolles, J.L., Acar, C., Auricchio, F., 2018. Complementary Role of the Computed Biomodelling through Finite Element Analysis and Computed Tomography for Diagnosis of Transcatheter Heart Valve Thrombosis. *Biomed Res. Int.* 2018. <https://doi.org/10.1155/2018/1346308>
- Nishimura, R.A., Otto, C.M., Bonow, R.O., Carabello, B.A., Erwin, J.P., Guyton, R.A., O’Gara, P.T., Ruiz, C.E., Skubas, N.J., Sorajja, P., Sundt, T.M., Thomas, J.D., 2014. 2014 AHA/ACC guideline for the management of patients with valvular heart disease: A report of the American college of cardiology/American heart association task force on practice guidelines. *J. Am. Coll. Cardiol.* 63. <https://doi.org/10.1016/j.jacc.2014.02.536>
- Nistal, F., Garcia-Martinez, V., Arbe, E., Fernandez, D., Artinano, E., Mazorra, F., Gallo, I., 1990. In vivo experimental assessment of polytetrafluoroethylene trileaflet heart valve prosthesis. *J. Thorac. Cardiovasc. Surg.* 99. [https://doi.org/10.1016/s0022-5223\(20\)31464-1](https://doi.org/10.1016/s0022-5223(20)31464-1)
- Nkomo, V.T., Gardin, J.M., Skelton, T.N., Gottdiener, J.S., Scott, C.G., Enriquez-Sarano, M., 2006. Burden of valvular heart diseases: a population-based study. *Lancet* 368, 1005–1011. [https://doi.org/10.1016/S0140-6736\(06\)69208-8](https://doi.org/10.1016/S0140-6736(06)69208-8)
- Nobili, M., Morbiducci, U., Ponzini, R., Del Gaudio, C., Balducci, A., Grigioni, M., Maria Montecvecchi, F., Redaelli, A., 2008. Numerical simulation of the dynamics of a bileaflet prosthetic heart valve using a fluid-structure interaction approach. *J. Biomech.* 41, 2539–2550. <https://doi.org/10.1016/j.jbiomech.2008.05.004>
- Otto, C., 2007. Principles of Echocardiography.
- Otto, C.M., Kuusisto, J., Reichenbach, D.D., Gown, A.M., O’Brien, K.D., 1994.

Characterization of the early lesion of “degenerative” valvular aortic stenosis: Histological and immunohistochemical studies. *Circulation* 90, 844–853. <https://doi.org/10.1161/01.CIR.90.2.844>

Peskin, C.S., 2002. The immersed boundary method. *Acta Numer.* 11, 479–517. <https://doi.org/10.1017/S0962492902000077>

Pfensig, S., Kaule, S., Sämann, M., Stiehm, M., Grabow, N., Schmitz, K.P., Siewert, S., 2017. Assessment of heart valve performance by finite-element design studies of polymeric leaflet-structures. *Curr. Dir. Biomed. Eng.* 3, 631–634. <https://doi.org/10.1515/cdbme-2017-0132>

Piatti, F., Sturla, F., Marom, G., Sheriff, J., Claiborne, T.E., Slepian, M.J., Redaelli, A., Bluestein, D., 2016. Polymeric Valve Using a Fluid-Structure Interaction Approach 48, 3650–3658. <https://doi.org/10.1016/j.jbiomech.2015.08.009>. Hemodynamic

Milhorini Pio, S., Bax, J., Delgado, V., 2020. How valvular calcification can affect the outcomes of transcatheter aortic valve implantation. *Expert Rev. Med. Devices* 17, 773–784. <https://doi.org/10.1080/17434440.2020.1789456>

Pisani, G., Scaffa, R., Ieropoli, O., Amico, M.D., Maselli, D., Morbiducci, U., Paulis, R. De, 2013. Role of the sinuses of Valsalva on the opening of the aortic valve. *J. Thorac. Cardiovasc. Surg.* 145, 999–1003. <https://doi.org/10.1016/j.jtcvs.2012.03.060>

Pop, G.A.M., Duncker, D.J., Gardien, M., Vranckx, P., Versluis, S., Hasan, D., Slager, C.J., 2002. The clinical significance of whole blood viscosity in (cardio)vascular medicine. *Neth. Heart J.* 10, 512–516.

Qin, T., Caballero, A., Mao, W., Barrett, B., Kamioka, N., 2021. Patient-specific analysis of bicuspid aortic valve hemodynamics using a fully coupled fluid-structure interaction (FSI) model.

Rahmani, B., Tzamtzis, S., Ghanbari, H., Burriesci, G., Seifalian, A.M., 2012. Manufacturing and hydrodynamic assessment of a novel aortic valve made of a new nanocomposite polymer. *J. Biomech.* 45, 1205–1211. <https://doi.org/10.1016/j.jbiomech.2012.01.046>

Rahmani, B., Tzamtzis, S., Sheridan, R., Mullen, M.J., Yap, J., Seifalian, A.M., Burriesci, G., 2017. In Vitro Hydrodynamic Assessment of a New Transcatheter Heart Valve Concept (the TRISKELE). *J. Cardiovasc. Transl. Res.* 10, 104–115. <https://doi.org/10.1007/s12265-016-9722-0>

Rahmani, B., Tzamtzis, S., Sheridan, R., Mullen, M.J., Yap, J., Seifalian, A.M., Burriesci, G., 2016. A new transcatheter heart valve concept (the TRISKELE): Feasibility in an acute preclinical model. *EuroIntervention* 12, 901–908. <https://doi.org/10.4244/EIJV12I7A148>

Resor, C.D., Bhatt, D.L., 2019. Polymeric Heart Valves: Back to the Future? *Matter* 1, 30–32. <https://doi.org/10.1016/j.matt.2019.06.003>

Rodriguez-Gabella, T., Voisine, P., Puri, R., Pibarot, P., Rodés-Cabau, J., 2017. Aortic Bioprosthetic Valve Durability: Incidence, Mechanisms, Predictors, and Management of Surgical and Transcatheter Valve Degeneration. *J. Am. Coll. Cardiol.* 70, 1013–1028. <https://doi.org/10.1016/j.jacc.2017.07.715>

Roe, B.B., 1969. Late follow-up studies on flexible leaflet prosthetic valves. *J. Thorac. Cardiovasc. Surg.* 58, 59–61. [https://doi.org/10.1016/s0022-5223\(19\)42628-7](https://doi.org/10.1016/s0022-5223(19)42628-7)

Rosamond, W., Flegel, K., Friday, G., Furie, K., Go, A., Greenlund, K., Haase, N., Ho, M.,

- Howard, V., Kissela, B., Kittner, S., Lloyd-Jones, D., McDermott, M., Meigs, J., Moy, C., Nichol, G., O'Donnell, C.J., Roger, V., Rumsfeld, J., Sorlie, P., Steinberger, J., Thom, T., Wasserthiel-Smoller, S., Hong, Y., 2007. Heart disease and stroke statistics - 2007 Update: A report from the American Heart Association Statistics Committee and Stroke Statistics Subcommittee, *Circulation*. <https://doi.org/10.1161/CIRCULATIONAHA.106.179918>
- Rossvoll, O., Samstad, S., Torp, H.G., Linker, D.T., Skjærpe, T., Angelsen, B.A.J., Hatle, L., 1991. The Velocity Distribution in the Aortic Anulus in Normal Subjects: A Quantitative Analysis of Two-dimensional Doppler Flow Maps. *J. Am. Soc. Echocardiogr.* 4, 367–378. [https://doi.org/10.1016/S0894-7317\(14\)80447-1](https://doi.org/10.1016/S0894-7317(14)80447-1)
- Rotman, O.M., Kovarovic, B., Chiu, W.C., Bianchi, M., Marom, G., Slepian, M.J., Bluestein, D., 2019. Novel Polymeric Valve for Transcatheter Aortic Valve Replacement Applications: In Vitro Hemodynamic Study. *Ann. Biomed. Eng.* 47, 113–125. <https://doi.org/10.1007/s10439-018-02119-7>
- Sakrana, A.A., Nasr, M.M., Ashamalla, G.A., Abuelatta, R.A., Naeim, H.A., El Tahlawi, M.A., 2016. Paravalvular leak after transcatheter aortic valve implantation: is it anatomically predictable or procedurally determined? MDCT study. *Clin. Radiol.* 71, 1095–1103. <https://doi.org/10.1016/j.crad.2016.07.016>
- Serrani, M., Brubert, J., Stasiak, J., De Gaetano, F., Zaffora, A., Costantino, M.L., Moggridge, G.D., 2016. A Computational Tool for the Microstructure Optimization of a Polymeric Heart Valve Prosthesis. *J. Biomech. Eng.* 138. <https://doi.org/10.1115/1.4033178>
- Shadden, S.C., Astorino, M., Gerbeau, J.F., 2010. Computational analysis of an aortic valve jet with Lagrangian coherent structures. *Chaos* 20. <https://doi.org/10.1063/1.3272780>
- Sirois, E., Wang, Q., Sun, W., 2011. Fluid Simulation of a Transcatheter Aortic Valve Deployment into a Patient-Specific Aortic Root. *Cardiovasc. Eng. Technol.* 2, 186–195. <https://doi.org/10.1007/s13239-011-0037-7>
- Smuts, A.N., Blaine, D.C., Scheffer, C., Weich, H., Doubell, A.F., Dellimore, K.H., 2011. Application of finite element analysis to the design of tissue leaflets for a percutaneous aortic valve. *J. Mech. Behav. Biomed. Mater.* 4, 85–98. <https://doi.org/10.1016/j.jmbbm.2010.09.009>
- Sodhani, D., Reese, S., Aksenov, A., Soğanci, S., Jockenhövel, S., Mela, P., Stapleton, S.E., 2018. Fluid-structure interaction simulation of artificial textile reinforced aortic heart valve: Validation with an in-vitro test. *J. Biomech.* 78, 52–69. <https://doi.org/10.1016/j.jbiomech.2018.07.018>
- Starr, A., Edwards, M.L., 1961. Mitral replacement: clinical experience with a ball-valve prosthesis. *Ann. Surg.* 154, 726–740. <https://doi.org/10.1097/00000658-196110000-00017>
- Stewart, B.F., Siscovick, D., Lind, B.K., Gardin, J.M., Gottdiener, J.S., Smith, V.E., Kitzman, D.W., Otto, C.M., 1997. Clinical factors associated with calcific aortic valve disease. *J. Am. Coll. Cardiol.* 29, 630–634. [https://doi.org/10.1016/S0735-1097\(96\)00563-3](https://doi.org/10.1016/S0735-1097(96)00563-3)
- Sturla, F., Ronzoni, M., Vitali, M., Dimasi, A., Vismara, R., Preston-Maher, G., Burriesci, G., Votta, E., Redaelli, A., 2016. Impact of different aortic valve calcification patterns on the outcome of transcatheter aortic valve implantation: A finite element study. *J. Biomech.* 49, 2520–2530. <https://doi.org/10.1016/j.jbiomech.2016.03.036>

- Sturla, F., Votta, E., Stevanella, M., Conti, C.A., Redaelli, A., 2013. Impact of modeling fluid-structure interaction in the computational analysis of aortic root biomechanics. *Med. Eng. Phys.* 35, 1721–1730. <https://doi.org/10.1016/j.medengphy.2013.07.015>
- Sun, L., Rajamannan, N.M., Sucusky, P., 2013. Defining the Role of Fluid Shear Stress in the Expression of Early Signaling Markers for Calcific Aortic Valve Disease 8. <https://doi.org/10.1371/journal.pone.0084433>
- Tam, H., Zhang, W., Infante, D., Parchment, N., Sacks, M., Vyavahare, N., 2017. Fixation of Bovine Pericardium-Based Tissue Biomaterial with Irreversible Chemistry Improves Biochemical and Biomechanical Properties. *J. Cardiovasc. Transl. Res.* 10, 194–205. <https://doi.org/10.1007/s12265-017-9733-5>
- Tango, A.M., Salmonsmith, J., Ducci, A., Burriesci, G., 2018. Validation and Extension of a Fluid–Structure Interaction Model of the Healthy Aortic Valve. *Cardiovasc. Eng. Technol.* 9, 739–751. <https://doi.org/10.1007/s13239-018-00391-1>
- Tan, L.T., Razon, T.L.J., Cuenza, L., 2020. Correlation of Computed Tomography- derived Aortic Valve Calcium Score with Severity of Aortic Stenosis on Echocardiography : A Single-Center Experience, in: *ECR 2020. European Society of Radiology, Bonifacio Global City/PH, Quezon City/PH, Manila/PH*, pp. 2020–2023. <https://doi.org/10.26044/ecr2020/C-12320>
- Terahara, T., Takizawa, K., Tezduyar, T.E., Bazilevs, Y., Hsu, M.C., 2020. Heart valve isogeometric sequentially-coupled FSI analysis with the space–time topology change method. *Comput. Mech.* 65, 1167–1187. <https://doi.org/10.1007/s00466-019-01813-0>
- Thubrikar, M.J., Aouad, J., Nolan, S.P., 1986. Patterns of calcific deposits in operatively excised stenotic or purely regurgitant aortic valves and their relation to mechanical stress. *Am. J. Cardiol.* 58, 304–308. [https://doi.org/10.1016/0002-9149\(86\)90067-6](https://doi.org/10.1016/0002-9149(86)90067-6)
- Tortora, G.J., Nielsen, M.T., 2012. *Principles of Human Anatomy*.
- Travaglino, S., Murdock, K., Tran, A., Martin, C., Liang, L., Wang, Y., Sun, W., 2020. Computational optimization study of transcatheter aortic valve leaflet design using porcine and bovine leaflets. *J. Biomech. Eng.* 142, 1–8. <https://doi.org/10.1115/1.4044244>
- Tzamtzis, S., Viquerat, J., Yap, J., Mullen, M.J., Burriesci, G., 2013. Numerical analysis of the radial force produced by the Medtronic-CoreValve and Edwards-SAPIEN after transcatheter aortic valve implantation (TAVI). *Med. Eng. Phys.* 35, 125–130. <https://doi.org/10.1016/j.medengphy.2012.04.009>
- Vahidkhah, K., Azadani, A.N., 2017. Supra-annular Valve-in-Valve implantation reduces blood stasis on the transcatheter aortic valve leaflets. *J. Biomech.* 58, 114–122. <https://doi.org/10.1016/j.jbiomech.2017.04.020>
- Vargas, H.A., Hoey, E.T.D., Gopalan, D., Agrawal, S.K.B., Sreaton, N.J., Gulati, G.S., 2009. Congenital and acquired conditions of the aortic root: Multidetector computed tomography features. *Postgrad. Med. J.* 85, 383–391. <https://doi.org/10.1136/pgmj.2008.075531>
- Vollebergh, F.E.M.G., Becker, A.E., 1977. Minor congenital variations of cusp size in tricuspid aortic valves: Possible link with isolated aortic stenosis. *Heart* 39, 1006–1011. <https://doi.org/10.1136/hrt.39.9.1006>
- Warren, B.A., Yong, J.L.C., 1997. Calcification of the aortic valve: Its progression and grading. *Pathology* 29, 360–368. <https://doi.org/10.1080/00313029700169315>

- Weinberg, E.J., Schoen, F.J., Mofrad, M.R.K., 2009. A computational model of aging and calcification in the aortic heart valve. *PLoS One* 4, 1–10. <https://doi.org/10.1371/journal.pone.0005960>
- Wu, W., Pott, D., Mazza, B., Sironi, T., Dordoni, E., Chiastra, C., Petrini, L., Pennati, G., Dubini, G., Steinseifer, U., Sonntag, S., Kuetting, M., Migliavacca, F., 2016. Fluid–Structure Interaction Model of a Percutaneous Aortic Valve: Comparison with an In Vitro Test and Feasibility Study in a Patient-Specific Case. *Ann. Biomed. Eng.* 44, 590–603. <https://doi.org/10.1007/s10439-015-1429-x>
- Wu, C., Saikrishnan, N., Chalekian, A.J., Fraser, R., Ieropoli, O., Retta, S.M., Joseph, R., Lee, S., Marquez, S., Mester, D., Pan, N., Vatanpour, S., Weinberg, C., Steinseifer, U., 2019. In-Vitro Pulsatile Flow Testing of Prosthetic Heart Valves: A Round-Robin Study by the ISO Cardiac Valves Working Group. *Cardiovasc. Eng. Technol.* 10, 397–422. <https://doi.org/10.1007/s13239-019-00422-5>
- Yoganathan, A.P., He, Z., Casey Jones, S., 2004. Fluid Mechanics of Heart Valves. *Annu. Rev. Biomed. Eng.* 6, 331–362. <https://doi.org/10.1146/annurev.bioeng.6.040803.140111>
- Zhiduleva, E. V., Irtyuga, O.B., Shishkova, A.A., Ignat’eva, E. V., Kostina, A.S., Levchuk, K.A., Golovkin, A.S., Rylov, A.Y., Kostareva, A.A., Moiseeva, O.M., Malashicheva, A.B., Gordeev, M.L., 2018. Cellular Mechanisms of Aortic Valve Calcification. *Bull. Exp. Biol. Med.* 164, 371–375. <https://doi.org/10.1007/s10517-018-3992-2>
- Zhu, Y., Chen, R., Juan, Y.H., Li, H., Wang, J., Yu, Z., Liu, H., 2018. Clinical validation and assessment of aortic hemodynamics using computational fluid dynamics simulations from computed tomography angiography. *Biomed. Eng. Online* 17, 1–12. <https://doi.org/10.1186/s12938-018-0485-5>

CHAPTER 3

Theoretical Background

This chapter gives the theoretical background for the finite element modelling that is used throughout this thesis. The following equations provide the basis for developing models that simulate structural and fluid dynamics problems. Section 3.1 introduces the core concepts of continuum mechanics; Section 3.2 examines the modelling of materials using constitutive laws and Section 3.3 examines the finite element method. In Section 3.4, the Navier Stokes equations for fluid dynamics and the immersed boundary method for fluid-structure interactions are examined.

3.1 Continuum Mechanics

Continuum mechanics is the analysis of the deformation and motion of mechanical bodies independent of a coordinate system, which provides the basis for the finite element method.

3.1.1 Notation

The notation used in this chapter is as follows. Bold face roman symbol is used for vector or tensor notation. The roman italic symbol is used for indicial notation. The dot product/ scalar product summation convention is as follows:

$$\mathbf{u} \cdot \mathbf{v} = u_i v_i = \sum_{i=1}^3 u_i v_i = u_1 v_1 + u_2 v_2 + u_3 v_3 \quad (3.1)$$

Where $i = 1, 2, 3$, and u and v are 3D vectors.

3.1.2 Deformation and Motion

A schematic of a body undergoing deformation is shown in Figure 3.1. The body, in the undeformed reference configuration Ω_{ref} undergoes a motion χ at time $t=0$ to the deformed current configuration Ω_c at time $t=t$. The position of a material point P is given by the vector \mathbf{X} , with respect to the origin O. This position vector \mathbf{X} can be described for all points within the reference configuration, known as the Lagrangian coordinates.

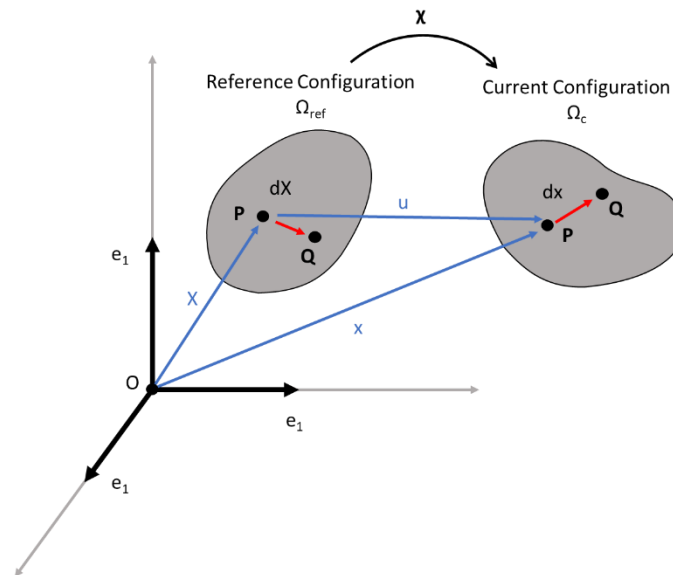


Figure 3.1 Schematic of undeformed reference body and deformed current body configurations

The position of material point P in the current configuration may be defined by:

$$\mathbf{x} = \chi(\mathbf{X}, t) \quad (3.2)$$

Where the position vector x defines the spatial Eulerian coordinates. The displacement of the material point P between the reference and current configurations can therefore be given as $\mathbf{u} = \mathbf{x} - \mathbf{X}$ which can be rearranged to:

$$\mathbf{u} = \chi(\mathbf{X}, t) - \mathbf{X} \quad (3.3)$$

A second material point Q exists on the body in the reference configuration and is related to the material point P by $\partial\mathbf{X}$. This is transformed to $\partial\mathbf{x}$ in the current configuration by the deformation gradient \mathbf{F} described as:

$$\mathbf{F} = \frac{\partial\chi}{\partial\mathbf{X}} = \frac{\partial\mathbf{x}}{\partial\mathbf{X}} \quad (3.4)$$

The determinant of \mathbf{F} is known as the Jacobian of the deformation gradient. It denotes the ratio of volume change from the reference configuration to the current configuration. The Jacobian is described as:

$$J = \det(\mathbf{F}) \quad (3.5)$$

The velocity \mathbf{v} of a material point P may be defined as:

$$\mathbf{v} = \frac{\partial\mathbf{x}}{\partial t} \quad (3.6)$$

The spatial velocity gradient \mathbf{L} is defined as:

$$\mathbf{L} = \frac{\partial\mathbf{v}}{\partial\mathbf{x}} \quad (3.7)$$

Which can also be expressed by:

$$\mathbf{L} = \dot{\mathbf{F}}\mathbf{F}^{-1} \text{ or } \dot{\mathbf{F}} = \mathbf{L}\mathbf{F} \quad (3.8)$$

This spatial velocity gradient \mathbf{L} is decomposed into the symmetric rate of deformation tensor \mathbf{D} and an asymmetric spin tensor \mathbf{W} .

$$\mathbf{L} = \mathbf{D} + \mathbf{W} \quad (3.9)$$

$$\mathbf{D} = \frac{1}{2}(\mathbf{L} + \mathbf{L}^T) = \text{sym}(\mathbf{L}) \quad (3.10)$$

$$\mathbf{W} = \frac{1}{2}(\mathbf{L} - \mathbf{L}^T) = \text{asym}(\mathbf{L}) \quad (3.11)$$

3.1.3 Strain Measures

Various strain measures can be constructed from the deformation gradient \mathbf{F} . A commonly used strain measure, the Green-Lagrange strain \mathbf{E} is defined by:

$$\mathbf{E} = \frac{1}{2}(\mathbf{F}^T \mathbf{F} - \mathbf{I}) \quad (3.12)$$

Where \mathbf{F}^T is the transpose of \mathbf{F} and \mathbf{I} is the identity tensor, such that $\mathbf{F} \cdot \mathbf{I} = \mathbf{F}$. The Green-Lagrange strain can also be given in the index notation, where:

$$E_{ij} = \frac{1}{2} \left(\frac{\partial u_i}{\partial x_j} + \frac{\partial u_j}{\partial x_i} + \frac{\partial u_k}{\partial x_i} \frac{\partial u_k}{\partial x_j} \right) \quad (3.13)$$

By assuming that the product of the infinitesimals is zero ($\frac{\partial u_k}{\partial x_j} \frac{\partial u_k}{\partial x_i} \approx 0$), the infinitesimal strain ϵ_{ij} is given by:

$$\epsilon_{ij} = \frac{1}{2} \left(\frac{\partial u_i}{\partial X_j} + \frac{\partial u_j}{\partial X_i} \right) \quad (3.14)$$

The left (\mathbf{B}) and right (\mathbf{C}) Cauchy Green tensors are measures of stretch that compose the deformation gradient \mathbf{F} .

$$\mathbf{C} = \mathbf{F}^T \mathbf{F} \quad (3.15)$$

$$\mathbf{B} = \mathbf{F} \mathbf{F}^T \quad (3.16)$$

The deformation gradient \mathbf{F} can be decomposed into an orthogonal rotation tensor \mathbf{R} and symmetric right and left stretch tensors \mathbf{U} and \mathbf{V} respectively.

$$\mathbf{F} = \mathbf{R} \mathbf{U} = \mathbf{V} \mathbf{R} \quad (3.17)$$

These stretch tensors \mathbf{U} and \mathbf{V} can be related to the right (\mathbf{C}) and left (\mathbf{B}) Cauchy Green Deformation tensors by:

$$\mathbf{V}^2 = \mathbf{B} \quad (3.18)$$

$$\mathbf{U}^2 = \mathbf{C} \quad (3.19)$$

The eigenvalues of \mathbf{U} are known as the principal stretches ($\lambda_{i=1,2,3}$), while the logarithmic strain tensor $\boldsymbol{\varepsilon}$ can be calculated from:

$$\boldsymbol{\varepsilon} = \ln \mathbf{V} \quad (3.20)$$

Strain energy density functions can be defined using strain invariants. The first three principal invariants of the right Cauchy-Green tensor (\mathbf{C}) are derived by:

$$I_1 = \text{tr}(\mathbf{C}) = \lambda_1^2 + \lambda_2^2 + \lambda_3^2 \quad (3.21)$$

$$I_2 = \frac{1}{2} [I_1^2 - \text{tr}(\mathbf{C}^2)] = \lambda_1^2 \lambda_2^2 + \lambda_1^2 \lambda_3^2 + \lambda_2^2 \lambda_3^2 \quad (3.22)$$

$$I_3 = \det(\mathbf{C}) = J^2 = \lambda_1^2 \lambda_2^2 \lambda_3^2 \quad (3.23)$$

3.1.4 Stress Measures

Cauchy stress or true stress, $\boldsymbol{\sigma}$, is a measure of the force per unit area in the deformed configuration. It is related to the traction vector \mathbf{t} , which is the force per unit area and a unit normal vector \mathbf{n} , as shown in Figure 3.2.

$$\mathbf{t} = \boldsymbol{\sigma} \mathbf{n} \quad (3.24)$$

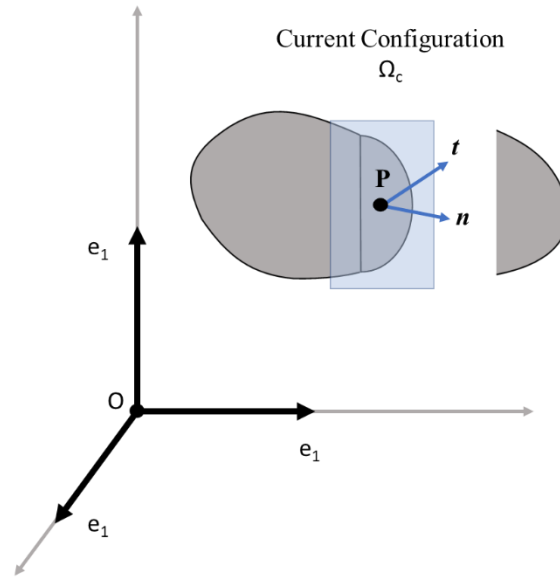


Figure 3.2 Schematic of traction t in current body configurations

The Cauchy Stress is composed of two symmetric parts, the deviatoric stress \mathbf{S} which controls the shape change, and the hydrostatic pressure p , which controls the volume change.

$$p = \frac{-\text{tr}(\boldsymbol{\sigma})}{3} \quad (3.25)$$

$$\boldsymbol{\sigma} = \mathbf{S} - p\mathbf{I} \quad (3.26)$$

The principal stresses are the eigenvalues of the Cauchy stress tensor. The Kirchhoff stress $\boldsymbol{\tau}$ is given by:

$$\boldsymbol{\tau} = J\boldsymbol{\sigma} \quad (3.27)$$

In the case of incompressible materials, the Kirchhoff stress is equal to the Cauchy stress. The first Piola-Kirchhoff stress \mathbf{P} is given by:

$$\mathbf{P} = J\boldsymbol{\sigma}\mathbf{F}^{-T} \quad (3.28)$$

It represents the force per unit area in the undeformed reference configuration. The nominal stress is related to the transpose of the Piola-Kirchhoff stress by:

$$\tilde{\sigma} = J\mathbf{F}^{-1}\boldsymbol{\sigma} = \mathbf{P}^T \quad (3.29)$$

Finally, the von Mises equivalent stress is given by:

$$\sigma_e = \sqrt{\frac{3}{2} S_{ij}S_{ij}} \quad (3.30)$$

3.2 Material Constitutive Behaviours

This thesis covers the finite element modelling of polymer valves of various designs, examining their performance in different hydrodynamic scenarios and various states of disease.

The polyurethane employed in these experiments was for modelling purposes assumed to be incompressible, isotropic, homogenous, and exhibiting a non-linear stress strain response. Or in the case of more complex progressively stiffening models (where strain thresholds dictated the resulting Young's Modulus) and fluid-structure interaction models, treated as linear elastic.

3.2.1 Elasticity

The material behaviour of the polymer valve in Chapter 5, 6, and 7 was assumed to be incompressible, isotropic, homogenous, and exhibiting a linear stress strain response. The elastic component for an isotropic material can be related to stress through the shear and bulk modulus. The bulk modulus K is given by:

$$K = \frac{E}{3(1 - 2\nu)} \quad (3.31)$$

Where E is the Young's Modulus and ν is the poisson's ratio. The shear modulus G is given by:

$$G = \frac{E}{2(1 + \nu)} \quad (3.32)$$

3.2.2 Isotropic Hyperelasticity

A material that exhibits a non-linear stress strain response and undergoes large deformations can be modelled using a hyperelastic model. These materials are too complex to model using a linear elastic relationship. In Chapter 4 of this thesis, the polymer valves are modelled using an Ogden hyperelastic material model. In a hyperelastic material model, the stress-strain relationship is derived from the strain energy density function Ψ . The first Piola-Kirchhoff stress \mathbf{P} is shown here as a derivative of the strain energy density function with respect to the deformation gradient \mathbf{F}

$$\mathbf{P} = \frac{\partial \Psi(\mathbf{F})}{\partial \mathbf{F}} \quad (3.33)$$

If it is transformed to the current configuration, we can derive the Cauchy stress $\boldsymbol{\sigma}$, shown here in terms of the right (\mathbf{C}) and left (\mathbf{B}) Cauchy-Green tensors:

$$\boldsymbol{\sigma} = J^{-1} \mathbf{F} \left(\frac{\partial \Psi(\mathbf{F})}{\partial \mathbf{F}} \right)^T = 2J^{-1} \mathbf{F} \left(\frac{\partial \Psi(\mathbf{C})}{\partial \mathbf{C}} \right) \mathbf{F}^T = 2J^{-1} \mathbf{F} \left(\frac{\partial \Psi(\mathbf{B})}{\partial \mathbf{B}} \right) \mathbf{F}^T \quad (3.34)$$

The strain energy density function for an isotropic material can be described as a function of the first three principal invariants, described in (3.21), (3.22) and (3.23).

$$\Psi(\mathbf{B}) = \Psi(I_1, I_2, I_3) \quad (3.35)$$

Using the chain rule, the derivative of the strain energy density yields the following:

$$\frac{\partial \Psi(\mathbf{B})}{\partial \mathbf{B}} = \frac{\partial \Psi}{\partial I_1} \frac{\partial I_1}{\partial \mathbf{B}} + \frac{\partial \Psi}{\partial I_2} \frac{\partial I_2}{\partial \mathbf{B}} + \frac{\partial \Psi}{\partial I_3} \frac{\partial I_3}{\partial \mathbf{B}} \quad (3.36)$$

Therefore, the derivatives of the invariants in terms of the left Cauchy-Green tensor \mathbf{B} are:

$$\frac{\partial I_1}{\partial \mathbf{B}} = \mathbf{I} \quad \frac{\partial I_2}{\partial \mathbf{B}} = I_1 \mathbf{I} - \mathbf{B} \quad \frac{\partial I_3}{\partial \mathbf{B}} = I_3 \mathbf{B}^{-1} \quad (3.37)$$

If these derivatives are substituted back into Equation (3.36) we get the Cauchy stress as a function of \mathbf{B} :

$$\boldsymbol{\sigma} = 2J^{-1} \left[I_3 \frac{\partial \Psi}{\partial I_3} \mathbf{I} + \left(\frac{\partial \Psi}{\partial I_1} + I_1 \frac{\partial \Psi}{\partial I_2} \right) \mathbf{B} - \frac{\partial \Psi}{\partial I_2} \mathbf{B}^2 \right] \quad (3.38)$$

When we assume a material to be incompressible, $I_3 = J = 1$ and the strain energy density function is reduced to a function of the first two strain invariants:

$$\Psi(\mathbf{B}) = \Psi(I_1, I_2) \quad (3.39)$$

For an incompressible hyperelastic material, the Cauchy stress can then be given

$$\text{by: } \boldsymbol{\sigma} = -p\mathbf{I} + 2W_1\mathbf{B} - 2W_2\mathbf{B}^{-1} \quad (3.40)$$

Where p is the hydrostatic pressure, $W_1 = \frac{\partial \Psi}{\partial I_1}$ and $W_2 = \frac{\partial \Psi}{\partial I_2}$.

3.3 Finite Element Method

The Finite Element Method (FEM) involves the discretisation of a body into a number of subdivision or elements connected by nodes to computationally solve continuum mechanics problems. Boundary conditions are applied and the constitutive equations are calculated for each element to measure the stress, strain and deformation of a body. The problems presented in this thesis are solved using the commercial solver Abaqus (Dassault Systemes, RI, USA). The following is an overview of the implicit and explicit integration schemes used for the non-linear problems presented in this thesis. More detail on these methods can be found in the Abaqus Theory Manual (Dassault Systemes, RI, USA).

3.3.1 Implicit Finite Element Method

Abaqus/Standard uses an implicit integration scheme. In this finite element method, the state of the model is updated from time t to time $t + \Delta t$. Abaqus uses a form of the Newton-Rhapson method, which is used to get convergence at each element, given below:

$$x_{i+1} = x_i - \frac{f(x_i)}{f'(x_i)} \quad (3.41)$$

The fundamental equation of the finite element method is given by the principal of virtual work (PVW).

$$\int_V \delta \boldsymbol{\varepsilon}^T \boldsymbol{\sigma} dV = \int_S \delta \mathbf{u}^T \mathbf{t} dS \quad (3.42)$$

Where $\boldsymbol{\sigma}$ is stress and \mathbf{t} is traction, and $\delta \boldsymbol{\varepsilon}$ and $\delta \mathbf{u}$ are the virtual strain and displacement vectors. dV is a reference volume with the surface dS . The FE code is then implemented over each elements' surface and volume, giving the following for displacement and strain:

$$\delta \mathbf{u} = \mathbf{N}_e \delta \mathbf{u}_e \quad (3.43)$$

$$\delta \boldsymbol{\varepsilon} = \mathbf{B}_e \delta \mathbf{u}_e \quad (3.44)$$

Where \mathbf{N}_e is the global shape function matrix and $\delta \mathbf{u}_e$ is the element nodal displacements.

Substituting into the PVW, we get the following:

$$\sum_e \int_{V_e} \delta \mathbf{u}_e^T \mathbf{B}_e^T \boldsymbol{\sigma}(\mathbf{u}_e) dV = \sum_e \int_{S_e} \delta \mathbf{u}_e^T \mathbf{N}_e^T \mathbf{t} dS \quad (3.45)$$

A global expression for the PVW can be obtained by changing out the element values for global values and removing the virtual displacement $\delta \mathbf{u}_e^T$, given in the following:

$$\int_V \widehat{\mathbf{B}}^T \boldsymbol{\sigma}(\mathbf{u}) dV - \int_S \widehat{\mathbf{N}}^T \mathbf{t} dS = 0 \quad (3.46)$$

Where $\widehat{\mathbf{B}}^T$ is the global shape function gradient matrix, $\widehat{\mathbf{N}}^T$ is the global shape function matrix, \mathbf{u} is the global nodal displacement. The out of balance residual force G can be calculated by finding the difference:

$$G(\mathbf{u}) = \int_V \widehat{\mathbf{B}}^T \boldsymbol{\sigma}(\mathbf{u}) dV - \int_S \widehat{\mathbf{N}}^T \mathbf{t} dS \quad (3.47)$$

To arrive at an equilibrium stress state in the body, this equation must be solved for convergence that

$$G(\mathbf{u}) = 0 \quad (3.48)$$

To achieve convergence, an iterative approach using the Newton-Rhapson method is employed and applied to the residual force vector,

$$\delta \mathbf{u}_{i+1} = \mathbf{u}_{i+1}^{t+\Delta t} - \mathbf{u}_i^{t+\Delta t} = - \left[\frac{\partial \mathbf{G}(\mathbf{u}_i^{t+\Delta t})}{\partial \mathbf{u}} \right]^{-1} \mathbf{G}(\mathbf{u}_i^{t+\Delta t}) \quad (3.49)$$

We can write this in terms of the tangent stiffness matrix \mathbf{K} :

$$\mathbf{K}(\mathbf{u}_{i+1}^{t+\Delta t}) = \frac{\partial \mathbf{G}(\mathbf{u}_i^{t+\Delta t})}{\partial \mathbf{u}} \quad (3.50)$$

$$\mathbf{K}(\mathbf{u}_{i+1}^{t+\Delta t}) \delta \mathbf{u}_{i+1} = \mathbf{G}(\mathbf{u}_i^{t+\Delta t}) \quad (3.51)$$

This will be solved until $\mathbf{G}(\mathbf{u}_i^{t+\Delta t})$ is below the convergence tolerance. We can rewrite the tangent stiffness matrix \mathbf{K} in terms of the displacement:

$$\mathbf{K}(\mathbf{u}) = \frac{\partial \mathbf{G}(\mathbf{u})}{\partial \mathbf{u}} = \frac{\partial}{\partial \mathbf{u}} \left(\int_V \widehat{\mathbf{B}}^T \boldsymbol{\sigma}(\mathbf{u}) dV - \mathbf{F}_{ext} \right)$$

$$\frac{\partial}{\partial \mathbf{u}} \left(\int_V \widehat{\mathbf{B}}^T \boldsymbol{\sigma}(\mathbf{u}) dV \right) = \int_V \widehat{\mathbf{B}}^T \frac{\partial \boldsymbol{\sigma}(\mathbf{u})}{\partial \mathbf{u}} dV$$

$$\int_V \widehat{\mathbf{B}}^T \frac{\partial \boldsymbol{\sigma}(\mathbf{u})}{\partial \boldsymbol{\varepsilon}} \frac{\partial \boldsymbol{\varepsilon}}{\partial \mathbf{u}} dV = \int_V \widehat{\mathbf{B}}^T \frac{\partial \boldsymbol{\sigma}(\boldsymbol{\varepsilon})}{\partial \boldsymbol{\varepsilon}} \widehat{\mathbf{B}} dV$$

$$\mathbf{K}(\mathbf{u}) = \int_V \widehat{\mathbf{B}}^T \mathbf{D}^{tan} \widehat{\mathbf{B}} dV \quad (3.52)$$

Where \mathbf{D}^{tan} is the Jacobian of the constitutive law:

$$\mathbf{D}^{tan} = \frac{\partial \boldsymbol{\sigma}(\boldsymbol{\varepsilon})}{\partial \boldsymbol{\varepsilon}} \quad (3.53)$$

In the implicit solution, it is required to invert the stiffness matrix \mathbf{K} , which increases the computational costs of the simulation.

3.3.2 Explicit Finite Element Method

An explicit solution is better suited to solving simulations involving large deformations and with complex contact interactions. In this thesis, Abaqus/Explicit is employed to create quasi-static simulations of polymer prosthetic heart valves under systolic and diastolic pressure conditions. In explicit integration, an iterative approach is not employed as in implicit. This avoids convergence issues and allows for simulation of complex non-linear problems. Acceleration and velocity are assumed constant at time point t , and are used to solve for the next time point $t + \Delta$. Central difference integration is used:

$$\mathbf{u}^{i+1} = \mathbf{u}^i + \Delta t^{i+1} \dot{\mathbf{u}}^{i+\frac{1}{2}} \quad (3.54)$$

$$\dot{\mathbf{u}}^{i+\frac{1}{2}} = \dot{\mathbf{u}}^{i-\frac{1}{2}} + \frac{\Delta t^{i+1} + \Delta t^i}{2} \ddot{\mathbf{u}}^i \quad (3.55)$$

Where \mathbf{u} is the displacement vector, $\dot{\mathbf{u}}$ the velocity vector and $\ddot{\mathbf{u}}$ the acceleration vector, and i is the increment number. The accelerations are then calculated by the following:

$$\ddot{\mathbf{u}}^i = \mathbf{M}^{-1}(\mathbf{F}^i - \mathbf{I}^i) \quad (3.56)$$

Where \mathbf{M} is the lumped mass matrix, \mathbf{F} is the vector of external forces and \mathbf{I} is the vector of internal element forces given by:

$$\mathbf{M} = \int_V \rho \mathbf{N} dV \quad (3.57)$$

$$\mathbf{I}^i = \int_V \mathbf{B}^T \boldsymbol{\sigma}^i dV \quad (3.58)$$

$$\mathbf{F}^i = \int_S \mathbf{N}^T \mathbf{t}^i dS + \int_V \mathbf{N}^T \mathbf{P}^i dV \quad (3.59)$$

We can rearrange the lumped mass matrix to get:

$$\mathbf{M}\ddot{\mathbf{u}} = \mathbf{F} - \mathbf{I} \quad (3.60)$$

As the lumped mass matrix \mathbf{M} is diagonalised, it is easy to invert, in comparison to \mathbf{K} in the implicit solution scheme. This allows for much faster computation times. As the explicit solution scheme does not have the same convergence criteria as implicit, much smaller increment sizes must be used to ensure accurate results. The stability limit is given by:

$$\Delta t \leq \frac{2}{\omega_{max}} \quad (3.61)$$

Where ω_{max} is the maximum element eigenvalue. The stability limit can also be written as:

$$\Delta t = \min \left(\frac{L^e}{c^d} \right) \quad (3.62)$$

Where L^e is the characteristic element length, and c^d is the dilatational wave speed, which is related to the material density ρ . Mass scaling can be employed in an explicit integration scheme to artificially increase the stability limit and result in faster run times. Care should be taken when using such an approach and it is generally recommended that the ratio of kinetic energy to internal energy be no more than 5% to ensure accurate results (Choi et al., 2002).

3.4 Navier Stokes

For solving fluid dynamics problems, the partial differential equations are solved in a Eulerian description. Conservation of mass and conservation of momentum are the two principal laws that govern the velocity of fluid. The conservation of mass is given by:

$$\frac{\partial \rho_f}{\partial t} + \nabla \cdot (\rho_f \vec{v}_f) = 0 \quad (3.63)$$

Where ρ_f is the fluid density and \vec{v}_f is the fluid velocity. For incompressible fluids where density is constant, the equation can be simplified to:

$$\nabla \cdot \vec{v}_f = 0 \quad (3.64)$$

For standard flow problems, the Navier Stokes equation is given by:

$$\rho_f \frac{\partial \vec{v}_f}{\partial t} + \rho_f \vec{v}_f \cdot \nabla \vec{v}_f = \bar{\sigma}_f + \vec{f}_f \quad (3.65)$$

This can be simplified by neglecting gravity and assuming incompressible:

$$\rho_f \frac{\partial \vec{v}_f}{\partial t} + \rho_f \nabla \cdot (\vec{v}_f \vec{v}_f) = \nabla \cdot \bar{\sigma}_f \quad (3.66)$$

3.5 Immersed Boundary Method

In Chapters 6 and 7 of this thesis, fluid-structure interaction simulations of flexible leaflets and prosthetic aortic valves are computed using the Coupled Eulerian Lagrangian (CEL) package available in Abaqus. In a Lagrangian description, the coordinates of nodes move along with the material and no material can pass between elements. In a Eulerian description the coordinates of the nodes are fixed and material flows through the mesh. The spatial coordinates of the material points change over time. The Abaqus/CEL method is an immersed boundary (IB) FSI simulation. It is a monolithic approach, where both the fluid and solid equations are

solved simultaneously. It uses the finite element method and employs an explicit time integration scheme. In contrast to flexible grid FSI techniques, such as Arbitrary Eulerian Lagrangian (ALE), where the mesh deforms with the structure, the IB technique utilises a fixed grid mesh, through which material flows, and a solid exists within the grid and in absence of fluid, as depicted in Figure 3.3. This method was first developed by Peskin for heart valves, in order to solve for the large deformation of the flexible leaflets (Peskin, 2002). To include the solid in the fluid, a weighting function is used to interpolate the fluid forces at the fluid-solid interface. This results in a body force term in the NS equations at the nearby elements. To account for the fluid on the solid, the velocity term governs the interaction. As these forces and velocities are spread over many nodes at the points of contact, the resulting fluid-structure interface is not as accurate as can be achieved in an ALE simulation. Rather, this fixed grid method is most useful in the simulation of highly elastic, large deformations where a flexible mesh would be incredibly complex to solve.

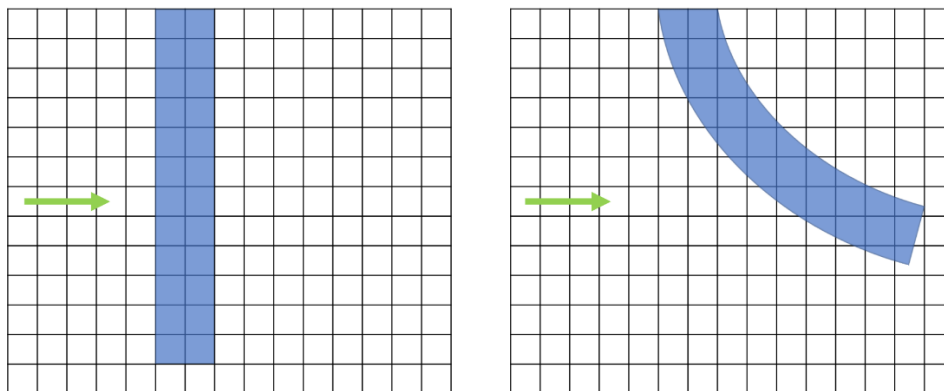
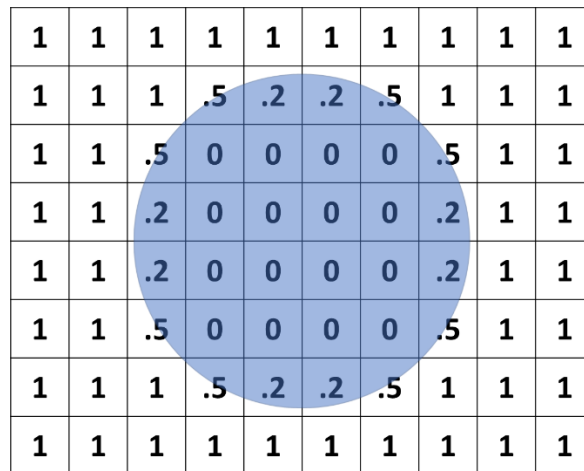


Figure 3.3 Representation of deformation of Lagrangian solid structure in the fixed Eulerian fluid domain

The fluid grid is discretised with Eulerian elements, while the structure is Lagrangian. The presence of the Lagrangian structure in the fluid domain is accounted for by a Volume-of-fluid (VOF) function. This parameter assumes a value of 0 if an element in the grid is fully bounded

by the Lagrangian structure, or a value of 1 if there is no structure and it is completely filled with fluid. This is depicted in Figure 3.4, which also shows how partially filled elements are assigned values between 1 and 0. At the start of the simulation, the initial VOF is predefined. The general explicit contact condition is enforced at the fluid solid interface.



1	1	1	1	1	1	1	1	1	1
1	1	1	.5	.2	.2	.5	1	1	1
1	1	.5	0	0	0	0	.5	1	1
1	1	.2	0	0	0	0	.2	1	1
1	1	.2	0	0	0	0	.2	1	1
1	1	.5	0	0	0	0	.5	1	1
1	1	1	.5	.2	.2	.5	1	1	1
1	1	1	1	1	1	1	1	1	1

Figure 3.4 Representation of volume of fluid (VOF) definition for a Lagrangian solid structure in the Eulerian fluid domain

3.6 References

Peskin, C.S., 2002. The immersed boundary method. *Acta Numer.* 11, 479–517. <https://doi.org/10.1017/S0962492902000077>

Choi, H.-H., Hwang, S.-M., Kang, Y.H., Kim, J., Kang, B.S., 2002. Comparison of Implicit and Explicit Finite-Element Methods for the Hydroforming Process of an Automobile Lower Arm. *Int. J. Adv. Manuf. Technol.* 20, 407–413. <https://doi.org/10.1007/s001700200170>

CHAPTER 4

In Silico Modelling of Aortic Valve Implants – Predicting in Vitro Performance using Finite Element Analysis

This chapter has been adapted from a journal publication ‘Whiting et al., (2022), In silico modelling of aortic valve implants–predicting in vitro performance using finite element analysis. J. Med. Eng. Technol. 46, 220–230. <https://doi.org/10.1080/03091902.2022.202650>’.

4.1 Introduction

Aortic stenosis is a valvular heart disease, whereby calcification build-up on the native valve leaflets leads to decreased blood flow and increased left ventricular hypertrophy (Adams et al., 2019). Severe aortic stenosis is treated with either surgical or transcatheter aortic valve replacement (TAVR), with over 300,000 valve replacements performed in the developed world each year (Manji et al., 2012). This number is expected to increase in the coming years with ageing demographics (Osnabrugge et al., 2013). Bioprosthetic heart valves (BHV) are now widely used and consist of either bovine or porcine pericardium tissue leaflets mounted on a stent frame, with the distinct advantage that they can be delivered minimally invasively. While

these devices have demonstrated good clinical outcomes (Daubert et al., 2017), there is significant room for further design improvements to enhance structural durability and long-term hemodynamic performance. This is a problem particularly in younger patients where the onset of structural valve degeneration can occur 10 to 15 years post implantation, requiring reoperation (Bradley, 2013; Friedewald et al., 2007; Kostyunin et al., 2020; Nishimura et al., 2014). Recently, there has been increasing interest in developing synthetic polymer leaflets as an alternative to bioprosthetic tissue leaflets in TAVR devices. While these polymeric valve devices are at an earlier stage of development, they have the potential to provide superior patient outcomes, as well as vastly improved efficiency in the manufacturability and reproducibility of TAVR devices (Claiborne et al., 2013a; Rotman et al., 2019). In developing the next generation of aortic valve replacements (AVRs), there are significant challenges that must be overcome to achieve suitable designs capable of withstanding the demanding functional requirements at the native aortic root. This applies to both bioprosthetic and synthetic leaflet-based aortic valve replacements (both surgical and TAVR), which must undergo stringent functional mechanical testing during the certification process.

The key mechanical requirements for an implanted aortic valve relate to both structural and hemodynamic performance. During an individual cardiac cycle, aortic valve implants should (i) provide minimal resistance to forward blood flow to maximise orifice area in the open configuration, (ii) have a low pressure differential to revert to the closed configuration, and (iii) facilitate rapid closure to reduce volume regurgitation or forward flow energy loss. Throughout their entire lifespan, aortic valve implants should be highly durable to withstand pressures and stresses experienced over the approximately 40 million cardiac cycles per year. The development of these devices takes place through both *in silico* modelling and *in vitro* bench testing, with the latter the more widely used, readily available, and standardised approach. *In vitro* bench testing is underpinned by ISO 5840:2021 (International Organisation for

Standardisation, 2021a, 2021b, 2021c), which is the international standard that provides guidelines, specifications and minimum design criteria that cardiac valve prostheses must fulfil to be deemed safe and effective for patients by the U.S. Food and Drug Administration (FDA) and relevant EU notified bodies. For hydrodynamic assessments, pulsatile flow bench test systems that simulate physiological conditions are used to assess valve hemodynamic performance. ISO 5840 defines acceptable values for key performance parameters of effective orifice area (EOA) and regurgitant fraction (RF) for surgical and transcatheter valve replacements operating at normotensive conditions at a range of orifice sizes (International Organisation for Standardisation, 2021b, 2021c). Many comprehensive studies comparing these parameters across valve designs have been carried out on commercial flow rigs (Rahmani et al., 2017, 2012; Rotman et al., 2019), which are also capable of investigating additional parameters such as the left ventricular energy loss, leakage volumes and transvalvular pressure drop (ΔP). These are further indicators of valve performance and useful in the design process. While durability and hydrodynamic testing according to ISO 5840 provides a comprehensive assessment of structural and hemodynamic performance of valves, the development pathway typically involves a trial-and-error process of design, prototyping and testing. Each design iteration requires an extensive suite of bench tests (International Organisation for Standardisation, 2021a, 2021b, 2021c) and relying solely on this method contributes to high development costs and increased time to market for aortic valve devices.

Computational modelling approaches have the potential to accelerate design timelines of aortic valves and optimise functional performance. However, predicting the structural and hemodynamic behaviour of aortic valve implants *in silico* represents a challenging multi-physics problem. For this, advanced fluid-structure interaction (FSI) simulations have been developed and used to analyse the flow profiles of valves (Kandail et al., 2018), as well as approximating EOA, RF and transvalvular ΔP (Gharaie and Morsi, 2015; Mao et al., 2016).

However, there are substantial drawbacks to FSI approaches, including complexity, robustness, large computational cost and development time, which has meant that uncoupled approaches are more widespread in the literature (Claiborne et al., 2013b). Computational fluid dynamics approaches have been used to explore valve hemodynamics (Bluestein et al., 2000; Dwyer et al., 2009; Ge et al., 2005), and typically focus on providing predictions of flow regimes and parameters such as wall shear stress or velocities by assuming the valve as a rigid boundary (Bluestein et al., 2000; Dwyer et al., 2009; Ge et al., 2005). Despite providing highly detailed predictions of local flow profiles, computational fluid dynamics offers surprisingly little insight into the overall hemodynamic performance of the valve in the context of the key parameters identified in ISO 5840 and in vitro bench testing. In particular, EOA, RF and transvalvular ΔP are bulk, or system-level, hemodynamic parameters and cannot be assessed based on the rigid boundary assumptions. On the other hand, finite element analysis (FEA) has been widely used for structural analysis of the aortic valve, predicting leaflet deformation in open and closed configurations (Arcidiacono et al., 2005; Burriesci et al., 2010; Claiborne et al., 2013a; Haj-Ali et al., 2008; Kim et al., 2008; Li and Sun, 2017, 2010; Serrani et al., 2016; Smuts et al., 2011). To date, the vast majority of FEA studies focus on a traditional stress analysis, with a view to optimising leaflet or frame design to enhance fatigue behaviour and overall durability (Claiborne et al., 2013a; Serrani et al., 2016; Smuts et al., 2011). While these approaches provide insight into structural integrity of the valve, very few studies have sought to exploit the potential of FEA in predicting hydrodynamic parameters that are key valve design characteristics. Importantly, the bulk hemodynamic parameters measured according to ISO 5840 through in vitro bench testing (e.g. EOA, RF and transvalvular ΔP) are largely related to compliance of the valve, which provides an opportunity for FEA to provide critical insight into hemodynamic performance characteristics of valve design.

The objective of this study is to investigate the potential of FEA to predict the hydrodynamic performance of aortic valve implants during the development phase. Several variations of tri-leaflet aortic valves were designed and manufactured using a synthetic polymer and hydrodynamic testing was carried out using a pulsatile flow rig according to ISO 5840, with bulk hydrodynamic parameters measured. An in silico framework was developed, which uses a mathematical model to apply pressure-based boundary conditions to three-dimensional finite element models of the aortic valves in systolic and diastolic configurations, with predicted outputs compared to the results from in vitro testing. Through regression analysis, the in silico parameters of leaflet coaptation area (LCA), geometric orifice area (GOA) and opening pressure were investigated as surrogate predictors for in vitro hydrodynamic parameters, RF, EOA and transvalvular ΔP performance, respectively. While the developed methods are demonstrated on surgical aortic valves, they could be applicable across both surgical and TAVR tri-leaflet valve designs.

4.2 Materials and Methods

4.2.1 Valve Design and Manufacture

Three unique aortic valves (A, B & C) were designed and manufactured from a synthetic polymer, as shown in Figure 4.1. Each valve featured a tri-leaflet design, with an internal orifice diameter of 23 mm (± 0.2 mm) and an embedded steel wire frame to provide radial reinforcement, with a skirt/suture ring around the basal circumference to enable mounting during in vitro testing. The characteristic dimensions of each valve design are listed in Table 4.1 and identified in Figure 4.1, where D represents the internal diameter (mm), t the leaflet thickness (mm), h the maximum leaflet height (mm), α the lunula angle ($^\circ$) and θ the insertion angle ($^\circ$) of the leaflet. Valve A is a generic valve design representative of commercial pericardial surgical prostheses, while Valve B was modified by increasing the strut height and

lunula angle, thereby decreasing the leaflet height at the centre of the valve. Valve C featured a unique orifice profile that increased the free-edge perimeter length.

A polyurethane elastomer variant developed at the University of Galway was used to manufacture the valves through a compression moulding procedure. Stainless steel compression moulds were fabricated based on CAD designs of each valve as shown in Figure 4.2.

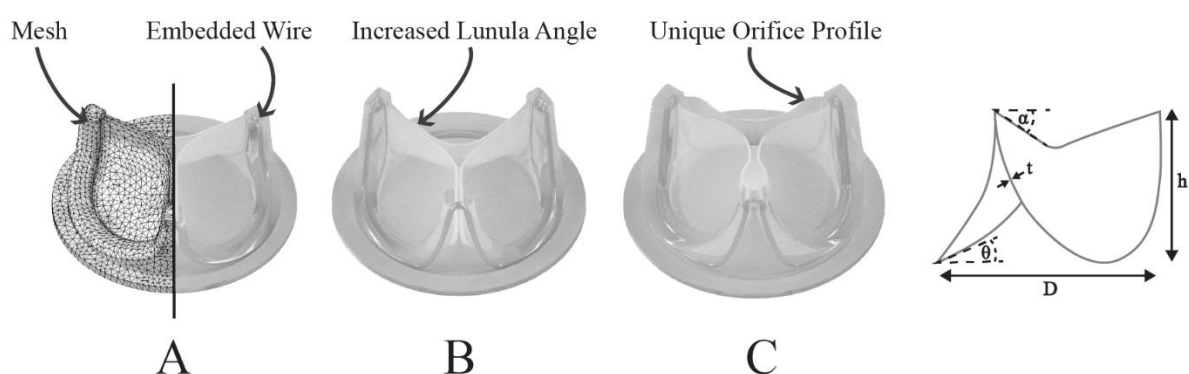


Figure 4.1 Unique valve designs A, B and C, where Valve A shows the finite element mesh. Design features of valves B and C are highlighted, while the characteristic valve dimensions are identified in the far-right schematic, where D represents the internal diameter (mm), t the leaflet thickness (mm), h the maximum leaflet height (mm), α the lunula angle ($^{\circ}$) and θ the insertion angle ($^{\circ}$) of the leaflet.

The reacted polymer mixture was transferred to compression moulds, compressed by a clamp and cured in an oven at 50°C for 4.5 hours. Once cured, the moulds were removed from the oven and allowed to cool to ambient temperature before removing the valves from the moulds.

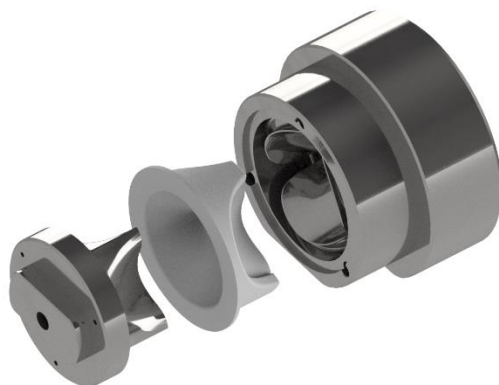


Figure 4.2 Compression mould for Valve C

Table 4.1 Characteristic Valve Dimensions

Valve	A	B	C
D – Internal Diameter (mm)	22.8	22.84	23
t – Leaflet Thickness (mm)	0.344	0.35	0.298
h – Leaflet Height (mm)	11.5	10	14.5
α – Lunula Angle ($^{\circ}$)	0	22.57	0
θ – Insertion Angle ($^{\circ}$)	0	0	58.1

4.2.2 In Vitro Testing

To evaluate the hydrodynamic performance of each valve, in vitro bench testing was performed using a Vivitro Pulse Duplicator (Figure 4.3a) (Vivitro Labs, Inc. Victoria, B.C.) according to ISO 5840. Valves were sealed in a mounting ring and placed in the aortic position between the ventricular sac and aorta of the flow rig. This flow rig reproduced cardiac pulsatile flow by compressing the ventricular sac and ejecting fluid through the aortic valve according to assigned stroke volume, systolic waveform and heart rate. Pressure transducers recorded the aortic, ventricular, and atrial pressures while a flow probe positioned directly below the valve took flow measurements during each cycle, as shown in Figure 4.3b. Valves were submerged in water for 2 hours prior to testing in 0.9% NaCl solution at room temperature (20°C). To investigate the hydrodynamic performance across a range of conditions, each valve was tested at increasing cardiac outputs of 2, 3, 4, 5, 6 and 7 L/min, while maintaining a constant mean aortic pressure of 100 mmHg, heart rate of 70 bpm and a systolic waveform occupying 35% of the cardiac cycle. The Vivitro rig was adapted to enable high-speed image capture using a Sony RX100 Mark IV camera (Figure 4.3a) at a frame rate of 1000fps to visualise open and closing

configurations of valves during testing. Vivitest software (Vivitro Labs, Inc. Victoria, B.C.) recorded pressure and flow measurements over 10 consecutive cycles, which were used to calculate several hydrodynamic parameters, namely the EOA, RF and transvalvular ΔP . The EOA is defined as the minimal cross-sectional area of the jet formed downstream of the aortic valve (Akins et al., 2008; Garcia and Kadem, 2006). It is often used during cardiac catheterisation to assess the severity of aortic stenosis in patients (Baumgartner et al., 2017; Nishimura et al., 2014). It is calculated using the Gorlin Formula (Gorlin and Gorlin, 1951) given by

$$EOA = \frac{Q_{RMS}}{51.6 \sqrt{\frac{\Delta P}{\rho}}} \quad (4.1)$$

where Q_{RMS} is the root mean squared forward flow (ml/sec), ΔP is the mean transvalvular pressure drop (mmHg) and ρ is the density of the test fluid (g/cm^3). The RF is a measure of aortic valve leakage and is calculated by the regurgitant volume (RG) as a fraction of the stroke volume (SV), as in Eq. (4.2)

$$RF = \frac{RG}{SV} \quad (4.2)$$

where RG is the sum of the closing volume and leakage volume (Figure 4.3b). The transvalvular ΔP , shown in Figure 4.3b, refers to the pressure gradient across the valve during systole where the ventricles contract ejecting blood into the aorta and pulmonary artery. It is calculated as the mean pressure difference between the start and end of the systole positive pressure drop. It is used to assess aortic stenosis, with pressure drops of greater than 40 mmHg being considered severe (Baumgartner et al., 2009). In the design of replacement valves, low pressure drops indicate ease of opening, which translates to a more efficient valve.

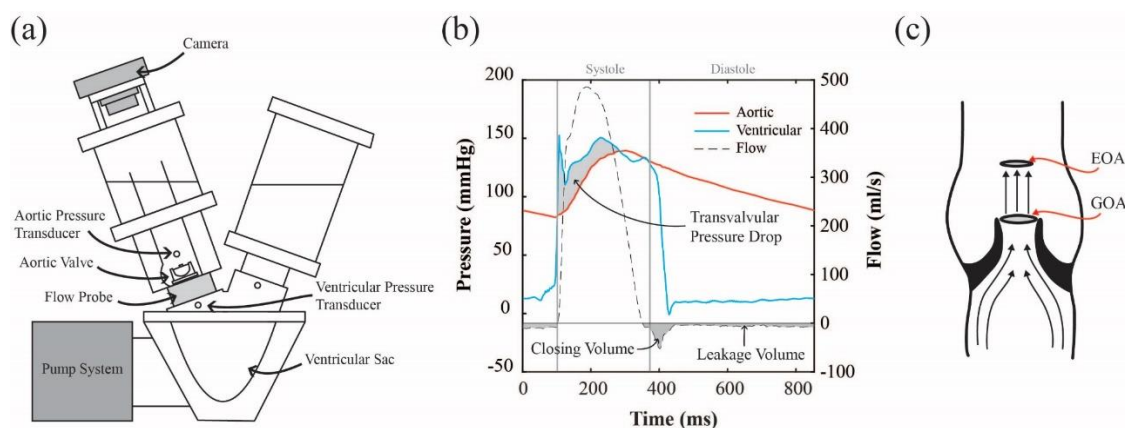


Figure 4.3 (a) Schematic of Vivitro Pulse Duplicator with pressure transducers and a flow probe which was used to carry out *in vitro* hydrodynamic testing, (b) a typical diagram of average flow measurements, aortic and ventricular pressures measured over 10 cardiac cycles and (c) a schematic showing the effective orifice area (EOA) as a measure of the downstream jet from the aortic orifice, where geometric orifice area (GOA) is measured as the opening area of the leaflets.

4.2.3 In Silico Modelling Framework

A three-dimensional finite element model of each tri-leaflet valve under systolic and diastolic pressure conditions was developed using the Abaqus/Explicit finite element code (Abaqus 2017, Simulia, RI, USA). Valve A, B and C models were meshed with approximately 29,000, 34,000 and 47,000 10-node modified quadratic tetrahedrons (C3D10R) respectively, as shown for Valve A in Figure 4.1. The wire frames were meshed using approximately 600 8-node linear brick, reduced integration, hourglass control elements (C3D8R), and assigned an embedded region constraint. This specifies the wire elements as embedded within the valve and constrains the translational degrees of freedom of each embedded node to interpolated values of the corresponding degrees of freedom of the host element in the valve domain. The material behaviour of the synthetic polymer was determined based on displacement-controlled uniaxial tensile tests, carried out on a Zwick Roell Uniaxial Testing machine, at a 5 mm/min displacement rate on a 100 N Load cell on test specimens manufactured from compression moulds. The D882–18 standard test method for tensile properties of thin plastic sheeting

(American Society for Testing and Materials, 2018) was modified for use with reduced length testing specimens (Length = 50 mm), which were submerged in water at room temperature (20°C) for at least 2 hours prior to testing. A second order non-linear isotropic Ogden (N=2) material model given by

$$U = \sum_{i=1}^N \frac{2\mu_i}{\alpha_i^2} (\bar{\lambda}_1^{\alpha_i} + \bar{\lambda}_2^{\alpha_i} + \bar{\lambda}_3^{\alpha_i} - 3) + \sum_{i=1}^N \frac{1}{D_i} (J^{el} - 1)^{2i} \quad (4.3)$$

where U is the strain energy potential, $\bar{\lambda}_j$, ($j = 1,2,3$) are the deviatoric principal stretches, J^{el} is the elastic volume ratio and μ_i , α_i and D_i are the material parameters shown in Table 4.2, was calibrated to the experimental data shown in Figure 4.4.

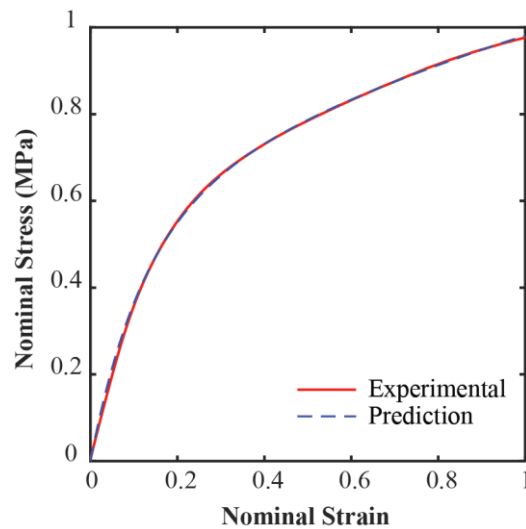


Figure 4.4 An Ogden (N=2) constitutive model was fitted to the experimental uniaxial tensile test results of the polymer

Table 4.2

Parameters for Ogden (N=2) constitutive model

μ_1	α_1	μ_2	α_2	D_1	D_2
-0.764 MPa	3.305	2.509 MPa	-5.764	0.05 MPa	0.05 MPa

The polymer was assigned a density of 1000 kg/m^3 . The wire frame was modelled as linear elastic and assigned the material properties of steel, with a Young's modulus of 200 GPa, a Poisson ratio of 0.3 and a density of 8050 kg/m^3 . A mathematical model was used to determine pressure-based boundary conditions for the valve leaflets to appropriately represent diastolic and systolic conditions during the cardiac cycle. A two-element Windkessel model and the simplified Bernoulli equation were used to determine pressure waveforms based on the prescribed inputs of cardiac output (L/min), heart rate (bpm) and mean aortic pressure (mmHg). These model inputs are the same parameters that were prescribed during *in vitro* experimental testing. For the diastolic pressure conditions, a two-element Windkessel model was used to generate a maximum aortic pressure for each cardiac output, given by

$$I(t) = \frac{P(t)}{R} + C \frac{dP(t)}{dt} \quad (4.4)$$

where I is the flow, P is the pressure, R is the resistance of the smaller arteries and C is the compliance of the aorta. For the systolic pressure condition, the Bernoulli equation was used to generate the estimated transvalvular ΔP for each cardiac output, given by

$$\Delta P = \frac{\rho}{2}(v_2^2 - v_1^2) + \rho gh \quad (4.5)$$

where ρ is the density of the test fluid, v is the velocity, g is the acceleration due to gravity and h is the height difference. These pressure conditions, shown in Table 4.3, were applied using a smooth step amplitude to fully close and then fully open the valve.

Table 4.3 FE pressure boundary conditions generated from Windkessel and Bernoulli models

Cardiac Output (L/min)	2	3	4	5	6	7
Bernoulli Systolic (mmHg)	12.24	13.65	16.62	18.15	21.25	24.91
Windkessel Diastolic (mmHg)	111.01	115.56	120.19	124.83	129.43	133.98

4.2.4 Surrogate hydrodynamic measures

Hydrodynamic parameters of EOA, RF and transvalvular ΔP were measured during *in vitro* testing to provide a measure of valve performance. In this study, several measures from the finite element simulations were investigated as surrogate measures for these experimental parameters.

Firstly, GOA, which is the anatomical area of the valve orifice, was investigated as a surrogate measure for EOA. From the models, the GOA was evaluated as the simulated opening area of the valve at systole, using the image processing toolbox in MATLAB (Mathworks, Natick, MA, USA). As shown in Figure 4.3c, EOA and GOA are separate measurements that both relate to the opening area of the valve. The EOA has been shown to be influenced by the anatomical opening area of the orifice, as well as the geometrical contraction profile of the orifice (Akins et al., 2008). Previous studies have already assumed that GOA was a suitable predictor of EOA (Akins et al., 2008), although there are limited examples of quantitative comparisons between these measures in the literature.

Secondly, LCA upon valve closure was investigated as a surrogate measure for RF. As cardiac outputs are increased, the pressure gradient across the valve rises. This increases the amount of contact between the leaflets, which would reduce the amount of fluid regurgitation. Previous studies have suggested that LCA is a reflection of RF, as it facilitates a larger surface area for distribution of the diastolic load across the leaflets (Claiborne et al., 2013a). However, again, a direct quantitative comparison between computational predictions and experimental observations has not been made in previous studies. Therefore, this study measures LCA from the simulations and evaluates its potential as a surrogate measure for RF.

Thirdly, the opening pressure required to achieve 40% of the maximum aortic valve orifice area ($P_{OA40\%}$) was investigated as a surrogate measure for the transvalvular ΔP during systole.

Similar approaches have been used previously, by observing the difference in time taken to open two valves, as well as the required pressures to open them when designing for a reduced transvalvular ΔP (Burriesci et al., 2010).

4.3 Results

4.3.1 Evaluation of Valve Deformation

In vitro and in silico deformations of each valve under investigation during systole and diastole at normotensive conditions of cardiac output 5 L/min are shown in Figure 4.5. In diastole, there was excellent qualitative agreement between in vitro and in silico results, with the FEA simulations predicting the twisting or pin-wheeling deformation in Valve A. Valve B demonstrated less compliance than Valve A, and this was captured in the FEA simulation. In the experimental test, the geometric orifice area at closing was larger than the FEA prediction. Valve C also exhibited pin-wheeling, which was captured in the FEA simulation. Also evident in both results is the gap between the leaflets during closure at the strut attachment points. In systole, there was reasonable qualitative agreement between in vitro and in silico opening configurations, although experimental results showed evidence of asymmetric opening in certain cases (likely caused by local flow instability), a feature that is not captured by FEA. The FEA contour plots highlight the von Mises stress distribution in each valve concentrated around the leaflet base attachment. The highest stress levels were observed in Valve C while Valve A had the lowest stress values.

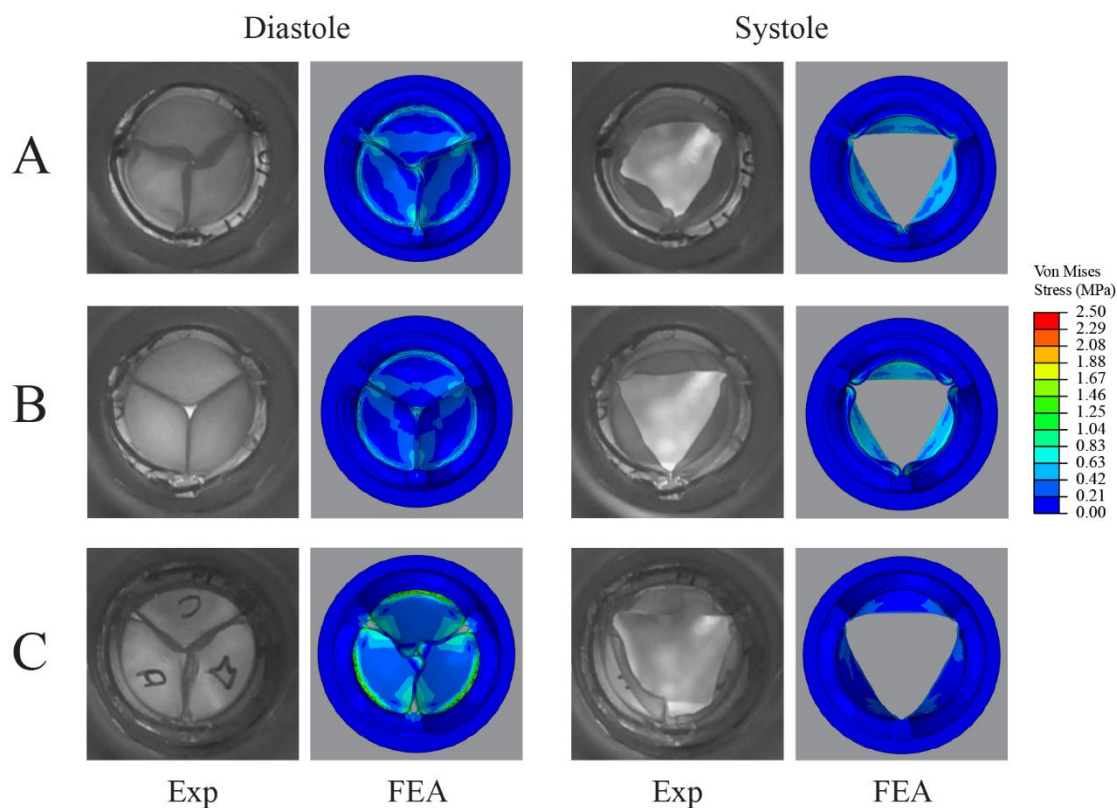


Figure 4.5 The diastolic and systolic positions of the valves at normotensive conditions of 5L/min were captured and viewed from the outflow (aortic) side of the valve. The experimental (EXP) in vitro hydrodynamic condition as viewed from the outflow tract, compared to the corresponding finite element analysis (FEA) valve simulation with stress contours showing the von Mises stress (MPa).

4.3.2 In Vitro Testing

Based on in vitro hydrodynamic testing of each valve, the mean values of EOA, RF and transvalvular ΔP are shown in Figure 4.6, with standard deviation represented by error bars (each valve tested over 10 cycles). The EOA was found to increase in each valve with increasing cardiac outputs, with the mean EOA over all the cardiac outputs for Valve A, B and C measured at 1.77 cm², 1.66 cm² and 2.53 cm² respectively, while Valve C had the highest EOA at each cardiac output. All three 23 mm valves meet the minimum requirements for EOA set out by ISO 5840, which is greater than or equal to 1.25 cm² at 5 L/min. RF decreased with increasing cardiac output in each valve, with the mean RF over the entire cardiac outputs for

Valve A, B and C measured at 8.08%, 5.19% and 21.12% respectively, while Valve C had the largest RF over the range of cardiac outputs. Valve A and B both met the ISO 5840 requirement of less than or equal to 10% RF at 5 L/min for a size 23 mm valve, while Valve C did not meet the requirement. The transvalvular ΔP increased in each valve with increasing cardiac output, with the mean transvalvular ΔP over the entire cardiac outputs for Valve A, B and C measured at 11.84 mmHg, 12.45 mmHg and 7.09 mmHg, respectively. Valve C had the lowest transvalvular ΔP generally over the range of cardiac outputs. The in vitro hydrodynamic transvalvular pressure profiles for each valve from 2-7 L/min are shown in Figure 4.7.

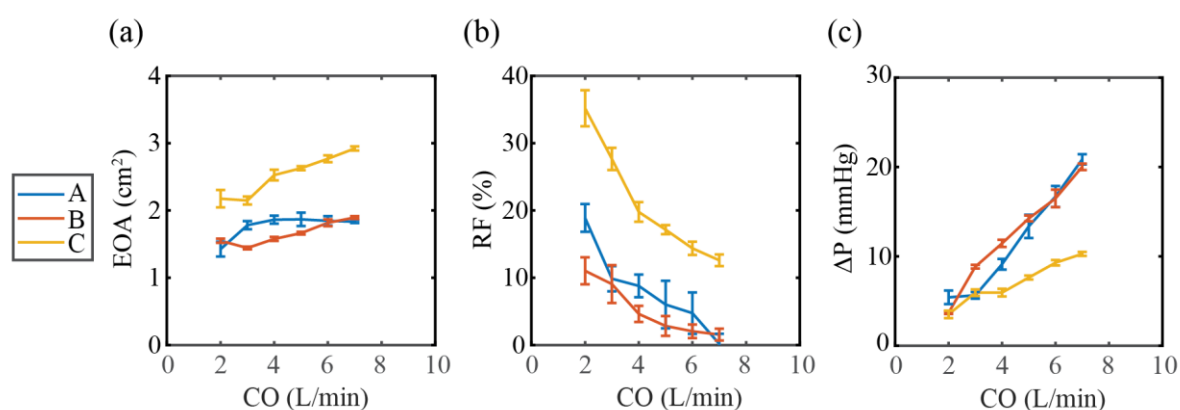


Figure 4.6 In vitro hydrodynamic parameters according to ISO 5840 of effective orifice area (EOA), regurgitant fraction (RF), and transvalvular pressure drop (ΔP), were measured with increasing cardiac output (CO) of 2-7 L/min and compared across the three valve geometries. Data is represented as the mean \pm SD, $n = 10$ (each valve tested over 10 cycles), (a) EOA with increasing CO for Valves A, B and C. (b) RF with increasing CO for Valves A, B and C. (c) Transvalvular ΔP with increasing CO for Valves A, B and C.

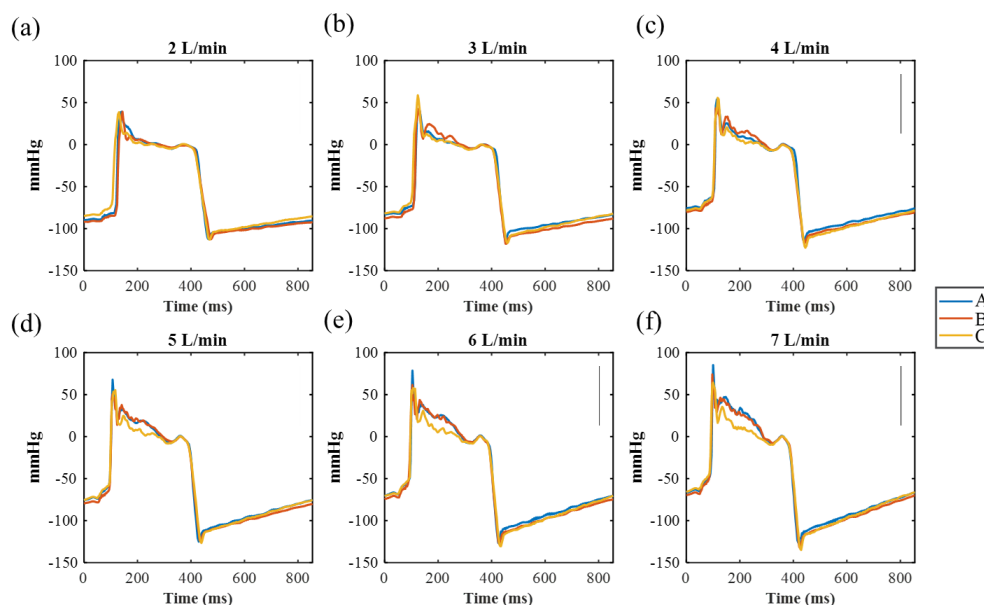


Figure 4.7 In vitro hydrodynamic transvalvular pressure profiles, were measured with increasing cardiac output (CO) of 2-7 L/min and compared across the three valve geometries.

4.3.3 Finite Element Analysis

The predicted values of GOA, LCA and $P_{OA40\%}$ with increasing cardiac output from the in silico models are shown in Figure 4.8. The GOA in each valve was higher as the cardiac output increased. Valve C had the highest GOA consistently at each cardiac output, while Valve B was consistently lowest. The LCA also rose with increasing cardiac output in each valve, with Valve A and B producing similar results. Valve C consistently had the lowest LCA for each cardiac output. The $P_{OA40\%}$ was lowest in Valve C at 1.95 mmHg, while Valve A and B had a $P_{OA40\%}$ of 7.46 mmHg and 10.4 mmHg, respectively.

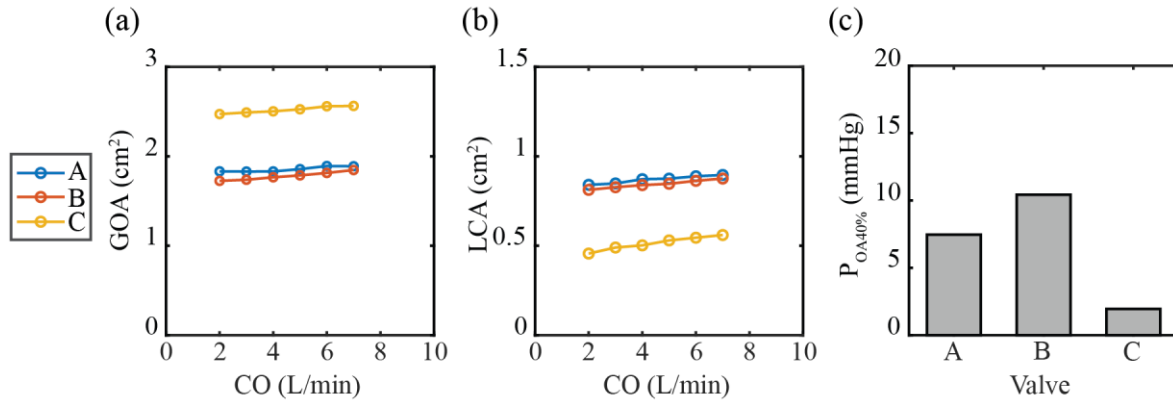


Figure 4.8 In silico measured parameters of (a) geometric effective orifice area (GOA) and (b) leaflet coaptation area (LCA) were compared across the three valve geometries, A, B, and C for calculated pressures corresponding to increasing cardiac outputs (CO) of 2-7 L/min. (c) The pressure to achieve 40% of each valves' orifice area ($P_{OA40\%}$) was measured for valves A, B and C.

4.3.4 Surrogate Measures

Regression analysis was used to determine correlations between the surrogate parameters evaluated in silico and the bulk hydrodynamic parameters determined through in vitro bench testing. Figure 4.9a shows the GOA (in silico) plotted against EOA (in vitro) for increasing cardiac output. A strong correlation between GOA and EOA was found with a r^2 value of 0.84. Figure 4.9b shows the LCA (in silico) plotted against RF (in vitro). A good correlation between LCA and RF was observed with an r^2 value of 0.68. Figure 4.9c shows the $P_{OA40\%}$ (in silico) plotted alongside the mean transvalvular ΔP over the entire cardiac outputs (in vitro). The lowest pressures were recorded in Valve C and are captured in both the $P_{OA40\%}$ and mean ΔP .

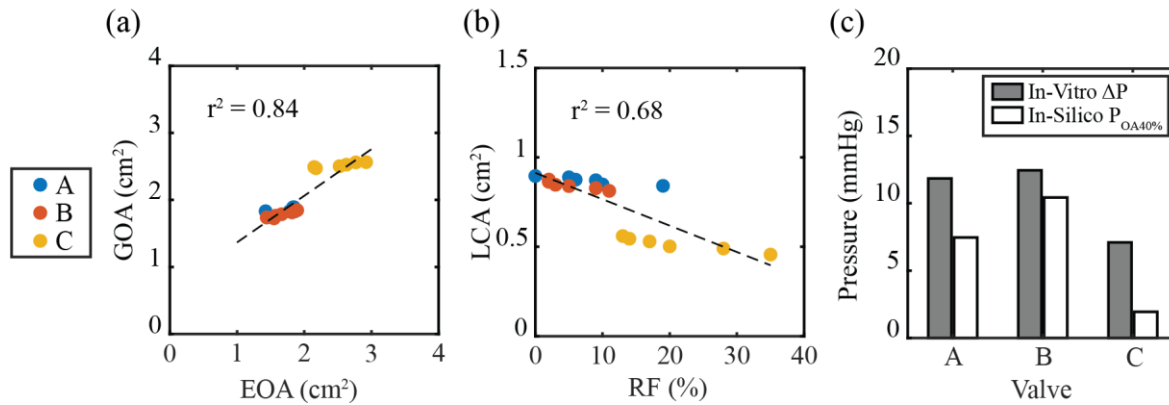


Figure 4.9 In silico surrogate measures were plotted against in vitro hydrodynamic parameters across the three valve geometries, A, B, and C. (a) Geometric effective orifice area (GOA) was plotted against the effective orifice area (EOA), while (b) leaflet coaptation area (LCA) was plotted against the regurgitant fraction (RF). (c) The pressure to achieve 40% of the orifice area ($P_{OA40\%}$) was plotted against the mean transvalvular pressure drop (ΔP) over the range of cardiac outputs.

4.4 Discussion

Through in vitro and in silico testing, this study outlines the potential for three-dimensional finite element modelling to be used as a predictor of the in vitro hydrodynamic performance of tri-leaflet aortic valve implants. Several variations of tri-leaflet polymeric aortic valves were designed and manufactured, and hydrodynamic testing carried out using a pulsatile flow rig according to ISO 5840. The in silico framework was developed to closely re-create these testing regimes and several of the predicted outputs were found to correlate with bulk hydrodynamic parameters measured experimentally across each valve type. These proposed surrogate measures consider in silico GOA as a surrogate measure for in vitro EOA, in silico LCA as a surrogate measure for in vitro RF and in silico $P_{OA40\%}$ as a surrogate measure for the in vitro transvalvular ΔP . Importantly, the in silico framework used Windkessel and Bernoulli models to generate pressure-based boundary conditions for all cardiac outputs considered, and thereby remained independent of the in vitro tests (e.g. was not calibrated to them). The results of this study demonstrate that this in silico testing framework can provide insight into both the structural and hemodynamic performance of aortic valve designs, which could potentially

streamline the development process and reduce the need for trial-and-error prototyping in the early design phase.

The use of finite element modelling in the design and analysis of AVRs has been widespread (Arcidiacono et al., 2005; Burriesci et al., 2010; Claiborne et al., 2013a; Haj-Ali et al., 2008; Kim et al., 2008; Li and Sun, 2017, 2010; Serrani et al., 2016; Smuts et al., 2011). The vast majority of these studies have been limited to predictions of structural performance, generally focussing on stress optimisation of the valve leaflets to optimise their long-term durability (Claiborne et al., 2013a; Serrani et al., 2016; Smuts et al., 2011). Indeed, certain studies have suggested that predictions of GOA could be used to reflect EOA (Burriesci et al., 2010), and/or that LCA may be used to indicate RF (Claiborne et al., 2013a; Xiong et al., 2010). However, our study is the first to demonstrate the suitability of such surrogate measures by comparing in silico and in vitro performance through regression analysis across several different valve designs and over a range of cardiac outputs. At systole, there were expected increases in both GOA and EOA observed as cardiac output increased, with an r^2 value of 0.84. This strong correlation supports the use of this FE measure as a surrogate for use with tri-leaflet valves. At diastole, the proposed surrogate measure for RF was the LCA between the leaflets. Increasing the coaptation area between leaflets has previously been assumed to improve hydrodynamic performance (Claiborne et al., 2013a; Xiong et al., 2010), but has not been validated as a measurement. In our testing, we demonstrated a direct inverse relation between the RF and LCA, with increasing cardiac outputs for three separate valve designs, with an r^2 value of 0.68. This good correlation shows that maximising LCA between leaflets in FEA modelling should produce lower RF fractions in a valve. It is not however the only factor to consider for RF. At valve closure, noticeable openings in the orifice for potential backflow were particularly prominent in Valve C due to the expanded free edge profile, while still present on a smaller scale in Valve A and B. This was thought to affect the overall RF of the valves. To identify a

measure of the transvalvular ΔP , we explored the systolic opening of the three valves and measured the predicted pressure at 40% of the maximum opening area ($P_{OA40\%}$). Similar approaches for transvalvular ΔP were proposed by Burriesci et al. where two valve designs were compared using FEA and *in vitro* testing and a reduced transvalvular ΔP was found to coincide with reduced stress levels and lower opening pressures (Burriesci et al., 2010). Our reported values clearly show that the measured transvalvular ΔP values across all valves coincide with trends predicted for $P_{OA40\%}$ in all valves. This demonstrates the potential of $P_{OA40\%}$ to be used as a surrogate measure when trying to minimise transvalvular ΔP during the valve design process. Taken together, these results demonstrate the ability of FEA models to provide surrogate predictions of the bulk hydrodynamic performance of valves. However, it is important to note that the correlations presented here may not translate to other valve types/designs, and therefore it may not be possible to determine actual values from the surrogate measures. Despite this, the study should encourage the use of FEA to provide an indicator of hydrodynamic performance before needing to develop more complex FSI models or prototyping valves for experimental testing, particularly when comparing early design variations.

Both the experimental and *in silico* models provide detailed information on both structural and hydrodynamic performance for each of the three tri-leaflet valves considered. The *in vitro* hydrodynamic testing shows that all three 23 mm valves meet the minimum requirements for EOA set out by ISO 5840, which is greater than or equal to 1.25 cm^2 at 5 L/min (International Standard, 2015). Valve C consistently showed the largest EOAs at each cardiac output and the lowest levels of transvalvular ΔP at higher cardiac outputs. This performance is likely attributed to the increased insertion angle (Table 4.1) and reduced curvature of the leaflet belly, which reduces the pressure required to open the leaflet. However, Valve C showed high levels of leakage, well above the ISO 5840 requirements of less than or equal to 10% RF at 5 L/min for

a size 23 mm valve, which was also reflected in the FEA with low levels of LCA. Valves A and B both met the ISO 5840 requirement for RF. Improvements to Valve C could be made by reducing the gap between the leaflets brought about by the unique orifice profile, in an effort to reduce the high levels of RF, but otherwise Valve C performed well. While not the purpose of this study, the FEA also provided predictions of structural performance (see Figure 4.5), highlighting the stress profile across the leaflets in each valve. Noticeably higher peak stresses around the leaflet basal attachment zones were evident in Valve C, which would suggest that this area should be reinforced for greater long-term performance. In addition, the pin-wheeling effect, a diastolic deformation of the leaflets, was observed in in vitro testing and replicated in the FEA. This effect can lower the long term performance of a valve by accelerating the fatigue damage of the leaflets (Rotman et al., 2018). Together with the in silico surrogate measures proposed in this study, this in silico framework may be used in combination to provide insight into both hydrodynamic and structural performance of valve designs.

There were certain limitations in this study. Peak pressure conditions were applied for the systolic and diastolic configurations; however, a better representation would be to apply a physiological pressure profile. Previous studies that have implemented this in their models typically simplify the valve model down to isolated leaflets (Arcidiacono et al., 2005; Burriesci et al., 2010), whereas our models represented the entire 3D geometry and included the embedded wire stent. This resulted in convergence issues when using a physiological pressure profile. Another limitation was found in the experimental testing where asymmetrical opening of the leaflets was observed, whereas the FEA models opened symmetrically. This has been previously described as a disadvantage of FEA compared to FSI models (Luraghi et al., 2017), however since the results are based on the incremental changes of final valve configurations it is not necessary for the purposes of this study. It is also worth noting that while three unique valve designs were investigated, Valves A and B showed similar responses for EOA,

transvalvular ΔP and RF. Increasing the range of this study by comparing a larger cohort of valves would support the results, but was decided to be out of the scope of this study which was considered adequate as an evaluation of the surrogate measures.

4.5 Conclusions

An in silico framework has demonstrated that finite element models can predict several surrogate measures for bulk hydrodynamic performance of aortic valves. Here, in silico GOA can act as a surrogate measure for in vitro EOA, in silico LCA can act as a surrogate measure for in vitro RF, while in silico $P_{OA40\%}$ can act as a surrogate measure for the in vitro transvalvular ΔP . The results of this study demonstrate that this in silico testing framework can provide insight into both structural and hemodynamic performance of aortic valve designs, which could potentially streamline the development process of aortic valve implants. It is the first study to directly compare these in silico parameters with their in vitro counterparts through an extensive study and regression analysis, contributing to the scientific knowledge for design of aortic valves.

4.6 References

- Adams, H.S.L., Ashokkumar, S., Newcomb, A., MacIsaac, A.I., Whitbourn, R.J., Palmer, S., 2019. Contemporary review of severe aortic stenosis. *Intern. Med. J.* 49, 297–305. <https://doi.org/10.1111/imj.14071>
- Akins, C.W., Travis, B., Yoganathan, A.P., 2008. Energy loss for evaluating heart valve performance. *J. Thorac. Cardiovasc. Surg.* 136, 820–833. <https://doi.org/10.1016/j.jtcvs.2007.12.059>
- American Society for Testing and Materials, 2018. Standard Test Method for Tensile Properties of Thin Plastic Sheeting, ASTM International. ASTM D882-18, Stand. Test Method Tensile Prop. Thin Plast. Sheeting, ASTM Int. West Conshohocken, PA, 2018, www.astm.org 1–12. <https://doi.org/10.1520/D0882-18>
- Arcidiacono, G., Corvi, A., Severi, T., 2005. Functional analysis of bioprosthetic heart valves. *J. Biomech.* 38, 1483–1490. <https://doi.org/10.1016/j.jbiomech.2004.07.007>
- Baumgartner, H., Falk, V., Bax, J.J., De Bonis, M., Hamm, C., Holm, P.J., Iung, B., Lancellotti, P., Lansac, E., Muñoz, D.R., Rosenhek, R., Sjögren, J., Tornos Mas, P., Vahanian, A., Walther, T., Wendler, O., Windecker, S., Zamorano, J.L., Roffi, M., Alfieri, O., Agewall, S., Ahlsson, A., Barbato, E., Bueno, H., Collet, J.P., Coman, I.M., Czerny, M., Delgado, V., Fitzsimons, D., Folliguet, T., Gaemperli, O., Habib, G., Harringer, W., Haude, M., Hindricks, G., Katus, H.A., Knuuti, J., Kolh, P., Leclercq, C., McDonagh, T.A., Piepoli, M.F., Pierard, L.A., Ponikowski, P., Rosano, G.M.C., Ruschitzka, F., Shlyakhto, E., Simpson, I.A., Sousa-Uva, M., Stepinska, J., Tarantini, G., Tche, D., Aboyans, V., Kzhdryan, H.K., Mascherbauer, J., Samadov, F., Shumavets, V., Van Camp, G., Loncar, D., Lovric, D., Georgiou, G.M., Linhartova, K., Ihlemann, N., Abdelhamid, M., Pern, T., Turpeinen, A., Srbinovska-Kostovska, E., Cohen, A., Bakhtashvili, Z., Ince, H., Vavuranakis, M., Temesvari, A., Gudnason, T., Mylotte, D., Kuperstein, R., Indolfi, C., Pya, Y., Bajraktari, G., Kerimkulova, A., Rudzitis, A., Mizariene, V., Lebrun, F., Demarco, D.C., Oukerraj, L., Bouma, B.J., Steigen, T.K., Komar, M., De Moura Branco, L.M., Popescu, B.A., Uspenskiy, V., Foscoli, M., Jovovic, L., Simkova, I., Bunc, M., de Prada, J.A.V., Stagmo, M., Kaufmann, B.A., Mahdhaoui, A., Bozkurt, E., Nesukay, E., Brecker, S.J.D., 2017. 2017 ESC/EACTS Guidelines for the management of valvular heart disease, *European Heart Journal*. <https://doi.org/10.1093/eurheartj/ehx391>
- Baumgartner, H., Hung, J., Bermejo, J., Chambers, J.B., Evangelista, A., Griffin, B.P., Iung, B., Otto, C.M., Pellikka, P.A., Quiñones, M., 2009. Echocardiographic Assessment of Valve Stenosis: EAE/ASE Recommendations for Clinical Practice. *J. Am. Soc. Echocardiogr.* 22, 1–23. <https://doi.org/10.1016/j.echo.2008.11.029>
- Bluestein, D., Rambod, E., Gharib, M., 2000. Vortex shedding as a mechanism for free emboli formation in mechanical heart valves. *J. Biomech. Eng.* 122, 125–134. <https://doi.org/10.1115/1.429634>
- Bradley, S.M., 2013. Aortic Valve Insufficiency in the Teenager and Young Adult: The Role of Prosthetic Valve Replacement. *World J. Pediatr. Congenit. Hear. Surg.* 4, 397–402. <https://doi.org/10.1177/2150135113488781>
- Burriesci, G., Marincola, F.C., Zervides, C., 2010. Design of a novel polymeric heart valve. *J. Med. Eng. Technol.* 34, 7–22. <https://doi.org/10.3109/03091900903261241>

- Claiborne, T.E., Sheriff, J., Kuetting, M., Steinseifer, U., Slepian, M.J., Bluestein, D., 2013a. In vitro evaluation of a novel hemodynamically optimized trileaflet polymeric prosthetic heart valve. *J. Biomech. Eng.* 135, 021021. <https://doi.org/10.1115/1.4023235>
- Claiborne, T.E., Xenos, M., Sheriff, J., Chiu, W.C., Soares, J., Alemu, Y., Gupta, S., Judex, S., Slepian, M.J., Bluestein, D., 2013b. Toward optimization of a novel trileaflet polymeric prosthetic heart valve via device thrombogenicity emulation. *ASAIO J.* 59, 275–283. <https://doi.org/10.1097/MAT.0b013e31828e4d80>
- Daubert, M.A., Weissman, N.J., Hahn, R.T., Pibarot, P., Parvataneni, R., Mack, M.J., Svensson, L.G., Gopal, D., Kapadia, S., Siegel, R.J., Kodali, S.K., Szeto, W.Y., Makkar, R., Leon, M.B., Douglas, P.S., 2017. Long-Term Valve Performance of TAVR and SAVR: A Report From the PARTNER I Trial. *JACC Cardiovasc. Imaging* 10, 15–25. <https://doi.org/10.1016/j.jcmg.2016.11.004>
- Dwyer, H.A., Matthews, P.B., Azadani, A., Jaussaud, N., Ge, L., Guy, T.S., Tseng, E.E., 2009. Computational fluid dynamics simulation of transcatheter aortic valve degeneration☆☆☆. *Interact. Cardiovasc. Thorac. Surg.* 9, 301–308. <https://doi.org/10.1510/icvts.2008.200006>
- Friedewald, V.E., Bonow, R.O., Borer, J.S., Carabello, B.A., Kleine, P.P., Akins, C.W., Roberts, W.C., 2007. The Editor's Roundtable: Cardiac Valve Surgery. *Am. J. Cardiol.* 99, 1269–1278. <https://doi.org/10.1016/j.amjcard.2007.02.040>
- Garcia, D., Kadem, L., 2006. What do you mean by aortic valve area: Geometric orifice area, effective orifice area, or Gorlin area? *J. Heart Valve Dis.*
- Ge, L., Leo, H.L., Sotiropoulos, F., Yoganathan, A.P., 2005. Flow in a mechanical bileaflet heart valve at laminar and near-peak systole flow rates: CFD simulations and experiments. *J. Biomech. Eng.* 127, 782–797. <https://doi.org/10.1115/1.1993665>
- Gharaie, S.H., Morsi, Y., 2015. A novel design of a polymeric aortic valve. *Int. J. Artif. Organs* 38, 259–270. <https://doi.org/10.5301/ijao.5000413>
- Gorlin, R., Gorlin, S.G., 1951. Hydraulic formula for calculation of the area of the stenotic mitral valve, other cardiac valves, and central circulatory shunts. I. *Am. Heart J.* 41, 1–29. [https://doi.org/10.1016/0002-8703\(51\)90002-6](https://doi.org/10.1016/0002-8703(51)90002-6)
- Haj-Ali, R., Dasi, L.P., Kim, H.S., Choi, J., Leo, H.W., Yoganathan, A.P., 2008. Structural simulations of prosthetic tri-leaflet aortic heart valves. *J. Biomech.* 41, 1510–1519. <https://doi.org/10.1016/j.jbiomech.2008.02.026>
- International Organisation for Standardisation, 2021a. ISO 5840:2021 Part 1: General requirements.
- International Organisation for Standardisation, 2021b. ISO 5840:2021 Part 2: Surgically implanted heart valve substitutes.
- International Organisation for Standardisation, 2021c. ISO 5840:2021 Part 3: Heart valve substitutes implanted by transcatheter techniques.
- International Standard, 2015. Cardiovascular implants - cardiac valve prostheses. Part 2: Surgically implanted heart valve substitutes 44, 55p.
- Kandail, H.S., Trivedi, S.D., Shaikh, A.C., Bajwa, T.K., O'Hair, D.P., Jahangir, A., LaDisa,

- J.F., 2018. Impact of annular and supra-annular CoreValve deployment locations on aortic and coronary artery hemodynamics. *J. Mech. Behav. Biomed. Mater.* 86, 131–142. <https://doi.org/10.1016/j.jmbbm.2018.06.032>
- Kim, H., Lu, J., Sacks, M.S., Chandran, K.B., 2008. Dynamic simulation of bioprosthetic heart valves using a stress resultant shell model. *Ann. Biomed. Eng.* 36, 262–275. <https://doi.org/10.1007/s10439-007-9409-4>
- Kostyunin, A.E., Yuzhalin, A.E., Rezvova, M.A., Ovcharenko, E.A., Glushkova, T. V., Kutikhin, A.G., 2020. Degeneration of bioprosthetic heart valves: Update 2020. *J. Am. Heart Assoc.* 9, 1–19. <https://doi.org/10.1161/JAHA.120.018506>
- Li, K., Sun, W., 2017. Simulated transcatheter aortic valve deformation: A parametric study on the impact of leaflet geometry on valve peak stress. *Int. j. numer. method. biomed. eng.* 33, 1–14. <https://doi.org/10.1002/cnm.2814>
- Li, K., Sun, W., 2010. Simulated thin pericardial bioprosthetic valve leaflet deformation under static pressure-only loading conditions: Implications for percutaneous valves. *Ann. Biomed. Eng.* 38, 2690–2701. <https://doi.org/10.1007/s10439-010-0009-3>
- Luraghi, G., Wu, W., De Gaetano, F., Rodriguez Matas, J.F., Moggridge, G.D., Serrani, M., Stasiak, J., Costantino, M.L., Migliavacca, F., 2017. Evaluation of an aortic valve prosthesis: Fluid-structure interaction or structural simulation? *J. Biomech.* 58, 45–51. <https://doi.org/10.1016/j.jbiomech.2017.04.004>
- Manji, R.A., Menkis, A.H., Ekser, B., Cooper, D.K.C., 2012. The future of bioprosthetic heart valves. *Indian J. Med. Res.* 135, 150–151.
- Mao, W., Li, K., Sun, W., 2016. Fluid–Structure Interaction Study of Transcatheter Aortic Valve Dynamics Using Smoothed Particle Hydrodynamics. *Cardiovasc. Eng. Technol.* 7, 374–388. <https://doi.org/10.1007/s13239-016-0285-7>
- Nishimura, R.A., Otto, C.M., Bonow, R.O., Carabello, B.A., Erwin, J.P., Guyton, R.A., O’Gara, P.T., Ruiz, C.E., Skubas, N.J., Sorajja, P., Sundt, T.M., Thomas, J.D., 2014. 2014 AHA/ACC guideline for the management of patients with valvular heart disease: A report of the American college of cardiology/American heart association task force on practice guidelines. *J. Am. Coll. Cardiol.* 63. <https://doi.org/10.1016/j.jacc.2014.02.536>
- Osnabrugge, R.L.J., Mylotte, D., Head, S.J., Van Mieghem, N.M., Nkomo, V.T., Lereun, C.M., Bogers, A.J.J.C., Piazza, N., Kappetein, A.P., 2013. Aortic stenosis in the elderly: Disease prevalence and number of candidates for transcatheter aortic valve replacement: A meta-analysis and modeling study. *J. Am. Coll. Cardiol.* 62, 1002–1012. <https://doi.org/10.1016/j.jacc.2013.05.015>
- Rahmani, B., Tzamtzis, S., Ghanbari, H., Burriesci, G., Seifalian, A.M., 2012. Manufacturing and hydrodynamic assessment of a novel aortic valve made of a new nanocomposite polymer. *J. Biomech.* 45, 1205–1211. <https://doi.org/10.1016/j.jbiomech.2012.01.046>
- Rahmani, B., Tzamtzis, S., Sheridan, R., Mullen, M.J., Yap, J., Seifalian, A.M., Burriesci, G., 2017. In Vitro Hydrodynamic Assessment of a New Transcatheter Heart Valve Concept (the TRISKELE). *J. Cardiovasc. Transl. Res.* 10, 104–115. <https://doi.org/10.1007/s12265-016-9722-0>
- Rotman, O.M., Bianchi, M., Ghosh, R.P., Kovarovic, B., Bluestein, D., 2018. Principles of TAVR valve design, modelling, and testing. *Expert Rev. Med. Devices* 15, 771–791.

<https://doi.org/10.1080/17434440.2018.1536427>

- Rotman, O.M., Kovarovic, B., Chiu, W.C., Bianchi, M., Marom, G., Slepian, M.J., Bluestein, D., 2019. Novel Polymeric Valve for Transcatheter Aortic Valve Replacement Applications: In Vitro Hemodynamic Study. *Ann. Biomed. Eng.* 47, 113–125. <https://doi.org/10.1007/s10439-018-02119-7>
- Serrani, M., Brubert, J., Stasiak, J., De Gaetano, F., Zaffora, A., Costantino, M.L., Moggridge, G.D., 2016. A Computational Tool for the Microstructure Optimization of a Polymeric Heart Valve Prosthesis. *J. Biomech. Eng.* 138. <https://doi.org/10.1115/1.4033178>
- Smuts, A.N., Blaine, D.C., Scheffer, C., Weich, H., Doubell, A.F., Dellimore, K.H., 2011. Application of finite element analysis to the design of tissue leaflets for a percutaneous aortic valve. *J. Mech. Behav. Biomed. Mater.* 4, 85–98. <https://doi.org/10.1016/j.jmbbm.2010.09.009>
- Xiong, F.L., Goetz, W.A., Chong, C.K., Chua, Y.L., Pfeifer, S., Wintermantel, E., Yeo, J.H., 2010. Finite element investigation of stentless pericardial aortic valves: Relevance of leaflet geometry. *Ann. Biomed. Eng.* 38, 1908–1918. <https://doi.org/10.1007/s10439-010-9940-6>

CHAPTER 5

An In Vitro and In Silico Investigation on the Effects of Calcification on Hydrodynamic Performance of Aortic Valves

5.1 Introduction

Aortic stenosis is a valvular heart disease, whereby a narrowing of the native valve orifice leads to inadequate cardiac output and increased left ventricular hypertrophy (Adams et al., 2019). It occurs in 2.8% of adults older than 75 years of age (Eveborn et al., 2013; Stewart et al., 1997). Although aortic stenosis may develop following rheumatic heart disease or be a direct consequence of a congenital bicuspid aortic valve (Mordi and Tzemos, 2012), it most commonly arises due to calcific aortic valve disease (CAVD) (Otto et al., 1997). In CAVD, leaflet calcification is driven by native valvular interstitial cells that acquire a pro-calcific profile in response to several pathological stimuli, such as increased calcium phosphate levels or low-density lipoprotein accumulation (Sun et al., 2013). Interestingly, it has been found that the development of calcification patterns has a mechanobiological basis, with studies (Arzani and Mofrad, 2017; Fisher et al., 2013; Weinberg et al., 2009) demonstrating that calcification

follows a strain-based progression model. Calcification of the native valves is more likely to occur on the aortic side of the leaflets (Otto et al., 1997) and, due to the complex mechanical environment of the native aorta, patterns are generally non-uniform and, in some cases, are asymmetric. Thubrikar (1986) investigated over 300 explanted valves with calcifications and found that the majority of leaflets had calcification patterns that (i) occurred along the line of cusp coaptation (see Figure 5.1a) or (ii) occurred as spokes spreading inwardly from the cusp attachment point towards cusp centre (see Figure 5.1a), with a minority of cases having an indiscernible calcification pattern. Symmetric calcification has been shown to be more common in females with smaller aortic root diameters, while asymmetric calcification lends to higher levels of cumulative calcification (Piayda et al., 2021). Asymmetric calcification of the leaflet cusps can lead to suboptimal results in transcatheter aortic valve implantation (Milhorini Pio et al., 2020) such as atrioventricular block caused by high levels of calcification in the left coronary cusp requiring pacemaker implantation (Fujita et al., 2016). Figure 5.1b shows clinical imaging examples of the variations that have been observed in calcification patterns, with Figure 5.1b (i-iii) showing highly asymmetric calcifications (Larroche et al., 2020; Milhorini Pio et al., 2020; Tan et al., 2020) and Figure 5.1b (iv-vi) showing more symmetric regional calcifications (Larroche et al., 2020; Sakrana et al., 2016; Vargas et al., 2009). While it is well-known that valvular calcification such as this leads to progressive stiffening/narrowing of the aortic valve orifice, there remain distinct challenges in clinical assessment of calcification and there is limited understanding of how non-uniform and/or asymmetric calcification of valve leaflets impacts hemodynamic performance.

In a clinical setting, two separate approaches are typically used to evaluate aortic stenosis and its effect on valvular performance. Firstly, the amount of valvular calcification can be determined using computed tomography (CT) imaging. Through this approach, the severity of calcification is generally quantified by establishing an Agatston score (Agatston et al., 1990).

This metric categorises calcification by multiplying the area of a lesion by a density score that corresponds to a Hounsfield units density range, summing the total values for each lesion. While this approach quantifies the severity of stenosis and calcification, it provides little information on the nature, pattern and location of calcification (Agatston et al., 1990) or, more importantly, the actual performance of the native valve. On the other hand, clinical evaluation of aortic stenosis through Doppler echocardiography can be used to estimate the hemodynamic parameters of the valve (Baumgartner et al., 2009). This approach directly estimates information on jet velocity, mean transaortic pressure gradient and the valve area determined by the continuity equation. Evaluation of the aortic valve area (AVA) by this method allows for aortic stenosis quantification as mild ($AVA \geq 1.5 \text{ cm}^2$), moderate ($1.0 \text{ cm}^2 \leq AVA < 1.5 \text{ cm}^2$), or severe ($AVA < 1.0 \text{ cm}^2$). Additional parameters of transvalvular ΔP and jet velocity have respective cut-off values defining severe aortic stenosis of 40/50 mmHg and 4 m/s (Baumgartner et al., 2009). Even though this approach is occasionally combined with the Agatston score, the latter is a bulk measure of calcification and there remains a lack of understanding of the relationship between specific features of aortic stenosis, the progression of calcification, and overall hemodynamic performance of the native valve.

Interestingly, valve calcification is not only limited to native valves, but can also create distinct problems for bioprosthetic aortic valve replacements (AVRs) (Capodanno et al., 2017; Dvir et al., 2018; Head et al., 2017; Kostyunin et al., 2020). When testing valves in vitro, hydrodynamic assessment using pulsatile flow bench test systems simulate physiological conditions and are used to assess valve hemodynamic performance. ISO 5840 defines acceptable values for key performance parameters of EOA and RF for a valve operating at normotensive conditions at a range of orifice sizes. Many comprehensive studies comparing these parameters across valve designs have been carried out on commercial flow rigs (Rahmani et al., 2017; Rotman et al., 2019). With respect to calcification, several studies have examined

the effects of calcification on a valve's hydrodynamic performance through in vitro tests (Barannyk et al., 2017; Falahatpisheh et al., 2017), all of which found a negative impact on the hydrodynamic parameters of the valve. Typically, these studies induce calcification in a valve by means of a calcifying solution (Boloori Zadeh et al., 2014) where the valve is uniformly and progressively calcified in accelerated wear testing, while being removed for hydrodynamic testing at various intervals. Meanwhile, other studies examined the effects of crimping in TAVR devices by using calcifying solution on valves post crimp (Zareian et al., 2019). While finite element analysis (FEA) is commonly used to perform structural and fatigue analysis of the native aortic valve and AVRs (Arcidiacono et al., 2005; Burriesci et al., 2010; Claiborne et al., 2013; Haj-Ali et al., 2008; Kim et al., 2008; Li and Sun, 2017, 2010; Serrani et al., 2016; Smuts et al., 2011), very few studies have been conducted to understand the role of calcification on either structural or hemodynamic performance of aortic valves. Halevi et al. (2015) have provided some of the most relevant information by relating the effects of leaflet calcification on the resulting systolic opening area and maximum resulting strains through both in vivo imaging and FEA. Computational studies that have considered calcification patterns have largely been focussed on using clinical calcification data to evaluate the impact of calcification on TAVR implantation (Dimasi et al., 2015; Finotello et al., 2017; McGee et al., 2019; Sturla et al., 2016). Few studies have investigated the effects of non-uniform calcification pattern development on hemodynamic performance of *either* native or bioprosthetic valves. However, the in silico surrogate framework developed in Chapter 4 provides a suitable framework to provide further insight into the effect of asymmetric and regional calcification on hydrodynamic performance.

The objective of this study is to investigate the role of non-uniform and asymmetric aortic stiffening on valvular performance using both in vitro testing and in silico modelling. This approach seeks to provide insight into the role of calcification on native aortic valve

performance by making use of a tri-leaflet polymer valve as a model for the native aortic valve. Various stiffened patterns are introduced on the aortic valves by applying cyanoacrylate to represent calcified regions. To establish stiffening patterns to be applied, a strain-based in silico calcification progression model was developed in FEA based on the work of Arzani and Mofrad (2017). For the in vitro testing, polymer valves were stiffened in several stages according to the desired calcification pattern and the resulting hydrodynamic performance characterised. The results of the in vitro experiment were used to verify the behaviour of an in silico model of the calcified valve leaflets and correlate decreasing hydrodynamic parameters with surrogate FEA measures, developed in Chapter 4. Using this approach, several different scenarios of calcification locations were investigated and their predicted effect on hydrodynamic performance evaluated, providing novel insight into the effect of calcification on aortic valve performance.

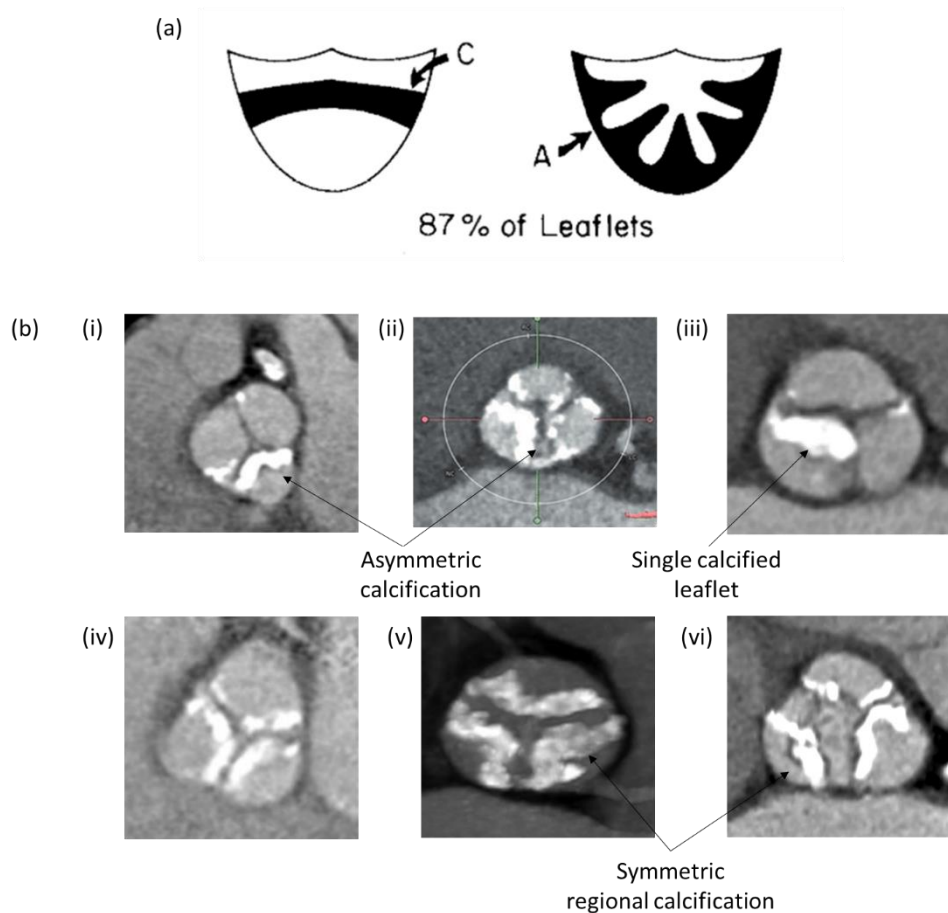


Figure 5.1 (a) diagram from Thubrikar et al. (1986) describing the calcification patterns present in 87% of explanted leaflets, where C is the line of cusp coaptation and A is the cusp attachment points and (b) planar images of aortic calcification, with several in vivo examples of asymmetric calcification (i-iii) and symmetric and regional calcification (iv-vi). Adapted from (i) Larroche et al. (2020) (ii) Milhorini et al. (2020) (iii) Tan et al. (2020) (iv) Larroche et al. (2020) (v) Sakrana et al. (2016) and (vi) Vargas et al. (2009)

5.2 Materials and Methods

5.2.1 Valve Design and Manufacture

To investigate the role of calcification on aortic valve performance, several polymeric surgical aortic valve prostheses were designed and manufactured from a synthetic polyurethane elastomer variant, developed at the University of Galway. The manufacturing process was similar to Chapter 4 and used the design of Valve B, described in Chapter 4, which featured a common tri-leaflet design with an internal orifice diameter of 23 mm (± 0.2 mm). This valve also had an embedded steel wire frame to provide radial reinforcement, and a skirt/suture ring

around the basal circumference to enable mounting during in vitro testing, as shown in Figure 5.2a. The manufactured valve was tested without calcification as a control for the in vitro testing. The valve was also tested using an in vitro stiffened model, whereby cyanocrylate was applied to the valve according to a range of different patterns that were determined computationally.

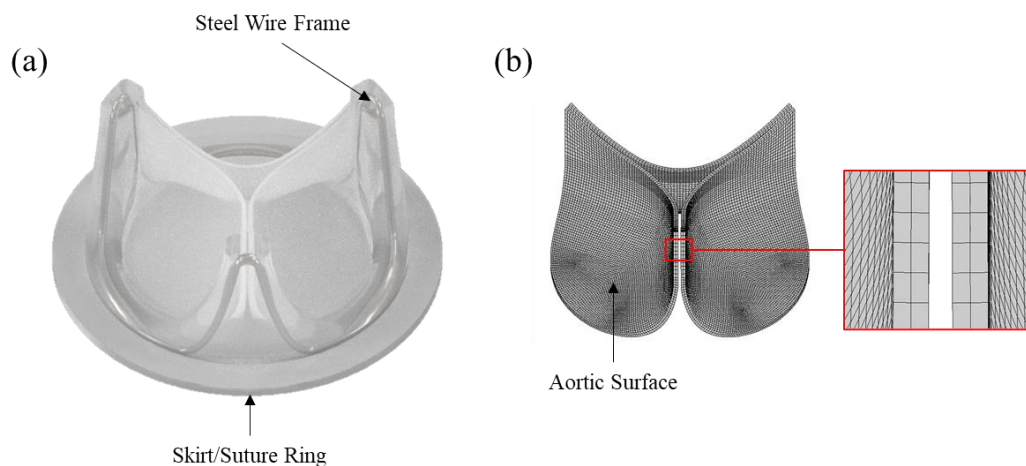


Figure 5.2 (a) 3D rendering of Tricuspid Valve Design. (b) Finite element Generated Mesh

5.2.2 In Silico Model of Calcification Progression

The calcification patterns considered in both the in vitro testing and subsequent in silico models were based on a strain-based calcification progression model, developed using a three-dimensional finite element model in Abaqus/Standard finite element code (Abaqus 2017, Simulia, RI, USA). This model considered only the valve leaflets, as shown in Figure 5.2b, which were discretised with ~5,000 8-noded brick, reduced integration elements (CD38R), having 2 elements across the leaflet thickness of 0.3 mm. For the strain-based calcification progression model, the leaflets were assumed to be linear elastic with a Young's Modulus of 3.8 MPa (based on the secant modulus to the linear region of the stress-strain response, as previously characterised in Chapter 4), with a Poisson's ratio of 0.45. A user-defined field (USDFLD) subroutine was written in FORTRAN to capture the development of calcification

throughout the leaflets, based on the peak strains experienced during systolic and diastolic pressure loads. The algorithm was applied to the top layer of aortic surface elements only, based on the observation that calcification occurs mainly on the aortic surface of the leaflets (Otto et al., 1994; Weinberg et al., 2010; Yip and Simmons, 2011). A full simulation cycle included a diastolic pressure of 100 mmHg, followed by a systolic pressure of 35 mmHg. The nodes at the fixed edges of the leaflets, which would be connected to the stent frame, were constrained in all directions, while diastolic and systolic pressure differences were applied to the aortic and ventricular surfaces of the leaflet. The peak strains experienced by the valve were recorded for each element and a strain threshold of 8.5% was used to initiate stiffening of the valve (Fisher et al., 2013). Any elements where the max strain surpassed this threshold were stiffened by increasing the Young's Modulus to 1 GPa, which was previously used by Halevi et al. (2015). By repeating the simulation over 50 cycles, the stiffened pattern was generated and used as a basis for subsequent in vitro tests and in silico modelling of calcified valves. The resulting patterns, shown in Figure 5.3 agreed qualitatively to those observed in Thubrikar's study (see Figure 5.1). In referring to the patterns, these are classified according to the percentage coverage as Mild (<15%), Moderate (> 15 and < 30%) and Severe (>30%).

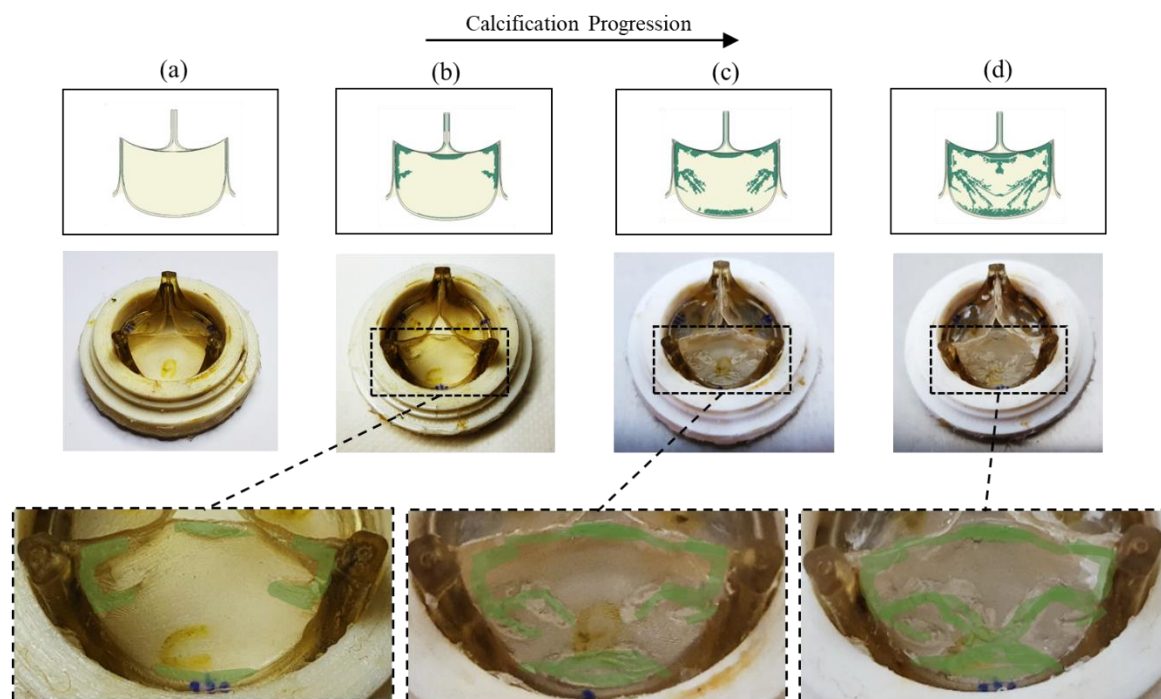


Figure 5.3 Application of the Generated Stiffening Pattern from the In Silico Model for the In Vitro Experiment for (a) 0%, (b) Mild (9%), (c) Moderate (24%) and (d) Severe (38%) coverage

5.2.3 In Vitro Testing of Stiffened Valve Hydrodynamics

To evaluate the hydrodynamic performance of a progressively stiffening valve, in vitro bench testing was performed using a Vivitro Pulse Duplicator (Vivitro Labs, Inc. Victoria, B.C.) according to ISO 5840. Three stages of stiffening, measured by percentage coverage (%) of the leaflets, were taken from the in silico generated calcification pattern shown in Figure 5.3. Calcification coverage of 9%, 24% and 38% leaflet area was tested. Following the control experiment, the valve was removed from the rig and dried. The in vitro stiffened model used cyanoacrylate to induce stiffening of the leaflets by direct application of cyanoacrylate to the aortic side of the leaflets under a microscope. Care was taken to apply each stage calculated from the in silico calcified model, as shown in Figure 5.3. Once the cyanoacrylate had cured,

the valve was returned to the flow rig and tested under the same beats per minute, stroke volume and mean aortic pressure (MAP) conditions.

Similar to Chapter 4, in vitro testing consisted of the valves being sealed in a mounting ring and placed in the aortic position between the ventricular sac and aorta of the flow rig. This flow rig reproduced cardiac pulsatile flow by compressing the ventricular sac, ejecting fluid through the aortic valve according to assigned stroke volume, systolic waveform and heart rate. Pressure transducers recorded the aortic, ventricular and atrial pressures, while a flow probe positioned directly below the valve took flow measurements during each cycle. The valves were tested in 0.9% NaCl solution at room temperature (≈ 20 °C). High-speed images were captured using a Sony RX100 Mark IV camera (Figure 5.4a) at a frame rate of 1000 fps to visualise open and closing configurations of valves during testing. Vivitest software (Vivitro Labs, Inc. Victoria, B.C.) recorded pressure and flow measurements over 10 consecutive cycles, which were used to calculate several hydrodynamic parameters, namely the effective orifice area (EOA) (Equation 4.1), regurgitant fraction (RF) (Equation 4.2) and transvalvular pressure drop (ΔP). The transvalvular ΔP refers to the pressure gradient across the valve during systole, shown in Figure 5.4b. To study the effects of calcification progression, the valve was first tested in its control state of no calcification with normotensive conditions of 70 bpm, 70 mL stroke volume and 100 mmHg MAP.

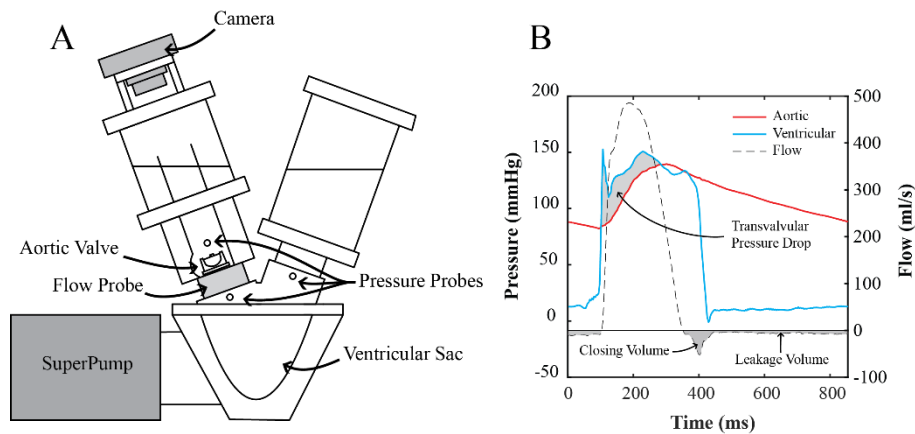


Figure 5.4 (a) Schematic of Vivitro Left Heart Simulator with pressure transducers and a flow probe which was used to carry out in vitro hydrodynamic testing, (b) a typical diagram of average flow measurements, aortic and ventricular pressures measured over 10 cardiac cycles

5.2.4 In Silico Performance of Stiffened Valve

5.2.4.1 Comparison of In Vitro and In Silico GOA

To create a comparable simulation to the in vitro experiments, the pattern generated by the calcification algorithm was exported to a new finite element model. In this case, each stage of calcification was independently modelled by creating an offset layer of elements on top of the leaflet surface, as shown in Figure 5.3. This offset layer was assigned a thickness of 0.15 mm, a Young's modulus of 1 GPa and Poisson's ratio of 0.45, to represent the stiffened region. Separate simulations for diastolic and systolic pressure conditions were investigated with increasing calcification coverage. A diastolic pressure of 100 mmHg was applied to the aortic side of the leaflets, corresponding to the MAP of 100 mmHg applied during the experimental in vitro testing. A systolic pressure of 35 mmHg was applied to the ventricular side. During the systolic configuration, the maximum GOA of the valve was recorded. To ensure the validity of this finite element approach, prior to investigating different calcification scenarios, the GOA of the in silico model with three calcified leaflets and increasing calcification coverage was compared with the in vitro GOA, shown later in Figure 5.8.

5.2.4.2 Symmetric, Asymmetric and Regional Calcification Patterns

Following the verification of the *in silico* calcification model, the effects of asymmetric and symmetric leaflet cusp calcification and regional calcification on overall hydrodynamic performance were examined. Asymmetric calcification was modelled by isolating calcification to a single leaflet (Valve I) and across two leaflets (Valve II), while three leaflet calcification (Valve III) was symmetrically calcified across all three leaflets. These scenarios are represented in Figure 5.5. Furthermore, the effects of regional based calcification on hydrodynamic performance are examined for Valve-III, estimated through the surrogate measures of LCA, GOA and the pressure required to open the valve to 40% ($\Delta P_{OA40\%}$). These measurements were investigated in Chapter 4 as suitable surrogate measures of *in vitro* measured RF, EOA and transvalvular ΔP respectively. *In silico* diastolic GOA was also investigated.

In Valve III-Upper, the calcification was isolated to the upper portion of the leaflet cusps. Valve III-Lower had calcification confined to the lower portion of the leaflet cusps. Valve III-Centre had the calcification confined to the middle or central region of the leaflet cusps, while Valve III-Sides had calcification isolated to the sides of the leaflet cusps. Each scenario is shown in Figure 5.5.

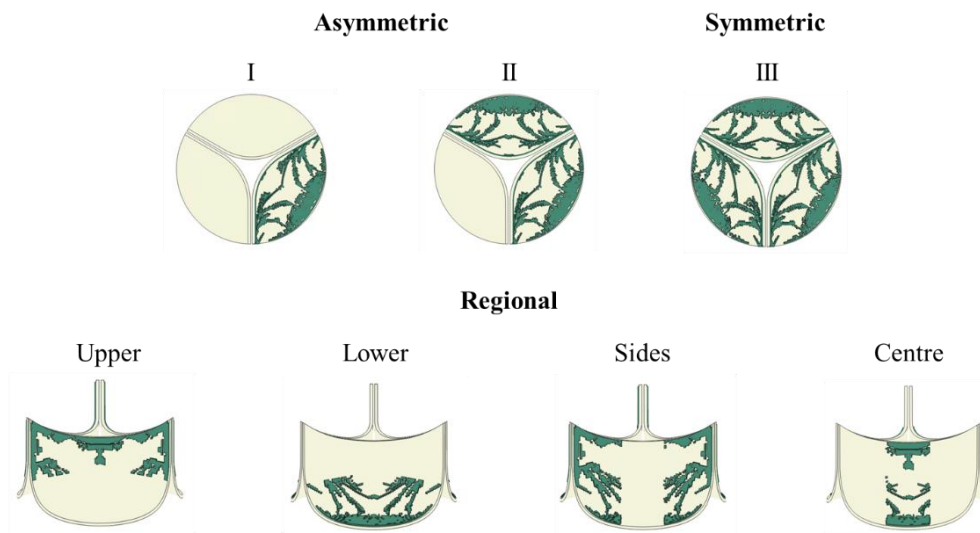


Figure 5.5 (Top-left) Asymmetric Calcification on Valve I (single leaflet) and Valve II (two leaflets), (Top-right) Symmetric calcification on Valve III (three uniformly calcified leaflets) (Bottom) Regional Calcification confined to the upper, lower, sides and centre regions of the valve cusps

5.3 Results

5.3.1 In Vitro Testing

In vitro hydrodynamic testing of Valve III was carried out for mild (9%), moderate (24%) and severe (38%) symmetric calcification patterns. The transvalvular pressure profiles with increasing calcification coverage, along with the aortic, ventricular pressure and flow profiles are shown in Figure 5.6. The mean values of EOA, RF and transvalvular ΔP are shown in Figure 5.7, with standard deviation represented by error bars (each valve tested over 10 cycles). The EOA decreased in each valve with increasing calcification, with an EOA of 1.26 cm^2 at 0% coverage decreasing to 0.7 cm^2 at 38% calcification coverage. The RF was higher with increasing calcification coverage, with RF being only 3.5% at 0% coverage, increasing to 19% for severe (38%) coverage. The transvalvular ΔP increased in the valve with increasing calcification, with the minimum transvalvular ΔP measuring at 19 mmHg at 0% coverage, rising to a peak of 60 mmHg at severe (38%) coverage.

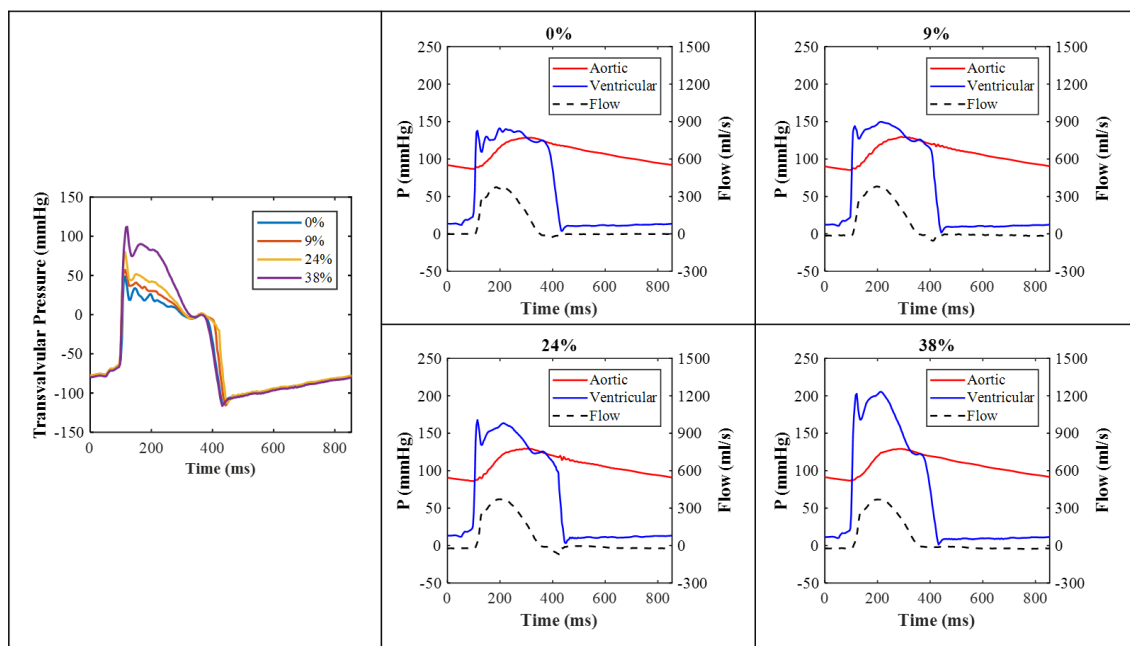


Figure 5.6 (left) *In vitro* hydrodynamic transvalvular pressure profiles with increasing calcification coverage (right) *In vitro* hydrodynamic aortic and ventricular pressure (mmHg) and flow profiles (mL/s) with increasing calcification coverage (%)

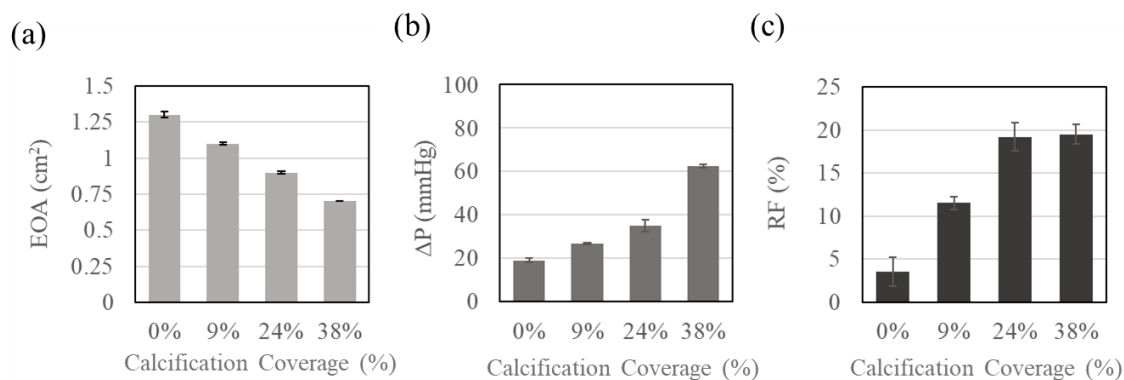


Figure 5.7 *In vitro* hydrodynamic parameters according to ISO 5840 of EOA, transvalvular pressure drop (ΔP), and RF, were measured for the tri-leaflet calcified valve (Valve III) with increasing calcification coverage. Data is represented as the mean \pm SD, $n = 10$ (valve tested over 10 cycles), (a) EOA with increasing calcification coverage. (b) Transvalvular ΔP with increasing calcification coverage. (c) RF with increasing calcification coverage.

5.3.2 In Silico Analysis

5.3.2.1 Model Verification

In vitro and in silico deformations of Valve III with increasing calcification coverage during systole and diastole are shown in Figure 5.8. In diastole, the FEA simulations predicted the increasing diastolic GOA, agreeing with the in vitro results. However, the in vitro test exhibited a pin-wheeling effect and crimp of the leaflets due to the calcification, which was not present in the FEA simulation. At systole, the in vitro experiment exhibited asymmetrical opening, with a gradual decrease in systolic GOA as calcification increased. For both mild (9%) and moderate (24%) calcification scenarios, the FEA simulations exhibited symmetric opening of the leaflets, but predicted similar GOAs to those measured experimentally. For the severe calcification pattern, the in silico model predicted a greater reduction in GOA compared to the experiments.

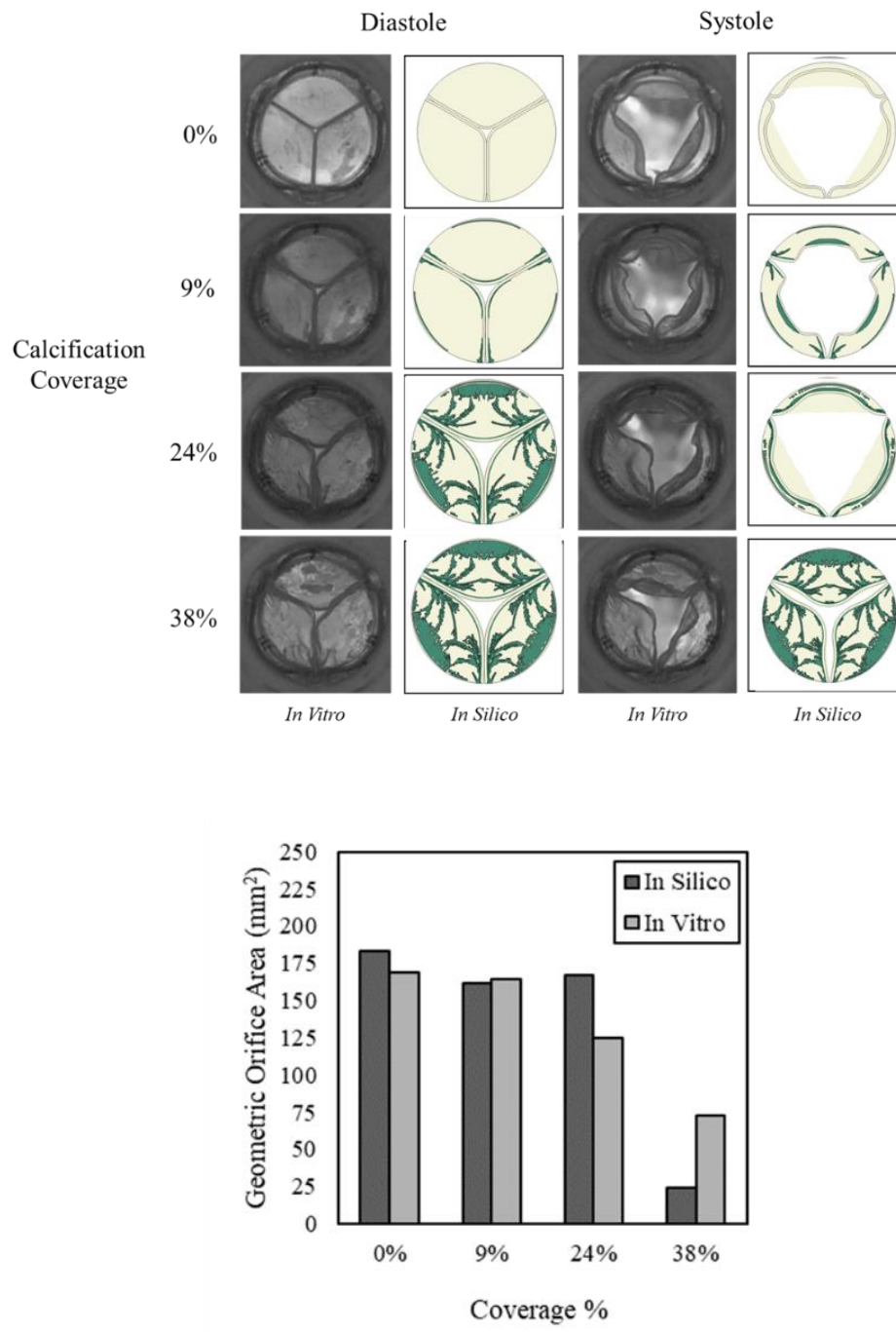


Figure 5.8 (Top) Validation of GOA of In Silico and In Vitro Experiments for the Tri-Leaflet Stiffened Valve, (bottom) The diastolic and systolic positions of the tri-leaflet stiffened aortic valve (III) were captured and viewed from the outflow (aortic) side of the valve. The in vitro hydrodynamic condition, as viewed from the outflow tract, compared to the corresponding in silico valve finite element simulation.

5.3.2.2 Asymmetric and Symmetric Calcification

The effects of asymmetric (Valve I and II) and symmetric calcification (Valve III) from the in silico model are described here, with the predicted values of systolic GOA with increasing calcification shown in Figure 5.9a. At systole, the GOA for the single, bi-leaflet and tri-leaflet stiffened valves (Valve I, Valve II and Valve III) decreased as calcification progressed. The greatest reduction in systolic GOA was in Valve III for the severe case, where stiffening was present in all the leaflets, decreasing from 170 mm² at 0% coverage to 20 mm² for severe stiffening (38% coverage). However, the mild and moderate cases of symmetric stiffening in Valve III showed much smaller reductions in GOA. Contrastingly, for asymmetric stiffening of both Valves I and II, there were more substantial reductions in GOA when compared at the same percentage coverage compared to the symmetric case (Valve III). For example, severe asymmetric coverage of two leaflet cusps in Valve II led to a substantial reduction in systolic GOA, reducing from 183 mm² at 0% coverage to 76 mm², which corresponded to 26% overall coverage. At the same percentage coverage, the symmetric case had a GOA of 168 mm². This indicates that severe asymmetric calcification of one or two leaflets can be more detrimental than more moderate calcification of all three leaflets for systolic GOA. The in silico model predicted values of diastolic GOA with increasing calcification are shown in Figure 5.9b. In diastole, the GOA for Valve I, Valve II and Valve III increased as calcification progressed. However, in this case, symmetric calcification was more detrimental to GOA than asymmetric, with diastolic GOA showing greater relative increases for Valve-III, rising to 10 mm² at 38% coverage but being consistently higher than Valve-I and II when similar coverage was present. The predicted values of in silico LCA with increasing calcification are shown in Figure 5.9c. For both the asymmetric and symmetrically calcified valves, the LCA decreased as calcification progressed. The greatest decrease was seen in Valve III, where the LCA reduced from 50 mm² to 20 mm² for the severe case (38% coverage). The smallest reduction was seen

in Valve I, which decreased to 42 mm² at 12% coverage. The predicted values of in silico pressure required to achieve 40% of the maximum opening area of the valve ($P_{OA40\%}$) with increasing calcification from the in silico model is shown in Figure 5.9d. The $P_{OA40\%}$ was greatest in the symmetrically-calcified Valve III, requiring a maximum pressure of 40mmHg, The $P_{OA40\%}$ was lowest in asymmetrically calcified Valve I at a peak of 13 mmHg at 12% coverage. These findings indicate that asymmetric calcification is not as detrimental to transvalvular pressure, compared to symmetric calcification.

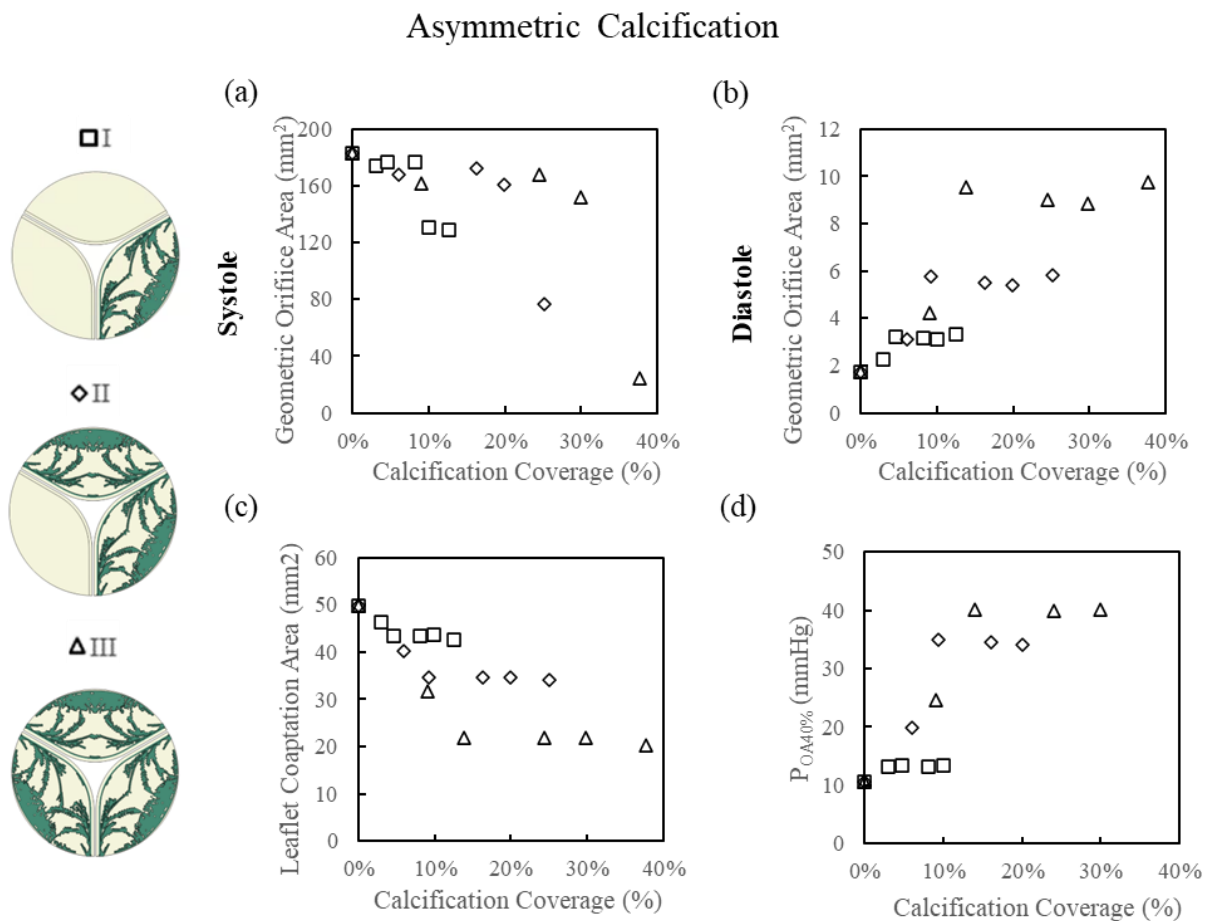


Figure 5.9 Effects of asymmetric calcification with increasing coverage for (a) Systolic Geometric Orifice Area, (b) Diastolic Geometric Orifice Area, (c) Leaflet Coaptation Area, (d) Pressure required to open the valve to 40%

5.3.2.3 Regional Calcification

The effect of regional calcification progression on systolic GOA is shown in Figure 5.10a. Valve III-Upper, III-Lower, III-Sides and III-Centre all predicted only a slight drop in systolic GOA, even for severe calcification cases, indicating that the regional cases examined had little effect on systolic GOA. On the other hand, the predicted values of diastolic GOA with increasing calcification coverage are shown in Figure 5.10b and substantial differences were seen. In particular, stiffening in the upper (Valve III-Upper) and side regions (Valve III-Sides) resulted in substantial increases in diastolic GOA, indicating that these configurations lead to incomplete valve closure at diastole, i.e. aortic regurgitation or back flow predicted to occur. The predicted values of in silico LCA with increasing calcification are shown in Figure 5.10c. These results aligned with the diastolic GOA trends, whereby the upper (Valve III-Upper) and side (Valve III-Sides) stiffened cases showed the lowest LCA values, again indicating incomplete closure of valves. In particular, Valve III-Upper saw the greatest drop in LCA with increasing calcification, reducing to 21 mm² at 15% coverage, while Valve III-Sides reduced to 30 mm² at 20% coverage. Finally, the predicted values of in silico pressure required to achieve 40% of the maximum opening area of the valve ($P_{OA40\%}$) with increasing calcification from the in silico model is shown in Figure 5.10d. Here, stiffening in both the upper (Valve III-Upper) and centre (Valve III-Centre) regions had little effect on the opening pressure required. Contrastingly, peak values of 39 mmHg for both Valve III-Lower and III-Sides respectively were required to open these valves in the most severe cases. These findings indicate the regional calcification could substantially influence transvalvular pressure for valves. A comparison of peak opening across all the calcification configurations is shown in Figure 5.11.

Regional Calcification

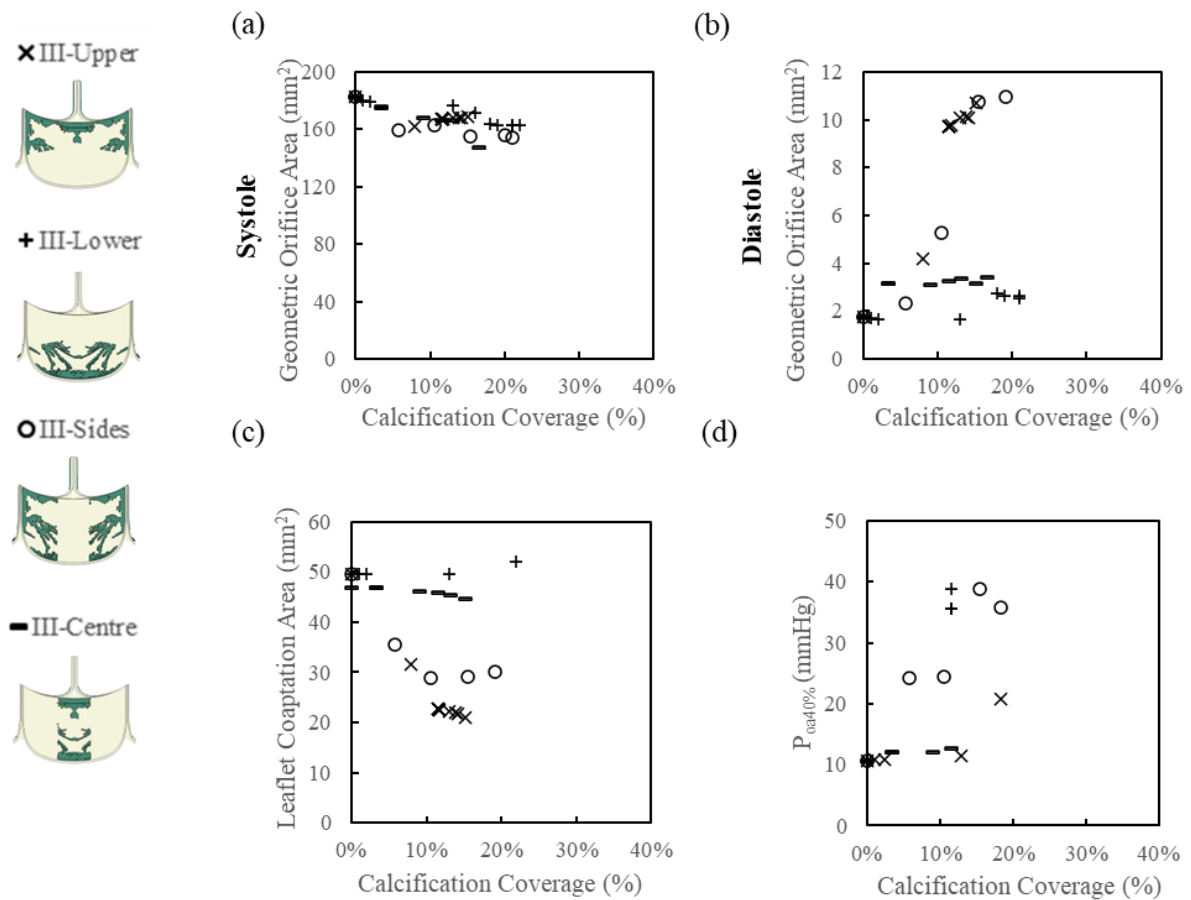


Figure 5.10 Effects of regional calcification for (a) Systolic Geometric Orifice Area, (b) Diastolic Geometric Orifice Area, (c) Leaflet Coaptation Area, (d) Pressure required to open the valve to 40%

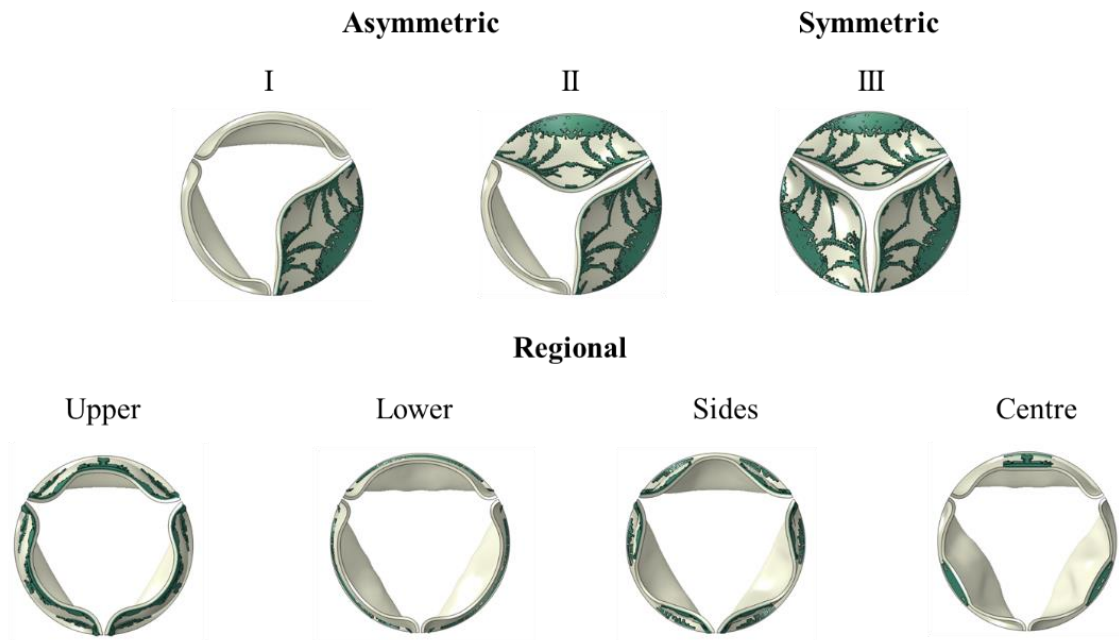


Figure 5.11 Deformation of each valve with peak calcification coverage at peak opening time.

5.4 Discussion

Through in vitro and in silico testing, this chapter used three-dimensional FEA to gain a greater understanding of the role of asymmetric and regional stiffening on the hydrodynamic performance of the aortic valve. This study makes use of a tri-leaflet polymer valve as a model for the native aortic valve. Hydrodynamic testing of progressively stiffened valves was carried out using a pulsatile flow rig according to ISO 5840, while an in silico framework was also developed to examine the effects of different calcification scenarios on potential hydrodynamic performance. There were several key findings from the study. In considering asymmetric calcification, it was observed that the more asymmetric the calcification coverage, the more detrimental this was to valve systolic GOA. In contrast however, symmetric calcification was actually more detrimental to transvalvular pressure, diastolic GOA and LCA, than asymmetric patterns. When considering regional based calcification, it was observed that stiffening

confined to the upper and side regions of the valves (Valve's III-Sides and III-Upper) impacted valve closure more significantly than stiffening confined to the centre and lower regions of the valve cusps. The results of this study demonstrate that this *in silico* testing framework can provide insight into the effects of calcification or stiffening on the hydrodynamic performance of native or prosthetic aortic valves.

While previous computational studies have investigated the effects of calcification on native aortic valve biomechanics, these have largely been focused on the role of calcification and its impact on TAVR deployment (Dimasi et al., 2015; McGee et al., 2019). For example, asymmetric calcification has been shown to impact TAVR implantation by creating atrioventricular nodal block by large levels of calcification on the coronary cusp (Fujita et al., 2016), which can result in the need for permanent pacemaker implantation. However, this study is one of the first to investigate the impact of different calcification patterns on the hydrodynamic performance of a tri-leaflet aortic valve, which has significance for native aortic valve biomechanics. These results clearly demonstrated that hydrodynamic performance is negatively impacted with increasing calcification for all scenarios considered. It was found that asymmetric calcification leading to greater reductions in systolic GOA, compared to symmetric calcification. In these asymmetric cases, calcification was more concentrated on either one or two leaflets, which could become quite severe and almost completely disable these leaflet(s) from opening during systole. Interestingly, when calcification was confined to one or two leaflets, it had a more severe impact on the overall GOA of a valve, when compared to similar coverage across three leaflets. On the other hand, symmetric calcification was the more detrimental to diastolic valve performance than asymmetric calcification, when diastolic GOA, LCA and valve opening pressure required were considered. While LCA reduced for all calcification cases considered, the symmetrically calcified Valve III saw the largest reduction in LCA, while the asymmetrically calcified Valve I saw the least degeneration. In these

scenarios, it appears that the non-calcified leaflets would conform to the disabled leaflets, resulting in smaller LCA decreases with asymmetric stiffening. The pressure required to open the valve saw the greatest increases in the symmetrically calcified Valve III, indicating that symmetric stiffening could be a more detrimental factor to transvalvular ΔP than asymmetric stiffening.

As Thubrikar et al. (1986) had identified the presence of various calcification patterns in the aortic valve, this Chapter also examined the effect of regional calcification across individual leaflets, with various patterns examined covering the valve cusps, the top (III-Upper), bottom (III-Lower), middle (III-Middle) and sides (III-Sides). Interestingly, these regional cases examined had very little effect on the systolic GOA. Diastolic GOA was most affected by upper and side leaflet cusp calcification. The GOA was also measured at peak diastole to examine the impact of increasing calcification coverage on the small orifices present at the centre and sides of the leaflets during diastole. As calcification increased, these orifices increased in size, which could, in turn, contribute to a larger RF upon valve closure. When the calcification was isolated to the lower region of the leaflet, there was a reduction in the GOA at diastole, indicating that when located in this area, closure of the leaflets was improved compared to calcification isolated to the upper and side regions. When calcification was confined to the upper and side regions of the leaflet cusp, the LCA reduced to similar levels as that of Valve III, however at a much lower calcification coverage % of the leaflet. This indicates that upper and side regional calcification of leaflet cusps was more significant than middle and lower regional calcification on valve closure and coaptation. Interestingly, when considering the pressure required to open the valve, calcification at the side of the leaflet cusps had a significant impact, but upper regional calcification did not, perhaps as this region was close to the free edge of the leaflet. Instead, the lower portion of the valve leaflets contributed to increased

pressures, indicating that this would generate a larger transvalvular ΔP for valve hydrodynamics.

Clinically, Doppler echocardiography and quantitative measurements such as the Agatston score have been relied on to describe the severity of aortic stenosis and levels of calcification (Baumgartner et al., 2017). What these methods do not focus on, or evaluate, is the effect of actual calcification location and patterns on the resulting valve performance. The measurements taken in this study for in silico measured parameters allow us to investigate which calcification locations and patterns are more detrimental to the hydrodynamic performance. It was found that calcification confined to the lower and side portions of the valve leaflets would lead to increased transvalvular ΔP . Calcification confined to the top and sides of the leaflet cusps impacted the LCA, comparatively to the symmetric Valve III, while symmetric calcification throughout each cusp was more detrimental to valve GOA than asymmetric calcification. Collectively, these results demonstrate the ability of FEA to investigate the impact of calcification growth on hydrodynamic performance in the aortic valve.

This study was limited in that the calcification patterns and isolated scenarios were based on an in silico generated calcification model. The algorithm could be improved by incorporating a non-uniform thickness of calcification or varying the stiffness of the calcification throughout the cusps. Or to further this study, the methods shown could be investigated on patterns and calcification locations derived from patient specific data. In addition, the valve examined in the in vitro pulsatile flow rig is a polymer surgical aortic valve, as opposed to a bioprosthesis or native valve. Since the geometry closely resembles that of the native valve being a tri-leaflet with semi-lunar cusps, and bulk parameters are being measured, the methods shown here directly relate to the native valve and the study should not be considered to only apply to a polymer valve replacement.

5.5 Conclusion

An in silico framework has demonstrated the ability of finite element modelling to investigate the effects of increasing calcification on the degeneration of hydrodynamic performance of the aortic valve. In silico surrogate measures were used to inform bulk hydrodynamic parameters, while specific calcification scenarios were investigated. The results showed that different forms of calcification, asymmetric or symmetric, or regional calcification locations can have very different impacts on the in silico measured parameters and the indicated in vitro hydrodynamic performance. It was found that asymmetric calcification was detrimental to valve systolic GOA. In contrast however, symmetric calcification was detrimental to transvalvular pressure, diastolic GOA and LCA. When considering regional based calcification, it was observed that stiffening confined to the upper and side regions of the valves (Valve's III-Sides and III-Upper) impacted valve closure more significantly than stiffening confined to the centre and lower regions of the valve cusps.

5.6 References

- Adams, H.S.L., Ashokkumar, S., Newcomb, A., MacIsaac, A.I., Whitbourn, R.J., Palmer, S., 2019. Contemporary review of severe aortic stenosis. *Intern. Med. J.* 49, 297–305. <https://doi.org/10.1111/imj.14071>
- Agatston, A.S., Janowitz, W.R., Hildner, F.J., Zusmer, N.R., Viamonte, M., Detrano, R., 1990. Quantification of coronary artery calcium using ultrafast computed tomography. *J. Am. Coll. Cardiol.* 15, 827–832. [https://doi.org/10.1016/0735-1097\(90\)90282-T](https://doi.org/10.1016/0735-1097(90)90282-T)
- Arcidiacono, G., Corvi, A., Severi, T., 2005. Functional analysis of bioprosthetic heart valves. *J. Biomech.* 38, 1483–1490. <https://doi.org/10.1016/j.jbiomech.2004.07.007>
- Arzani, A., Mofrad, M.R.K., 2017. A strain-based finite element model for calcification progression in aortic valves. *J. Biomech.* 65, 216–220. <https://doi.org/10.1016/j.jbiomech.2017.10.014>
- Barannyk, O., Fraser, R., Oshkai, P., 2017. A correlation between long-term in vitro dynamic calcification and abnormal flow patterns past bioprosthetic heart valves. *J. Biol. Phys.* 43, 279–296. <https://doi.org/10.1007/s10867-017-9452-9>
- Baumgartner, H., Falk, V., Bax, J.J., De Bonis, M., Hamm, C., Holm, P.J., Iung, B., Lancellotti, P., Lansac, E., Muñoz, D.R., Rosenhek, R., Sjögren, J., Tornos Mas, P., Vahanian, A., Walther, T., Wendler, O., Windecker, S., Zamorano, J.L., Roffi, M., Alfieri, O., Agewall, S., Ahlsson, A., Barbato, E., Bueno, H., Collet, J.P., Coman, I.M., Czerny, M., Delgado, V., Fitzsimons, D., Folliguet, T., Gaemperli, O., Habib, G., Harringer, W., Haude, M., Hindricks, G., Katus, H.A., Knuuti, J., Kolh, P., Leclercq, C., McDonagh, T.A., Piepoli, M.F., Pierard, L.A., Ponikowski, P., Rosano, G.M.C., Ruschitzka, F., Shlyakhto, E., Simpson, I.A., Sousa-Uva, M., Stepinska, J., Tarantini, G., Tche, D., Aboyans, V., Kzhdryan, H.K., Mascherbauer, J., Samadov, F., Shumavets, V., Van Camp, G., Loncar, D., Lovric, D., Georgiou, G.M., Linhartova, K., Ihlemann, N., Abdelhamid, M., Pern, T., Turpeinen, A., Srbinovska-Kostovska, E., Cohen, A., Bakhutashvili, Z., Ince, H., Vavuranakis, M., Temesvari, A., Gudnason, T., Mylotte, D., Kuperstein, R., Indolfi, C., Pya, Y., Bajraktari, G., Kerimkulova, A., Rudzitis, A., Mizariene, V., Lebrun, F., Demarco, D.C., Oukerraj, L., Bouma, B.J., Steigen, T.K., Komar, M., De Moura Branco, L.M., Popescu, B.A., Uspenskiy, V., Foscoli, M., Jovovic, L., Simkova, I., Bunc, M., de Prada, J.A.V., Stagmo, M., Kaufmann, B.A., Mahdhaoui, A., Bozkurt, E., Nesukay, E., Brecker, S.J.D., 2017. 2017 ESC/EACTS Guidelines for the management of valvular heart disease, *European Heart Journal*. <https://doi.org/10.1093/eurheartj/ehx391>
- Baumgartner, H., Hung, J., Bermejo, J., Chambers, J.B., Evangelista, A., Griffin, B.P., Iung, B., Otto, C.M., Pellikka, P.A., Quiñones, M., 2009. Echocardiographic Assessment of Valve Stenosis: EAE/ASE Recommendations for Clinical Practice. *J. Am. Soc. Echocardiogr.* 22, 1–23. <https://doi.org/10.1016/j.echo.2008.11.029>
- Boloori Zadeh, P., Corbett, S.C., Nayeb-Hashemi, H., 2014. In-vitro calcification study of polyurethane heart valves. *Mater. Sci. Eng. C* 35, 335–340. <https://doi.org/10.1016/j.msec.2013.11.015>
- Burriesci, G., Marincola, F.C., Zervides, C., 2010. Design of a novel polymeric heart valve. *J. Med. Eng. Technol.* 34, 7–22. <https://doi.org/10.3109/03091900903261241>
- Capodanno, D., Petronio, A.S., Prendergast, B., Eltchaninoff, H., Vahanian, A., Modine, T., Lancellotti, P., Sondergaard, L., Ludman, P.F., Tamburino, C., Piazza, N., Hancock, J., Mehilli,

- J., Byrne, R.A., Baumbach, A., Kappetein, A.P., Windecker, S., Bax, J., Haude, M., 2017. Standardized definitions of structural deterioration and valve failure in assessing long-term durability of transcatheter and surgical aortic bioprosthetic valves: A consensus statement from the European Association of Percutaneous Cardiovascular Interventions. *Eur. J. Cardio-thoracic Surg.* 52, 408–417. <https://doi.org/10.1093/EJCTS/EZX244>
- Claiborne, T.E., Sheriff, J., Kuetting, M., Steinseifer, U., Slepian, M.J., Bluestein, D., 2013. In vitro evaluation of a novel hemodynamically optimized trileaflet polymeric prosthetic heart valve. *J. Biomech. Eng.* 135, 021021. <https://doi.org/10.1115/1.4023235>
- Dimasi, A., Stevanella, M., Votta, E., Sturla, F., Burriesci, G., Redaelli, A., 2015. Finite element analysis of transcatheter aortic valve implantation in the presence of aortic leaflet calcifications. *Lect. Notes Appl. Comput. Mech.* 74, 101–115. https://doi.org/10.1007/978-3-319-10981-7_7
- Dvir, D., Bourguignon, T., Otto, C.M., Hahn, R.T., Rosenhek, R., Webb, J.G., Treede, H., Sarano, M.E., Feldman, T., Wijeyesundera, H.C., Topilsky, Y., Aupart, M., Reardon, M.J., Mackensen, G.B., Szeto, W.Y., Kornowski, R., Gammie, J.S., Yoganathan, A.P., Arbel, Y., Borger, M.A., Simonato, M., Reisman, M., Makkar, R.R., Abizaid, A., McCabe, J.M., Dahle, G., Aldea, G.S., Leipsic, J., Pibarot, P., Moat, N.E., Mack, M.J., Kappetein, A.P., Leon, M.B., 2018. Standardized Definition of Structural Valve Degeneration for Surgical and Transcatheter Bioprosthetic Aortic Valves. *Circulation* 137, 388–399. <https://doi.org/10.1161/CIRCULATIONAHA.117.030729>
- Eveborn, G.W., Schirmer, H., Heggelund, G., Lunde, P., 2013. The evolving epidemiology of valvular aortic stenosis . The Tromsø Study 396–400. <https://doi.org/10.1136/heartjnl-2012-302265>
- Falahatpisheh, A., Morisawa, D., Toosky, T.T., Kheradvar, A., 2017. A calcified polymeric valve for valve-in-valve applications. *J. Biomech.* 50, 77–82. <https://doi.org/10.1016/j.jbiomech.2016.11.027>
- Finotello, A., Morganti, S., Auricchio, F., 2017. Finite element analysis of TAVI: Impact of native aortic root computational modeling strategies on simulation outcomes. *Med. Eng. Phys.* 47, 2–12. <https://doi.org/10.1016/j.medengphy.2017.06.045>
- Fisher, C.I., Chen, J., Merryman, W.D., 2013. Calcific nodule morphogenesis by heart valve interstitial cells is strain dependent. *Biomech. Model. Mechanobiol.* 12, 5–17. <https://doi.org/10.1007/s10237-012-0377-8>
- Fujita, B., Kütting, M., Seiffert, M., Scholtz, S., Egron, S., Prashovikj, E., Börgermann, J., Schäfer, T., Scholtz, W., Preuss, R., Gummert, J., Steinseifer, U., Ensminger, S.M., 2016. Calcium distribution patterns of the aortic valve as a risk factor for the need of permanent pacemaker implantation after transcatheter aortic valve implantation. *Eur. Heart J. Cardiovasc. Imaging* 17, 1385–1393. <https://doi.org/10.1093/ehjci/jev343>
- Haj-Ali, R., Dasi, L.P., Kim, H.S., Choi, J., Leo, H.W., Yoganathan, A.P., 2008. Structural simulations of prosthetic tri-leaflet aortic heart valves. *J. Biomech.* 41, 1510–1519. <https://doi.org/10.1016/j.jbiomech.2008.02.026>
- Halevi, R., Hamdan, A., Marom, G., Mega, M., Raanani, E., Haj-Ali, R., 2015. Progressive aortic valve calcification: Three-dimensional visualization and biomechanical analysis. *J. Biomech.* 48, 489–497. <https://doi.org/10.1016/j.jbiomech.2014.12.004>

- Head, S.J., Çelik, M., Kappetein, A.P., 2017. Mechanical versus bioprosthetic aortic valve replacement. *Eur. Heart J.* 38, 2183–2191. <https://doi.org/10.1093/eurheartj/ehx141>
- Kim, H., Lu, J., Sacks, M.S., Chandran, K.B., 2008. Dynamic simulation of bioprosthetic heart valves using a stress resultant shell model. *Ann. Biomed. Eng.* 36, 262–275. <https://doi.org/10.1007/s10439-007-9409-4>
- Kostyunin, A.E., Yuzhalin, A.E., Rezvova, M.A., Ovcharenko, E.A., Glushkova, T. V., Kutikhin, A.G., 2020. Degeneration of bioprosthetic heart valves: Update 2020. *J. Am. Heart Assoc.* 9, 1–19. <https://doi.org/10.1161/JAHA.120.018506>
- Larroche, J., Panh, L., Lhermusier, T., Bataille, V., Marachet, M.A., Chollet, T., Petermann, A., Bouisset, F., Boudou, N., Marcheix, B., Rousseau, H., Galinier, M., Carrié, D., Lairez, O., Lavie-Badie, Y., 2020. Impact of aortic valve calcification severity on device success after transcatheter aortic valve replacement. *Int. J. Cardiovasc. Imaging* 36, 731–740. <https://doi.org/10.1007/s10554-019-01759-7>
- Li, K., Sun, W., 2017. Simulated transcatheter aortic valve deformation: A parametric study on the impact of leaflet geometry on valve peak stress. *Int. j. numer. method. biomed. eng.* 33, 1–14. <https://doi.org/10.1002/cnm.2814>
- Li, K., Sun, W., 2010. Simulated thin pericardial bioprosthetic valve leaflet deformation under static pressure-only loading conditions: Implications for percutaneous valves. *Ann. Biomed. Eng.* 38, 2690–2701. <https://doi.org/10.1007/s10439-010-0009-3>
- McGee, O.M., Sun, W., McNamara, L.M., 2019. An in vitro model quantifying the effect of calcification on the tissue–stent interaction in a stenosed aortic root. *J. Biomech.* 82, 109–115. <https://doi.org/10.1016/j.jbiomech.2018.10.010>
- Milhorini Pio, S., Bax, J., Delgado, V., 2020. How valvular calcification can affect the outcomes of transcatheter aortic valve implantation. *Expert Rev. Med. Devices* 17, 773–784. <https://doi.org/10.1080/17434440.2020.1789456>
- Mordi, I., Tzemos, N., 2012. Bicuspid aortic valve disease: A comprehensive review. *Cardiol. Res. Pract.* 1. <https://doi.org/10.1155/2012/196037>
- Otto, C.M., Burwash, I.G., Legget, M.E., Munt, B.I., Fujioka, M., Healy, N.L., Kraft, C.D., Miyake-Hull, C.Y., Schwaegler, R.G., 1997. Prospective study of asymptomatic valvular aortic stenosis: Clinical, echocardiographic, and exercise predictors of outcome. *Circulation* 95, 2262–2270. <https://doi.org/10.1161/01.CIR.95.9.2262>
- Piayda, K., Dannenberg, L., Zako, S., Maier, O., Bosbach, G., Polzin, A., Afzal, S., Jung, C., Westenfeld, R., Kelm, M., Zeus, T., Veulemans, V., 2021. Predictors of calcification distribution in severe tricuspid aortic valve stenosis. *Int. J. Cardiovasc. Imaging* 37, 2791–2799. <https://doi.org/10.1007/s10554-021-02248-6>
- Rahmani, B., Tzamtzis, S., Sheridan, R., Mullen, M.J., Yap, J., Seifalian, A.M., Burriesci, G., 2017. In Vitro Hydrodynamic Assessment of a New Transcatheter Heart Valve Concept (the TRISKELE). *J. Cardiovasc. Transl. Res.* 10, 104–115. <https://doi.org/10.1007/s12265-016-9722-0>
- Rotman, O.M., Kovarovic, B., Chiu, W.C., Bianchi, M., Marom, G., Slepian, M.J., Bluestein, D., 2019. Novel Polymeric Valve for Transcatheter Aortic Valve Replacement Applications: In Vitro Hemodynamic Study. *Ann. Biomed. Eng.* 47, 113–125. <https://doi.org/10.1007/s10439-018-02119-7>

- Sakrana, A.A., Nasr, M.M., Ashamalla, G.A., Abuelatta, R.A., Naeim, H.A., El Tahlawi, M.A., 2016. Paravalvular leak after transcatheter aortic valve implantation: is it anatomically predictable or procedurally determined? MDCT study. *Clin. Radiol.* 71, 1095–1103. <https://doi.org/10.1016/j.crad.2016.07.016>
- Serrani, M., Brubert, J., Stasiak, J., De Gaetano, F., Zaffora, A., Costantino, M.L., Moggridge, G.D., 2016. A Computational Tool for the Microstructure Optimization of a Polymeric Heart Valve Prosthesis. *J. Biomech. Eng.* 138. <https://doi.org/10.1115/1.4033178>
- Smuts, A.N., Blaine, D.C., Scheffer, C., Weich, H., Doubell, A.F., Dellimore, K.H., 2011. Application of finite element analysis to the design of tissue leaflets for a percutaneous aortic valve. *J. Mech. Behav. Biomed. Mater.* 4, 85–98. <https://doi.org/10.1016/j.jmbbm.2010.09.009>
- Stewart, B.F., Siscovick, D., Lind, B.K., Gardin, J.M., Gottdiener, J.S., Smith, V.E., Kitzman, D.W., Otto, C.M., 1997. Clinical factors associated with calcific aortic valve disease. *J. Am. Coll. Cardiol.* 29, 630–634. [https://doi.org/10.1016/S0735-1097\(96\)00563-3](https://doi.org/10.1016/S0735-1097(96)00563-3)
- Sturla, F., Ronzoni, M., Vitali, M., Dimasi, A., Vismara, R., Preston-Maher, G., Burriesci, G., Votta, E., Redaelli, A., 2016. Impact of different aortic valve calcification patterns on the outcome of transcatheter aortic valve implantation: A finite element study. *J. Biomech.* 49, 2520–2530. <https://doi.org/10.1016/j.jbiomech.2016.03.036>
- Sun, L., Rajamannan, N.M., Sucusky, P., 2013. Defining the Role of Fluid Shear Stress in the Expression of Early Signaling Markers for Calcific Aortic Valve Disease 8. <https://doi.org/10.1371/journal.pone.0084433>
- Tan, L.T., Razon, T.L.J., Cuenza, L., 2020. Correlation of Computed Tomography- derived Aortic Valve Calcium Score with Severity of Aortic Stenosis on Echocardiography : A Single-Center Experience, in: *ECR 2020. European Society of Radiology, Bonifacio Global City/PH, Quezon City/PH, Manila/PH*, pp. 2020–2023. <https://doi.org/10.26044/ecr2020/C-12320>
- Thubrikar, M.J., Aouad, J., Nolan, S.P., 1986. Patterns of calcific deposits in operatively excised stenotic or purely regurgitant aortic valves and their relation to mechanical stress. *Am. J. Cardiol.* 58, 304–308. [https://doi.org/10.1016/0002-9149\(86\)90067-6](https://doi.org/10.1016/0002-9149(86)90067-6)
- Vargas, H.A., Hoey, E.T.D., Gopalan, D., Agrawal, S.K.B., Sreaton, N.J., Gulati, G.S., 2009. Congenital and acquired conditions of the aortic root: Multidetector computed tomography features. *Postgrad. Med. J.* 85, 383–391. <https://doi.org/10.1136/pgmj.2008.075531>
- Weinberg, E.J., Schoen, F.J., Mofrad, M.R.K., 2009. A computational model of aging and calcification in the aortic heart valve. *PLoS One* 4, 1–10. <https://doi.org/10.1371/journal.pone.0005960>
- Zareian, R., Tseng, J.C., Fraser, R., Meganck, J., Kilduff, M., Sarraf, M., Dvir, D., Kheradvar, A., 2019. Effect of stent crimping on calcification of transcatheter aortic valves. *Interact. Cardiovasc. Thorac. Surg.* 29, 64–73. <https://doi.org/10.1093/icvts/ivz024>

CHAPTER 6

2D Fluid-Structure Interaction Modelling of Aortic Leaflet Dynamics using the Abaqus Coupled Eulerian Lagrangian (CEL) Approach

6.1 Introduction

The design and manufacture of aortic valve replacements (AVRs) is a multifaceted process that can be greatly aided by computational simulations. Finite element analysis (FEA) has been widely used to understand the function of native aortic leaflets and to improve the design of AVR devices. For the native valve, FEA has been used to predict valve deformation under physiological loading (Labrosse et al., 2010), or to predict mechano-biological aspects such as strain-based calcification growth patterns (Arzani and Mofrad, 2017). In Chapter 4, it was demonstrated that FEA could estimate the in vitro hydrodynamic performance of an AVR by analysing several surrogate parameters associated with valve hydrodynamics (Whiting et al., 2022). While this approach provided useful insight into valve performance, at relatively low computational cost, these simulations were limited to a structural analysis and relied on several assumptions on boundary conditions to represent the effect of the hydrodynamic loading on

the boundary valve problem. However, structural FEA valve simulations apply uniform aortic and ventricular pressures to the leaflet surfaces, thereby simulating systolic and diastolic conditions. This uniform application of the pressure load results in symmetric opening of the leaflets, which is typically not observed *in vitro* or *in vivo*. To fully represent the hydrodynamic flow and its effect on leaflet biomechanics, a coupled fluid-structure interaction (FSI) simulation is required.

Typically, FSI simulation approaches fall into one of two categories, (i) the Arbitrary Lagrangian Eulerian (ALE) method, where the fluid mesh conforms to the Lagrangian structure as it moves, or (ii) the immersed boundary (IB) approach, where Lagrangian and Eulerian domains are overlaid on top of one another (Peskin, 2002). Luraghi et al. (2017) used an ALE-based approach to demonstrate the benefits of FSI over finite element-based structural models for heart valve simulations, showing the ability of the FSI simulation to capture the asymmetric leaflet kinematics. Many studies have been performed using ALE-based FSI approaches to investigate heart valve biomechanics, with studies investigating the effects of calcification on TAVR performance (Halevi et al., 2016; Luraghi et al., 2020) and comparing the hydrodynamic performance between SAVR and TAVR valves (Ghosh et al., 2018). This has the added benefit of enabling detailed predictions of parameters not measurable *in vivo*, such as wall shear stress (Laadhari and Székely, 2017; Sodhani et al., 2018). A limited number of FSI studies have experimentally validated their FSI models by comparing with *in vitro* testing using pulsatile flow rigs (Gharaie et al., 2018; Luraghi et al., 2017; Tango et al., 2018). Many other studies have only presented computational results from FSI simulations, and not included any experimental validation (Borowski et al., 2018; Chen and Luo, 2018; Hedayat et al., 2017; Kandail et al., 2018). As there are many FSI techniques, and many custom-built codes, there remains a significant need for approaches that provide experimental validation to FSI techniques before they can be more widely used for *in silico* bench testing.

Apart from providing insight and understanding to the *in vivo* performance of AVRs, FSI also has the potential to speed up the design and development process by replicating the *in vitro* hydrodynamic testing required for ISO 5840. A limited number of studies have sought to use FSI models using the ALE approach to conduct *in silico* bench testing, with various authors estimating hydrodynamic performance of AVRs (Ghosh et al., 2018; Luraghi et al., 2019; Piatti et al., 2016). Of particular interest to this chapter are the hydrodynamic parameters from ISO 5840, namely EOA and transvalvular ΔP , both of which serve as an important metric of valve performance during the development process. While several studies have measured these parameters, very few have conducted any experimental validation of the predicted parameters from *in silico* bench testing. Luraghi et al. (2017) focused on comparing the geometric orifice area (GOA) across experimental, FSI and structural finite element analysis (FEA) models, finding a 5% difference between FSI and experiment, but a much larger 46.5% difference between the structural FEA and experiment. Gharaie et al. (2018) also focused on comparing EOA and GOA, finding a 5.7% percentage error between *in silico* and *in vitro* experiments. Alternative to the ALE-based approach, studies using the IB approach employ a fixed fluid mesh, through which the Lagrangian structure moves. This results in a more computationally efficient simulation, at the expense of fluid leaflet boundary resolution. This was demonstrated by Bavo et al. (2016) who evaluated the method compared to ALE for modelling aortic heart valve deformation (Bavo et al., 2016). The IB technique used in this study was termed Coupled Eulerian Lagrangian (CEL), which uses the IB method commercially available within the Abaqus Explicit Package (Dassault Systemes, RI, Providence). However, Bavo et al. (2016) did not include an experimental comparison in the study, and it appears that there are no other published works that have investigated the Abaqus/CEL method further for valve design. Thus, the motivation for this chapter is to address the experimental validation of the Abaqus/CEL method for aortic valve, given that it is a commercially available method and has already been

proven to perform sufficient simulations for deformation of aortic valves under pulsatile conditions.

This study investigates the potential of Abaqus/CEL to perform a hydrodynamic analysis of aortic valves according to the ISO 5840 standard by replicating the results measured from an in vitro pulsatile flow rig in 2D. An experimental flow chamber was designed and manufactured to quantify the deformation of a polymer leaflet under steady-state flow conditions. Following on from this benchmarking, the Abaqus/CEL method was used to investigate the fluid and structural biomechanics of a 2D aortic valve representation in both a healthy and diseased state. Hydrodynamic parameters from ISO 5840, including effective orifice area (EOA) and transvalvular pressure drop (ΔP), were evaluated from these simulations to investigate the potential of this method for conducting in silico bench testing

6.2 Materials and Methods

6.2.1 In Vitro Flow Rig Design, Build and Testing

An in vitro flow rig was designed to investigate the deformation of a polymer leaflet under steady-state flow conditions as a benchmark case for the FSI model developed using the Abaqus/CEL method. A schematic of the test set up is shown in Figure 6.1, whereby the polymer leaflet sits within a rectangular channel, with flow entering and exiting the region through circular inlet and outlet ports.

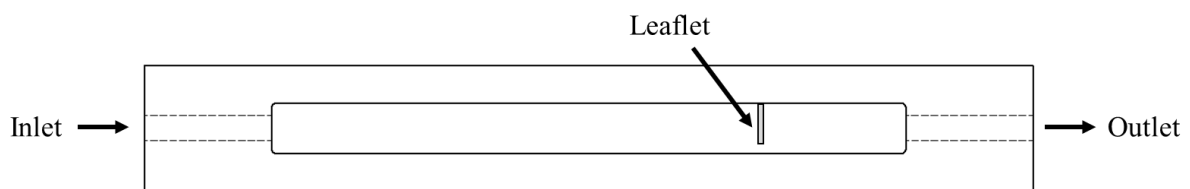


Figure 6.1 Experimental set up of the flow rig showing the inlet, outlet and 500 mm long channel, with the polymer leaflet positioned 400 mm downstream of the inlet

The dimensions of the channel region were determined based on Computational Fluid Dynamics (CFD) simulations carried out using ANSYS/CFX software. These were conducted to ensure fully-developed laminar flow conditions during the tests carried out. For these simulations, the fluid domain of the channel region was modelled along with circular inlet and outlet ports in the absence of the polymer leaflet. The domain was meshed with 515,000 hexagonal elements and a uniform velocity of 0.03 m/s was applied at the inlet. This flow regime corresponded to a dimensionless 1 Number of $Re = 600$ at the inlet port and $Re = 988$ in the rectangular channel, calculated by Equation 6.1:

$$Re = \frac{\rho u L}{\mu} \quad (6.1)$$

Where L is the characteristic length (m), μ is the dynamic viscosity of water ($\text{kg m}^{-1} \text{s}^{-1}$), u is the velocity (m/s) and ρ is the density (kg/m^3). A parametric study was carried out to determine a suitable entrance length (L_e) in the channel to ensure fully developed flow, where it was determined that an entrance length of $L_e = 400$ mm was required to have a system free of entrance effects. The velocity contour plot and streamlines of the experimental flow chamber under steady-state conditions is shown in Figure 6.2a. The velocity flow profiles across the Y-axis is shown at 0.1 m, 0.2 m, 0.3 m and 0.4 m along the X-axis, with fully developed laminar channel flow at $L_e = 400$ mm evident in Figure 6.2b.

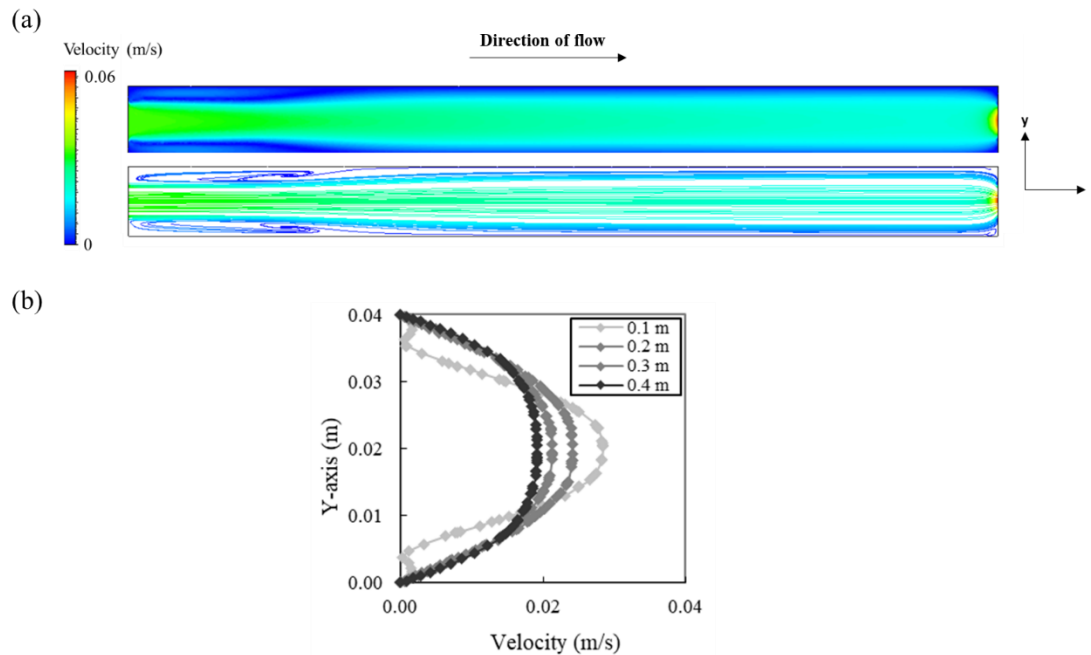


Figure 6.2 (a) Velocity contour and streamline profiles of flow chamber under steady state conditions (b) velocity flow profile in the Y-axis at points along the X-axis

Based on the CFD-based design process, the custom-built flow rig was manufactured from a 0.7 m long rectangular block of polycarbonate. The resulting channel, described in Figure 6.3 and having dimensions of length 0.5 m, height 0.04 m and depth 0.028 m, was machined into the face of the block and a clear acrylic faceplate was mounted on a rubber gasket to allow for observation of deformation under flow. Inlet and outlet ports of 0.02 m diameter were machined at each end of the channel.

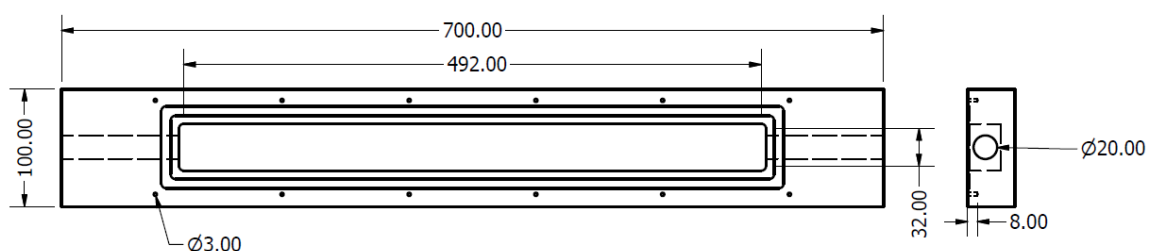


Figure 6.3 General dimensions of machined acrylic rectangular block for experimental flow chamber

A rectangular polymer leaflet of dimensions 30 mm x 20 mm x 1mm was manufactured using a commercially available polyurethane, Dragonskin 10 (Smooth-On, Inc. Pennsylvania, USA).

This leaflet was attached to a mounting plate with a compression fit and secured from the top of the chamber 400 mm from the circular inlet port (see Figure 6.4b) to allow for channel flow to fully develop.

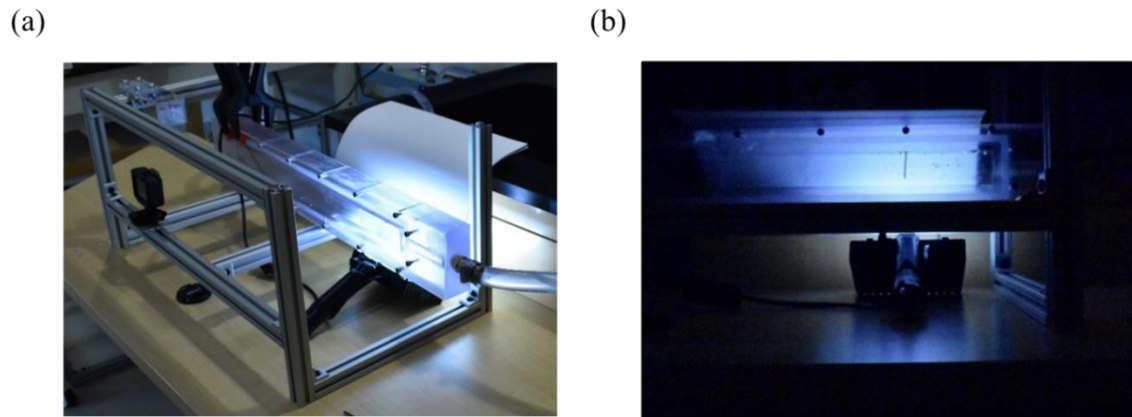


Figure 6.4 (a) Experimental apparatus showing acrylic flow chamber with tubing and camera (b) front lit view for capturing video suitable for post-processing displacement data points

The experimental chamber was filled with water and all air bubbles were removed from the system. Water was fed into the system at a flow rate of 3 L/min from a mains water supply via the inlet tubing. The deformation of the leaflet was recorded with a camera at 30 fps. To capture flow movement, a coloured dye was added to the fluid.

6.2.2 Coupled Eulerian Lagrangian Fluid-Structure Interaction

An FSI model was created using Abaqus/CEL. The Abaqus/CEL approach is an IB method of FSI modelling with the Abaqus Explicit Package (Simulia, 2017, Providence, RI, USA). The Abaqus/CEL method assumes that the Eulerian fluid domain is fixed in space as the Lagrangian structure moves through it. This is demonstrated schematically in Figure 6.5.

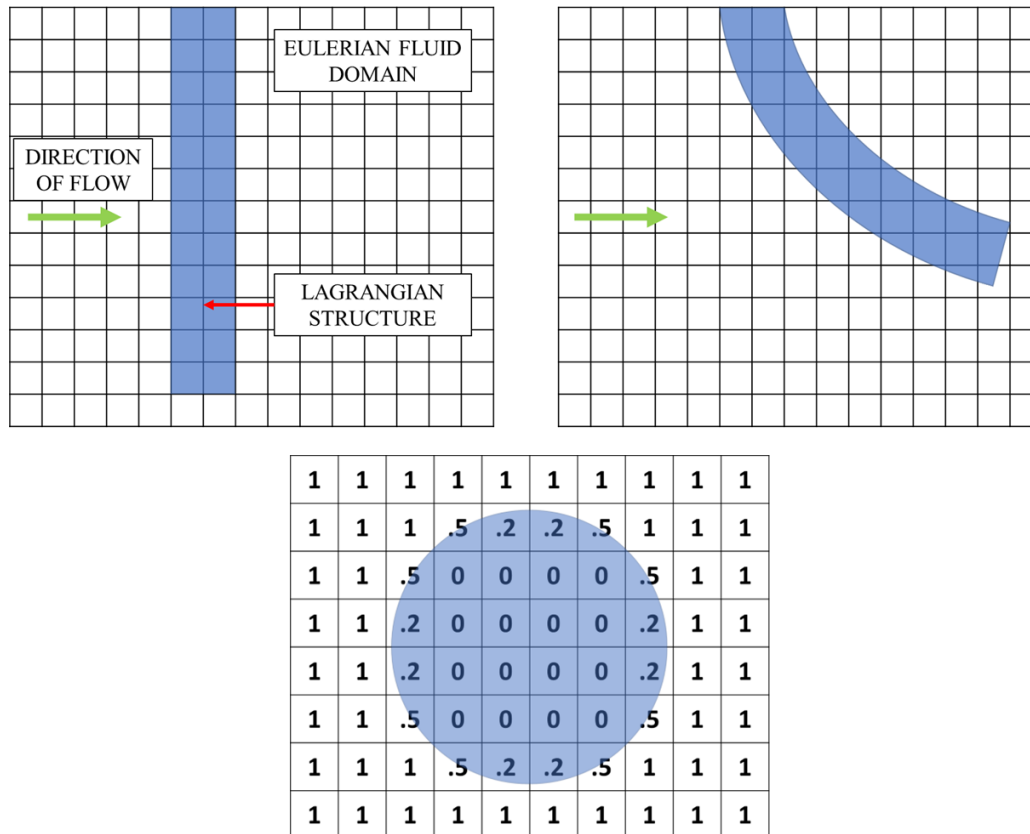


Figure 6.5 (Top row) Representation of deformation of Lagrangian solid structure in the fixed Eulerian fluid domain. (Bottom) Representation of volume of fluid definition for a Lagrangian solid structure in the Eulerian fluid domain

The presence of this Lagrangian structure in the Eulerian domain is accounted for by the inclusion of an external body force term in the Navier-Stokes equations. To initialise the presence of the Lagrangian structure, a volume of fluid (VOF) function is specified, which is the fraction of fluid occupying each Eulerian element. Here, values of zero are prescribed for elements completely occupying the Lagrangian structure, values of one prescribed for elements completely occupying the Eulerian domain and values between zero and one assigned for those occupying both domains. This definition is updated throughout the simulation as the Lagrangian structure moves through the domain

An equation of state, the $U_s - U_p$ formulation, was used to model the fluid in the Eulerian domain and is given by:

$$U_s = C_0 + sU_p \quad (6.1)$$

Where U_s is the linear shock velocity, U_p is the particle velocity, C_0 is the speed of sound in the fluid, and s is a parameter of the approximation.

6.2.2.1 Channel Flow with Analytical Solution

Many existing implementations of the Abaqus/CEL approach in the literature consider non-flow-based problems to accommodate severe large-deformation structural problems (Ducobu et al., 2017, 2016), (Morrison et al., 2018), (Qiu et al., 2011), or some limited fluid-based problems such as water impact phenomena (Ahmadzadeh et al., 2014). Due to its limited use in traditional fluid flow problems, an initial verification of the Abaqus/CEL method for 2D channel flow was conducted. A fluid domain that represented two parallel plates of infinite width was meshed with 1,950 8-noded hexahedral Eulerian elements with reduced integration (EC3D8R), with bias towards the walls as shown in Figure 6.6a. To enforce no-slip conditions, a zero-velocity boundary condition was prescribed at the wall nodes.

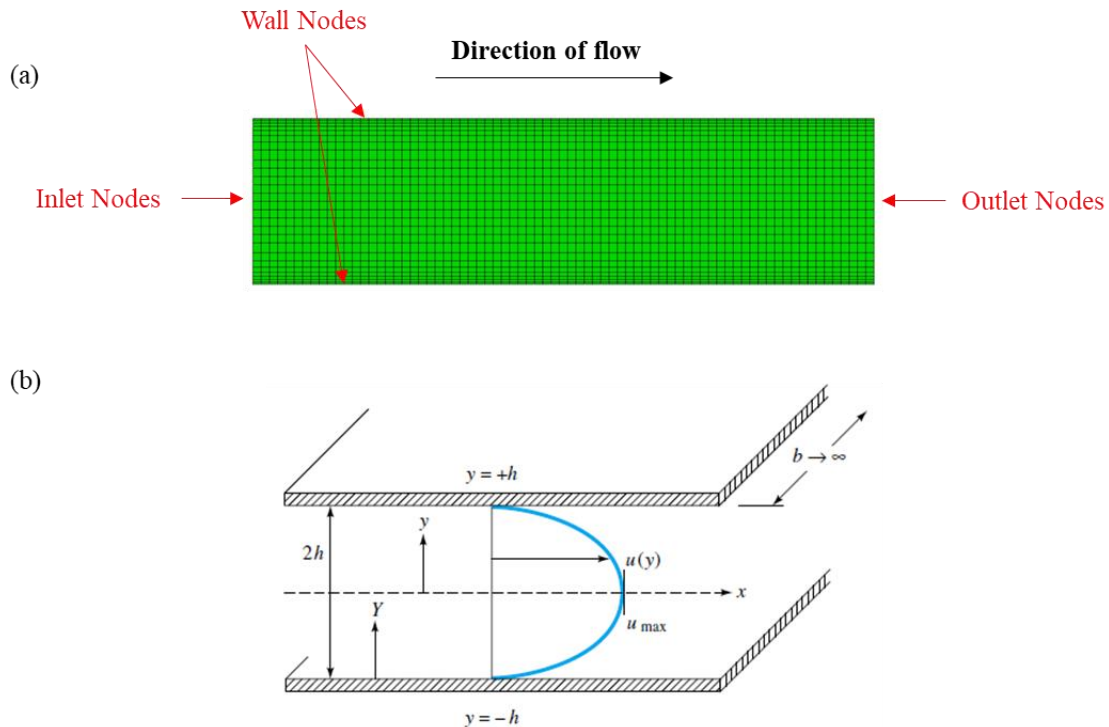


Figure 6.6. (a) Abaqus/CEL parallel plate flow fluid domain, showing biased mesh towards walls for better resolution with the enforced no-slip condition. (b) Fully developed parallel plate flow. Adapted from *Fluid Mechanics 4th Edition* (F. White)

A velocity of 0.001 m/s was assigned to the inlet nodes, which resulted in a low Reynolds number ($Re = 4$). The fluid was assumed to be water, which had a density of $\rho = 1,000 \text{ kg/m}^3$, a viscosity of $\mu = 0.001 \text{ Pa}\cdot\text{s}$ and a speed of sound of $C_0 = 1,450 \text{ m/s}$. These properties were prescribed using the U_s - U_p formulation in Abaqus. The results were compared to the analytical solution for parallel plate flow, which is represented schematically in Figure 6.6b and given by the following equation,

$$u = \frac{1}{2\mu} \left[-\frac{dp}{dx} (p + \rho gz) \right] (h^2 - y^2) \quad (6.2)$$

where u is the velocity at position y , μ is the viscosity, $\frac{dp}{dx}$ is the pressure gradient, h is half the height of the domain, p is the density, g is acceleration due to gravity and z is the increase in height, which was zero (e.g. $\rho gz = 0$).

The development of channel flow in the Abaqus/CEL simulation is shown in the velocity contour plot in Figure 6.7a. Here, once the flow becomes fully-developed, the predicted velocity profile by Abaqus/CEL matches exactly the analytical solution as shown in Figure 6.7b.

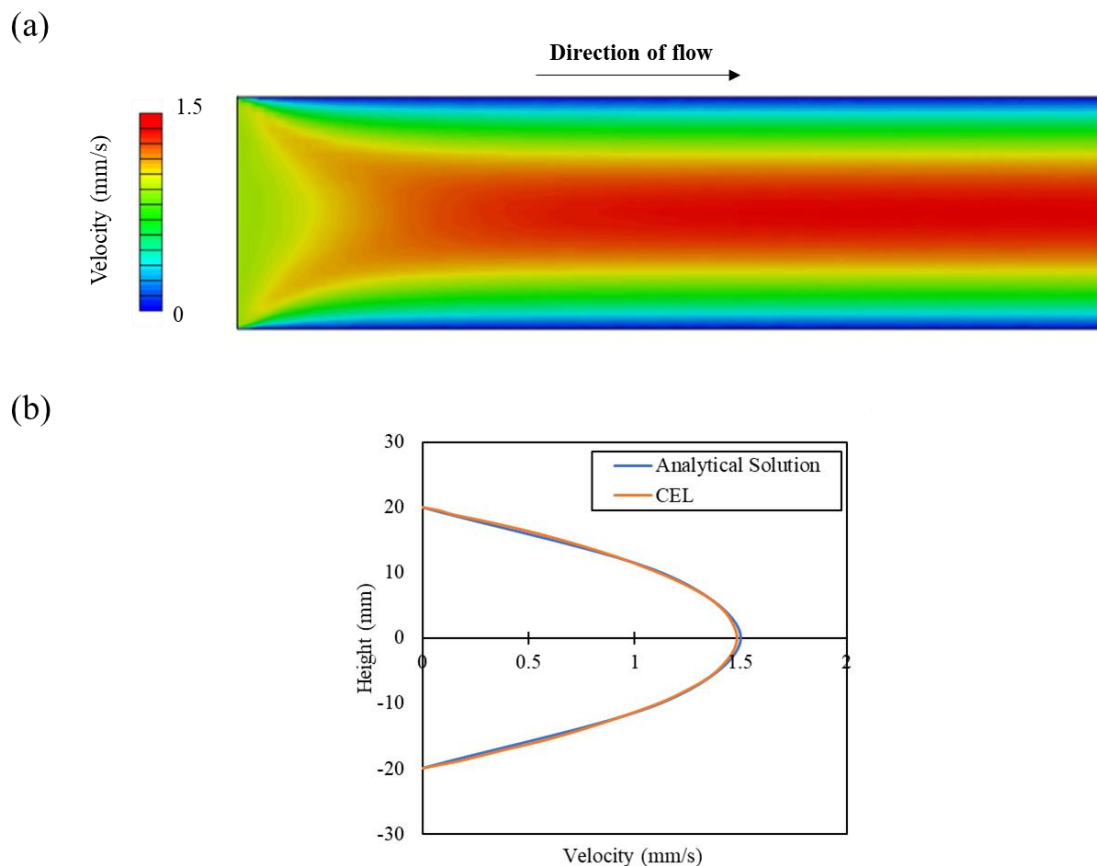


Figure 6.7 (a) Velocity contour plot for parallel plate flow Abaqus/CEL simulation showing the development of channel flow. (b) Velocity profile of Abaqus/CEL simulation and Analytical solution for parallel plate flow

6.2.2.2 Abaqus/CEL FSI Flow Chamber with Polymer Leaflet

Following the demonstration of channel flow, a model of the experimental flow chamber with polymer leaflet was created using Abaqus/CEL. The fluid domain was modelled as per the dimensions of the experimental chamber, measuring $L = 0.5$ m, $W = 0.028$ m and $H = 0.04$ m. The fluid domain was modelled with 225,515 8-noded hexahedral Eulerian elements with reduced integration (EC3D8R), as shown in Figure 6.8a. Inlet and outlet nodes were assigned

at the start and end of the domain to correspond to 20 mm diameter orifices. Water was considered a Newtonian fluid with a density of $\rho = 1,000 \text{ kg/m}^3$ and a viscosity of $\mu = 0.001 \text{ Pa}\cdot\text{s}$. The speed of sound was assigned a compressibility factor of 10 ($C_0 = 145 \text{ m/s}$) to reduce the computational cost of the model. This was previously demonstrated by Bavo et al. (2016) to be a suitable modification for achieving convergence of the simulation using the Abaqus/CEL approach. No-slip conditions were assigned to the walls of the fluid domain. A velocity boundary condition of 68.3 mm/s was applied to the nodes at the inlet, while the velocity at the outlet was unconstrained with a zero pressure condition.

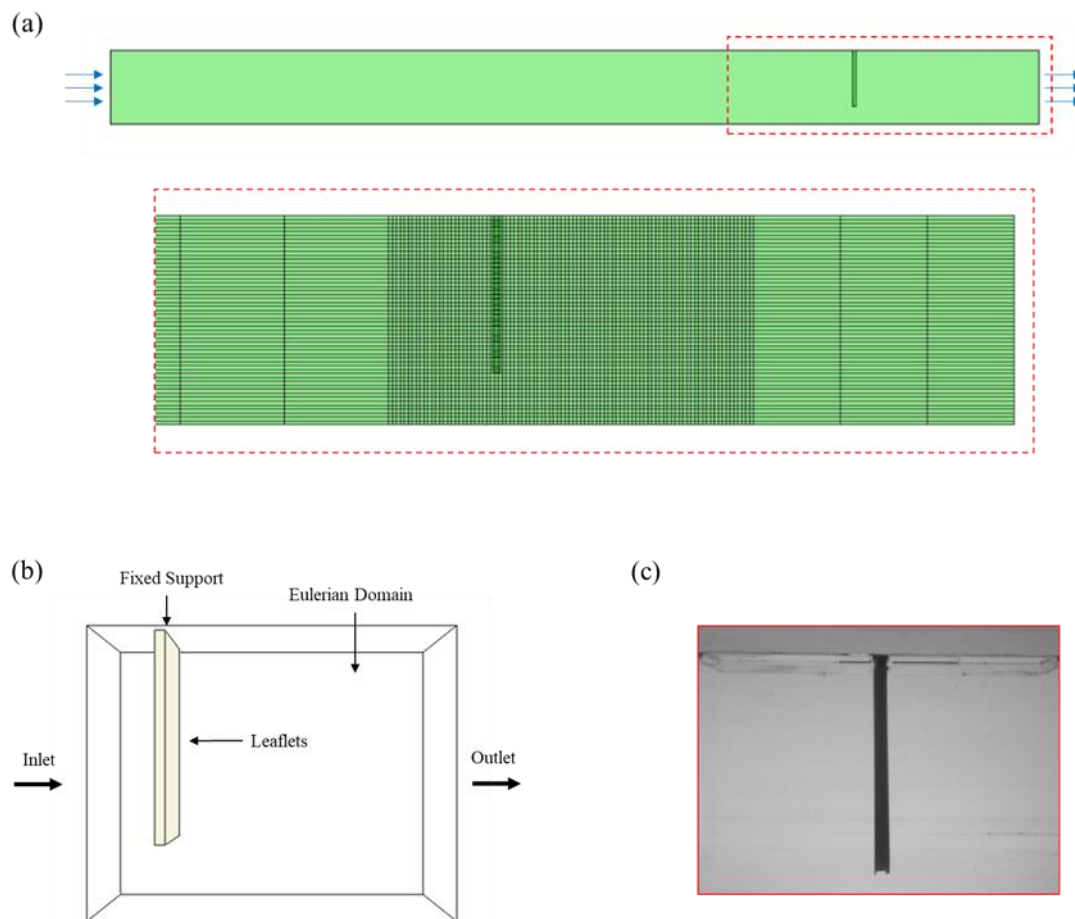


Figure 6.8 (a) Abaqus/CEL Flow Chamber fluid domain and mesh, with 20 mm diameter inlet and outlet ports. (b) Close-up of leaflet geometry in Eulerian domain (c) Experimental leaflet

A Lagrangian structure to represent the polymer leaflet was included in the model (see Figure 6.8b and 6.8c), which was meshed with 600 8-noded hexahedral elements with reduced integration (C3D8R). Contact between the fluid and solid was included using the in-built general contact algorithm for Abaqus Explicit simulations. The mechanical behaviour of the silicon leaflet was determined through experimental testing as per the ASTM D638 standard, which defines standard test methods for tensile testing of plastics. Tensile dog-bone samples (n=5) were manufactured from Dragonskin 10 (Smooth-on, Inc. Pennsylvania, USA) and axially tested using a uniaxial test machine (Zwick Roell, GmbH & Co., Germany) until failure, at a displacement rate of 5 mm/min as shown in Figure 6.9a.

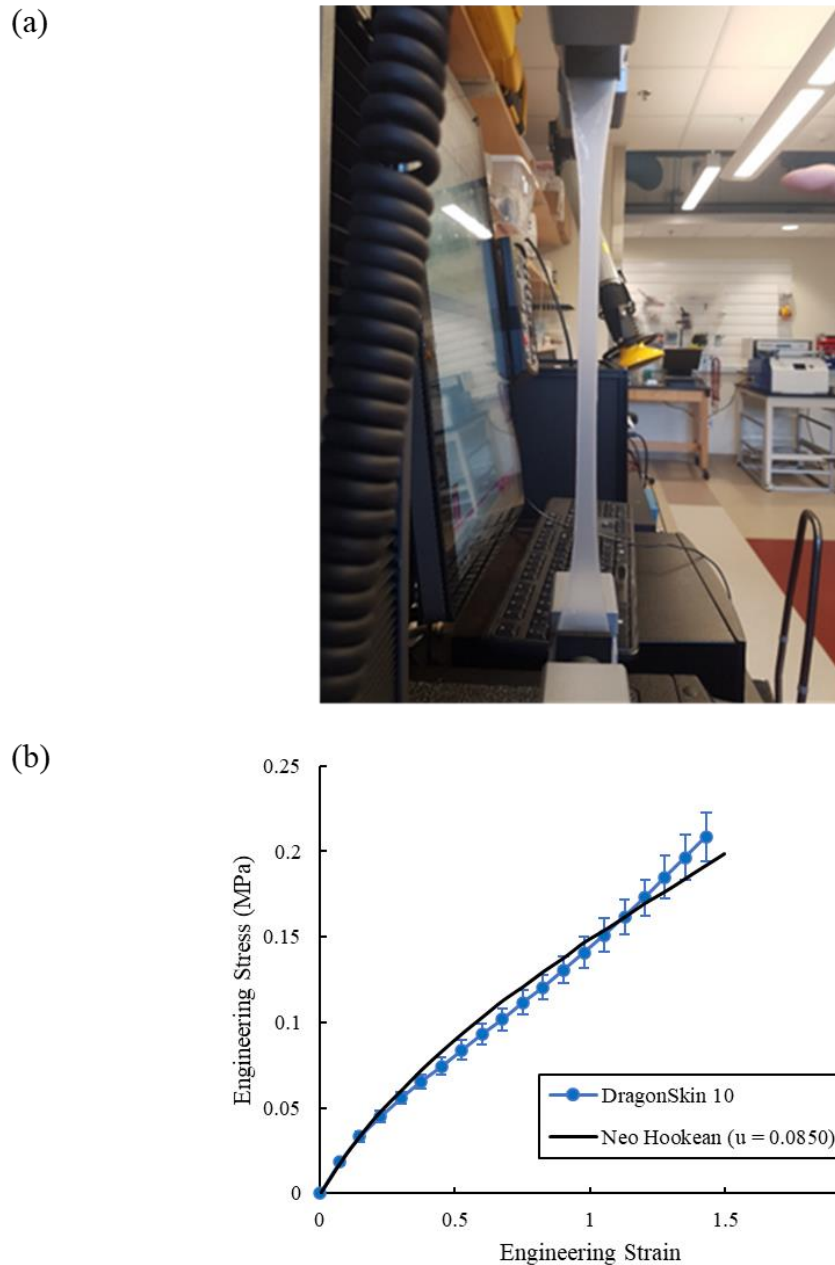


Figure 6.9 (a) Destructive testing of DragonSkin 10 in a uniaxial testing machine. (b) Material characterisation of DragonSkin 10 for a sample size of $n = 5$ where the average engineering stress strain is plotted with error bars representing the standard deviation at each point. The Neo–Hookean model fit is overlaid on the experimental results showing a good fit.

The resulting stress-strain behaviour showed a certain degree of non-linearity and a material calibration process was used to fit the constitutive behaviour using a compressible Neo-Hookean hyperelastic material model, whose strain energy density function may be expressed by the following relation,

$$W = \frac{u}{2}(I_1 - 3) \quad (6.3)$$

where W is the strain energy per unit reference volume, and I_1 is the first invariant. It was found that a shear modulus $u = 0.0850$ MPa provided a good fit to the experimental data, as shown in Figure 6.9b.

6.2.3 Abaqus/CEL Modelling of In Silico 2D Valve Flow

To investigate the potential of Abaqus/CEL for AVR design, a 2D valve simulation was modelled according to the geometry used by Amindari et al. (2017) shown in Figure 6.10b. The objective of this work was to (i) directly compare the predictions of the Abaqus/CEL approach to their simulation, which used an ALE solution scheme and (ii) investigate the potential of FSI simulations for in silico testing of aortic valve parameters, similar to in vitro testing.

6.2.3.1 Numerical model

Figure 6.11 shows a schematic of the model that was developed, whereby the fluid domain was discretised with 39,468 8-noded hexahedral Eulerian elements with reduced integration (EC3D8R). The aortic walls and leaflets were discretised with 1,722 8-noded hexahedral Lagrangian elements with reduced integration (C3D8R), as shown in Figure 6.11. The aortic walls had a zero-velocity flow condition to model a no-slip boundary condition. The leaflets were fixed at the beginning of the aortic sinus. The idealised sinus and valve leaflets were representative of a typical native leaflet geometry. The valve leaflets had a Young's Modulus of $E = 2$ GPa, a Poisson's ratio of $\nu = 0.3$ and a density of $\rho = 1,000$ kg/m³. To investigate the effects of leaflet stiffening, a subsequent simulation was carried out where the leaflets had a Young's Modulus to $E = 20$ GPa, similar to Amindari et al. (2017). A velocity boundary condition of 1 m/s, with the profile shown in Figure 6.10a, was applied to the nodes at the inlet, while the outlet had zero-pressure condition. An Abaqus/Explicit general contact condition was

defined between the fluid and the Lagrangian surfaces. Blood was modelled with a density $\rho = 1,060 \text{ kg/m}^3$, viscosity of $\mu = 0.003 \text{ Pa}\cdot\text{s}$ and a speed of sound $C_0 = 1,570 \text{ m/s}$. Based on these simulations, the resulting values for the following parameters were measured: the Maximum Jet Velocity (m/s), which is the maximum axial velocity emerging from the aortic orifice; the maximum transvalvular pressure gradient (TPG) (mmHg) across the valve; the maximum Orifice Diameter (mm); and maximum Opening Ratio (OR) of the valve orifice. These were evaluated and compared directly to the results of Amindari et al. (2017).

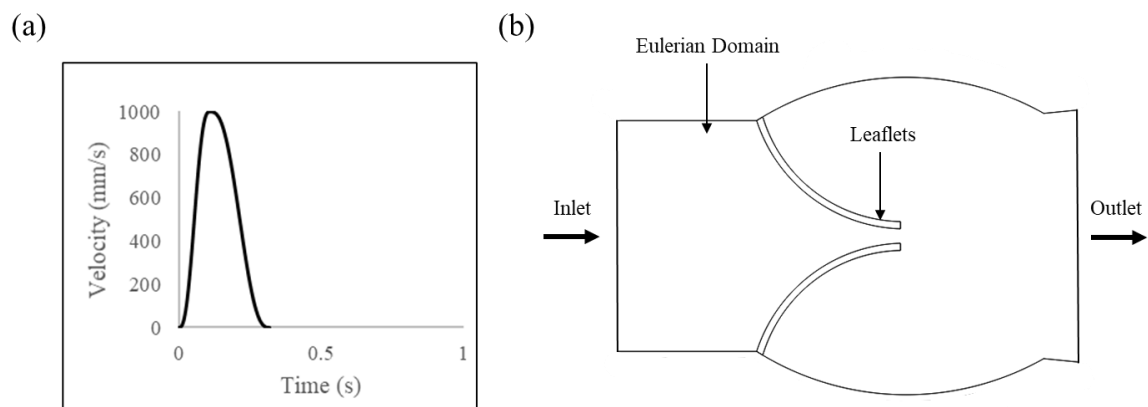


Figure 6.10: (a) Velocity inlet profile (b) Geometry of the 2D aortic valve based on Amindari et al. (2017)

6.2.3.2 In Silico Bench Testing.

These simulations were also used to measure the in vitro valve parameters, as a proof-of-concept demonstration for in silico bench testing. Here, the results from the Abaqus/CEL simulation were used to evaluate key parameters identified in ISO-5840, whereby the EOA and transvalvular ΔP , were determined from the model. These measurements were made using a “virtual probe” located in a similar position to the Vivitro pulsatile flow rig described in Chapters 4 and 5, shown in Figure 6.11.

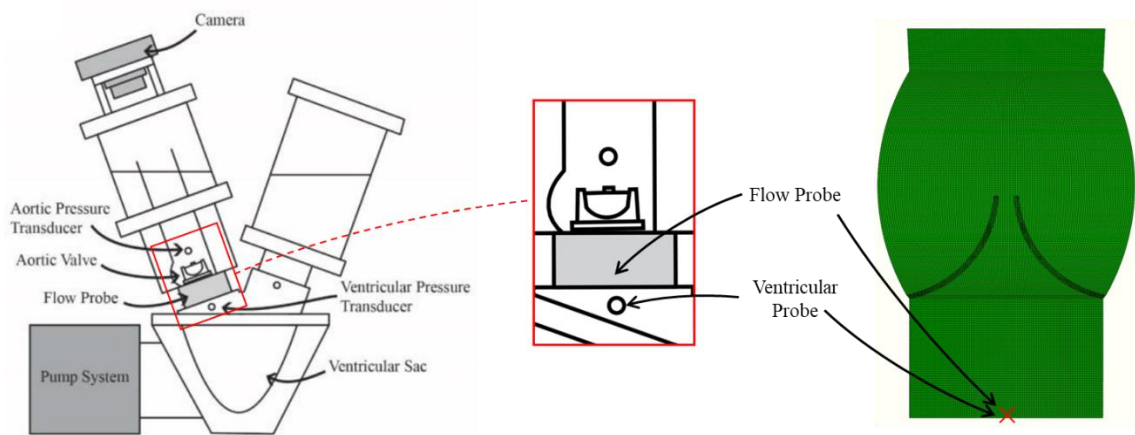


Figure 6.11 Vivitro Pulsatile Flow Rig Probe positions demonstrated on Abaqus/CEL model mesh

As before, the EOA was defined as the minimal cross-sectional area of the jet formed downstream of the aortic valve (Akins et al., 2008; Garcia and Kadem, 2006). It is often used during cardiac catheterisation to assess the severity of aortic stenosis in diseased patients (Baumgartner et al., 2017; Nishimura et al., 2014). It was calculated using the Gorlin Formula (Gorlin and Gorlin, 1951), which was provided in Equation 4.1. The transvalvular ΔP was calculated from the average pressure difference over the systolic period and Q_{RMS} was calculated from the applied velocity boundary condition. The flow and ventricular pressure were measured from a single node at the ventricular side of the valve.

6.3 Results

6.3.1 In Vitro and In Silico Fluid-Structure Interaction of Leaflet Deformation

The in silico Abaqus/CEL model deformation was overlaid on the in vitro flow rig polymer leaflet deformation in Figure 6.12. The Abaqus/CEL simulation provided a close response once it reached a steady state at 5s in the simulation, matching the deformation seen in vitro.

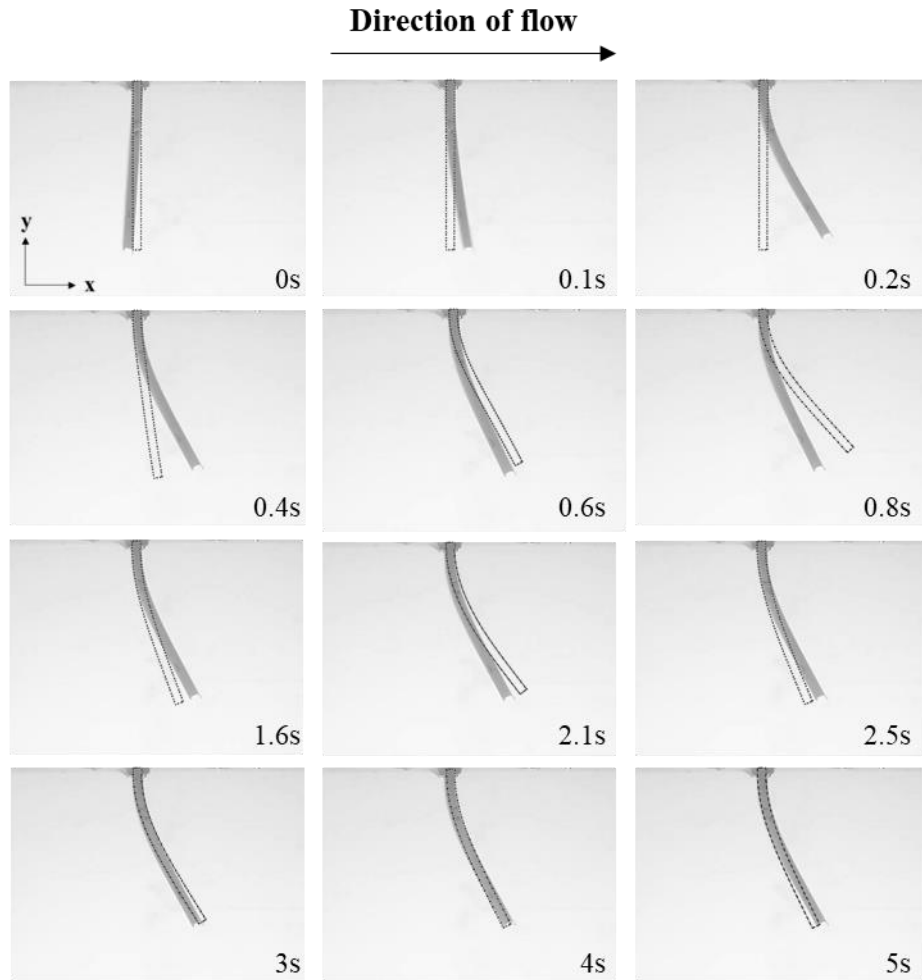


Figure 6.12 Deformation of the leaflet observed in vitro (solid) and in silico overlaid (dashed line), for various time-points until the leaflet reached a steady-state deformation.

The x-displacement deformation of the in silico and in vitro leaflet tip is shown in Figure 6.13.

The Abaqus/CEL simulation showed a high degree of initial oscillation, which was greater than the level of oscillation observed experimentally. Once the simulation reached a steady-state the predicted deflection of the leaflet closely matched the experimental value.

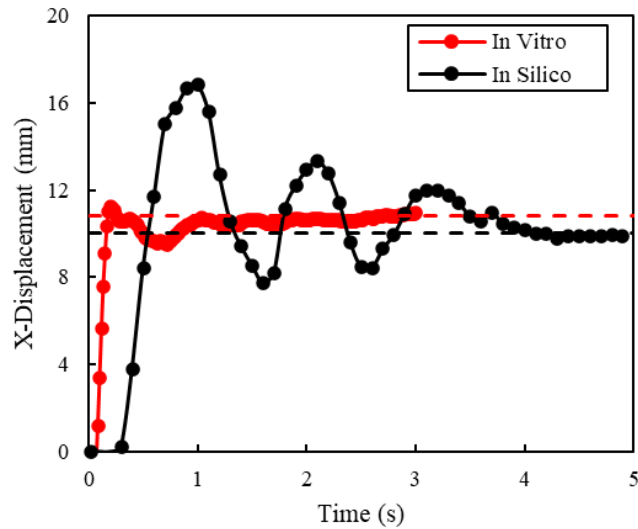


Figure 6.13 Measured x -displacement of the leaflet tip in both the *in silico* model and *in vitro* setups.

Figure 6.14a shows the resulting qualitative flow patterns from the leaflet testing, which was visualised by adding a coloured dye to the fluid upstream of the leaflet. The presence of vortices can be seen as the fluid moves around the leaflet. Figure 6.14b shows the corresponding velocity vector plots from the Abaqus/CEL simulation at steady-state conditions, which shows qualitatively similar features. In both experimental and computational models, the resulting fluid motion showed a maximum jet velocity beneath the leaflet, and indicated a wake region directly behind the leaflet.

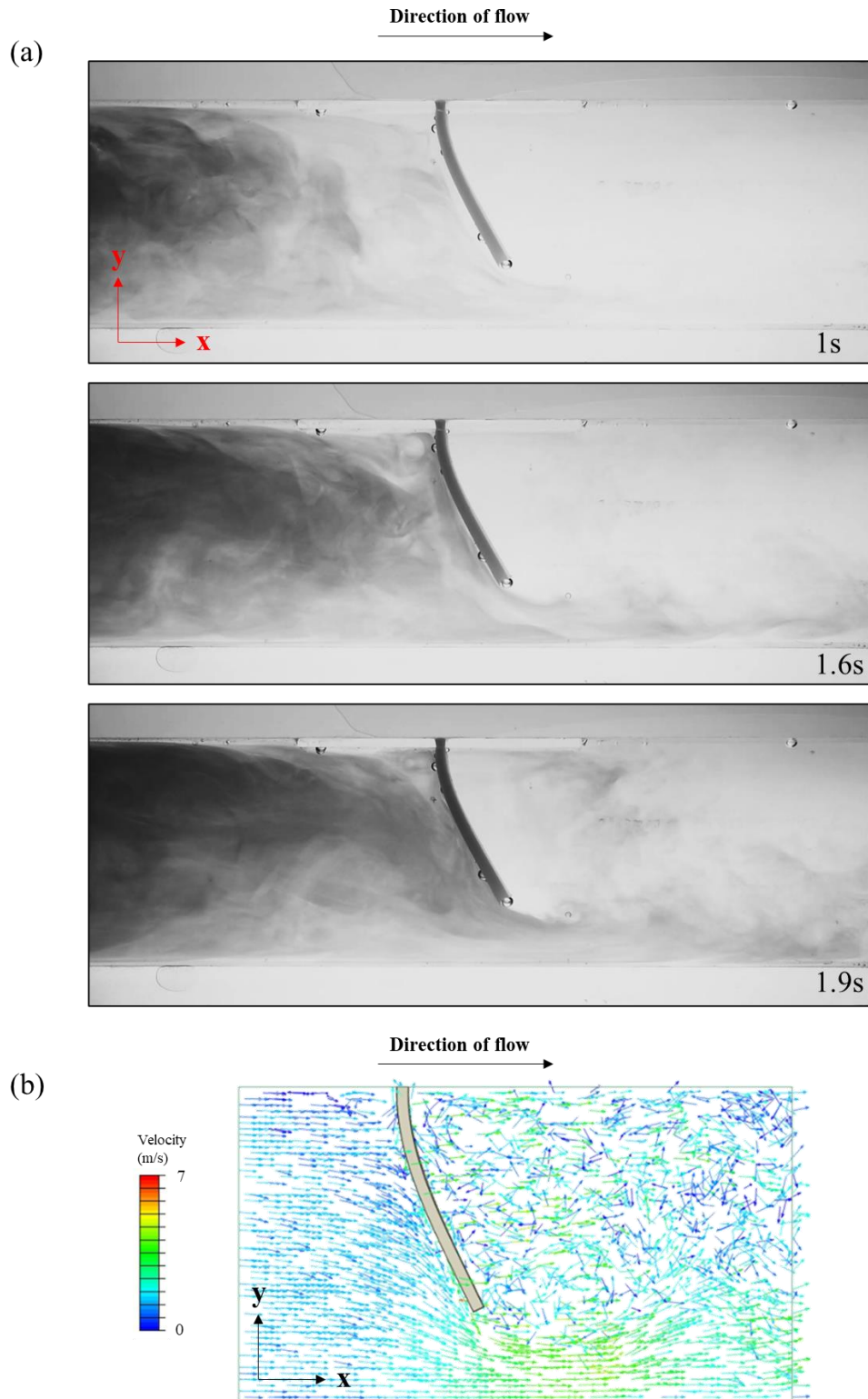


Figure 6.14 (a) Qualitative flow pattern testing, with time-steps normalised to the steady state configuration; a coloured dye was added to the fluid upstream of the leaflet and the resulting fluid motion was observed. (b) Velocity vectors in m/s in the in silico model once it had reached steady-state.

6.3.2 Fluid-structure Interaction of a 2D Aortic Valve

Figure 6.15 shows the resulting velocity contours and deformation for the 2D aortic valve during the simulation, alongside the results from Amindari et al. (2017) who used an ALE approach. Both ALE and Abaqus/CEL models show comparable predictions over each time point, although there are certain differences observed during leaflet opening, with the Abaqus/CEL method predicting higher jet velocities.

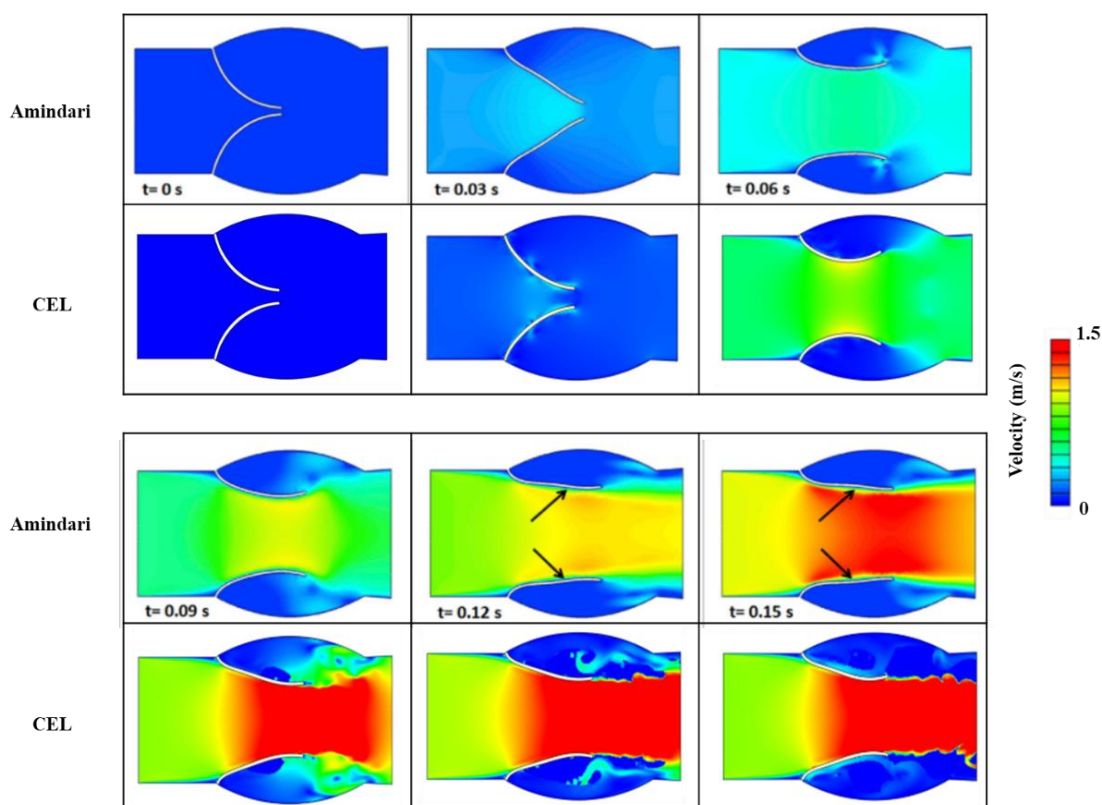


Figure 6.15 Velocity contour plots comparing healthy valve deformation across Abaqus/CEL and Amindari et al. (2017) simulations at each time-point.

From the predicted velocity and pressure values, the average transvalvular pressure gradient and flow rate in m^3/s were calculated, with results summarised in Table 6.1. As the stiffness of the valve leaflets increased to represent a stenosis or stiffening caused by calcific disease, the maximum jet velocity and maximum transvalvular pressure gradient increased, while the maximum orifice diameter and opening ratio decreased. Comparing results from both studies,

the maximum jet velocity increased for the stiffened valve in both the Abaqus/CEL approach and the ALE approach by Amindari et al. (2017). The Abaqus/CEL prediction was 11% higher for the healthy case, and 4% higher for the diseased case when compared to Amindari et al. (2017). The maximum transvalvular pressure gradient increased across both simulations from healthy to diseased states. Again, the Abaqus/CEL approach gave a 72% higher prediction in the healthy case and a 20% higher prediction in the diseased state. The maximum orifice diameter and opening ratio showed comparable decreases from healthy to diseased. For the maximum orifice diameter, the Abaqus/CEL simulation was 17% lower in the healthy state, and 12% lower in the diseased state. For the maximum opening ratio, the Abaqus/CEL was 20% lower in the healthy state and 16% lower in the diseased state.

Table 6.1 Comparison of results for healthy and stenosed valves reported by Amindari et al. (2017) with the Abaqus/CEL model

	Young's Modulus (MPa)	Maximum Jet Velocity (m/s)		Maximum Transvalvular Pressure Gradient (MPa)		Maximum Orifice Diameter (mm)		Maximum Opening ratio	
		Amindari	CEL	Amindari	CEL	Amindari	CEL	Amindari	CEL
Healthy	2	1.57	1.75	633	1,087	14	11.6	70%	56%
Diseased	20	2.38	2.48	2559	3,078	9	7.9	45%	38%

The velocity flow profiles for each valve in the healthy and diseased state are shown in Figure 6.16. The opening ratio is restricted as stiffening of the valve is increased, and increased jet velocities develop.

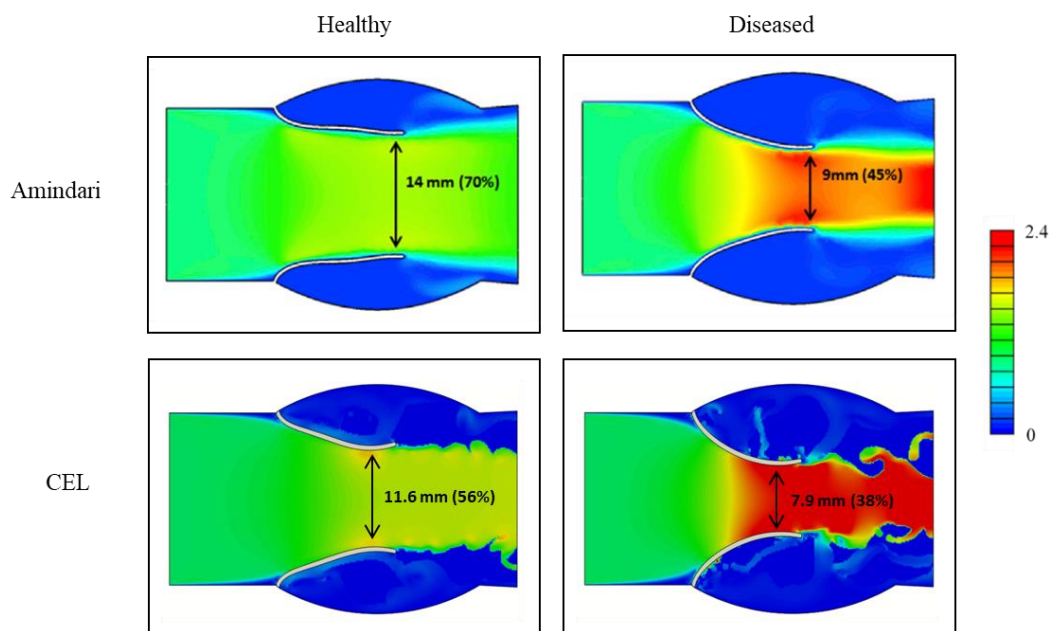


Figure 6.16 Velocity contour plots showing maximum opening diameter and maximum opening ratio for healthy and diseased valves

6.3.3 Measurement of Hydrodynamic Parameters

Having established the Abaqus/CEL method's ability to reproduce realistic deformation in an experimental leaflet, with comparable results to previous FSI studies in 2D leaflets, the model was then used to investigate its potential to measure the hydrodynamic parameters described in ISO 5840 standard for AVRs (which typically require in vitro pulsatile flow rigs). The following pressure and flow profiles were measured for the healthy and stenosed 2D valve simulations, shown in Figure 6.17.

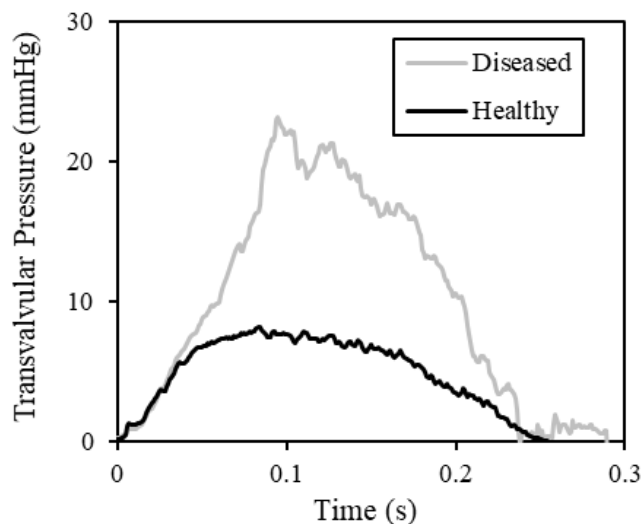


Figure 6.17 Transvalvular pressure profiles for 2D Abaqus/CEL simulations of healthy and diseased aortic valves

From these pressure and flow measurements, the Q_{rms} , transvalvular ΔP and EOA could be measured, as shown in Table 6.2. The transvalvular ΔP increased by 89% from the normal to diseased state, while the EOA reduced by 32% from the normal to diseased state.

Table 6.2 Hydrodynamic Parameters for healthy and diseased valves obtained from Abaqus/CEL models

	Young's Modulus (MPa)	Transvalvular ΔP (mmHg)	Effective Orifice Area (cm ²)
Healthy	2	4.95	1.18
Diseased	20	9.38	0.8

6.4 Discussion

In this study, the potential of Abaqus/CEL to be used to conduct in silico bench testing of aortic valves according to ISO 5840 was investigated. An in vitro flow rig was designed and manufactured to provide an initial benchmark of polymer leaflet deformation under 2D fluid flow, with predictions of the FSI model matching the predicted steady-state deformation and kinematics of this leaflet under flow. The model was extended to consider a 2D aortic valve simulation and compared to previous work of Amindari et al. (2017). Through this approach,

the Abaqus/CEL method produced comparable results to this ALE method. By evaluating pressure and flow parameters across the model, the ISO 5840 hydrodynamic parameters used for heart valve design could be determined, outlining the potential for this approach to be used for in silico design of AVRs.

While many FSI models have been proposed, very few have undergone robust experimental validation. Generally, studies that have presented validated models have tended to use bulk measurements of valve opening area or valve leaflet deformation (Gharaie et al., 2018; Ghosh et al., 2018). Few studies, if any, have examined the kinematics of a single leaflet under flow. In this chapter, a novel experimental rig was developed that allowed for the observation of a flexible leaflet deformation under 2D steady flow. The design of the rig was carefully considered by using CFD simulations to ensure the resulting flow profile followed rectangular channel flow conditions and that the region of interest was free of entrance effects. With these results, the flow rig was manufactured and the deformation of a polymer leaflet was investigated under steady-flow conditions. Under these conditions, it was found that the Abaqus/CEL approach predicted similar leaflet deformation once both systems had reached steady-state conditions. However, it is important to note that the ISO 5840 parameter of EOA is evaluated over the duration of the systolic cycle, and thus would require validation activities throughout the opening period of a valve. This study represents the first verification of the Abaqus/CEL approach in such a flow-based problem and highlighted its potential to be used to investigate the fluid and structural biomechanics of AVRs. Furthermore, this study is one of the first to provide a direct comparison between FSI simulations and experimental deformation of a single valve leaflet, as the majority of other validation approaches have investigated overall valve performance and focussed on metrics such as GOA (Gharaie et al., 2018; Luraghi et al., 2017). The experimental approach that has been developed here has the potential to be more

widely used as a first-step validation to FSI simulations and has already been used elsewhere to provide validation to other FSI simulations (Mcloone et al., 2021).

To investigate the potential of Abaqus/CEL method for *in silico* bench testing, the model was extended to consider 2D valve simulations and compared to the previous work of Amindari et al. (2017), which used a coupled FSI simulation developed in the ALE method. This approach required both fluid and solid domains to conform to one another and can present certain challenges in modelling the full systolic opening of AVRs, as demonstrated by Bavo *et al.* (2016). The Abaqus/CEL method showed comparable performance to the study of Amindari et al. (2017), and captured similar relative reductions in performance between the healthy and diseased valves. However, certain differences were observed, in particular the predicted jet velocity and maximum TPG by the Abaqus/CEL approach were higher than Amindari et al. (2017), while the maximum orifice diameter and opening ratios were also lower using the Abaqus/CEL approach. However, this study demonstrated the ability of the Abaqus/CEL approach to generate and extract the ISO 5840 hydrodynamic parameters of transvalvular and EOA. While validation of these parameters is more difficult, clear differences between the healthy and diseased valve were observed in the parameter study undertaken. Here, increases in transvalvular ΔP , and a reduction in EOA were evident in the simulations of the stiffened valve, as would be expected. Being able to measure the ISO 5840 standard parameters, this study shows the potential of Abaqus/CEL to be used in 3D valve models. This is relevant as the design and manufacture of heart valve replacement is a long process. Trial-and-error prototyping, followed by extensive *in vitro* testing is time intensive. The development of FSI methods that could replicate the *in vitro* pulsatile flow rigs would be of great benefit and could compare valve designs early in the development process.

Other limitations of the 2D Abaqus/CEL approach presented here include that only the systolic phase is considered. As has been previously documented for other FSI approaches (Bavo et al.,

2016), 2D representations of the aortic valve tend to result in leaflet inversion when diastolic conditions are predicted. For that reason, this study therefore only focused on the systolic period of the valve and measured the systolic parameters. The Abaqus/CEL method was also shown to be capable of measuring bulk parameters but was limited in its ability to maintain a constant fluid volume in the domain. The initial definition of the VOF saw regions of void form at the systolic sides of the leaflets as the simulation progressed throughout systole. This is a significant limitation as it does not allow for measurement of velocity profiles or pressures in the sinus. Rather, the jet velocity profile remained intact as it emerged from the leaflets, allowing for measurement of the EOA and TPG, as well as deformation metrics. However, the models still provided reasonable predictions of valve performance and the study included one of the first initial validations for leaflet deformation. The results here suggest that the model can be extended to 3D to investigate the performance of realistic AVRs, and potentially paves the way for in silico bench testing of these devices once an appropriate validation strategy is used. This is the subject of Chapter 7, where an in vitro study of a tricuspid and bicuspid valve is recreated using a 3D FSI simulation in Abaqus/CEL.

6.5 Conclusions

In this chapter, an experimental flow rig was developed to compare the deformation of a flexible leaflet under flow with 2D FSI simulations using the Abaqus/CEL method, with the intention to use the work as a basis for more complicated 3D models. The comparison of leaflet deformation showed good agreement. Furthermore, the Abaqus/CEL method was then used to recreate 2D valve simulations from the literature which again gave comparable results. The results of this chapter indicate that the method is suitable for further development of the 3D valve models, which is addressed in Chapter 7.

6.6 References

- Ahmadzadeh, M., Saranjam, B., Hoseini Yard, A., Binesh, A.R., 2014. Numerical simulation of sphere water entry problem using Eulerian-Lagrangian method. *Appl. Math. Model.* 38, 1673–1684. <https://doi.org/10.1016/j.apm.2013.09.005>
- Akins, C.W., Travis, B., Yoganathan, A.P., 2008. Energy loss for evaluating heart valve performance. *J. Thorac. Cardiovasc. Surg.* 136, 820–833. <https://doi.org/10.1016/j.jtcvs.2007.12.059>
- Amindari, A., Saltik, L., Kirkkopru, K., Yacoub, M., Yalcin, H.C., 2017. Assessment of calcified aortic valve leaflet deformations and blood flow dynamics using fluid-structure interaction modeling. *Informatics Med. Unlocked* 9, 191–199. <https://doi.org/10.1016/j.imu.2017.09.001>
- Arzani, A., Mofrad, M.R.K., 2017. A strain-based finite element model for calcification progression in aortic valves. *J. Biomech.* 65, 216–220. <https://doi.org/10.1016/j.jbiomech.2017.10.014>
- Baumgartner, H., Falk, V., Bax, J.J., De Bonis, M., Hamm, C., Holm, P.J., Iung, B., Lancellotti, P., Lansac, E., Muñoz, D.R., Rosenhek, R., Sjögren, J., Tornos Mas, P., Vahanian, A., Walther, T., Wendler, O., Windecker, S., Zamorano, J.L., Roffi, M., Alfieri, O., Agewall, S., Ahlsson, A., Barbato, E., Bueno, H., Collet, J.P., Coman, I.M., Czerny, M., Delgado, V., Fitzsimons, D., Folliguet, T., Gaemperli, O., Habib, G., Harringer, W., Haude, M., Hindricks, G., Katus, H.A., Knuuti, J., Kolh, P., Leclercq, C., McDonagh, T.A., Piepoli, M.F., Pierard, L.A., Ponikowski, P., Rosano, G.M.C., Ruschitzka, F., Shlyakhto, E., Simpson, I.A., Sousa-Uva, M., Stepinska, J., Tarantini, G., Tche, D., Aboyans, V., Kzhdryan, H.K., Mascherbauer, J., Samadov, F., Shumavets, V., Van Camp, G., Loncar, D., Lovric, D., Georgiou, G.M., Linhartova, K., Ihlemann, N., Abdelhamid, M., Pern, T., Turpeinen, A., Srbinovska-Kostovska, E., Cohen, A., Bakhutashvili, Z., Ince, H., Vavuranakis, M., Temesvari, A., Gudnason, T., Mylotte, D., Kuperstein, R., Indolfi, C., Pya, Y., Bajraktari, G., Kerimkulova, A., Rudzitis, A., Mizariene, V., Lebrun, F., Demarco, D.C., Oukerraj, L., Bouma, B.J., Steigen, T.K., Komar, M., De Moura Branco, L.M., Popescu, B.A., Uspenskiy, V., Foscoli, M., Jovovic, L., Simkova, I., Bunc, M., de Prada, J.A.V., Stagmo, M., Kaufmann, B.A., Mahdhaoui, A., Bozkurt, E., Nesukay, E., Brecker, S.J.D., 2017. 2017 ESC/EACTS Guidelines for the management of valvular heart disease, *European Heart Journal*. <https://doi.org/10.1093/eurheartj/ehx391>
- Bavo, A.M., Rocatello, G., Iannaccone, F., Degroote, J., Vierendeels, J., Segers, P., 2016. Fluid-Structure Interaction Simulation of Prosthetic Aortic Valves: Comparison between Immersed Boundary and Arbitrary Lagrangian-Eulerian Techniques for the Mesh Representation. *PLoS One* 11. <https://doi.org/10.1371/journal.pone.0154517>
- Borowski, F., Sämman, M., Pfensig, S., Wüstenhagen, C., Ott, R., Kaule, S., Siewert, S., Grabow, N., Schmitz, K.P., Stiehm, M., 2018. Fluid-structure interaction of heart valve dynamics in comparison to finite-element analysis. *Curr. Dir. Biomed. Eng.* 4, 259–262. <https://doi.org/10.1515/cdbme-2018-0063>
- Chen, Y., Luo, H., 2018. A computational study of the three-dimensional fluid–structure interaction of aortic valve. *J. Fluids Struct.* 80, 332–349. <https://doi.org/10.1016/j.jfluidstructs.2018.04.009>
- Ducobu, F., Arrazola, P.J., Rivière-Lorphèvre, E., Zarate, G.O. De, Madariaga, A., Filippi, E., 2017. The CEL Method as an Alternative to the Current Modelling Approaches for Ti6Al4V

Orthogonal Cutting Simulation. *Procedia CIRP* 58, 245–250. <https://doi.org/10.1016/j.procir.2017.03.188>

Ducobu, F., Rivière-Lorphèvre, E., Filippi, E., 2016. Application of the Coupled Eulerian-Lagrangian (CEL) method to the modeling of orthogonal cutting. *Eur. J. Mech. A/Solids* 59, 58–66. <https://doi.org/10.1016/j.euromechsol.2016.03.008>

Garcia, D., Kadem, L., 2006. What do you mean by aortic valve area: Geometric orifice area, effective orifice area, or Gorlin area? *J. Heart Valve Dis.*

Gharaie, S.H., Mosadegh, B., Morsi, Y., 2018. In Vitro Validation of a Numerical Simulation of Leaflet Kinematics in a Polymeric Aortic Valve Under Physiological Conditions. *Cardiovasc. Eng. Technol.* 9, 42–52. <https://doi.org/10.1007/s13239-018-0340-7>

Ghosh, R.P., Marom, G., Rotman, O.M., Slepian, M.J., Prabhakar, S., Horner, M., Bluestein, D., 2018. Comparative fluid-structure interaction analysis of polymeric transcatheter and surgical aortic valves' hemodynamics and structural mechanics, *Journal of Biomechanical Engineering*. <https://doi.org/10.1115/1.4040600>

Gorlin, R., Gorlin, S.G., 1951. Hydraulic formula for calculation of the area of the stenotic mitral valve, other cardiac valves, and central circulatory shunts. I. *Am. Heart J.* 41, 1–29. [https://doi.org/10.1016/0002-8703\(51\)90002-6](https://doi.org/10.1016/0002-8703(51)90002-6)

Halevi, R., Hamdan, A., Marom, G., Lavon, K., Ben-Zekry, S., Raanani, E., Bluestein, D., Haj-Ali, R., 2016. Fluid–structure interaction modeling of calcific aortic valve disease using patient-specific three-dimensional calcification scans. *Med. Biol. Eng. Comput.* 54, 1683–1694. <https://doi.org/10.1007/s11517-016-1458-0>

Hedayat, M., Asgharzadeh, H., Borazjani, I., 2017. Platelet activation of mechanical versus bioprosthetic heart valves during systole. *J. Biomech.* 56, 111–116. <https://doi.org/10.1016/j.jbiomech.2017.03.002>

Kandail, H.S., Trivedi, S.D., Shaikh, A.C., Bajwa, T.K., O'Hair, D.P., Jahangir, A., LaDisa, J.F., 2018. Impact of annular and supra-annular CoreValve deployment locations on aortic and coronary artery hemodynamics. *J. Mech. Behav. Biomed. Mater.* 86, 131–142. <https://doi.org/10.1016/j.jmbbm.2018.06.032>

Laadhari, A., Székely, G., 2017. Eulerian finite element method for the numerical modeling of fluid dynamics of natural and pathological aortic valves. *J. Comput. Appl. Math.* 319, 236–261. <https://doi.org/10.1016/j.cam.2016.11.042>

Labrosse, M.R., Lobo, K., Beller, C.J., 2010. Structural analysis of the natural aortic valve in dynamics: From unpressurized to physiologically loaded. *J. Biomech.* 43, 1916–1922. <https://doi.org/10.1016/j.jbiomech.2010.03.020>

Luraghi, G., Matas, J.F.R., Beretta, M., Chiozzi, N., Iannetti, L., Migliavacca, F., 2020. The impact of calcification patterns in transcatheter aortic valve performance: a fluid-structure interaction analysis. *Comput. Methods Biomech. Biomed. Engin.* 24, 375–383. <https://doi.org/10.1080/10255842.2020.1817409>

Luraghi, G., Migliavacca, F., García-González, A., Chiastra, C., Rossi, A., Cao, D., Stefanini, G., Rodriguez Matas, J.F., 2019. On the Modeling of Patient-Specific Transcatheter Aortic Valve Replacement: A Fluid–Structure Interaction Approach. *Cardiovasc. Eng. Technol.* 10, 437–455. <https://doi.org/10.1007/s13239-019-00427-0>

- Luraghi, G., Wu, W., De Gaetano, F., Rodriguez Matas, J.F., Moggridge, G.D., Serrani, M., Stasiak, J., Costantino, M.L., Migliavacca, F., 2017. Evaluation of an aortic valve prosthesis: Fluid-structure interaction or structural simulation? *J. Biomech.* 58, 45–51. <https://doi.org/10.1016/j.jbiomech.2017.04.004>
- Mcloone, M., Fan, Y., Whiting, R., Conway, C., Roche, E., Quinlan, N., 2021. Fluid-Structure Interaction of a Thin Elastic Leaflet – a Comparison of Computational Methods. *European Society of Biomechanics*.
- Morrison, N., Gorash, Y., Hamilton, R., 2018. Consideration of fluid-structure interaction with the CEL approach for the FE-prediction of a blow-off pressure for an elastomeric seal. *24th Int. Conf. Fluid Seal.* 31–45.
- Nishimura, R.A., Otto, C.M., Bonow, R.O., Carabello, B.A., Erwin, J.P., Guyton, R.A., O’Gara, P.T., Ruiz, C.E., Skubas, N.J., Sorajja, P., Sundt, T.M., Thomas, J.D., 2014. 2014 AHA/ACC guideline for the management of patients with valvular heart disease: A report of the American college of cardiology/American heart association task force on practice guidelines. *J. Am. Coll. Cardiol.* 63. <https://doi.org/10.1016/j.jacc.2014.02.536>
- Peskin, C.S., 2002. The immersed boundary method. *Acta Numer.* 11, 479–517. <https://doi.org/10.1017/S0962492902000077>
- Piatti, F., Sturla, F., Marom, G., Sheriff, J., Claiborne, T.E., Slepian, M.J., Redaelli, A., Bluestein, D., 2016. Polymeric Valve Using a Fluid-Structure Interaction Approach 48, 3650–3658. <https://doi.org/10.1016/j.jbiomech.2015.08.009>. Hemodynamic
- Qiu, G., Henke, S., Grabe, J., 2011. Application of a Coupled Eulerian-Lagrangian approach on geomechanical problems involving large deformations. *Comput. Geotech.* 38, 30–39. <https://doi.org/10.1016/j.compgeo.2010.09.002>
- Simulia, 2017. Dassault Systèmes, Providence, RI.
- Sodhani, D., Reese, S., Aksenov, A., Soğancı, S., Jockenhövel, S., Mela, P., Stapleton, S.E., 2018. Fluid-structure interaction simulation of artificial textile reinforced aortic heart valve: Validation with an in-vitro test. *J. Biomech.* 78, 52–69. <https://doi.org/10.1016/j.jbiomech.2018.07.018>
- Tango, A.M., Salmonsmith, J., Ducci, A., Burriesci, G., 2018. Validation and Extension of a Fluid–Structure Interaction Model of the Healthy Aortic Valve. *Cardiovasc. Eng. Technol.* 9, 739–751. <https://doi.org/10.1007/s13239-018-00391-1>
- Whiting, R., Sander, E., Conway, C., Vaughan, T.J., 2022. In silico modelling of aortic valve implants—predicting in vitro performance using finite element analysis. *J. Med. Eng. Technol.* 46, 220–230. <https://doi.org/10.1080/03091902.2022.202650>

CHAPTER 7

3D Fluid-Structure Interaction Modelling of Bicuspid and Tricuspid Aortic Valve Hydrodynamic Performance

7.1 Introduction

In Chapter 6, it was demonstrated that the Abaqus Coupled Eulerian Lagrangian (CEL) method offers the potential to conduct *in silico* bench testing using a 2D representation of valve leaflets and an aortic root. However, this 2D model did not account for the tri-leaflet arrangement of the valve or the geometrical profile of the leaflet cusps, and thus cannot describe a realistic deformation of the leaflets. Furthermore, it has been shown that 2D valve fluid-structure interaction (FSI) simulations are unable to predict diastolic pressure conditions as the 2D geometry results in inversion of the 2D leaflet cusps (Amindari et al., 2017; Bavo et al., 2016). In Chapters 4 and 5, 3D finite element-based models were used to enable surrogate predictions of *in vitro* hydrodynamic performance of tri-leaflet aortic valve implants by using the

Windkessel and Bernoulli models to generate pressure-based boundary conditions representing the effect of the fluid domain on the valve. While these provided insight into several key metrics of valvular performance, the results generally predicted uniform deformation of the valve, which tends to be an unrealistic representation of the leaflet deformation (Luraghi et al., 2017). To fully represent more complex valve deformation, a 3D simulation of the interaction between fluid and structural components of the aortic valve is required.

Several 3D FSI frameworks have previously been implemented to predict the fluid and structural performance of aortic valve replacements (AVRs). These have simulated valvular flow through the aorta (Kandail et al., 2018) or have replicated in vitro experimental set-ups (Gharaie et al., 2018; Ghosh et al., 2018). These models have predicted overall deformation and leaflet kinematics in the valve, as well as velocity and pressure profiles, wall shear stresses at the leaflet-wall-blood boundary (Kandail et al., 2018) and blood flow vortices (Gharaie et al., 2018) in the fluid domain. However, during the valve development process, the performance of an AVR in relation to the ISO 5840 standard is of particular interest. Specifically, the performance of prototype valves in the context of the ISO 5840 requires benchtop evaluation of effective orifice area (EOA), regurgitant fraction (RF) and transvalvular pressure drop (ΔP) using in vitro pulsatile flow rigs (Rahmani et al., 2017, 2012; Rotman et al., 2019). Several authors have proposed that FSI simulations could also be used to determine these parameters in silico (Chen and Luo, 2018; Hsu et al., 2015; Mao et al., 2016), although few studies have included any comparison to in vitro experiments or in vivo data (Borowski et al., 2018; Chen and Luo, 2018; Flamini et al., 2016). While some studies have compared in silico predictions to particle integrated velocimetry (PIV) data (Abu Bakar et al., 2018) and Doppler velocimetry (Luraghi et al., 2019), only a limited number of studies have directly compared in silico predictions to ISO 5840 parameters determined from experimental testing (Ghosh et al., 2018; Piatti et al., 2016; Sturla et al., 2020). Ghosh et al. (2018) evaluated the performance of a

surgical (SAVR) and transcatheter aortic valve design (TAVR) using an Arbitrary Lagrangian Eulerian (ALE) approach. The *in silico* simulations were compared to *in vitro* test results obtained from a pulse duplicator system, where the models were found to show good qualitative agreement with the experiment in terms of both GOA and valve deformation. Furthermore, the EOA was evaluated and found to be within 15% of the value determined *in vitro*. This approach offers excellent potential in valve design and could enable the development of virtual prototyping during the development phase. However, the ALE FSI model framework is computationally expensive, and typically requires an adaptive meshing algorithm to capture large deformation leaflet kinematics. For better computational efficiency, immersed boundary (IB) simulations have also been used (Flamini et al., 2015), whereby a flexible Lagrangian structure deforms within a fixed Eulerian mesh, similar to the Abaqus/CEL method which was used in Chapter 6. To the author's knowledge, Bavo et al. (2016) presented the only 3D aortic valve implementation of an immersed boundary FSI model using the Abaqus/CEL approach. Their study investigated the differences between the Abaqus/CEL method and ALE FSI techniques when applied to heart valve simulations. Despite the fact that the Abaqus/CEL method had previously been more widely implemented in non-flow based simulations (e.g. orthogonal cutting, soil erosion, and high impact simulations (Ahmadzadeh et al., 2014; Ducobu et al., 2017, 2016; Morrison et al., 2018; Qiu et al., 2011), Bavo et al. (2016) showed that the method was capable of predicting flow through an aortic valve, while also predicting leaflet deformation and flow velocities similar to the ALE method. While it was concluded that the Abaqus/CEL method was better suited to modelling high-speed deformation during the opening systolic phase of the valve when compared with the mesh conforming ALE method, their study did not include any experimental component to provide validation for either model. To the author's knowledge, FSI predictions of valve performance determined through the

Abaqus/CEL approach have never been compared to experimental tests and this limits their applicability in the development of such devices.

In this chapter, a 3D FSI model was developed using the commercially-available Abaqus/CEL method. The study examines the potential of the FSI method to predict hydrodynamic performance of AVRs by comparing results directly with in vitro data from experimental testing using a pulsatile flow rig. This study is unique to the existing literature in that it includes an in-depth comparison between in silico predictions and in vitro flow measurements on both a tricuspid and bicuspid valve configuration. The FSI method was evaluated for its capability to measure the ISO 5840 required parameters of EOA and transvalvular ΔP .

7.2 Materials and Methods

7.2.1 Aortic Valve Design

A surgical AVR was designed and manufactured from a synthetic polyurethane elastomer variant, developed at the University of Galway. This design was identical to those used in Chapters 4 and 5 and featured a common tri-leaflet design with an internal orifice diameter of 23 mm (± 0.2 mm), an embedded steel wire frame to provide radial reinforcement, and a skirt/suture ring around the basal circumference to enable mounting during in vitro testing, as shown in Figure 7.1. For the bicuspid version of the valve, cyanoacrylate was applied between two of the leaflets to enforce cohesion and constrain their movement.

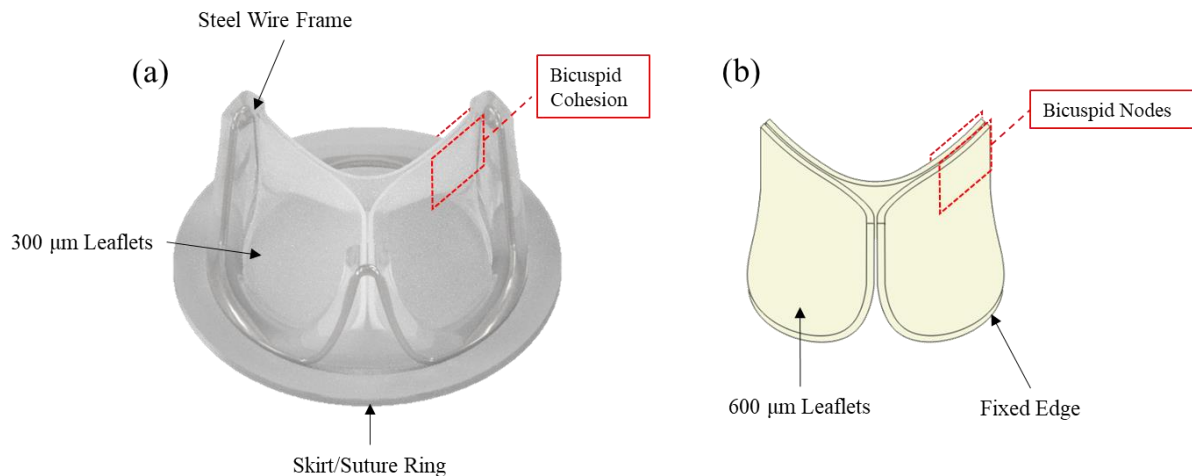


Figure 7.1 (a) Valve Geometry showing tricuspid valve and highlights region for cohesion in the bicuspid version. (b) 3D geometry of the valve leaflets showing location of bicuspid nodes.

7.2.2 In Vitro Hydrodynamic Testing

To evaluate the hydrodynamic performance of the tricuspid and bicuspid valves, in vitro bench testing was performed using a Vivitro Pulse Duplicator (Vivitro Labs, Inc. Victoria, B.C.) according to ISO 5840. Testing consisted of the valves being sealed in a mounting ring and placed in the aortic position between the ventricular sac and aorta of the flow rig, as described in Chapters 4 and 5 and shown in Figure 7.2a. The flow rig was filled with 0.9% NaCl solution at room temperature (≈ 20 °C). High-speed images were captured using a Sony RX100 Mark IV camera at a frame rate of 1000 fps to visualise open and closing configurations of valves during testing. Vivitest software (Vivitro Labs, Inc. Victoria, B.C.) recorded pressure and flow measurements over 10 consecutive cycles, which were used to calculate several hydrodynamic parameters, namely the EOA, RF and transvalvular ΔP , as shown in Figure 7.2b. To compare the performance of the bicuspid and tricuspid aortic valve, each valve was tested at 4 L/min Cardiac Output with a MAP of 100 mmHg.

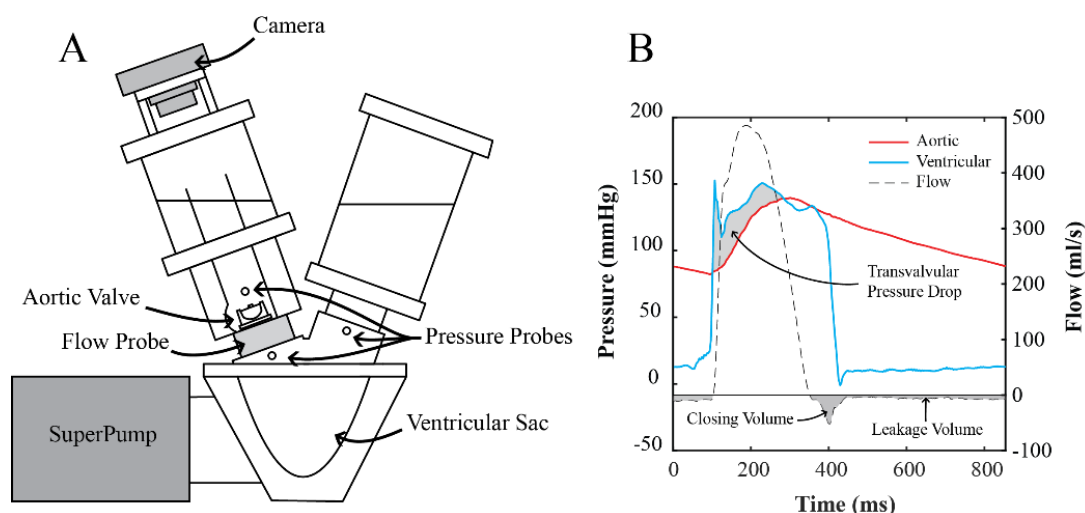


Figure 7.2 (a) Schematic of Vitro Left Heart Simulator with pressure transducers and a flow probe which was used to carry out in vitro hydrodynamic testing, (b) a typical diagram of average flow measurements, aortic and ventricular pressures measured over 10 cardiac cycles

7.2.3 FSI Model Formulation

An FSI model of the AVR devices undergoing pulsatile testing was developed in Abaqus/CEL. The geometry of the FSI model was based on the Vitro pulse duplicator flow rig. Here, the aortic valve was housed below the aortic pressure transducer and outflow tract, while above the ventricular sac were the flow probe and pressure transducer (see Figure 7.3a). For the FSI model, this section was modelled as the region of interest and a fluid domain of length 30 mm and diameter of 20 mm was considered (see Figure 7.3b). This meant that the overall mesh was limited to the width of the leaflets to reduce the computational power required to model the entire outflow tract. The fluid domain was meshed with 971,600 8-noded Eulerian reduced integration elements (EC3D8R) (see Figure 7.3c). To reduce computational time, the valve leaflets were scaled to twice their original thickness ($t = 600 \mu\text{m}$), which was compensated by reducing the Young's modulus two-fold ($E = 1.9 \text{ MPa}$). The leaflets were meshed with 52,380 hexahedral 8-noded Lagrangian elements (C3D8) (see Figure 7.3c). The valve leaflets were modelled independently of the valve skirt and stent posts. The stent/post attachment edges of

the leaflets were assigned a fixed boundary condition, while the free edges of the leaflet were unconstrained.

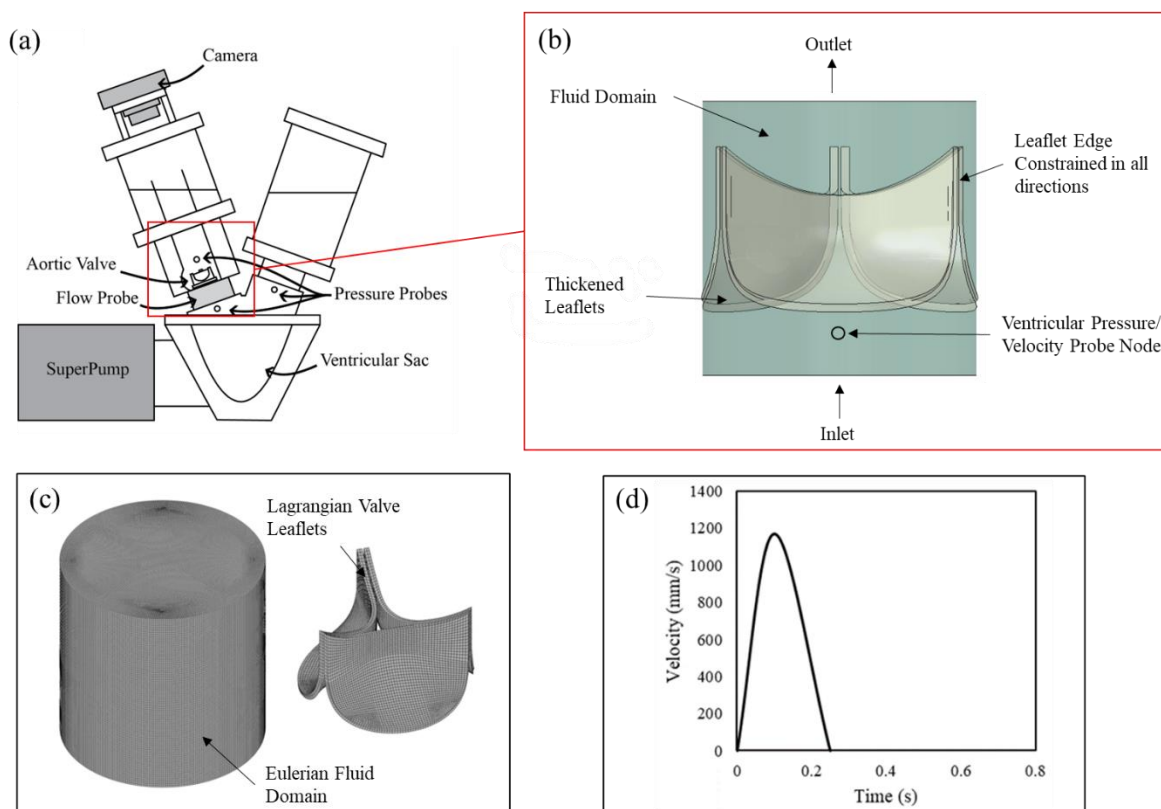


Figure 7.3 (a) Schematic of Vitro Left Heart Simulator with pressure transducers and a flow probe which was used to carry out in vitro hydrodynamic testing, (b) Fluid domain and leaflets assembly showing placement of probe node (c) Eulerian fluid domain mesh (left) and structural Lagrangian valve leaflet mesh (right), (d) In silico applied velocity profile boundary condition at inlet

The fluid domain was assigned a physiological velocity profile at the inlet as shown in Figure 7.3d, which corresponded to a 4 L/min flow rate in the fluid domain. The outlet was assigned a free outflow boundary condition. The walls were assigned no-slip conditions, while the contact between the fluid and leaflets was modelled using the default penalty contact method. A probe node was defined just below the aortic valve to measure the resulting pressure and flow. An equation of state, the $U_s - U_p$ formulation, was used to model the fluid in the Eulerian domain and is given by:

$$U_s = C_0 + sU_p \quad (7.1)$$

Where U_s is the linear shock velocity, U_p is the particle velocity, C_0 is the speed of sound in the fluid, and s is a parameter of the approximation. To examine the change in response from thickening the leaflets, structural simulations comparing the 300 μm and 600 μm thick leaflets at a Young's modulus of 3.8 MPa and 1.9 MPa respectively were performed. Systolic (35 mmHg) and Diastolic (100 mmHg) pressure loads were applied as in Chapter 5. The maximum Logarithmic Strain, von Mises stress and GOA were compared across each valve and Cardiac Phase. Figure 7.4 shows the von Mises stress for each condition. The change from 300 μm to 600 μm leaflets in diastole resulted in a 19% increase in Logarithmic Strain, and a 40% decrease in von Mises Stress. In systole, the changes resulted in a 10% decrease in Logarithmic Strain, and a 47% decrease in von Mises Stress. Looking at the GOA in Systole, there was a slight drop of 5% from the 300 μm leaflets to the 600 μm leaflets. These results highlighted the difference in stress and strain response from changing the modulus and thickness of the leaflets, while showing that the GOA at systole remained representative.

Table 7.1 Max Principal Stress and Logarithmic Strain for 300 μm and 600 μm leaflets in Diastolic and Systolic Conditions

Leaflet Thickness	Young's Modulus	Cardiac Phase	Logarithmic Strain	von Mises Stress	Geometric Orifice Area
<i>μm</i>	<i>MPa</i>		<i>%</i>	<i>MPa</i>	<i>mm^2</i>
300	3.8	Diastole	0.139	0.528	N/A
		Systole	0.414	1.681	175.01
600	1.9	Diastole	0.166	0.318	N/A
		Systole	0.373	0.897	167.11

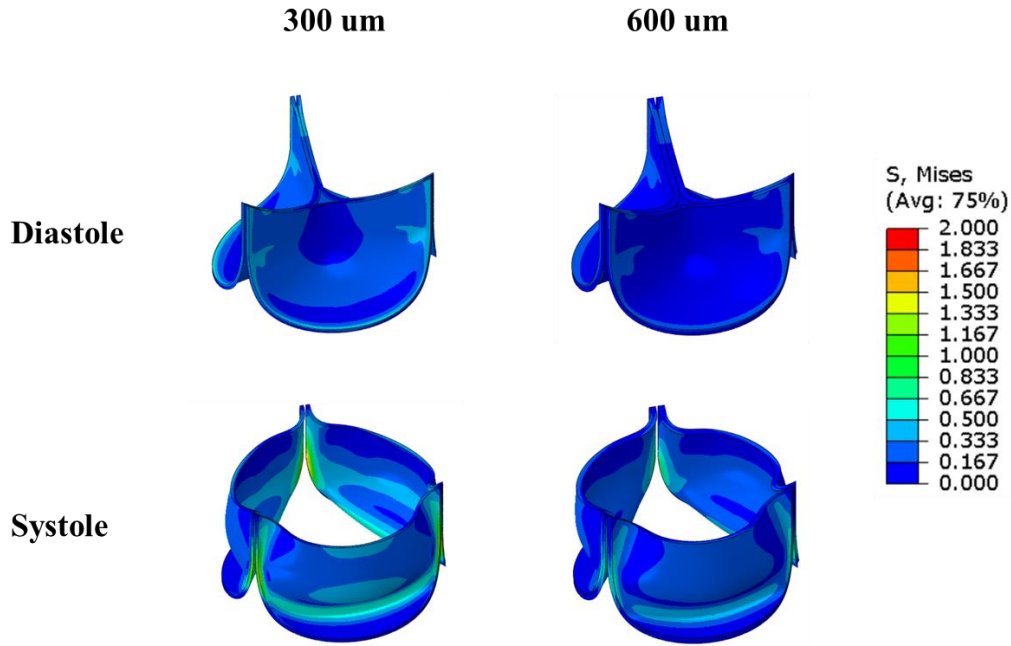


Figure 7.4 von Mises stress contour plot (MPa) for 300 μm and 600 μm thick leaflets in Diastolic and Systolic conditions

7.2.4 Hydrodynamic Parameters

The FSI model was used to evaluate both the EOA and the transvalvular ΔP , through the use of virtual probes that determined the velocity and pressure at specific points in the model. These measurements were taken at the same locations as those taken in the pulsatile flow rig itself. Again, the EOA was defined as the minimal cross-sectional area of the jet formed downstream of the aortic valve (Akins et al., 2008; Garcia and Kadem, 2006) and was calculated for both using the Gorlin Formula (Gorlin and Gorlin, 1951) given by,

$$EOA = \frac{Q_{RMS}}{51.6 \sqrt{\frac{\Delta P}{\rho}}} \quad (7.2)$$

where Q_{RMS} is the root mean squared forward flow (ml/sec), ΔP is the mean transvalvular pressure drop (mmHg) and ρ is the density of the test fluid (g/cm^3). The Q_{RMS} is calculated by:

$$Q_{RMS} = \sqrt{\frac{\int_{t_1}^{t_2} Q(t)^2 dt}{t_2 - t_1}} \quad (7.3)$$

The transvalvular ΔP , refers to the pressure gradient across the valve during systole where the ventricles contract ejecting blood into the aorta and pulmonary artery. It was calculated as the mean pressure difference between the start and end of the systole positive pressure drop.

7.3 Results

7.3.1 In Vitro and In Silico Comparison

In vitro hydrodynamic testing of both a tricuspid and bicuspid valve was carried out using the Vivitro pulsatile flow rig (ViVitro Labs, Inc., Victoria, BC, Canada). The aortic and ventricular pressure and flow profiles for each valve are shown in Figure 7.5. These results show that the bicuspid valve exhibits a larger transvalvular pressure drop than the tricuspid valve. This is evident from the high ventricular pressure during the systolic period with forward flow rate.

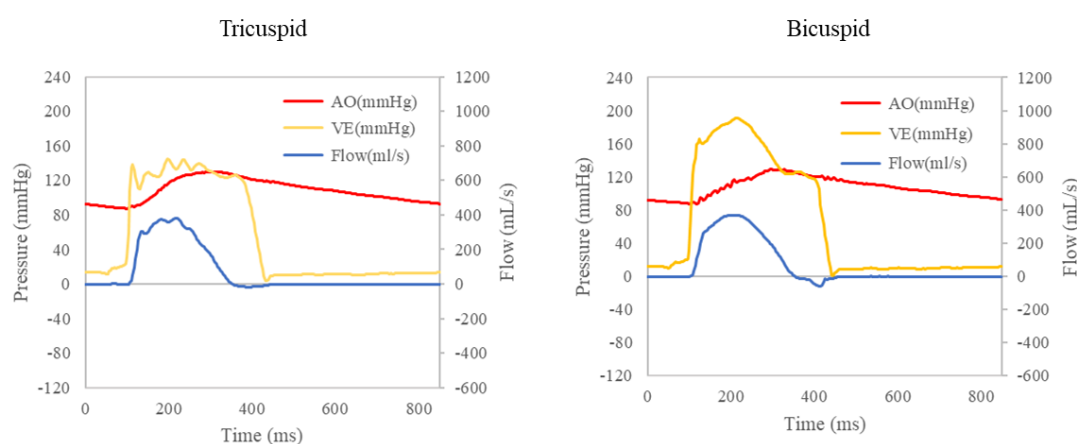


Figure 7.5 In vitro hydrodynamic pressure and flow profiles for the Tricuspid and Bicuspid valve, where AO is the aortic pressure and VE is the ventricular pressure

The in vitro deformation of the valve at peak systole is shown in Figure 7.6a. Here, the three tricuspid leaflets can be seen to extend open, in contrast to the bicuspid valve where the artificial raphe between two of the leaflets results in a much smaller orifice. The transition of the valve from closed to open at the start of systole is shown in Figure 7.6a. Here, both valves open rapidly over a period of 0.02s. Also shown in Figure 7.6a is the predicted in silico deformation of the valves. Here, there is qualitatively good agreement between the opening

profiles comparing the in vitro and in silico tests. In particular, the in silico model captures asymmetric opening for the tricuspid valve, with some oscillation of the leaflets evident, similar to what was observed in vitro (see Figure 7.6a). For both in vitro and in silico deformations, the bicuspid valve has an eccentric opening profile, and a smaller geometric orifice area (GOA). Comparing performance quantitatively, Figure 7.6b shows a graph of the measured GOA from both the in silico and in vitro simulations. The in silico model closely predicts the maximum GOA for both bicuspid and tricuspid valves over the course of the opening systolic phase. Here, it is also evident that there is greater oscillation of the valve GOA in the experimental test over the course of the cycle, particularly for the tricuspid valve. While the in silico model captures oscillation in the leaflets when open, it seems the GOA more steadily increases during the opening systolic phase.

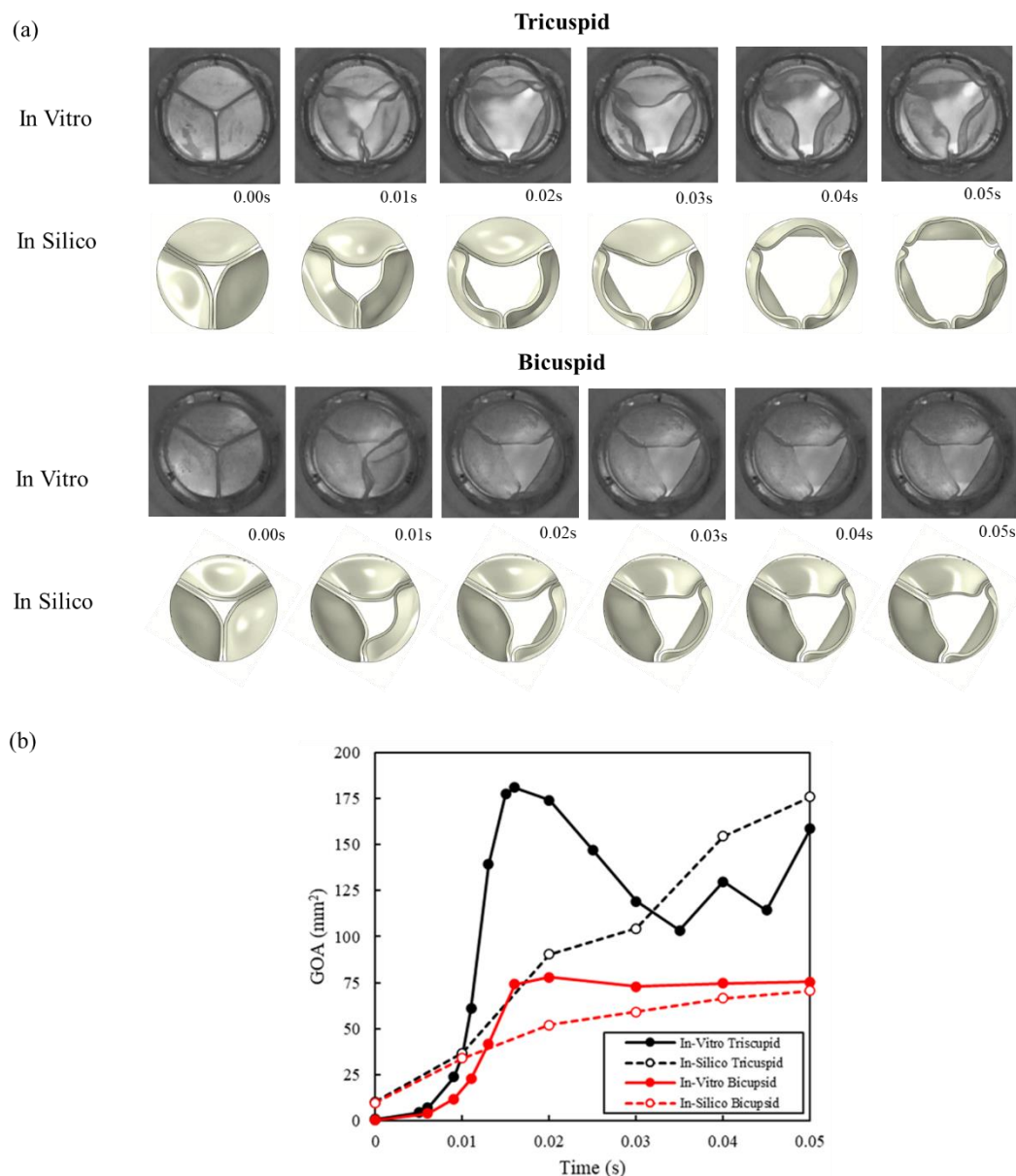


Figure 7.6 (a) Valve deformation at 0 – 0.05s (normalised to start of opening) for bicuspid and tricuspid valves. (b) GOA over time for the in silico and in vitro bicuspid and tricuspid experiments

7.3.2 In Silico Hydrodynamic Testing

The measured values of EOA and transvalvular ΔP for the in vitro experiments and in silico simulations are shown in Table 7.2. Here, the in silico measurements of these ISO parameters are taken by virtual probe nodes at the relevant locations in the model. Both in silico and in vitro approaches predict a substantially higher transvalvular ΔP for the bicuspid valve, with a 5% difference in predictions. Similarly, both approaches predict lower EOAs for the bicuspid

valve, with a 3% difference in predictions for the bicuspid case. However, there is a greater difference between in vitro and in silico predictions for transvalvular ΔP and EOA in the tricuspid case. Here, the in silico prediction for transvalvular ΔP was ~80% higher compared with the in vitro test, while the predicted EOA was 33% lower than the experimental value.

Table 7.2 Hydrodynamic performance parameters for bicuspid and tricuspid valves

Valve	Transvalvular Pressure Drop ΔP (mmHg)		Effective Orifice Area (cm ²)	
	In Vitro	In Silico	In Vitro	In Silico
Bicuspid	55.8	58.8	0.747	0.77
Tricuspid	16.2	29.8	1.5	1

7.3.3 Fluid and Structural In Silico Results

The FSI simulations provided results for both fluid and structural components of the valves being tested. Figure 7.7 shows the velocity flow profiles throughout systole for both the bicuspid and tricuspid valves. Here, higher velocities were observed through the bicuspid valve, where free deformation was confined to one leaflet cusp. The bicuspid valve shows an eccentric velocity profile, emerging away from the centre of the valve and to the side where the orifice can open. The tricuspid valve features a velocity profile that oscillates around the centre of the orifice.

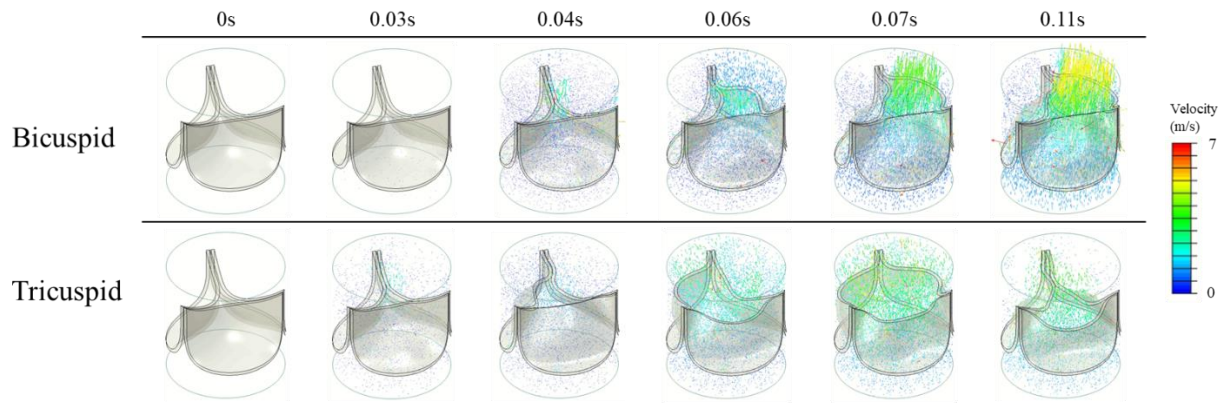


Figure 7.7 Velocity flow profiles with valve deformation at time-points spanning 0 – 0.11s for bicuspid (top) and tricuspid (bottom) valves

The valve von Mises stress distribution with valve deformation is plotted in Figure 7.8a. The bicuspid valve showed higher stress in the one unconstrained leaflet. The tricuspid valve in contrast had the stress distributed evenly throughout the three leaflets. A violin plot in Figure 7.8b describes the distribution of the stress, where the peak and median von Mises stress at systole are higher in the bicuspid valve compared to the tricuspid valve.

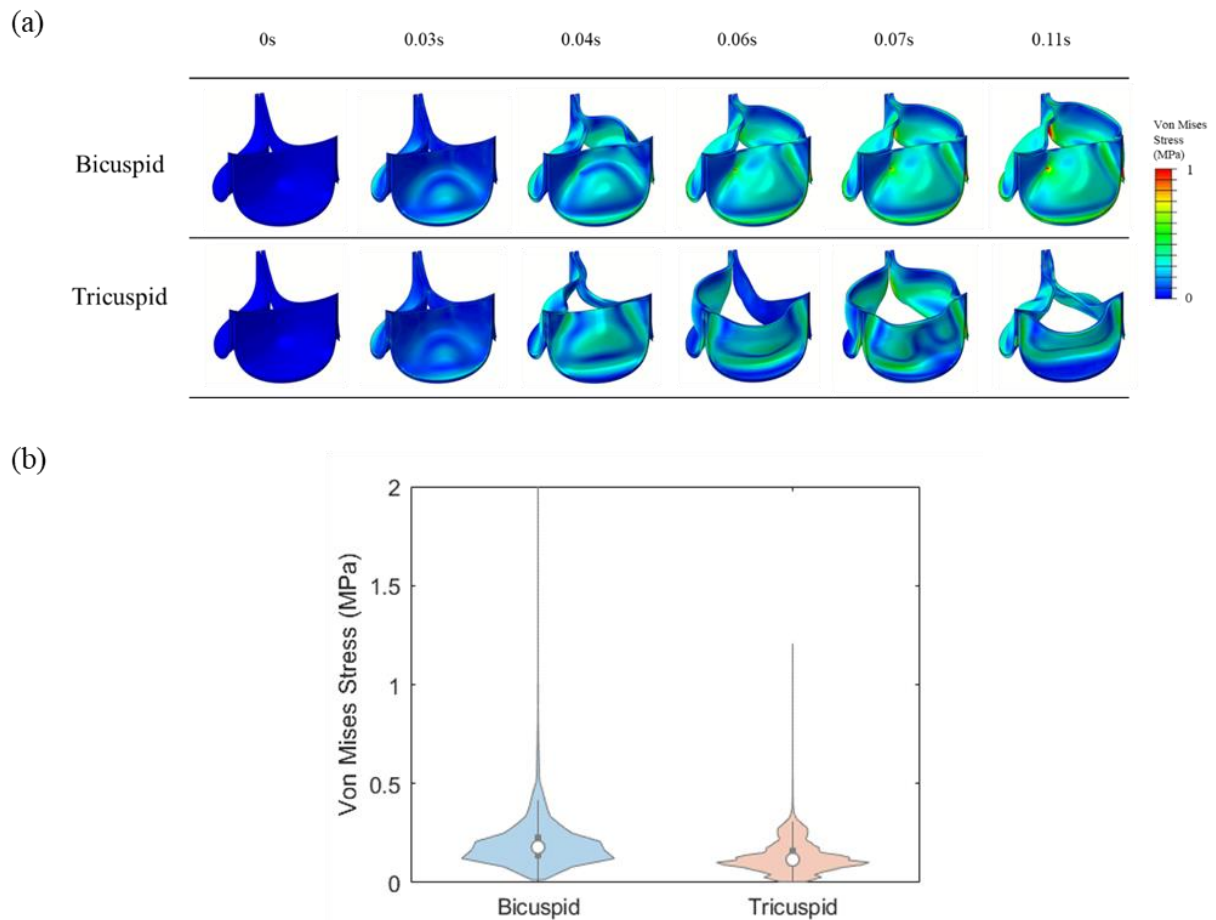


Figure 7.8 (a) von Mises Stress (MPa) Contour plots with valve deformation at time-points spanning 0 – 0.11s for bicuspid (top) and tricuspid (bottom) valves (b) Violin plot of the von Mises stress at 0.11s across the bicuspid and tricuspid valves

7.4 Discussion

In this chapter, a 3D FSI model was developed using the commercially-available Abaqus/CEL method to examine the potential of FSI to predict hydrodynamic performance of replacement heart valves. This study provides an in-depth comparison between in silico predictions and in vitro flow measurements on both a tricuspid and bicuspid valve configuration in the context of the ISO 5840 standard. It was found that the FSI simulations could capture qualitative and quantitative features of valve deformation, with the in silico models closely predicting maximum GOAs in both valve configurations. Comparing the predictions of ISO 5840 parameters, the in silico model captured the distinct performance differences between bicuspid and tricuspid valves and provided a close match for EOA and transvalvular ΔP for the bicuspid valve. However, the in silico model did not provide accurate predictions for EOA and transvalvular ΔP for the tricuspid valve. This study has important implications for wider FSI simulations in the aortic field, as it suggests that validation of models by examining GOA in isolation may not be sufficient.

A wide range of 3D FSI frameworks have been implemented to predict the fluid and structural performance of AVRs. While several authors have proposed that FSI simulations could also be used for in silico bench testing to enable predictions of ISO 5840 parameters (Chen and Luo, 2018; Hsu et al., 2015; Mao et al., 2016), few studies have included any comparison to in vitro experiments or in vivo data (Borowski et al., 2018; Chen and Luo, 2018; Flamini et al., 2016). This study investigated the potential of the Abaqus/CEL method to predict performance metrics of EOA and ΔP , as well as comparing the GOA and leaflet motion. Many other studies have compared FSI predictions to experimental leaflet kinematics and opening configurations. In many cases, this has been done somewhat qualitatively where side-by-side comparisons of valve deformation are compared (Gharaie et al., 2018), or in other cases the maximum GOA between model and experiment are compared as a validation step. Similarly, this study

demonstrated that the in silico models could closely predict the maximum GOAs in both valve configurations, however, the in silico models demonstrated that the GOA over the course of the pressure cycle were not in agreement throughout, particularly for the tricuspid case. As a consequence of this, the predicted EOA for the tricuspid case was much lower than what was measured experimentally. For in vitro testing, the measured EOA is determined based on the Gorlin formula, which uses the ratio of flow rate to transvalvular ΔP (Gorlin and Gorlin, 1951) averaged over the cardiac cycle. This raises an important issue in the context of validation of FSI simulations for aortic valve design, in that EOA measured according to the context of ISO 5840 is evaluated over the course of the entire pressure cycle. Therefore, validation activities for aortic valves cannot be based on a single time-point or based on a peak value (e.g. GOA), but instead should consider the overall valve performance during the opening systolic step. Despite this, while the predicted in silico results for the tricuspid case were not in agreement with experiments, it is worth noting that the bicuspid configuration provided very good agreement with the measured experimental values, where the predicted EOA and transvalvular ΔP within 5% of experimental values. The bicuspid model may have provided a better prediction as it is a more stable configuration, having only one free leaflet, compared to three in the tricuspid case. This meant that during the opening systolic phase, there were fewer dynamic effects and less oscillation observed experimentally and computationally, making it easier to capture overall deformation. This perhaps provides some potential for further FSI studies of valves using the Abaqus/CEL method, with further model and parameters optimisation required for more complex tricuspid cases.

This chapter provided a quantitative comparison of the performance of a tricuspid and bicuspid valve using both in vitro hydrodynamic analysis and FSI simulations. While a polymer prosthetic valve was used, the study was conducted using generic tricuspid and bicuspid valve designs and these findings could be relevant in understanding the performance of native valves

and congenital or acquired bicuspid valves. Bicuspid valves are present in approximately 1-2% of the population worldwide (Sievers and Schmidtke, 2007) and at least a third of patients with bicuspid aortic valves develop pathologies such as calcific aortic valve disease, aortic stenosis or regurgitation (Verma and Siu, 2014). While clinical studies have established that bicuspid valves exhibit stenotic performance, this study provided quantitative results from in vitro experiments highlighting the difference in transvalvular pressure drop and EOA when compared with a tricuspid valve. In particular, it was demonstrated that the bicuspid valve showed substantially higher pressure gradients, an eccentric jet and higher jet velocities and reduced EOA, compared to the tricuspid. Based on the FSI approach, it was also found that this bicuspid configuration subjected the valves to increased levels of valvular stress. These results highlight the substantial alterations to valvular biomechanics in bicuspid configurations and provide insight into why clinical studies have shown that approximately one quarter of patients with a bicuspid valve presented with high jet velocities and pressure gradients, while half of the patients presented with aortic regurgitation (Michelena et al., 2011).

This study has several limitations that mainly arose due to the complexity of the modelling framework that was implemented. Firstly, the FSI simulation did not provide an accurate prediction of EOA in the tricuspid case and saw distinct differences in the predicted GOA over the loading cycle. One reason this may have arisen is due to the immersed boundary formulation of the Abaqus/CEL, which utilises an initial definition of the fluid location within the Eulerian domain using a volume of fluid (VOF) function. Throughout the simulation, there were areas of large deformation and acceleration and the fluid region separated from the leaflets resulting in void regions. This was present behind the leaflets, while the jet velocity profile emerging from the valve orifice during systole remained intact, allowing for pressure and velocity measurements. However, this void region could have affected the predicted results and the feature was previously described by Bavo et al (2016). For this reason, the study did

not focus on diastole, which thereby means that RF was not predicted. The Abaqus/CEL implementation also resulted in certain imperfections near the fluid-solid boundary, which meant that there was little focus on parameters such as local flow velocities or wall shear stress. The fluid-solid boundary is implemented through the general contact algorithm in Abaqus Explicit. Forces are transferred at the boundaries of fluid and solid, but due to the fixed fluid mesh and moving Lagrangian structure, are interpolated across the elements where the interaction occurs. This results in a less accurate condition at the boundaries than in a flexible ALE mesh simulation. In addition, the Abaqus/CEL method is incapable of modelling turbulence, and is better suited to laminar flow, which the high velocity pulsatile flow of a heart valve is not. This is an obvious omission of the study and the Abaqus/CEL method. A mesh independence study was omitted due to the computational scale of the FSI model. Rather the work here has relied on the experimental comparisons to gauge the validity of the model. Finally, due to the computational cost, it was necessary to thicken the valve leaflets in the FSI simulation to achieve a larger minimum element size in the fluid domain, which is governed by the VOF, which requires at least 3 elements in the fluid domain across the Lagrangian structure. To compensate for this, the elastic modulus of the leaflet was scaled accordingly to provide a structure that exhibited the same axial stiffness. While this represents a simplification of the actual conditions, it was found that both the bicuspid and tricuspid cases showed similar leaflet deformations and so this appeared to be a reasonable assumption. It is worth noting that many other finite element and FSI simulations on aortic valves have simplified the leaflets to 2D shell elements, which would suffer from limitations to those in this chapter.

7.5 Conclusions

In this study, the Abaqus/CEL method was used to investigate its potential to model and evaluate the hydrodynamic performance of aortic valves. It represented the first direct comparison of the Abaqus/CEL method with a pulsatile flow rig for AVRs. The study

examined a bicuspid and tricuspid valve in silico, with an in vitro counterpart to evaluate the accuracy of the simulations. Hydrodynamic performance was measured in terms of EOA and transvalvular ΔP , while the overall leaflet deformation and GOA were also examined. It was found that while there was good agreement across the models and experiment for the bicuspid valve, there was difficulty simulating the tricuspid valve due to the highly dynamic nature of the unconstrained leaflets and several limitations of the method.

7.6 References

- Abu Bakar, H., Abas, A., Mokhtar, N.H., Razak, N., Hamid, M.N.B.A., 2018. Particle image velocimetry and finite volume method study of bi-leaflet artificial heart valve. *J. Appl. Fluid Mech.* 11, 1365–1375. <https://doi.org/10.29252/jafm.11.05.28808>
- Ahmadzadeh, M., Saranjam, B., Hoseini Fard, A., Binesh, A.R., 2014. Numerical simulation of sphere water entry problem using Eulerian-Lagrangian method. *Appl. Math. Model.* 38, 1673–1684. <https://doi.org/10.1016/j.apm.2013.09.005>
- Akins, C.W., Travis, B., Yoganathan, A.P., 2008. Energy loss for evaluating heart valve performance. *J. Thorac. Cardiovasc. Surg.* 136, 820–833. <https://doi.org/10.1016/j.jtcvs.2007.12.059>
- Amindari, A., Saltik, L., Kirkkopru, K., Yacoub, M., Yalcin, H.C., 2017. Assessment of calcified aortic valve leaflet deformations and blood flow dynamics using fluid-structure interaction modeling. *Informatics Med. Unlocked* 9, 191–199. <https://doi.org/10.1016/j.imu.2017.09.001>
- Bavo, A.M., Rocatello, G., Iannaccone, F., Degroote, J., Vierendeels, J., Segers, P., 2016. Fluid-Structure Interaction Simulation of Prosthetic Aortic Valves: Comparison between IB and Arbitrary Lagrangian-Eulerian Techniques for the Mesh Representation. *PLoS One* 11. <https://doi.org/10.1371/journal.pone.0154517>
- Borowski, F., Sämam, M., Pfensig, S., Wüstenhagen, C., Ott, R., Kaule, S., Siewert, S., Grabow, N., Schmitz, K.P., Stiehm, M., 2018. Fluid-structure interaction of heart valve dynamics in comparison to finite-element analysis. *Curr. Dir. Biomed. Eng.* 4, 259–262. <https://doi.org/10.1515/cdbme-2018-0063>
- Chen, Y., Luo, H., 2018. A computational study of the three-dimensional fluid–structure interaction of aortic valve. *J. Fluids Struct.* 80, 332–349. <https://doi.org/10.1016/j.jfluidstructs.2018.04.009>
- Ducobu, F., Arrazola, P.J., Rivière-Lorphèvre, E., Zarate, G.O. De, Madariaga, A., Filippi, E., 2017. The CEL Method as an Alternative to the Current Modelling Approaches for Ti6Al4V Orthogonal Cutting Simulation. *Procedia CIRP* 58, 245–250. <https://doi.org/10.1016/j.procir.2017.03.188>
- Ducobu, F., Rivière-Lorphèvre, E., Filippi, E., 2016. Application of the Coupled Eulerian-Lagrangian (CEL) method to the modeling of orthogonal cutting. *Eur. J. Mech. A/Solids* 59, 58–66. <https://doi.org/10.1016/j.euromechsol.2016.03.008>
- Flamini, V., DeAnda, A., Griffith, B.E., 2016. IB-finite element model of fluid–structure interaction in the aortic root. *Theor. Comput. Fluid Dyn.* 30, 139–164. <https://doi.org/10.1007/s00162-015-0374-5>
- Garcia, D., Kadem, L., 2006. What do you mean by aortic valve area: Geometric orifice area, effective orifice area, or Gorlin area? *J. Heart Valve Dis.*
- Gharaie, S.H., Mosadegh, B., Morsi, Y., 2018. In Vitro Validation of a Numerical Simulation of Leaflet Kinematics in a Polymeric Aortic Valve Under Physiological Conditions. *Cardiovasc. Eng. Technol.* 9, 42–52. <https://doi.org/10.1007/s13239-018-0340-7>
- Ghosh, R.P., Marom, G., Rotman, O.M., Slepian, M.J., Prabhakar, S., Horner, M., Bluestein, D., 2018. Comparative fluid-structure interaction analysis of polymeric transcatheter and

- surgical aortic valves' hemodynamics and structural mechanics, *Journal of Biomechanical Engineering*. <https://doi.org/10.1115/1.4040600>
- Gorlin, R., Gorlin, S.G., 1951. Hydraulic formula for calculation of the area of the stenotic mitral valve, other cardiac valves, and central circulatory shunts. I. *Am. Heart J.* 41, 1–29. [https://doi.org/10.1016/0002-8703\(51\)90002-6](https://doi.org/10.1016/0002-8703(51)90002-6)
- Hsu, M.C., Kamensky, D., Xu, F., Kiendl, J., Wang, C., Wu, M.C.H., Mineroff, J., Reali, A., Bazilevs, Y., Sacks, M.S., 2015. Dynamic and fluid–structure interaction simulations of bioprosthetic heart valves using parametric design with T-splines and Fung-type material models. *Comput. Mech.* 55, 1211–1225. <https://doi.org/10.1007/s00466-015-1166-x>
- Kandail, H.S., Trivedi, S.D., Shaikh, A.C., Bajwa, T.K., O’Hair, D.P., Jahangir, A., LaDisa, J.F., 2018. Impact of annular and supra-annular CoreValve deployment locations on aortic and coronary artery hemodynamics. *J. Mech. Behav. Biomed. Mater.* 86, 131–142. <https://doi.org/10.1016/j.jmbbm.2018.06.032>
- Luraghi, G., Migliavacca, F., García-González, A., Chiastra, C., Rossi, A., Cao, D., Stefanini, G., Rodriguez Matas, J.F., 2019. On the Modeling of Patient-Specific Transcatheter Aortic Valve Replacement: A Fluid–Structure Interaction Approach. *Cardiovasc. Eng. Technol.* 10, 437–455. <https://doi.org/10.1007/s13239-019-00427-0>
- Luraghi, G., Wu, W., De Gaetano, F., Rodriguez Matas, J.F., Moggridge, G.D., Serrani, M., Stasiak, J., Costantino, M.L., Migliavacca, F., 2017. Evaluation of an aortic valve prosthesis: Fluid-structure interaction or structural simulation? *J. Biomech.* 58, 45–51. <https://doi.org/10.1016/j.jbiomech.2017.04.004>
- Mao, W., Li, K., Sun, W., 2016. Fluid–Structure Interaction Study of Transcatheter Aortic Valve Dynamics Using Smoothed Particle Hydrodynamics. *Cardiovasc. Eng. Technol.* 7, 374–388. <https://doi.org/10.1007/s13239-016-0285-7>
- Michelena, H.I., Khanna, A.D., Mahoney, D., Margaryan, E., Topilsky, Y., Suri, R.M., Eidem, B., Edwards, W.D., Sundt, T.M., Enriquez-Sarano, M., 2011. Incidence of aortic complications in patients with bicuspid aortic valves. *JAMA - J. Am. Med. Assoc.* 306, 1104–1112. <https://doi.org/10.1001/jama.2011.1286>
- Morrison, N., Gorash, Y., Hamilton, R., 2018. Consideration of fluid-structure interaction with the CEL approach for the FE-prediction of a blow-off pressure for an elastomeric seal. *24th Int. Conf. Fluid Seal.* 31–45.
- Piatti, F., Sturla, F., Marom, G., Sherif, J., Claiborne, T.E., Slepian, M.J., Redaelli, A., Bluestein, D., 2016. Polymeric Valve Using a Fluid-Structure Interaction Approach 48, 3650–3658. <https://doi.org/10.1016/j.jbiomech.2015.08.009.Hemodynamic>
- Qiu, G., Henke, S., Grabe, J., 2011. Application of a Coupled Eulerian-Lagrangian approach on geomechanical problems involving large deformations. *Comput. Geotech.* 38, 30–39. <https://doi.org/10.1016/j.compgeo.2010.09.002>
- Rahmani, B., Tzamtzis, S., Ghanbari, H., Burriesci, G., Seifalian, A.M., 2012. Manufacturing and hydrodynamic assessment of a novel aortic valve made of a new nanocomposite polymer. *J. Biomech.* 45, 1205–1211. <https://doi.org/10.1016/j.jbiomech.2012.01.046>
- Rahmani, B., Tzamtzis, S., Sheridan, R., Mullen, M.J., Yap, J., Seifalian, A.M., Burriesci, G., 2017. In Vitro Hydrodynamic Assessment of a New Transcatheter Heart Valve Concept (the TRISKELE). *J. Cardiovasc. Transl. Res.* 10, 104–115.

<https://doi.org/10.1007/s12265-016-9722-0>

- Rotman, O.M., Kovarovic, B., Chiu, W.C., Bianchi, M., Marom, G., Slepian, M.J., Bluestein, D., 2019. Novel Polymeric Valve for Transcatheter Aortic Valve Replacement Applications: In Vitro Hemodynamic Study. *Ann. Biomed. Eng.* 47, 113–125. <https://doi.org/10.1007/s10439-018-02119-7>
- Sievers, H.H., Schmidtke, C., 2007. A classification system for the bicuspid aortic valve from 304 surgical specimens. *J. Thorac. Cardiovasc. Surg.* 133, 1226–1233. <https://doi.org/10.1016/j.jtcvs.2007.01.039>
- Sturla, F., Piatti, F., Jaworek, M., Lucherini, F., Pluchinotta, F.R., Siryk, S. V., Giese, D., Vismara, R., Tasca, G., Menicanti, L., Redaelli, A., Lombardi, M., 2020. 4D Flow MRI hemodynamic benchmarking of surgical bioprosthetic valves. *Magn. Reson. Imaging* 68, 18–29. <https://doi.org/10.1016/j.mri.2020.01.006>
- Sturla, F., Ronzoni, M., Vitali, M., Dimasi, A., Vismara, R., Preston-Maher, G., Burriesci, G., Votta, E., Redaelli, A., 2016. Impact of different aortic valve calcification patterns on the outcome of transcatheter aortic valve implantation: A finite element study. *J. Biomech.* 49, 2520–2530. <https://doi.org/10.1016/j.jbiomech.2016.03.036>
- Verma, S., Siu, S.C., 2014. Aortic Dilatation in Patients with Bicuspid Aortic Valve. *N. Engl. J. Med.* 370, 1920–1929. <https://doi.org/10.1056/nejmra1207059>

CHAPTER 8

Concluding Remarks and Future Perspectives

8.1 Summary of Key Contributions

Over 300,000 aortic valve replacement (AVR) procedures are performed in the developed world each year (Manji et al., 2012). The complex function of the aortic valve results in difficulties designing AVRs, with significant amounts of trial-and-error prototyping and extensive experimental testing required to evaluate their performance. Computational simulations have the potential to streamline the development process, although there are still key issues in the implementation and validation of modelling approaches. These need to be addressed to ensure robust predictions of both structural and hydrodynamic performance of AVRs.

The overall contribution of this thesis has been to develop several *in silico* modelling frameworks to predict both the structural and hydrodynamic performance of polymer-based AVRs. Firstly, a finite element analysis (FEA) approach was developed that enabled predictions of the hydrodynamic performance of AVRs, which had the potential to streamline the design process of these devices. Furthermore, both 2D and 3D fluid-structure interaction

(FSI) models were developed to provide structural and hydrodynamic insight into AVRs, which could be utilised for in silico bench testing. Throughout each study, detailed experimental testing was carried out in parallel with all model development to provide relevant model input data and serve as a means for verification and validation of models that were developed. The key scientific contributions were to provide detailed insight into how asymmetric and non-uniform calcification affected valvular performance, while also providing insight into the relative differences in valvular performance between bicuspid and tricuspid valve configurations. The thesis also highlighted the distinct challenges in validating FSI-based models of structural and hydrodynamic performance of AVRs, while providing much-needed experimental data to this community.

In **Chapter 4**, an experimental investigation into the in silico modelling of aortic valves was performed with extensive in vitro comparisons. It was demonstrated through in silico modelling that finite element simulations could predict several surrogate measures for bulk hydrodynamic performance of aortic valves (Whiting et al., 2022). The proposed measures were in silico geometric orifice area (GOA), leaflet contact area (LCA) and pressure at 40% opening ($P_{OA40\%}$), which were proposed as surrogate measures for effective orifice area (EOA), regurgitant fraction (RF) and transvalvular pressure (ΔP) respectively. This was the first study to directly compare these in silico parameters with their in vitro counterparts through an extensive study and regression analysis, contributing to the scientific knowledge for design of aortic valves. It was shown that the in silico testing framework developed provided insight into both structural and hemodynamic performance of aortic valve designs, finding Valve A and B to produce comparable results, while Valve C had increased EOA but with increased RF. Furthermore, it was shown through in vitro hydrodynamic testing that all 23 mm polymer valve prototypes tested met the minimum requirements of 1.25cm^2 for EOA set out by ISO 5840, while Valve C was the only valve to fail the requirement of $\leq 10\%$ RF.

Following on from the work of the previous chapter, in **Chapter 5**, an in silico framework demonstrated the ability of structural finite element modelling to investigate the effects of increasing calcification on the degeneration of hydrodynamic performance of the aortic valve. Specific calcification scenarios, asymmetric or symmetric, and regional calcification were investigated. These results clearly demonstrated that hydrodynamic performance is negatively impacted with increasing calcification for all scenarios considered. It was found that the more asymmetric the calcification coverage, the more detrimental this was to valve systolic GOA. In contrast however, symmetric calcification was actually more detrimental to transvalvular pressure, diastolic GOA and LCA than asymmetric patterns. For highly unsymmetric patterns, where calcification was confined to one leaflet, it was found that non-calcified leaflets would conform to the disabled leaflet, resulting in reasonably adequate diastolic conditions. The results of this study demonstrated that this in silico testing framework could provide insight into the effects of calcification or stiffening on the hydrodynamic performance of native or prosthetic aortic valves.

Having expanded on the ability of structural FEA to assess the hydrodynamic performance of the valve, the thesis then looked to the development of fully coupled FSI simulations. While many FSI models have been proposed, very few have undergone robust experimental validation. **Chapter 6** presented the development of a benchmarking flow rig for validation of an immersed boundary FSI method. In this chapter, a novel experimental rig was developed that allowed for the observation of a flexible leaflet deformation under 2D steady flow. This study was used to provide the first verification of the Abaqus Coupled Eulerian Lagrangian (CEL) approach in such a flow-based problem and highlighted its potential to be used to investigate the fluid and structural biomechanics of AVRs. Furthermore, this study is one of the first to provide a direct comparison between FSI simulations and experimental deformation of a single valve leaflet. This experimental approach has the potential to be more widely used

as a first-step validation to FSI simulations and has already been implemented to provide validation to other FSI simulations (Mcloone et al., 2021). A further comparison of the Abaqus/CEL model with Arbitrary Lagrangian Eulerian (ALE) 2D valve models from the literature (Amindari et al., 2017) was carried out, showcasing the ability of the method to observe differences in performance of valves in healthy or diseased states.

Chapter 7 directly follows on from the preliminary models of Chapter 6 to develop three-dimensional models of the aortic valve using the Abaqus/CEL FSI method. Two valve configurations, a bicuspid and tricuspid valve, were simulated and compared to in vitro testing in a Vivitro pulse duplicator system. The Abaqus/CEL model was capable of predicting a difference in the hydrodynamic performance between the two valves, but was not ideal for the highly turbulent flow simulation, lacking accuracy with separation of fluid from structure. This study represented the first direct comparison of the Abaqus/CEL method with a pulsatile flow rig for heart valve application and highlighted the challenges with validating such a complex FSI model. Nevertheless, this study provided quantitative insight into the structural and hydrodynamic performance of both bicuspid and tricuspid valve configurations.

8.2 Future Recommendations

The work presented in this thesis has addressed several key topics in relation to aortic valve replacements and the in silico modelling that is used to aid the design and development of these devices. This section provides a discussion of future perspectives.

The computational framework developed in Chapter 4 demonstrated the potential of structural FEA modelling to predict surrogate hydrodynamic performance of tri-leaflet polymer-based AVRs. While this model was used in Chapter 5 to investigate the effect of non-uniform calcification on hydrodynamic performance, the methodology could be more widely applied to investigate other design aspects of tri-leaflet AVRs. Due to the efficiency of the method, a

design of experiments and/or design optimisation strategy could be used to maximise/minimise several of the objective functions related to hydrodynamic and structural performance of the valve. Furthermore, while the valves considered in the study were surgical AVRs, it is expected that the same methodology could be also be applied to transcatheter AVRs. As these are more susceptible to eccentricity upon implantation, it would be of significant interest to investigate how valve eccentricity affects the surrogate hydrodynamic parameters under such a deformed configuration. Finally, it should also be noted that the surrogate parameters in Chapter 4 were validated based on hydrodynamic testing of several tri-leaflet polymer valve designs. To increase the credibility of this model, and make it more widely applicable, further valve types and cases could be included as additional validation for this approach.

This thesis presented one of the first 2D benchmark problems for leaflet deformation in Chapter 6 and showed that the Abaqus/CEL approach was generally able to predict both the structural and hydrodynamic characteristics of this problem in Chapter 6. However, the extension of the model to three dimensions in Chapter 7 led to several challenges in the implementation and validation of this Abaqus/CEL approach. In particular, the computational cost involved required simplifications to the geometry such that only the leaflets themselves were considered, with these being thickened to reduce the need for a highly resolved mesh at the fluid solid interface. While this configuration still predicted leaflet deformations that were similar to those in the experimental flow rig, the hydrodynamic parameter determined through the computational and experimental approaches were not quite comparable. Therefore, there is certainly room for further model development using this approach. In fact, the results of this chapter highlighted that individual measurements of geometric features at individual time-points may not be sufficient to validate the performance of such models, which has important implications for the wider fields. During the course of this project, guidance has been published by the ASME through the V&V40 standard (American Society of Mechanical Engineers,

2018), which provides a risk-informed credibility assessment framework to guide the development of requirements for computational modelling of medical devices. A key part of this is model verification, which requires a detailed investigation of model parameters (e.g. numerical and material) to understand the level of sensitivity in the model predictions to selection of parameters. Due to the substantial complexity of FSI models, and in some cases the lack of availability of open-source code information, detailed verification of models would be extremely useful. Beyond this, the process of validation is also described by the V&V40 standard, whereby additional evidence from in vitro testing and any other supporting pertinent information could be used to assess the level of model credibility, according to a set of prescribed credibility factors.

Finally, the experimental components of this study used prototype polymer valves that were manufactured in-house with a novel polymer that is currently being used as a basis for a newly developed AVR. The in vitro hydrodynamic testing in Chapter 4 showed that all three 23 mm valves meet the minimum requirements for EOA set out by ISO 5840, which is greater than or equal to 1.25 cm^2 at 5 L/min (International Organisation for Standardisation, 2021). While the valves tested were surgical in nature, the development of a TAVR that utilises a suitable polymer is in the near future. Several groups discussed in the literature have developed and tested promising designs such as the Foldax and TRISKELE valves (Kereiakes et al., 2021; Rahmani et al., 2016). The future direction for heart valves could very quickly be directed to this area should an easily manufacturable and cost-effective polymer solution come to market. The modelling could then shift from valve design to polymer durability and fatigue life under different conditions.

8.3 References

- American Society of Mechanical Engineers, 2018. *Assessing the Credibility of Computational Modeling Through Verification and Validation: Application to Medical Devices*, ASME. American Society of Mechanical Engineers.
- Amindari, A., Saltik, L., Kirkkopru, K., Yacoub, M., Yalcin, H.C., 2017. Assessment of calcified aortic valve leaflet deformations and blood flow dynamics using fluid-structure interaction modeling. *Informatics Med. Unlocked* 9, 191–199. <https://doi.org/10.1016/j.imu.2017.09.001>
- Blackman, D.J., Saraf, S., MacCarthy, P.A., Myat, A., Anderson, S.G., Malkin, C.J., Cunnington, M.S., Somers, K., Brennan, P., Manoharan, G., Parker, J., Aldalati, O., Brecker, S.J., Dowling, C., Hoole, S.P., Dorman, S., Mullen, M., Kennon, S., Jerrum, M., Chandrala, P., Roberts, D.H., Tay, J., Doshi, S.N., Ludman, P.F., Fairbairn, T.A., Crowe, J., Levy, R.D., Banning, A.P., Ruparelia, N., Spence, M.S., Hildick-Smith, D., 2019. Long-Term Durability of Transcatheter Aortic Valve Prostheses. *J. Am. Coll. Cardiol.* 73, 537–545. <https://doi.org/10.1016/j.jacc.2018.10.078>
- International Organisation for Standardisation, 2021. ISO 5840:2021 Part 2: Surgically implanted heart valve substitutes.
- Kaneko, T., Aranki, S.F., 2013. Anticoagulation for Prosthetic Valves. *Thrombosis* 2013, 1–4. <https://doi.org/10.1155/2013/346752>
- Kereiakes, D.J., Answini, G.A., Yakubov, S.J., Rai, B., Smith, J.M., Duff, S., Shannon, F.L., Sakwa, M., Beith, J., Heimansohn, D., 2021. Preliminary Evaluation of a Novel Polymeric Valve Following Surgical Implantation for Symptomatic Aortic Valve Disease. *JACC Cardiovasc. Interv.* 14, 2754–2756. <https://doi.org/10.1016/j.jcin.2021.08.071>
- Kostyunin, A.E., Yuzhalin, A.E., Rezvova, M.A., Ovcharenko, E.A., Glushkova, T. V., Kutikhin, A.G., 2020. Degeneration of Bioprosthetic Heart Valves : Update 2020 1–19. <https://doi.org/10.1161/JAHA.120.018506>
- Manji, R.A., Menkis, A.H., Ekser, B., Cooper, D.K.C., 2012. The future of bioprosthetic heart valves. *Indian J. Med. Res.* 135, 150–151.
- Mcloone, M., Fan, Y., Whiting, R., Conway, C., Roche, E., Quinlan, N., 2021. Fluid-Structure Interaction of a Thin Elastic Leaflet – a Comparison of Computational Methods. *European Society of Biomechanics*
- Rahmani, B., Tzamtzis, S., Sheridan, R., Mullen, M.J., Yap, J., Seifalian, A.M., Burriesci, G., 2016. A new transcatheter heart valve concept (the TRISKELE): Feasibility in an acute preclinical model. *EuroIntervention* 12, 901–908. <https://doi.org/10.4244/EIJV12I7A148>
- Rodriguez-Gabella, T., Voisine, P., Puri, R., Pibarot, P., Rodés-Cabau, J., 2017. Aortic Bioprosthetic Valve Durability: Incidence, Mechanisms, Predictors, and Management of Surgical and Transcatheter Valve Degeneration. *J. Am. Coll. Cardiol.* 70, 1013–1028. <https://doi.org/10.1016/j.jacc.2017.07.715>
- Whiting, R., Sander, E., Conway, C., Vaughan, T.J., 2022. In silico modelling of aortic valve implants—predicting in vitro performance using finite element analysis. *J. Med. Eng. Technol.* 46, 220–230. <https://doi.org/10.1080/03091902.2022.2026506>